Imperial College London
Department of Mechanical Engineering

Alternate Passage Divergence of Wide Chord Transonic Fan Blades

Yaozhi Lu

March 13, 2020

Submitted in part fulfilment of the requirements for the degree of
Doctor of Philosophy in Mechanical Engineering of Imperial College London and
the Diploma of Imperial College

Abstract

Due to manufacturing tolerance and deterioration during operation, fan blades in the same engine exhibit geometric variability. The absence of symmetry will inevitably exacerbate and contribute to the complexities of running geometry prediction as the blade variability is bound to be amplified by aerodynamic and centrifugal loading. In this study, the fan blade untwist (which is the blade deformation between its static condition and running condition) related phenomenon known as Alternate Passage Divergence (APD) is addressed. As the name suggests, APD manifests as alternating passage geometry (and hence alternating tip stagger pattern) when the fan stage is operating close to/at peak efficiency condition. APD can introduce adverse influence on fan performance, aeroacoustics behaviour, and high cycle fatigue characteristics of the blade. In this study, the APD behaviours of two transonic fan blade designs are compared. The main objective of the study is to identify the parameters contributing to the APD phenomenon.

After the formation of alternating tip stagger pattern, APD's unsteady effect can cause the blades from one group (segmented by tip stagger angle) to switch to the other, creating a travelling wave pattern around the circumference. It was found from numerical assessment on a randomly mis-staggered assembly that real engines can potentially experience such travelling disturbance and suffer fatigue damage. The phenomenon is termed APD-induced Non-Synchronous Vibration (NSV) and is abbreviated as NSV in this study. An idealised case is used to capture the bulk behaviour from the more complex cases in real engines and to decipher the underlying mechanism of this travelling disturbance. The results indicate that the driving force originates from the interaction between passage shock displacement and the passage geometry.

Based on the findings on APD & NSV, vibration attenuation methods are explored. Using machine learning techniques, a passive attenuation method is found to minimise the chance of NSV manifestation for a given set of fan blades. Alternatively, active attenuation method is implemented through blade redesign which modifies the passage geometry.

Statement of Originality

The work presented in this thesis is, to the best of the candidate's knowledge, original and the candidate's own work, except as acknowledged in the text. The material has not been submitted, either in whole or in part, for a degree or comparable award of Imperial College London or any other university or institution.

Yaozhi Lu
March 13, 2020

Copyright Declaration

Acknowledgements

The last few years spent on the PhD project have been extremely exciting to me. I would like to use the opportunity to reflect on the journey and tip my hat to the friends who have helped me along the way.

> "It's funny that pirates were always going around searching for treasure, and they never realised that the real treasure was the fond memories they were creating."
>
> Jack Handey

Firstly, I would like to thank my supervisor Prof Mehdi Vahdati for his support and encouragement in the last 4 years. I first met Dr Vahdati on a sunny October afternoon while enquiring the Wind Turbine Aeroelasticity MSc project. He introduced me to the fascinating world of aeroelasticity problems during that meeting which has lasted nearly 5 years. Prof Vahdati's seeming impatience is rooted in his raging desire for answers to the research questions and his burning passion for the research field. Prof Vahdati, through his passionate questioning, taught me the value of 'less is more' when telling stories through data. I genuinely appreciate his honest and direct feedback to my work. Other than simply providing course correction, they provide me with an objective overview of my various ventures which helps me to prioritise projects and to manage risks.

Mehdi has firm commitment to the joy of research and unwavering academic integrity. When it comes to publishing research findings, he has strong emphasis on the importance of quality over quantity and ensures every single sentence is verifiable by data. Mehdi is also very open-minded and willing to take risks in research projects. This is strongly evidenced by him giving me the option of experimenting with Machine-Learning-based vibration attenuation techniques, which is arguably outside the original domain of the research. I have learnt a lot from working with Mehdi on this study, and have adopted more flexible and creative approach to solving problems. Beyond the world of research, I enjoyed working with Prof Vahdati on various research outreach projects. Though having to explain to a teenager that the spiral on a Trent 500 fan's spinner does not make it a drill is far from the highlights of my study, I unquestionably delight in planning and coordinating these events.

I'm deeply indebted to Dr Sina Cornelia Stapelfeldt who kindly agrees to be my secondary supervisor for the later half of the journey. Dr Stapelfeldt has offered substantial support, both technical and non-technical, to my research. She is an adept sailor (both metaphorically and literally) and had helped me to ride out the storm when I felt rudderless and oarless, stuck in the eddies of aeroelasticity. I'm extremely grateful for Sina and her friend Blue's continued support and much needed encouragement to help me navigate through the shallow waters in this study. With the three qualities: dream big, get things done, and genuine kindness towards cats, Dr Stapelfeldt is exactly the type of person I enjoy working with.

The Alternate Passage Divergence (APD) study, by its very nature, involves a delicate game of balance with geometry, motion, and aerodynamics. Unsurprisingly, my early effort in elaborating it is widely scattered in a labyrinth of confusion. Therefore, I have deep appreciation of Sina's patience and effort in editing those three inter-linked papers. Through our discussion, she highlighted to me the importance of the underlying messages that words can convey to the readers in a subtle fashion. This had significantly improved the readability of those writings. The most important non-technical skills I've learnt from her are having the courage to say 'I don't know' or 'I was wrong' when presented with challenging evidence, and gracefully accept when others concede their mistakes. These subtle traits let me admit my own ignorance, learn from mistakes, and avoid wasting time defending a wrong position in a futile attempt to avoid embarrassment. Upon reflection, I believe these are in fact the most valuable lessons learnt during the past 4 years of my PhD study.

I would also like to express my gratitude to the friends from Vibration University Technology Centre (VUTC), some of whom are photographed in Figure 1[1]. I was fortunate to have worked with them and really appreciate their support. In particular, I would like to express my special thanks to Dr Zhao and Dr Sureshkumar for sharing their diverse first hand experience with aeroelasticity and aeroacoustics with me. They are the true friends who would grab a chair and listen to my sometimes convoluted description of the problem while others inch towards the door. I

---

[1] Photo taken by Ms Caterina Paralta. On the 1265th day after the start of the PhD project.

Figure 1: VUTC at the Institution of Mechanical Engineers, 2019-05-29.

have learnt a lot from Dr Zhao who has provided guidance to my research since my MSc project. I am also indebted to Dr Sureshkumar whose burning and sometimes concerning passion with programme optimisation had left deep impact on my work. At the same time, I would like to thank Dr Wenqiang Zhang, Mr Venkatesh Suriyanarayanan, and Mr Jose Moreno for their companionship and the many interesting conversations we had in Prince's Gardens. In particular, I would like to thank Dr Zhang for sharing his passion for food and the numerous food-induced adventures with me.

A big thank you, or apology, is due to Mr Peter Higgs. As the VUTC administrator, Mr Higgs has helped me in various administrative issues during my PhD study. During various research outreach projects (Imperial Festival 2017 and 2018) and the technical lecture at the Institution of Mechanical Engineers (IMechE), Peter had shared his wisdom on inter-institutional collaborations with me and offered me vital assistance on the logistics with the precision and efficiency of an invading air force. I deeply appreciate the effort he has put into helping me and for being extremely patient with me.

Throughout the study, I'm also deeply indebted to the help from my industrial sponsor, Rolls-Royce plc. I have learnt a lot from the discussions with Dr Jeff Green, Dr Mark Wilson, Dr Bharat Lad, and Dr Sopholic Patsias. As a student working on a relatively new topic, I have benefited tremendously from the expertise they have shared with me and I am grateful for their help. I would like to express my special thanks to Dr Bharat Lad for allowing me the flexibility to explore some of the new ideas and incorporating some rather unconventional approaches into the existing framework. More importantly, through our incremental understanding of the research problem at hand, we are able to understand the problem better, ask better clarifying questions to direct the research, and push the envelope slightly further. More importantly, I'm grateful for Dr Lad's insights on the industrial relevance of this study and how we can find practical approaches from a macro perspective.

My experience of writing research papers has made me truly appreciate the effort that the reviewers, review chairs, and journal editors have put in to improve the quality of my writing. In particular, I would like to take this opportunity to thank Professor Roque Corral from ITP Aero. The early drafts of my last paper in 2019 were adequate at most, and I appreciate Prof Corral's decision for offering me the chance for a major revision. While editing the paper, I started to understand how some of the reviewers' comments were formed. In fact, I realised that I had overlooked some of my previous results' importance. Thus, I was able to fill in the gap in the reasoning and clarified some of the ambiguous messages. I highly appreciate Prof Corral's recognition of the study and for giving me the revision opportunity.

During the last year of my PhD, I am honoured to have worked with colleagues on the IMechE Greater London Region Young Member Panel. In particular, I enjoyed working on projects with Ms Roshni Wijesekera, and Mr Isfhan Choudhry. At the same time, I am grateful for having been invited to the Aston Martin Red Bull Racing Formula One Team's factory and the All Party Parliamentary Engineering Group (APPEG) meeting in the House of Lords, Parliament of the United Kingdom. From those visits and projects, I gained first-hand experience of managing large scale projects. In addition, the experiences deepened my understanding of the connection among research, engineering, and policy making.

This is also a good opportunity for me to thank my friend Dr Peng Wang[2] from

---

[2] Now at Advanced Design Technology Ltd, Shanghai office.

University College London. Dr Wang had tutored me in *FORTRAN*[3] during my undergraduate study and had introduced me to the field of turbomachinery research. Many of the precursors to the pre-processing programs used in this study are written in *FORTRAN* and our many discussions have proven beneficial for my understanding of the research and industry landscape. Additionally, I appreciate his insights from the engineering consulting perspective and the numerous business opportunities he has provided.

I would like to thank my friend Dr Abel B. Cortinas[4] from Massachusetts Institute of Technology. We first met in 2016 during the Imperial College London - Massachusetts Institute of Technology Global Fellow Program[5]. Over the many conversations we had under the star spangled banner accompanied by the occasional blaring ambulance sirens, Dr Cortinas has shared with me his journey through the PhD study and academia. I appreciate his honest opinions and the enormous effort he has put in to answer my multi-faceted and often endless questions.

Needless to say, the support from my parents, Mr Manchao Lu and Ms Shifang Wang, have been indispensable during my study. I have learnt a lot from my father's entrepreneurship, and my mother's business acumen and problem solving skills. They have been exceptionally supportive with my decision to pursue a PhD and I am deeply indebted to them.

---

[3] Short for *Formula Translation. "FORTRAN, the greatest of the programming languages." - the Simpsons.*

[4] Now at L.E.K. Consulting, Boston office.

[5] Also known as the 'Massachusetts Institute of Technology - Imperial College London Global Fellows Program' by colleagues from Cambridge, MA, USA.

To my parents

If people sat outside and looked at the stars each night, I'll bet they'd live a lot differently. When you look into infinity, you realise that there are more important things than what people do all day.

Bill Watterson, Calvin and Hobbes

Contents

List of Tables

List of Figures

Nomenclature

Abbreviations

1F	First Flapwise Mode
1T	First Torsional Mode
2F	Second Flapwise Mode
APD	Alternate Passage Divergence
CART	Classification and Regression Tree
CF	Centrifugal
CFD	Computational Fluid Dynamics
CPU	Central Processing Unit
ENS	Ensemble
EO	Engine Order
ESS	Engine Section Stator
FEA	Finite Element Analysis
FFT	Fast Fourier Transform
FSI	Fluid-Structure Interaction
GE	General Electric
HCF	High Cycle Fatigue
HPC	High Performance Computing
LE	Leading Edge
LRC	Logistic Regression Classification/Classifier
ML	Machine Learning
MPT	Multiple Pure Tone
MRO	Maintenance, Repair, and Overhaul
MSE	Mean Square Error
ND	Nodal Diameter

NSV	Non-Synchronous Vibration
OGV	Outlet Guide Vane
RMSE	Root Mean Square Error
RR	Rolls-Royce plc
SLS	Sea-Level-Static
SVC	Support Vector Classification/Classifier
SVM	Support Vector Machine
TE	Trailing Edge
TNR	True Negative Rate
TPR	True Positive Rate
VUTC	Vibration University Technology Centre, Imperial College London

Greek Symbols

Φ	Mass Normalised Mode Shape
σ	Sigmoid Function
θ	Feature Weight
ζ	Damping Ratio
ω_n	Natural Frequency

Latin Symbols

$\ddot{q}$	Acceleration (modal)
$\ddot{x}$	Acceleration (actual)
$\dot{q}$	Velocity (modal)
$\dot{x}$	Velocity (actual)
$\hat{p}$	Estimated Probability
$\hat{y}$	Predicted Class
C	Damping
E	Entropy (impurity measure in the CART algorithm)
F	Force (Matrix)
f	Force (vector)
G	Gini Index
h	Hypothesis Function
J	Cost Function
K	Stiffness (Matrix)

k	Modal Stiffness
M	Mass (Matrix)
m	Modal Mass
m	Number of instances (Machine Learning)
q	Modal Displacement
r	Mode Number
X	Geometry
x	Feature (Machine Learning)
x	Physical Displacement
y	Actual Class
$p_{i,j}$	Ratio of Class k instances among the training instances in the i^{th} mode.

Chapter 1

Introduction

> Anticipating problems and figuring out how to solve them is actually the opposite of worrying: it's productive.
>
> Chris Hadfield
> *An Astronaut's Guide to Life on Earth [1]*

1.1 Chapter Introduction

The research conducted in this thesis revolves around providing better running geometry prediction of transonic fan blades and to anticipate the aeroelastic instabilities accompanied by the current fan blade development trend. In order to formulate the research questions, it is necessary to understand the relevant engineering issues involved. Therefore, this chapter starts by investigating the current trend in civil aviation industry and to explore the implication of these trends on the civil jet engine manufacturers. Thus, this provides the background of the research and highlights the industrial relevance of the study. This is followed by the introduction of the guiding questions the study is designed to answer.

Secondly, an overview of the aeroelastic issue of interest is presented. Together with a literature review, the overview explores how each of the aeroelastic issue's adverse effects can impact fan performance and how that alters the fan designer's design approach. Lastly, a detailed breakdown of the thesis structure, which explains how each chapter is integrated into the study and how it address the research problems, is presented.

1.2 The Future of Civil Aviation and Motivation for the Study

1.2.1 Rising Demand for Civil Air Transport

Over the past few decades, the civil aviation industry has witnessed a steady increase in the global demand for air transport despite various crises that had hampered global economic development. As illustrated by the historical trends in Figure 1.1[1] , both the passenger transport and the freight services sector show an approximately 5% compound annual growth rate. More importantly, as illustrated by the year-to-year growth rate breakdown in Figure 1.2, the crises' effects tend to be short-lived regardless of the nature of the disruption. Besides, in terms of time period of influence and changes in annual growth rate, the crises affect the two sectors slightly differently. Thus, it is reasonable to extrapolate that the global demand will experience steady and enduring growth, and it is widely agreed that the air traffic is expected to experience an approximately 4.5% compound annual growth rate in the foreseeable future [5].

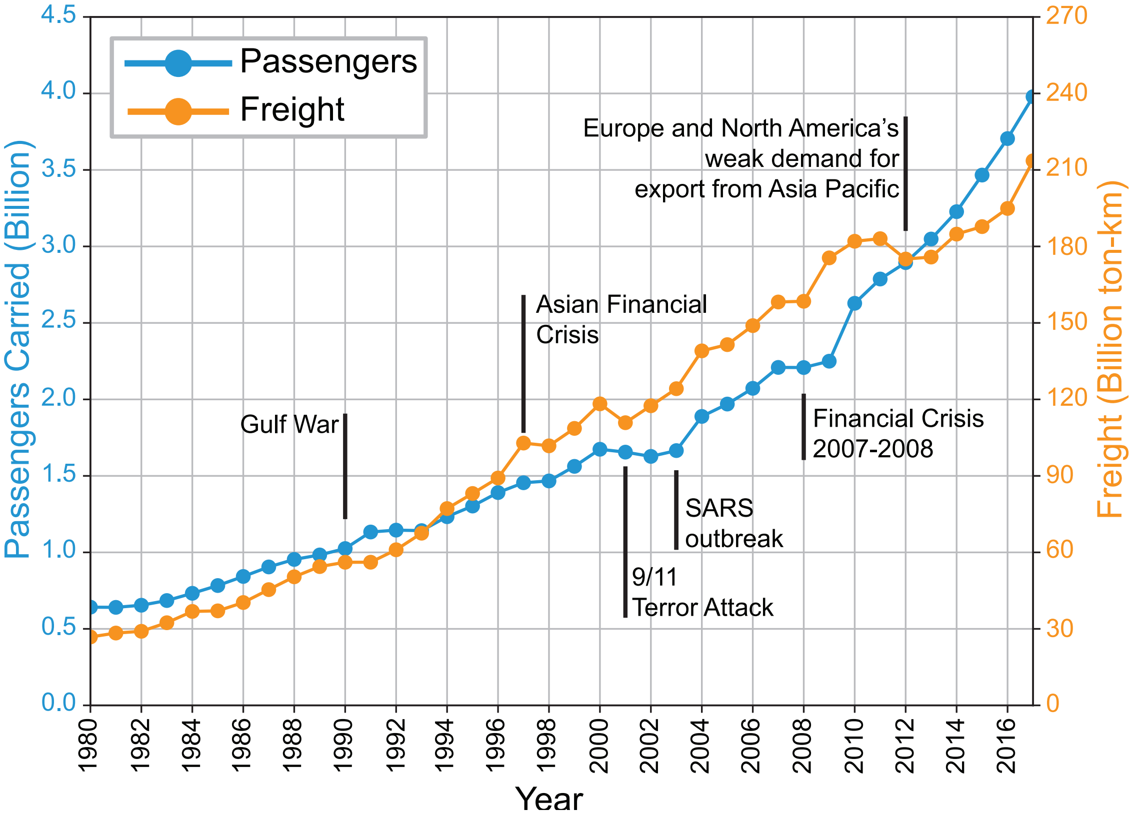

Figure 1.1: Trend in global air transport.

---

[1] Source: International Civil Aviation Organization [2–4].

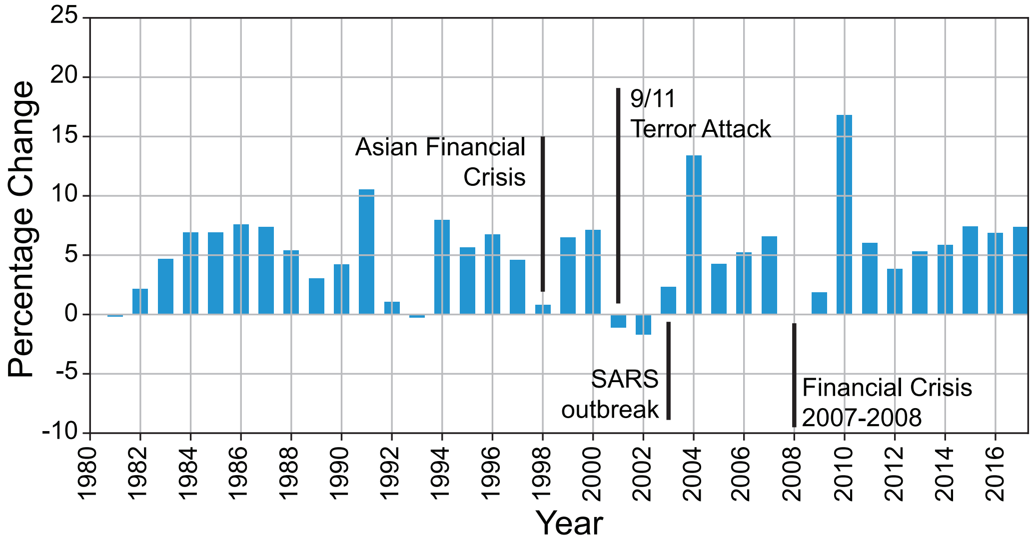

(a) Passengers carried.

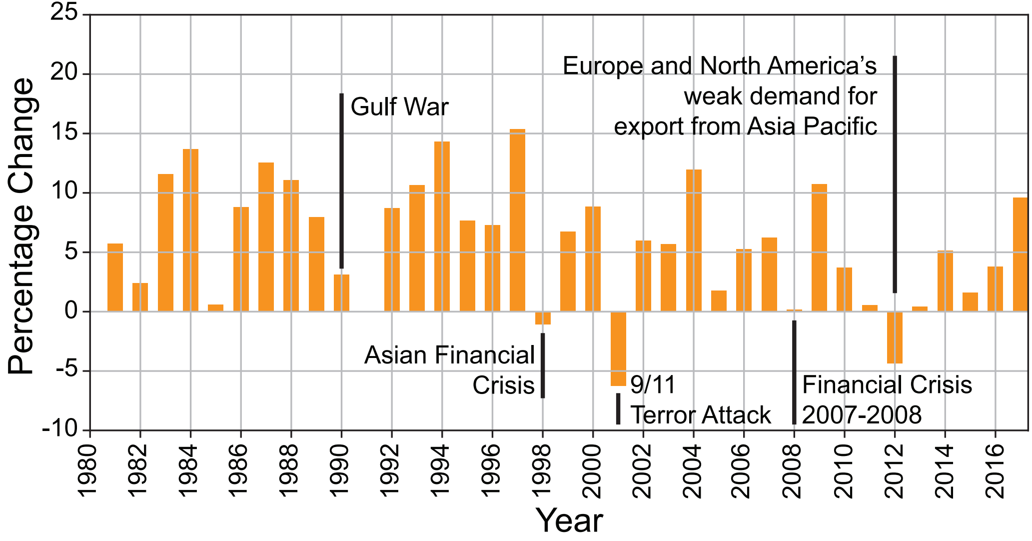

(b) Air freight.

Figure 1.2: Growth in global air transport.

1.2.2 Consequences of the Rising Demand

Two implications from the positive forecast for global air transport are: (1) the global aircraft fleet will expand to anticipate the increase in demand, and (2) it provides significant incentive for civil jet engine manufactures to develop more efficient engines to stay ahead of the competition and to reduce the engines' environmental impact (i.e. reduced emission). The discussion in this thesis is primarily focused on the high by-pass ratio turbofan engines, such as the one shown in Figure 1.3[2]. They are widely used on narrow body and wide body commercial aircraft which account for 77.9% of global commercial air transport fleet[3] in 2019 [6].

---

[2] Adapted from the Advance 3 render image © Rolls-Royce plc.

[3] The other two minor sectors are regional jets and turboprops.

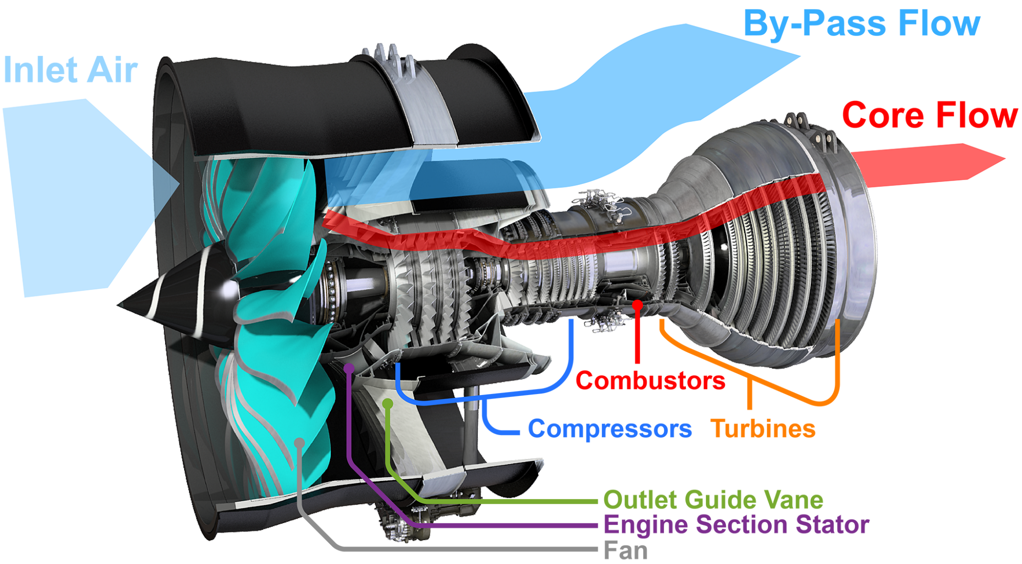

Figure 1.3: Modern high bypass ratio turbofan engine.

Expanding Global Fleet and Maintenance Sector

It is estimated [6] that the global fleet will grow at a rate of 3.6% for the period from 2019 to 2029[4]. The ageing fleets in some of the fastest growing regions[5] poses strong demand for the Maintenance, Repair, and Overhaul (MRO) sector which is estimated to grow at a rate of 3.5% globally in the same period. Engine maintenance constitutes a significant portion of this market. In 2019, 40.8% (approximately 33.4 billion US dollars) of global commercial aviation MRO spending is on the engines [6]. This is true even for jet engine manufacturers. In the case of Rolls-Royce plc's civil aerospace division, the underlying revenue from after market service accounts for over half (52% to 58%) of the total underlying revenue over the 2015-2018 period [5, 7–9]. At the same time, the global cost of unscheduled maintenances (i.e. through cancellation, delay, and aircraft lease) is also in the range of tens of billions USD and can also inflict significant reputation damage to the parties involved (i.e. carrier, aircraft manufacturer, and engine manufacturer) [5, 10]. Therefore, there is strong incentive for the engine manufacturers to improve engine reliability and to limit the maintenance cost in order to make their engines more attractive to the customers.

---

[4] More detailed data are included in Appendix A.

[5] Asia Pacific, China, and India are expected to account for 59.9% (6995 aircraft) of the global fleet growth for the period from 2019 to 2029 [6].

The Search for More Efficient Engines

In recent years, jet engine manufacturers have adopted the practice (shown in Figure 1.4[6]) of using longer and lighter fan blades in turbofan engines, with the increase in by-pass ratio and hence the increase in fan diameter being the primary driver for fan performance optimisation [12]. This is clearly evident from the development trends [13–31] of the fan blade captured in Figure 1.5. By segmenting the data points into those manufactured by one company (i.e. Rolls-Royce plc) and those by other manufacturers, the evolution of designs under the same design philosophy can be observed. Another seismic shift accompanying this development trend is the switch from hollow titanium fan blades (e.g. Trent 1000 and GP7200) to carbon-titanium-composite[7] (e.g. GEnx and Rolls-Royce Ultrafan) fan blades to save weight and thus improve performance.

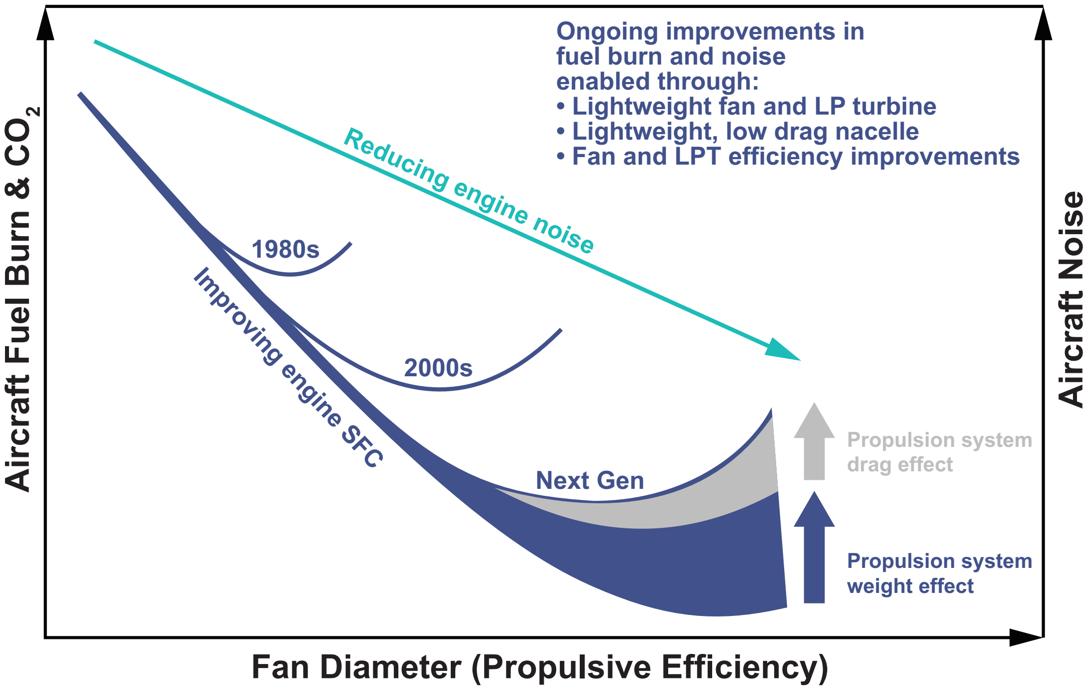

Figure 1.4: Development trends for Fans in Civil Aero Engines.

The trend of introducing longer and more flexible blades complicates the running geometry prediction of the blades while the blade architecture change (i.e. from titanium to composite-titanium) demands shift in the assessment method. This will be elaborated in the following sections.

---

[6] Adapted from Whurr, 2013 [11].

[7] The main structure is fabricated with carbon-fibre composite and a titanium leading edge is used to minimise the effect of Foreign Object Damage (FOD). The root of the blade is typically made of titanium.

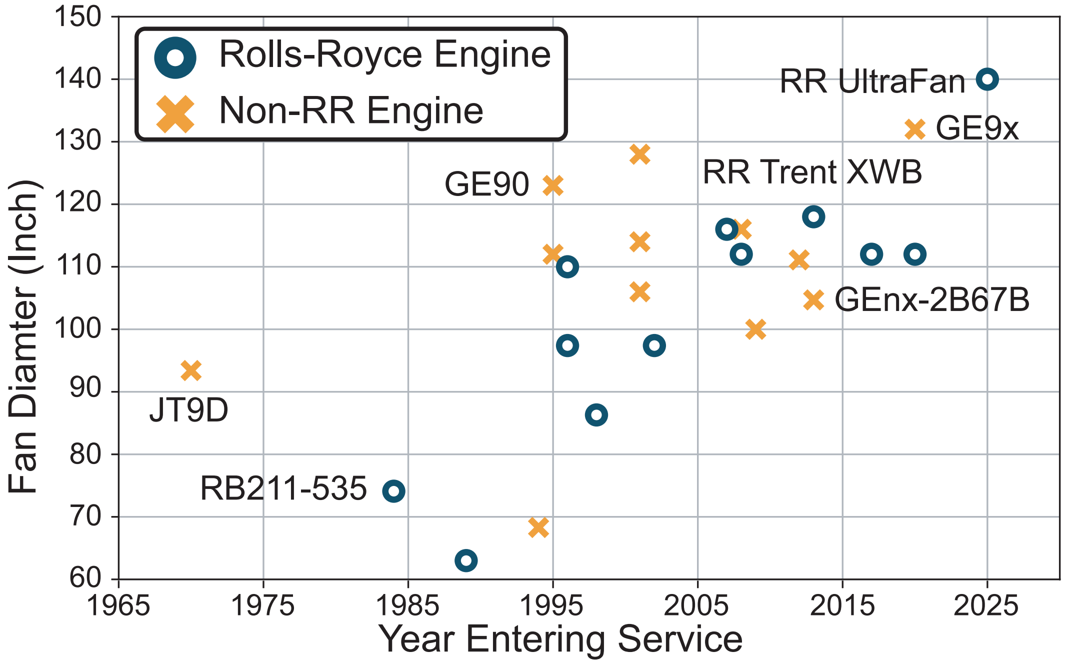

Figure 1.5: Trend in civil turbofan fan diameter.

1.2.3 Motivation for this Study and Introduction to Alternate Passage Divergence

In order to understand the research question in this study, it is vital to have a basic understanding of the fan aerodynamics and its untwist behaviour. Detailed discussion will continue in Chapter 3. The fan characteristics map, such as the schematics shown in Figure 1.6, can be divided into three regions based on the passage shock position at blade tip. As illustrated in Figure 1.7, Type A flow condition (a.k.a. unstarted flow) can be characterised by the expelled shock at the tip where as Type C flow condition (a.k.a. started flow) is characterised by the swallowed passage shock. The intermediate flow condition, Type B, is signified by the passage shock resting on the leading edge of the trailing blade (in term of rotation). In term of operating conditions, Type A flow condition occurs towards the stall side of the constant speed lines while Type C flow condition occurs towards the choke side. Type B flow condition occurs in-between the two extremes and is typically where the peak efficiency condition is [32–34]. As will be demonstrated in Chapter 3, across the same constant speed line, blades under Type A flow condition experience the most aerodynamically induced moment while those associated with Type C experience the least amount. As the name suggest, under the intermediate flow of Type B, the amount of aerodynamically induced moment on the blades is in-between those at the other two conditions.

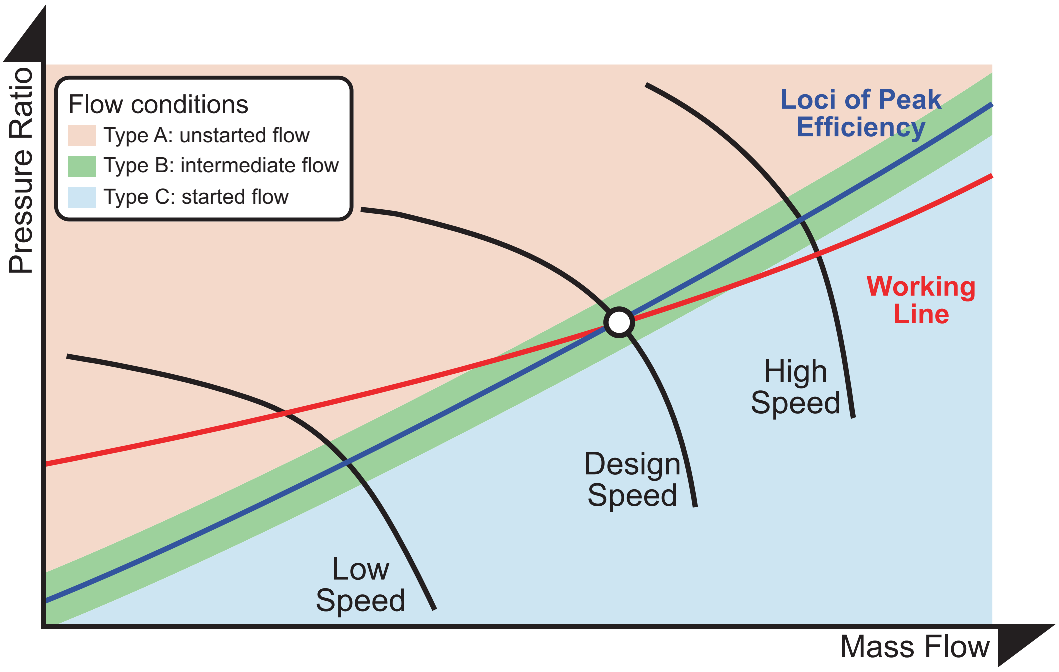

Figure 1.6: Schematic fan characteristic map.

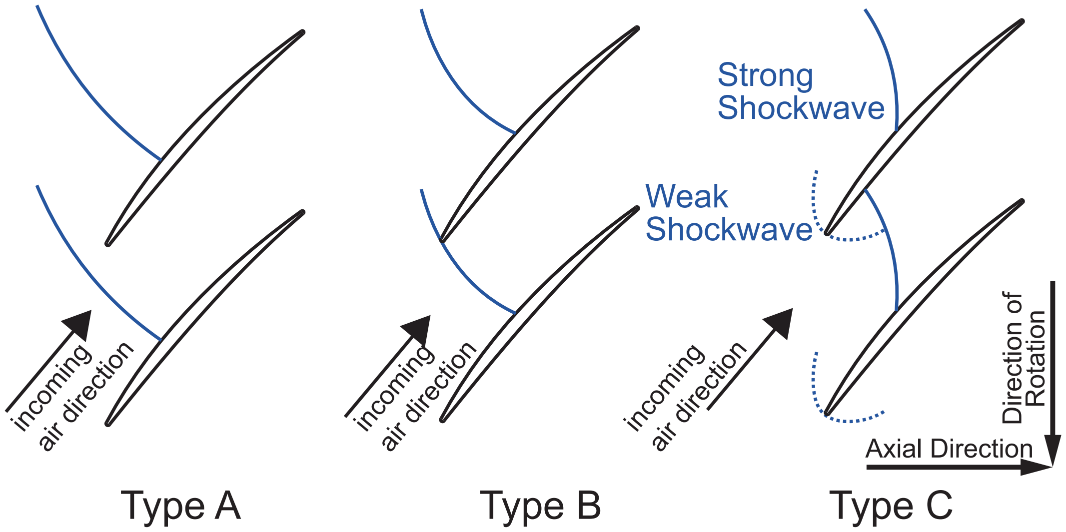

Figure 1.7: 3 types of flow regime and the shockwave structure at blade tip.

The working line in Figure 1.6 represents the loci of possible operating conditions of a fan. This is due to the fact that most civil gas turbine engines have a fixed exhaust nozzle, with the exception of the Rolls-Royce Olympus engine (a.k.a. Bristol Siddeley Olympus) which has a variable nozzle [35]. As the name suggests, the curve labelled 'Loci of Peak Efficiency' represents the peak efficiency operating condition at various engine speeds. As illustrated in Figure 1.6, the two curves mentioned above usually intersect at the design speed. Thus, at low speed, the fan tends to operate at Type A flow regime while operating condition switches to Type C at high speed. The fan tends to operates close to /at the peak efficiency (and thus Type B flow condition) at the design speed.

As illustrated in Figure 1.8, due to the enormous centrifugal and aerodynamic loading during operation, the tip stagger of the fan blades tends to be reduced from its static value and thus the geometry change from static condition[8] to running condition[9] is also termed ‘untwist’. This terminology originates from the fact that the the blade’s stagger angle is low at the hub and high at the tip. The mechanism behind this behaviour will be examined in detail in Chapter 3. Thus, as shown in Figure 1.3, the fan blades are ‘twisted’ by design. Prediction of running shape is done routinely in industry [36] numerically using coupled and/or uncoupled aeroelastic computations.

Due to the inherent manufacturing tolerance [37] and deterioration during operation, fan blades in the same engine exhibit geometric variability even when they are stationary. As illustrated by the schematics in Figure 1.9, the absence of symmetry will inevitably exacerbate and contribute to the complexities of running geometry prediction as the blade variability is bound to be amplified by the significant aerodynamic and centrifugal loading. Consequently, geometric variability complicates the fan blade’s untwist behaviour and makes accurate running geometry prediction difficult.

At the same time, the fan blade development trend necessitates the development of numerical running geometry prediction technique. As mentioned earlier, the carbon-titanium-composite architecture is being incorporated into fan blade design. Such construction makes it difficult to capture the structural and thus aeroelastic behaviour of the blade accurately through rig test[10] [38, 39]. To be more specific, the physical size of the scaled fan blades makes it difficult to include the metal leading edge [38] and poses challenges to control the thickness of the carbon fibre component [39]. Consequently, it is difficult to mimic the structural behaviour of the full-size fan blade accurately through rig test and hence makes it far less possible to accurately capture the aeroelastic behaviour. Further more, the increasing fan diameter imposes a limit on the availability and choice for testing facilities for full-size engine test [40]. Thus, it becomes increasingly vital to develop numerical assessment methods at early design stage. To be more specific, it is important to develop methods that can predict the running geometry /untwist behaviour of the blades accurately.

---

[8] Also known as the ‘cold’ geometry.

[9] Also known as the ‘hot’ geometry.

[10] Experimental testing on a scaled model.

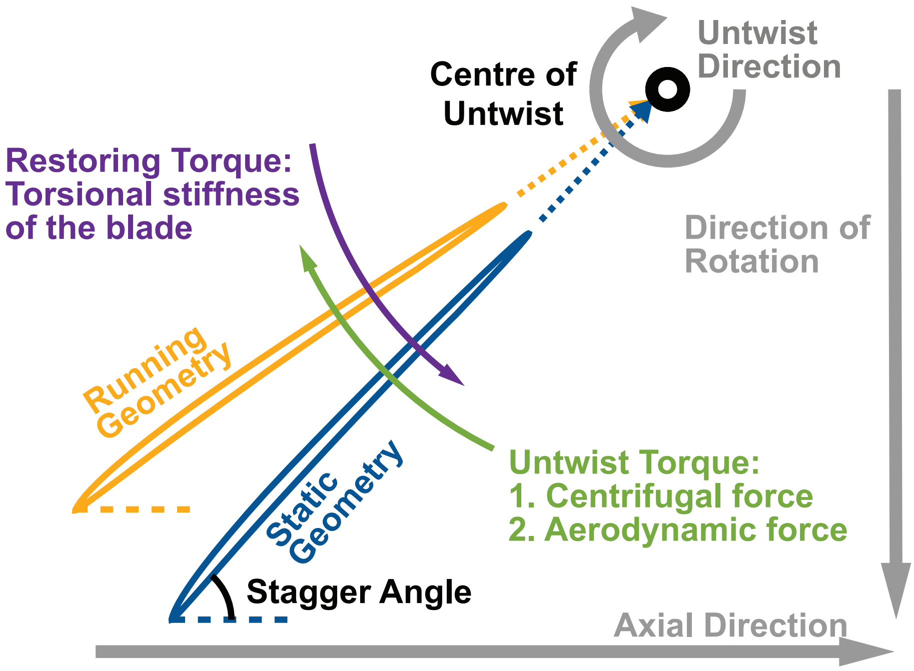

Figure 1.8: Fan blade untwist.

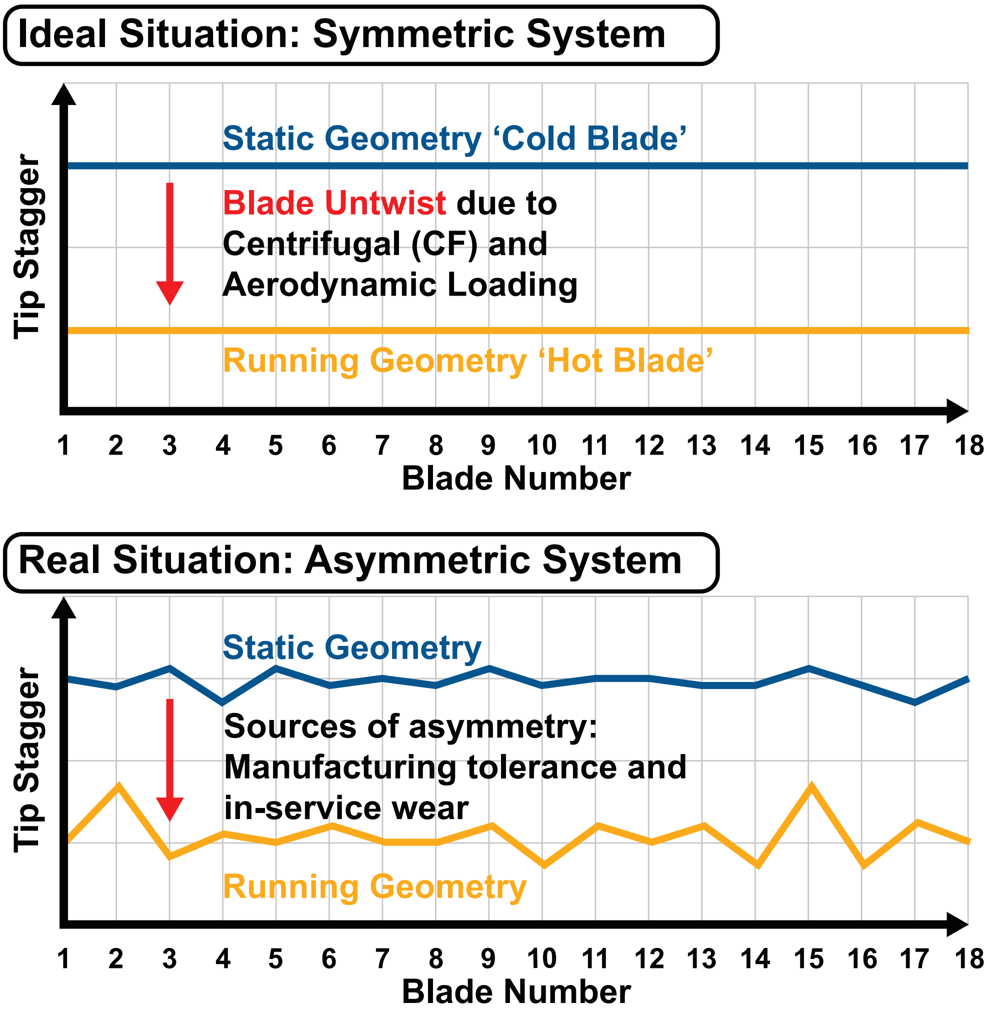

Figure 1.9: Untwist on a fan assembly.

In this study, an untwist related phenomenon termed *Alternative Passage Divergence* (APD) is investigated. As the name suggests, APD manifests as alternating passage geometry (and hence alternating tip stagger pattern) when the fan stage is operating close to/at peak efficiency condition.

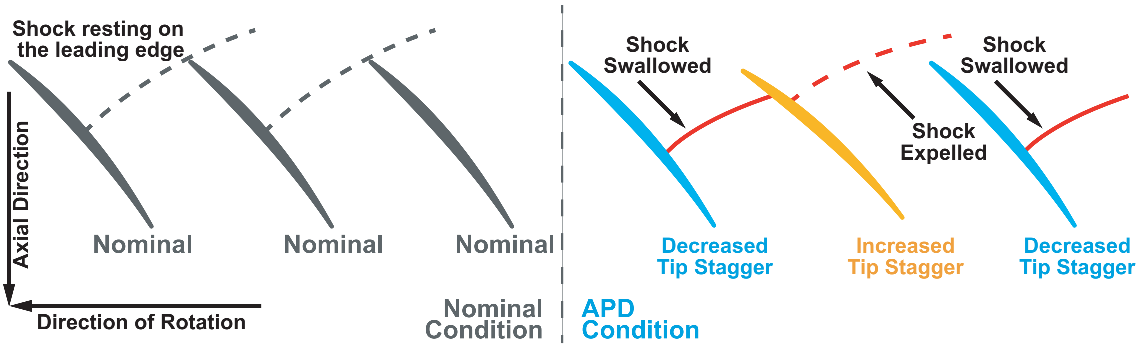

Figure 1.10: Schematics of passage shock and geometry configuration at fan tips during APD.

As illustrated by the schematics in Figure 1.10, under nominal condition when all the fan blades have the same tip stagger angle, the passage shocks rest on the trailing blades' leading edges. However, the presence of geometric variability can cause the assembly to adopt the alternating passage shock and tip stagger pattern, shown on the right side of Figure 1.10. In fact, a single mis-staggered blade is sufficient to trigger this phenomenon through the process illustrated in Figure 1.11. In short, the initial mis-staggering forces the aeromechanical properties (i.e. passage shock location and tip stagger angle) to deviate from the nominal condition and re-establish equilibrium through APD behaviour, resulting in the pattern in Figure 1.10. As this process repeats, the alternating pattern will develop throughout the entire fan assembly as illustrated by Figure 1.11. In most cases, the motion will terminate once the alternating pattern is adopted by the entire fan assembly.

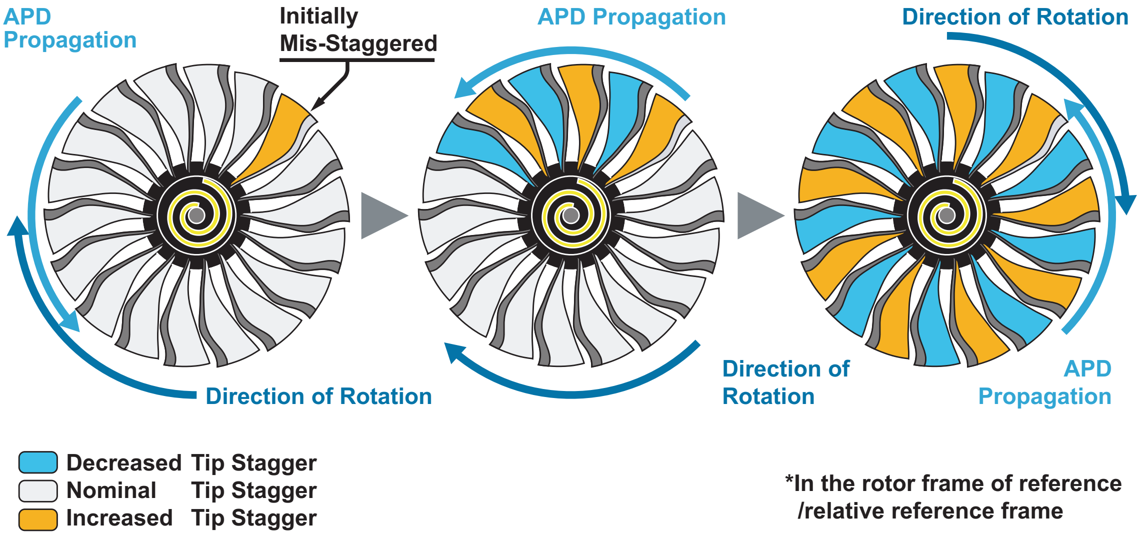

Figure 1.11: Schematics of APD behaviour development.

Under certain conditions, the initial disturbance (i.e. APD propagation in Figure 1.11) continues even after the assembly has adopted the alternating patterns. Consequently, this can result in an aeromechanical disturbance propagating around the annulus perpetually, potentially leading to High Cycle Fatigue (HCF). This unsteady behaviour is termed *Nonsynchronous Vibration* (NSV) as the behaviour is not linked to the multiples of enigne shaft speed.

Note that in this thesis, for clarity, the term *Nonsynchronous Vibration* (NSV) is interchangeable with dynamic/unsteady *Alternative Passage Divergence* (APD) behaviour. The main reason for the different names, as compared to the approach of using 'steady' and 'unsteady' to differentiate them, lies behind the fact that APD itself has a transient unsteady phase (i.e. illustrated in Figure 1.11) before the alternating pattern is established.

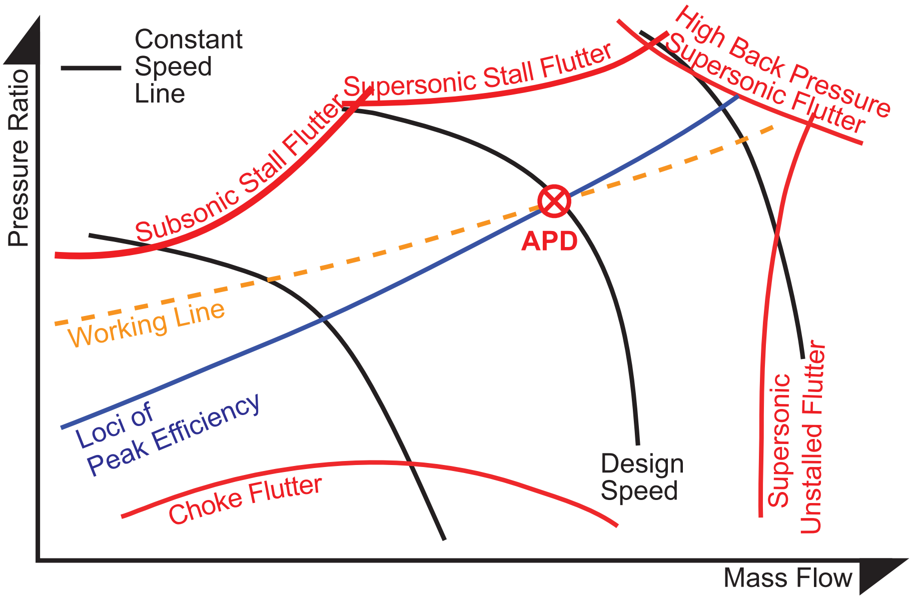

Figure 1.12: Aeroelastic instability boundaries on a fan map.

APD can introduce adverse effects such as fan performance deterioration and aeroacoustic noise. It's dynamic behaviour, NSV, can adversely influence the high cycle fatigue characteristics of the blade. From the civil aviation industry's point of view, the feature that makes APD stands out from other types of aeroelastic instabilities, such as flutter and forced response, is the operating condition where it manifests. As illustrated by schematics in Figure 1.12[11], all the well known aeroelastic instability issues occur at /near the stability boundary. This, by definition, makes them off-design problems. Forced response, on the other hand, can be eliminated from operation with the aid of the Campbell diagram. In contrast, APD behaviour is

---

[11] Adapted from Cumpsty [41] and Mikolajczak et al. [42].

located at /close to the design point where the fan assembly is designed to operate at and has the highest efficiency. In addition, APD can transform into NSV behaviour which can lead to high cycle fatigue and even component failure. Thus, APD & NSV's proximity to the design point makes the fan blades highly susceptible to HCF issues.

Evidently, the above mentioned characteristics of APD & NSV highlight the importance of investigating their underlying mechanism and deriving attenuating methods to prevent the highly undesirable outcomes such as fan blade failure and operation downtime.

1.3 APD Behaviour Demonstrated through Blade Tip Timing

The APD behaviour can be demonstrated by tip stagger measurements through the Blade Tip Timing (BTT) technique [32, 43, 44]. In essence, the tip stagger of a running fan blade can be measured by a pair of stationary light sensors. The stagger angle can be calculated through the rotation speed and the time difference between the time of arrival of the leading edge and trailing edge at the measurement position. The resolution of the stagger angle measurement is approximately 0.001° [44].

The contour plot shown in Figure 1.13 is derived from BTT measurement on an 18-blade transonic fan built for research purpose. At each time step, the relative stagger angles in the assembly (relative to the mean value at the time step of interest) are normalised by the range which is the difference between the highest stagger angle value and the lowest one. Red colour denotes stagger angles higher than the mean value at the time of interest whereas blue colour indicates the stagger angle is lower than the mean. By performing calculation at each time step, the contour in Figure 1.13 is revealed. It is important to note that the variation of mean value over time is insignificant as compared to the stagger angle range at any time step.

Three observations can be made from Figure 1.13. Firstly, the alternating blue and red bands at each time step indicate that the blades on the fan are exhibiting alternating tip stagger. Thus the APD behaviour mentioned earlier is captured by the BTT measurement. Secondly, the hatch/diagonal pattern (as compared to horizontal parallel bands) observed demonstrates that the pattern is propagating around the annulus. This is the dynamic phase of APD behaviour (i.e. NSV behaviour). Further investigation of its mechanism will be conducted in Chapter 4. Lastly, as time progresses, the tip stagger of each blade switches from lower values to higher values and vice versa. This switching mechanism is termed the *NSV Transfer*

Window and it is fundamental to the NSV behaviour. Detailed analysis including investigation into its controlling parameters will be presented in Chapter 4.

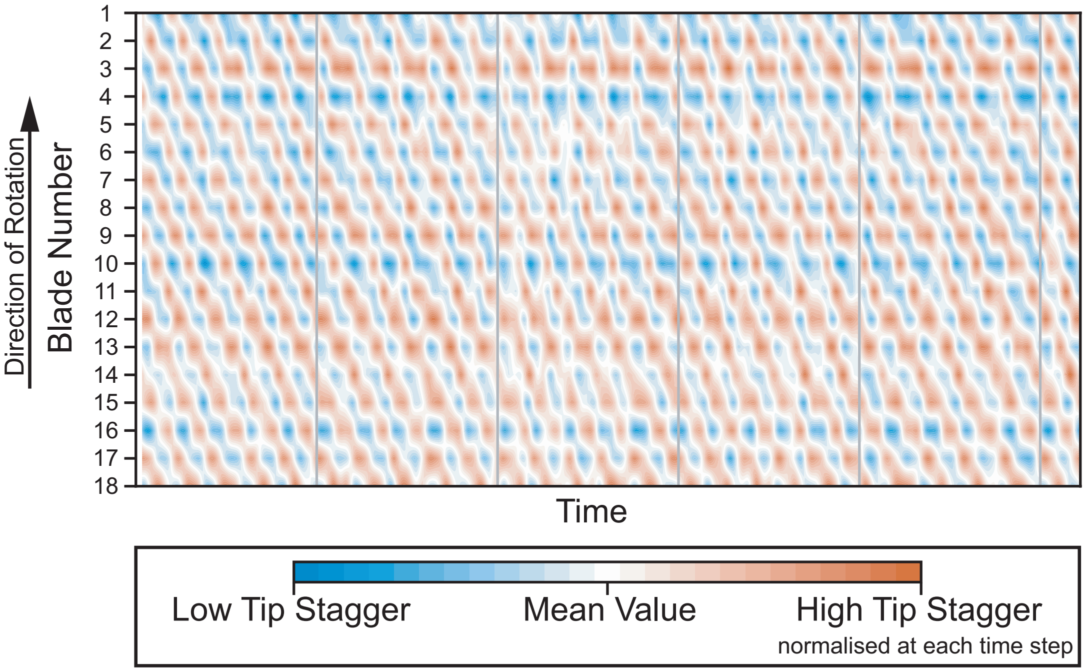

Figure 1.13: APD behaviour demonstrated through BTT measurement.

1.4 Objectives

To address the above mentioned issues, the following questions need to be answered.They are arrange in the same sequence they are answered in this thesis.

- Where does APD/NSV occur on the fan performance map?
- What type of influence do APD and NSV have on performance and life expectancy of blades?
- What triggers NSV?
- What is the speed /frequency of the NSV propagation around the assembly?
- What is the amplitude of APD and NSV (in term of stagger angle)? Is there a limit?
- What are the blade geometric characteristics that make the blade exhibit APD and NSV behaviour?
- What are the controlling factors? Which of them are controllable and which of them are not?

This thesis, written 1428 days after the questions are formulated, attempts to answer these questions.

As the majority of modern high by-pass turbofan engines [15, 21, 24–27] have an even number of fan blades, the majority of the APD & NSV study is centred around fans with an even number of blades. Discussion regarding fan designs with an odd number of blades will be presented in Section 4.5.3.

It is also important to note that this study is aimed to solve /anticipate an engineering problem. Therefore, compromises between pure academic interests and industrial applicability often rise and the approach most applicable in /relevant to industry is prioritised. The author will attempt to address both sides of the argument whenever applicable. Additionally, the nature of this study also dictates that, as the study progresses, the focus shifts from theoretical understanding of the phenomena to exploring engineering optimisation methods.

1.5 Literature Review

1.5.1 Previous APD & NSV Study

To the best of the author's knowledge, there are few studies in this particular field (i.e. APD & NSV). In the precursor study by Wilson et al. [45], APD behaviour was investigated on a fan with an even number of straight blades[12]. The test cases investigated are primarily with one mis-staggered blade in an otherwise uniformly staggered assembly with even number of blades. The underlying mechanisms of the zig-zag pattern and its propagation shown in Figure 1.14[13] and Figure 1.15[14] respectively had been explained. Besides, it was demonstrated that APD tends to occur near the peak efficiency condition of the blade. However, the intensity of the APD behaviour was not quantified which is partly due to the lack of computation resource. In term of investigating the adverse effects of APD, the initial study focused on the efficiency deterioration on one constant speed line.

Through the model truncation study carried out, Wilson [32] was able to demonstrate that the bulk untwist behaviour could be represented by the first three modes: first flapwise mode, second flapwise mode, and first torsional mode. The alternative and arguably more accurate approach to this is to include a significantly higher number of mode shapes in the aeroelastic computation such that more complex behaviour of the structure can be captured. However, the simplified approach was chosen as a compromise between the accuracy and computation efficiency[15] which is vital from the industry perspective.

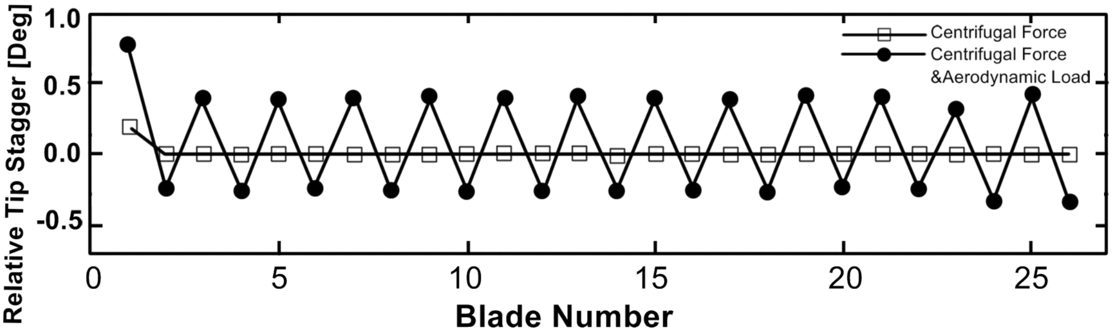

Figure 1.14: Tip stagger pattern before & after pressure untwist.

In term of computation domain choice for APD & NSV study, it is demonstrated by Wilson et al. [45] that the inclusion of the tip gap can only change the untwist

---

[12] The same fan blade is investigated in this study and is named as Fan 2. Further details are introduced in Chapter2.

[13] Figure 1.14 and 1.15 are adapted from Wilson [32].

[14] The transient behaviour captured by Figure 1.15 is previously shown through the schematics in Figure 1.11.

[15] In terms of required computation resources and time for pre- and post-processing.

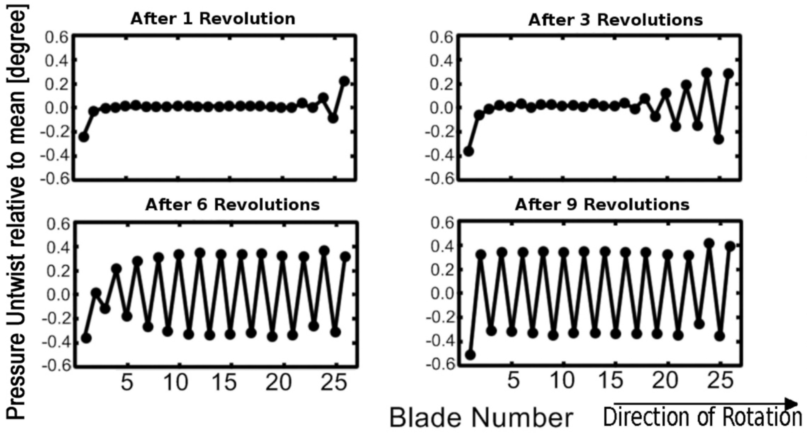

Figure 1.15: Blade untwist snapshots showing transient behaviour towards steady state.

results marginally and the APD behaviour is insensitive to tip gap effects. Thus, this justifies the exclusion of tip gap which improves computational efficiency in this study.

Lastly, NSV behaviour was observed by Wilson et al. [45]. The NSV behaviour was triggered on a case with two mis-staggered blade diametrically opposite to each other in the assembly. It was mentioned that an equilibrium was not established between the structural domain and fluid domain. The complex interference between the propagation patterns originated from the two mis-staggered blades respectively had caused numerical instability which forced the investigation to abort. The NSV behaviour was described in detail. However, detailed investigation of the underlying mechanism was not conducted. Based on the initial assessment, it was hypothesised that a fully mis-staggered fan blade can exhibit perpetual NSV behaviour. A decade later, this hypothesis is validated in this study which demonstrates that NSV behaviour can continue in the assembly for at least 100 revolutions.

1.5.2 Adverse Effects of APD

As a result of the augmented geometric variability, the APD phenomenon can significantly influence noise and aerodynamic efficiency of the fan assembly. The travelling disturbance introduced by APD & NSV can also make the fan blades susceptible to high cycle fatigue. Lastly, APD may influence aeromechanical stability because stagger variations are known to affect fan flutter [46]. The following section summarises some of the studies regarding the effect blade stagger variability in a fan assembly.

Aeroacoustics

Blade-to-blade stagger variability which can be amplified by the APD phenomenon is known to have significant influence on the aeroacoustics of the fan. The difference in the blade tip stagger angles is deemed to be the cause of irregularity in the pressure field and upstream shockwave strength, leading to Multiple Pure Tone noise (also known as the 'Buzz-Saw' noise) [47–50]. However, most of these researches [47, 49, 50] have attributed blade-to-blade to stagger variation to manufacturing tolerances which are significantly smaller than the stagger variation with APD. Besides, as Wilson [45] had pointed out, they focused on static stagger variability in the assembly and failed to account for running stagger variability such as the situation in which APD and NSV appear.

Mistuning induced APD

A major source of blade-to-blade static geometry variability is mistuning which originates from deviations in material, manufacturing tolerance, and in-service wear. Consequently, there will be slight differences in either mode shapes or frequencies among blades in an assembly [51, 52] even if there is no noticeable difference in the blades' static geometry[16]. However, while in operating condition, the addition of centrifugal loading and aerodynamic loading will untwist a mistuned assembly differently from the tuned assemblies for it has slight deviation in material stiffness. Hence, the running geometry of a mistuned assembly will be different from that of a tuned assembly. Through aerodynamic coupling and structural coupling through blade-disc assembly, mistuning can have a significant impact on aeroelastic stability [53], forced response, and resonance [51, 52, 54]. It is agreed among researchers [51, 53, 54] that moderate mistuning can improve aeroelastic stability (i.e. flutter) of rotor and is thus deemed a favourable design choice.

In a mistuned assembly, the difference in running geometry between mistuned blades and tuned blades would serve as a source of mis-staggering. Thus, as will be demonstrated in this study, mistuning can lead to APD behaviour in the assembly. Together with the fact that intentional mistuning is often used to mitigate flutter behaviour, this discovery means the engine manufacturers need to re-evaluate the use of mistuning as a flutter attenuation measure.

High Cycle Fatigue

More importantly, it was discovered by Wilson et al. [45] that under certain conditions APD can also show unsteady behaviour with an aeromechanical disturbance

---

[16] Fan blade geometry under static condition is also termed 'cold' blade. This is with reference to their running geometry - 'hot' blades when the fan blades are in operation.

propagating around the annulus perpetually. Thus, it is important to understand the unsteady APD behaviour because High Cycle Fatigue (HCF) is deemed as the most significant source for failure [55, 56]. In particular, Pratt & Whitney [55] reported a 24% of the component failures in military gas turbine engines[17] comes from high cycle fatigue. In some of the extreme cases seem in commercial aviation, fatigue damage is known to lead to the undesirable blade-off events [57–59]. From the engine operators' perspective, this means operation downtime and unscheduled maintenance. Consequently, it incurs tremendous financial cost and reputation damage to both the engine operators and manufacturers [5].

To avert such undesirable outcomes, the gas turbine engine development sector [56,60–62] has adopted two main approaches to mitigate the adverse impact of HCF: (1) to design the system so that component-compromising resonances are outside the operating envelope and (2) to quantify the vibration behaviour and tolerate those at insignificant levels [60]. Both approaches are attempted in dealing with the vibratory behaviour in this study.

1.6 Structure of the Thesis

This thesis is divided into 7 chapters and its macro structure is outlined in Figure 1.16. The text in the centre resembles a table of contents. The arrows map the relationship between chapters and how they link to the core objectives of the study. On the right, the brackets groups the chapters into two classes: those focusing on the steady effect (i.e. APD) and those focusing on the unsteady effect (i.e. unsteady APD or NSV). The arrows on the left shows how the chapters unfolding the NSV behaviour and its attenuation techniques are linked to each other and to the core theme of the study.

The contents in the study are grouped into chapters based on their functions in the APD & NSV storyline. The current chapter, Chapter 1 touches on the background of this study. It focuses on the necessity of this area of research from both the civil aviation business perspective and engineering optimisation perspective. A literature review is included to outline the research work conducted with regard to the potential adverse effects of APD & NSV. The chapter concluded by highlighting the fact that the APD & NSV behaviour is a design operating condition problem and is expected to get worse following the trend of increasing fan diameter. The initial questions guiding the research are listed to show where the industrial interests lie. Chapter 2 discusses theoretical background behind the solver and various analysis techniques

---

[17] To the best of the author's knowledge, corresponding statistics on civil gas turbine engines are not available in the public domain.

(i.e. pre and post processing) used. It also points out the assumptions and compromises made to make the general APD & NSV behaviour modelling possible in a computationally efficient way, thus offering directions for future improvement.

The majority of Chapter 3 is dedicated to exploring the APD behaviour: its controlling factors, optimal operating conditions, and the adverse effects. A comparison between two fan blade designs are carried out to illustrate how the difference in key geometrical features can dictate the APD behaviour and intensity. Given the context of this research (i.e. to solve/anticipate an engineering problem), a reduced order model for locating APD behaviour is explored and validated on the two fan blade designs such that the fan blade design cycle can be optimised.

Chapter 4, 5, and 6 are allocated for the discussion of the NSV behaviour. Due to the multifaceted complexity and impractical computational requirement in analysing the NSV behaviour of a randomly mis-staggered pattern, Chapter 4 adopts a simplified approach of using an idealised mis-stagger pattern to do parametric studies on NSV first. A few influencing factors are found as a results and the approach is deemed feasible for early design stage assessment. Consequently, based on these findings, a novel machine-learning-based passive vibration attenuation technique is discussed in Chapter 5 while blade redesign based active vibration attenuation approach is discussed in Chapter 6. The later redesign approach has also been found to be effective against the static APD behaviour. The two attenuation techniques can help to minimise the vibration of fan blades at different stages of their life cycle, either in design stage or in operation. Ultimately, they facilitate the avoidance of NSV induced fatigue damage, helping to avoid the tremendous cost from unscheduled maintenance and to minimise risks.

Chapter 7 summaries the main findings from the study and provides brief answers to the guiding questions. An overview of the findings are then presented through a commercial aviation industry perspective. The chapter also links back to Chapter 2 to reflect on the simplifications made and to suggest future quantitative improvements. Lastly, the chapter reviews the novel approach adopted in Chapter 5 and lists a few suggestions for further investigations.

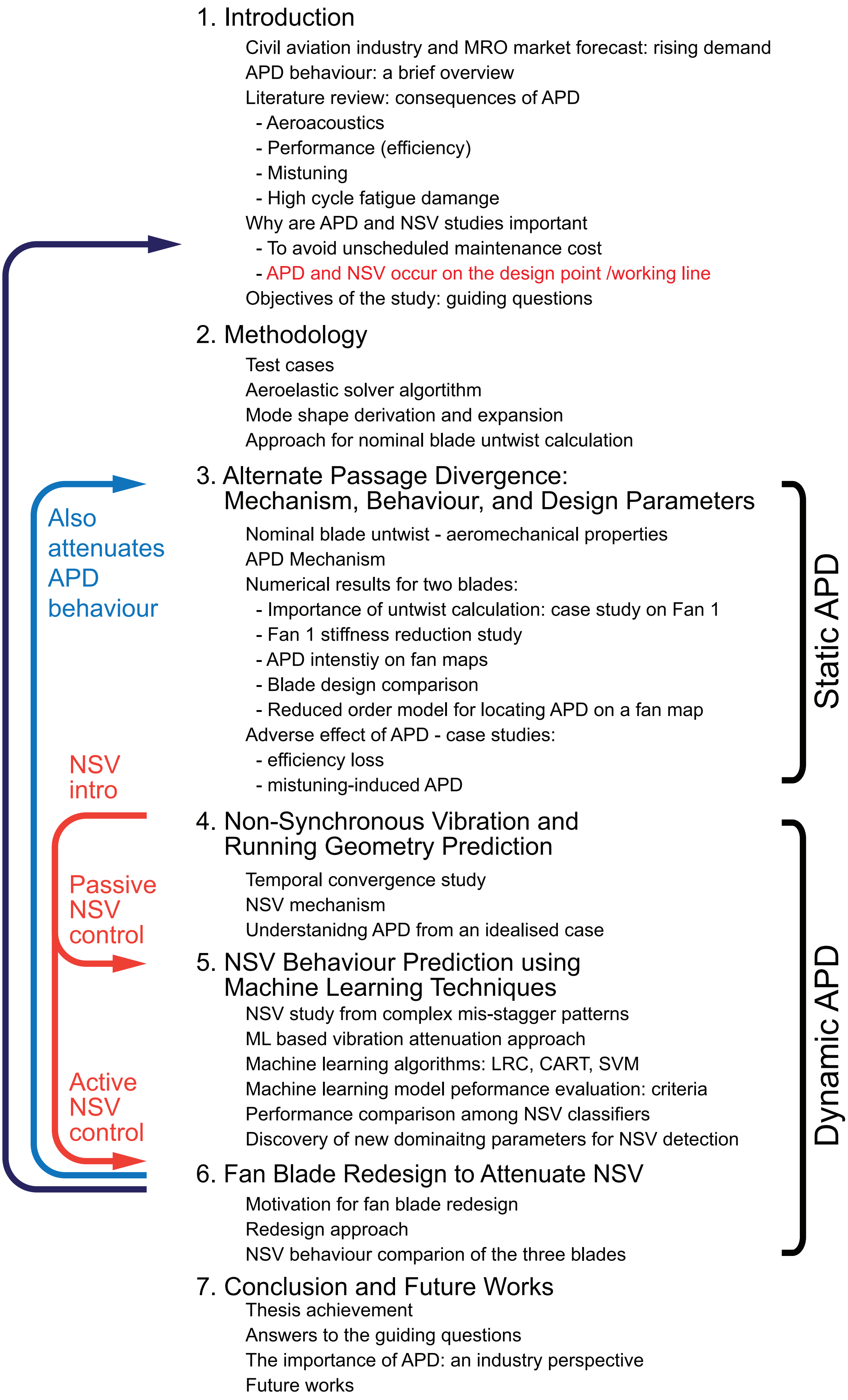

Figure 1.16: Thesis structure.

1.7 Publications

Selected components of this thesis have been published through the following mediums [63–67] (in anti-chronological order):

1. Lu, Y., Green, J., Stapelfeldt, S.C., and Vahdati, M., 2019. “Effect of Geometric Variability on Running Shape and Performance of a Transonic Fan”. *Journal of Turbomachinery, 09, pp. 1–9.*

    - Conference proceeding version[18]:
      Lu, Y., Green, J., Vahdati, M., and Stapelfeldt, S. C., 2018. “Effect of Geometry Variability on Fan Performance and Aeromechanical Characteristics”. In 15th International Symposium on Unsteady Aerodynamics, Aeroacoustics and Aeroelasticity of Turbomachines, Oxford, UK.

2. Lu, Y., Lad, B., Green, J., Stapelfeldt, S. C., and Vahdati, M., 2019. “Effect of Geometry Variability on Transonic Fan Blade Untwist”. *International Journal of Turbomachinery, Propulsion and Power, 4(3)..*

    - Nominated[19] for the ‘Best Paper Award’ at the 13th European Turbomachinery Conference, Lausanne, Switzerland, 8-12 April 2019.

3. Lu, Y., Lad, B., Vahdati, M., and Stapelfeldt, S. C., 2019. “Nonsynchronous Vibration Associated with Transonic Fan Blade Untwist”. In ASME Turbo Expo 2019: Turbomachinery Conference and Exposition, Phoenix AZ, USA, American Society of Mechanical Engineers.

    - Recommended for publication in the Journal of Turbomachinery.

4. Lu, Y., Zhao, F., Salles, L., and Vahdati, M., 2017. “Aeroelastic Analysis of NREL Wind Turbine”. In ASME Turbo Expo 2017: Turbomachinery Technical Conference and Exposition,Charlotte NC, USA, American Society of Mechanical Engineers.

---

[18] The title modification is meant to put the topic of the study into better focus.

[19] One of the 5 nominated papers. There are 136 papers in total at the conference.

Contents from Chapter 5 and 6 are in preparation[20] for the following publications:

1. Lu, Y., Lad, B., and Vahdati, M., "Transonic Fan Blade Redesign Approach to Attenuate Nonsynchronous Vibration".
    - Accepted by the ASME Turbo Expo 2020: Turbomachinery Technical Conference and Exposition.
    - Recommended for publication in the Journal of Turbomachinery.
2. Lu, Y., and Vahdati, M., "Detecting Nonsynchronous Vibration in Transonic Fan Untwist using Machine Learning Techniques".
    - Accepted by the ASME Turbo Expo 2020: Turbomachinery Technical Conference and Exposition.

---

[20] As of March 13, 2020.

Chapter 2

Methodology

> All models are wrong, but some models are useful.
>
> Professor George E.P. Box FRS [68, 69]

2.1 Chapter Introduction

In this chapter, the Fluid-Structure Interaction (FSI) solution scheme used in this study is introduced. Firstly, the test cases, two fans, used in this study are discussed. This is followed by the discussion about the Fluid-Structure-Interaction solution scheme used in this study. In particular, its underlying assumptions and compromises in the engineering context are highlighted and discussed. The discussion is centred around the boundary condition and computation domain choice. Lastly, the approach for investigating untwist using the aeroelastic solver is illustrated. Additionally, through the examination of the mode shapes and deformed blade shapes, the decision as to why the later discussion focuses on the changes in aeromechanical property at the fan blade tips is explained.

Note that the methodology for the machine learning techniques used in Chapter 5 is described in the Chapter 5 for clarity.

2.2 Test Cases: Two Transonic Fans

In this study, APD behaviour is intentionally introduced onto two research fans, referred to as Fan 1 and Fan 2. Both fans are designed for long-haul commercial airliners. Key parameters are tabulated in Table 2.1. Detailed discussion about covered passage geometry will be introduced in Chapter 3. Fan 1 is of a modern fan design. Fan 2 is the same fan used in the study by Wilson et al. [45] and has been proven to be prone to APD & NSV behaviour. The two research fans are separated in time by more than 15 years.

Table 2.1: Comparison of Fan Parameters.

	Fan 1	Fan 2
Aspect Ratio (Blade Height/Mid-Span Chord)	2.0	2.3
By-Pass Ratio	8-12	5-7
Number of Blades	18	26
Tip Stagger Angle	63-68°	65-70°
Blade shape	Swept	Straight
Covered Passage Geometry at the tip	divergent	convergent-divergent
Covered Passage Length at the tip (as % chord length)	Approx. 14%	Approx. 28%

All the analysis are performed at the Sea-Level-Static (SLS) conditions. In contrast to the conditions at cruise altitude, the SLS condition has considerably higher air density, higher ambient pressure, and higher mechanical speed (due to the higher temperature). As a result, the fan blades are subject to greater untwist which amplifies the blade variability to a greater extent than at cruise altitude.

2.3 Aerodynamic & Aeroelastic Solver - AU3D

The computations for this study are performed using the in-house aeroelastic solver AU3D which has been validated for numerous fans and compressors at design and off-design conditions [46, 60, 70–74]. The core components of the solver have not been changed for the past 25 years.

Aerodynamic Analysis. The underlying flow solver is a 3D time-accurate Reynolds-Averaged Navier-Stokes (RANS) solver [75]. The unsteady flow cases are computed using the Unsteady Reynolds-Averaged Naiver-Stokes (URANS) equations. The flow variables are represented on the nodes of a generic semi-structured grid and numerical fluxes are evaluated along the edges of the grid. The numerical fluxes are evaluated using Roe's flux vector difference splitting together with the Jameson-Schmidt-Turkel scheme [76]. The solution method is implicit, with second order accuracy in time and space. For this study, the one-equation Spalart-Allmaras turbulence model [77] is used to close the equations. The parameters in the model have been adjusted for high speed fan blades to attain good agreement up to the stability limit [72, 74]. To be more specific, the constants in the turbulence models are tuned to achieve agreement with experimental data in terms of pressure ratio and overall radial distribution. The parameters are held constant in all studies. Additional details of the modification will be presented in the next section.

Formulation of the solver has been discussed extensively by Sayma et al. [78,79] and the key equations are presented here. For a control volume Ω with boundary Γ and outward normal of the boundary $\overrightarrow{n} = \begin{pmatrix} n_1 \\ n_2 \\ n_3 \end{pmatrix}$ in the rotating frame where a blade row rotates with angular velocity ω about the x-axis, the governing equation can be written in the conservative form as:

$$\frac{\mathrm{d}}{\mathrm{d}t}\int_{\Omega}\mathbf{U}d\Omega + \oint_{\Gamma}\left(\mathbf{F}_i - \mathbf{G}_i\right)n_i d\Gamma = \int_{\Omega}\mathbf{S}d\Omega \tag{2.1}$$

Definitions of the left hand side terms in Equation 2.1 can be expressed as:

- The solution vector of conservative variable $\mathbf{U}$:

$$\mathbf{U} = \begin{bmatrix} \rho \\ \rho\overrightarrow{u} \\ \rho e \end{bmatrix} \tag{2.2}$$

  where $\overrightarrow{u}$ is the flow velocity (in the absolute reference frame), ρ is the density of the fluid, and e is the specific total energy.

- The inviscid flux vector $\mathbf{F}_i$:

$$\mathbf{F}_i = \mathbf{U}\left(u_i - w_i\right) + \begin{bmatrix} 0 \\ p\overrightarrow{\delta_i} \\ \rho u_i \end{bmatrix} \tag{2.3}$$

  where $\overrightarrow{w} = \begin{pmatrix} w_1 \\ w_2 \\ w_3 \end{pmatrix}$ is the velocity in the rotating frame, $\overrightarrow{\delta} = \begin{pmatrix} \delta_1 \\ \delta_2 \\ \delta_3 \end{pmatrix}$ denotes the Kronecker delta function, and p is the pressure.

- The viscous flux vector $\mathbf{G}_i$:

$$\mathbf{G}_i = \begin{bmatrix} 0 \\ \overrightarrow{\sigma_i} \\ u_i\sigma_{ij} + \kappa\frac{\partial T}{\partial x_i} \end{bmatrix} \tag{2.4}$$

  where κ represents the effective thermal conductivity, T denotes temperature,

$\overrightarrow{\sigma_{ij}} = \begin{pmatrix} \sigma_{1i} \\ \sigma_{2i} \\ \sigma_{3i} \end{pmatrix}$, and σ_{ij} denotes the viscous stress tensor.

The right hand side term in Equation 2.1 can be expressed as:

$$\mathbf{S} = \begin{bmatrix} 0 \\ 0 \\ -\rho\omega u_2 \\ \rho\omega u_3 \\ 0 \end{bmatrix} \tag{2.5}$$

In AU3D, the flow variables are represented on the nodes and numerical fluxes are evaluated along the edges of the mesh. For vertex I which is connected to vertices (J_1, J_2, ... , J_n), the semi-discrete form of Equation 2.1 can be expressed as:

$$\frac{\mathrm{d}}{\mathrm{d}t}\left(\Omega_I \mathbf{U}_I\right) + \sum_{s=1}^{n} \frac{1}{2} \mid \eta_{\vec{IJ_s}} \mid \left(F_{IJ_s} - G_{IJ_s}\right) + \mathbf{B}_i = \Omega_I \mathbf{S}_I \tag{2.6}$$

where $\mathbf{U}_I$ is the solution vector at I, F_{IJ_s} denotes the inviscid flux along edge IJ_s, G_{IJ_s} denotes the viscous flux along edge IJ_s, $\mathbf{B}_i$ is the boundary integral. $\eta_{\vec{IJ_s}}$ is the side weight. Ω_I is the control volume bounded by the region connected by the median of the cells surrounding vertex I.

Further details about the solver can be found in the literature by by Sayma et al. [78, 79].

Modification of one-equation model and validation of the aerodynamic solver. The modifications made to the Original Spalart-Allmaras (OSA) model [77] has been presented in details by Lee et al. [74]. The modification has been recognised by various research groups [80,81] and adopted [81]. The key changes are summarised here.

The original one equation model can be denoted as [74, 82]:

$$\frac{\partial \hat{\nu}}{\partial t} + u_j \frac{\partial \hat{\nu}}{\partial x_j} = c_{b1}\left(1 - f_{t2}\right) \hat{S}\hat{\nu} - \textit{destruction terms} + \textit{diffusion terms} \tag{2.7}$$

where $\hat{\nu}$ is the corrected turbulent viscosity, u_j denotes the velocity component in the jth direction, t represents time, x_j denotes the Cartesian coordinate vector, f_{t2}

is the trip function, c_{b1} is an empirical constant, and $\hat{S}$ is the modified vorticity. Additional definitions are provided by the following equations:

$$\hat{S} = S + \frac{\hat{\nu}}{\kappa^2 d^2} f_{\nu 2} \tag{2.8}$$

$$S = \sqrt{2\Omega_{ij}\Omega_{ij}} \tag{2.9}$$

$$\Omega_{ij} = \frac{1}{2}\left(\frac{\partial u_i}{\partial x_j} - \frac{\partial u_j}{\partial x_i}\right) \tag{2.10}$$

$$f_{\nu 2} = 1 - \left(\frac{\chi}{1 + \chi f_{\nu 1}}\right) \tag{2.11}$$

$$f_{\nu 1} = \frac{\chi^3}{\chi^3 + c_{\nu 1}^3} \tag{2.12}$$

where $c_{\nu 1}$ is an empirical constant and

$$\chi = \frac{\hat{\nu}}{\nu} \tag{2.13}$$

The first term on the right hand side of Equation 2.7 is the production term. It has been modified to improve the accuracy in flow solution prediction near the stability limit. The $\hat{S}$ term (i.e. Equation 2.8) in the original production term is modified as:

$$\hat{S_{mod}} = \beta S + \frac{\hat{\nu}}{\kappa^2 d^2} f_{\nu 2} \tag{2.14}$$

where

$$\beta = C_s \times C_{vh} \tag{2.15}$$

$$C_s = \frac{ch_1 \times \tanh\left[a_1 P^2\right]}{\tanh(1.0)} + 1.0 \tag{2.16}$$

$$C_{vh} = \frac{ch_2 \times \tanh\left[a_2 H^2\right]}{\tanh(1.0)} + 1.0 \tag{2.17}$$

ch_1 and ch_2 are the newly introduced constants for the Modified Spalart-Allmaras (MSA) model. ch_1 is determined to be 0.5 whereas ch_2 is determined to be 0.7 through a numerical study [74]. The scaling factor a_1 is a mesh-dependent constant whereas a_2 is chosen as 3 [74]. The β parameter approaches 1 in a smooth flow field and hence the $\hat{S_{mod}}$ term converges to the $\hat{S}$ term in the OSA.

The validation of the model against experimental data is also presented by Lee et al. [74] and is reproduced in Figure 2.1 to 2.3. The validation is first performed on the Axisymmetric Transonic Bump case from NASA [82] and the validation data are presented in Figure 2.1. The validation effort is then extended onto fan cases. As presented by [74], the validation is performed on rig sized[1] fan designs which are representative of the fans, in terms of aerodynamic behaviour, used in this study. The fans used by Lee et al. [74] are denoted as Fan A* and Fan B* to avoid confusion with Fan A and Fan B in this study. The validation results demonstrate that the the modification produces reasonable accurate steady state solution at operating conditions away from the stability limit. This is important as these are the flow regime where the APD & NSV behaviours manifest.

---

[1] There are no steady state experimental data from engine sized fans.

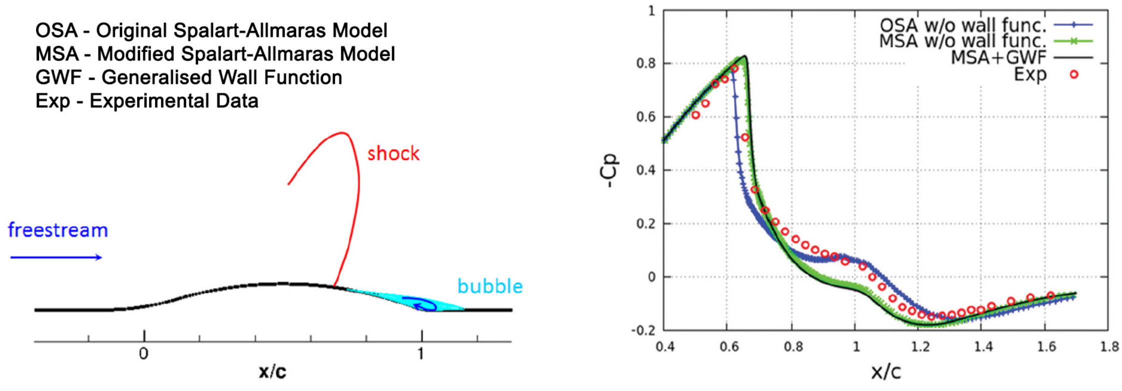

(a) Geometry and Flow Features

(b) Pressure Distribution

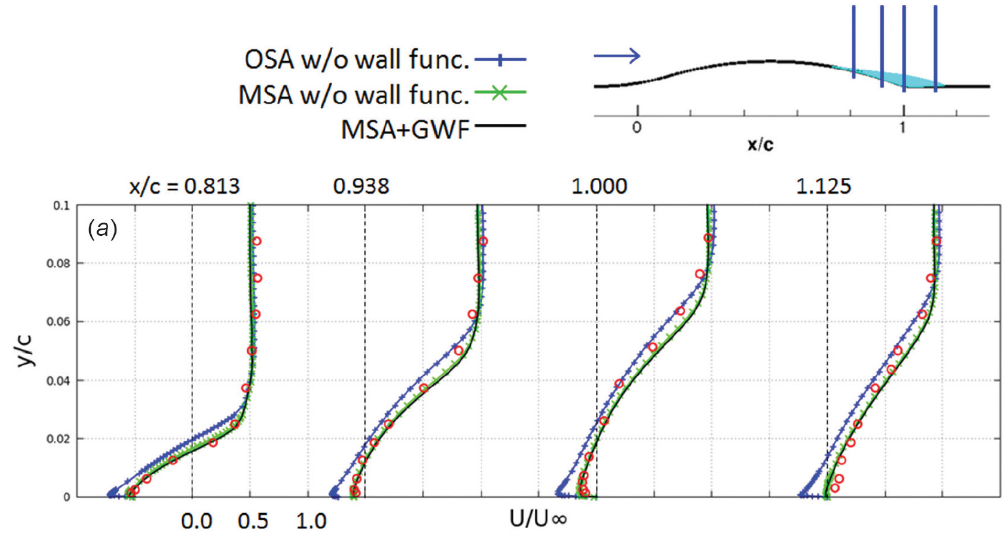

(c) Profile of streamwise velocity

Figure 2.1: Experimental Validation of the solver (NASA test case). Reproduced from Lee et al. 2018.

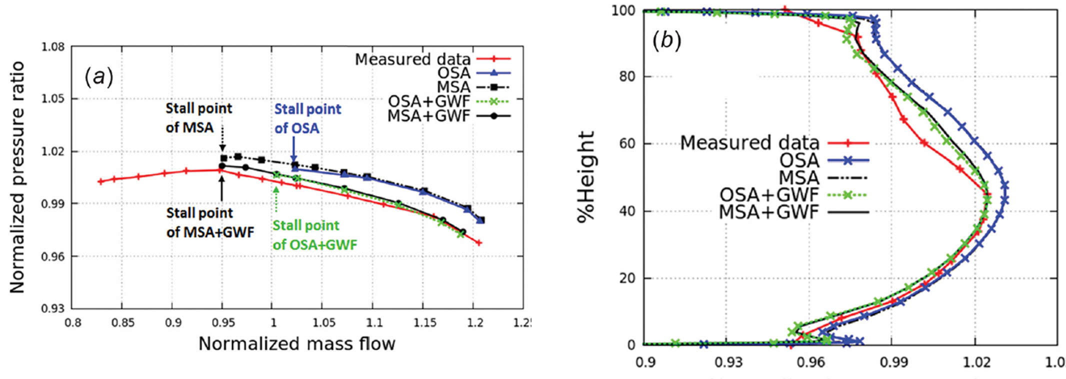

OSA - Original Spalart-Allmaras Model
MSA - Modified Spalart-Allmaras Model
GWF - Generalised Wall Functoin

Figure 2.2: Experimental Validation of the solver (Fan A* at part speed). (a) Fan A*'s characteristic map. (b) distribution of stagnation pressure at 1.07 normalised mass flow. Reproduced from Lee et al. 2018.

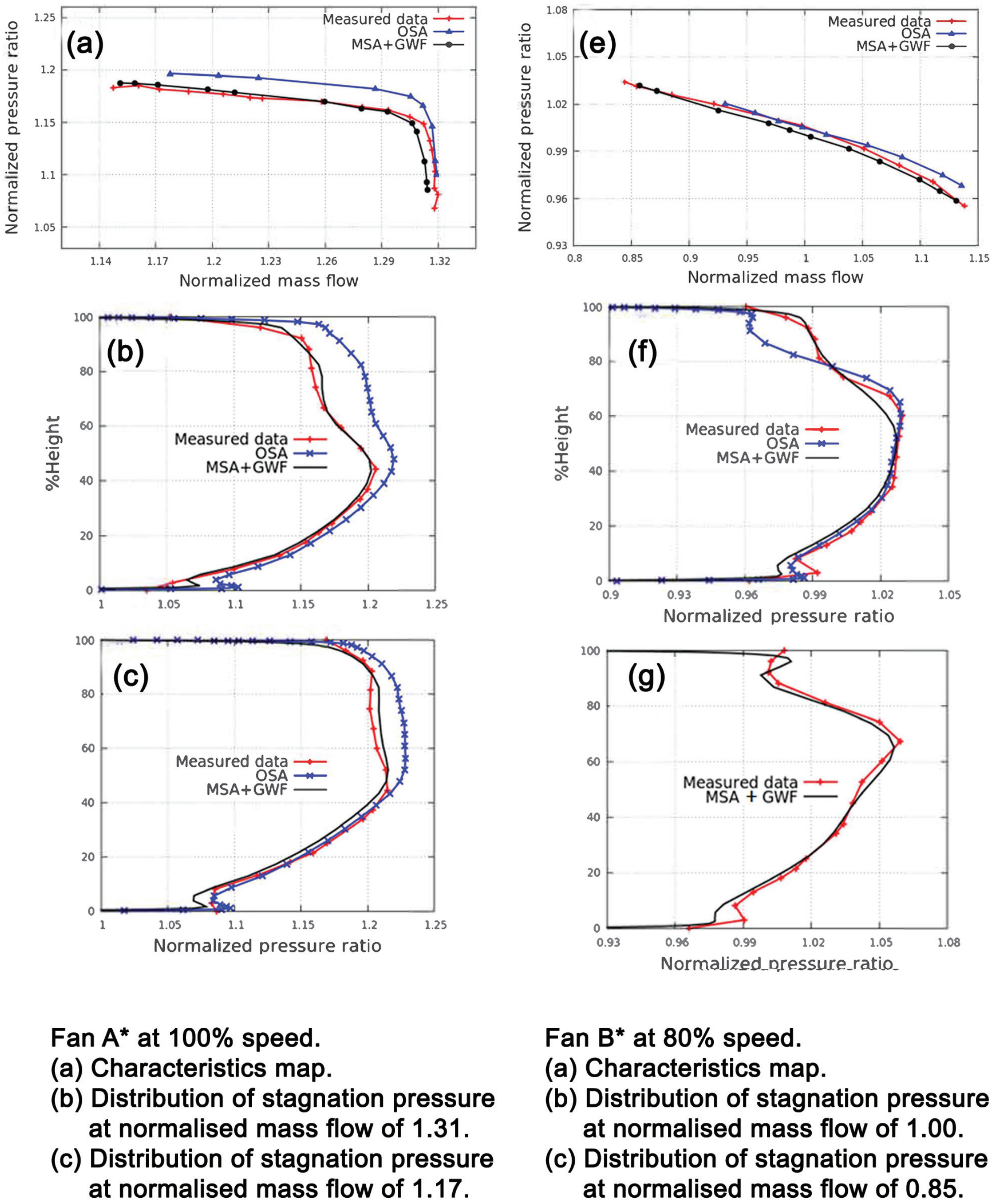

Fan A* at 100% speed.
(a) Characteristics map.
(b) Distribution of stagnation pressure at normalised mass flow of 1.31.
(c) Distribution of stagnation pressure at normalised mass flow of 1.17.

Fan B* at 80% speed.
(a) Characteristics map.
(b) Distribution of stagnation pressure at normalised mass flow of 1.00.
(c) Distribution of stagnation pressure at normalised mass flow of 0.85.

Figure 2.3: Experimental Validation of the solver (Fan A* at design speed and Fan B* at part speed). Reproduced from Lee et al. 2018.

Aeroelastic Analysis. The aeroelastic analysis is performed in a partially coupled fashion [70,79] in which fluid and structural domain are solved alternately with data exchanged at the fluid structure boundary at each time step. The underlying assumption of this aeroelastic model is that the structural motion could be represented by linear superposition of a few fixed modes. As the mass ratio[2] is high, it is generally accepted that the mode shapes are unaffected by the aerodynamics unsteady forces [83] and this assumption is valid. Mode shapes for aeroelastic analysis are obtained from a Finite Element (FE) solver (Rolls-Royce SC03) and are interpolated onto the CFD grid. This aeroelastic solution approach differs from the fully coupled analysis as the FE analysis is not conducted during each time step and hence it is computationally less demanding.

The aeroelastic computation starts by solving Equation 2.18 for each mode [70]:

$$M\ddot{x} + C\dot{x} + Kx = f_{Aerodynamic} + f_{Centrifugal} \tag{2.18}$$

in matrix notation:

$$[M]\{\ddot{x}\} + [C]\{\dot{x}\} + [K]\{x\} = \{f_A\} + \{f_{CF}\} \tag{2.19}$$

where $[M]$,$[C]$, and $[K]$ are mass, damping, and stiffness matrices respectively. $\{x\}$, $\{f_A\}$,and $\{f_{CF}\}$ are vectors of displacements, aerodynamic forces, and centrifugal forces respectively.

Equation 2.19 can be further simplified. The displacement vector could be decomposed into displacement due to aerodynamic load and displacement due to centrifugal load. Thus,

$$\{x\} = \{x_A\} + \{x_{CF}\} \tag{2.20}$$

$$[K]\{x_{CF}\} = \{f_{CF}\} \tag{2.21}$$

Assuming the centrifugal (CF) force remain constant during the blade untwist process, Equation 2.19 can be simplified to only include the aerodynamic force when the fan blade's initial geometry accounts for CF loading at the corresponding fan speed. Thus,

$$[M]\{\ddot{x_A}\} + [C]\{\dot{x_A}\} + [K](\{x_A\} + \{x_{CF}\}) = \{f_A\} + \{f_{CF}\} \tag{2.22}$$

---

[2] Which is the ratio between the mass of the blade and the mass for the fluid influenced by its movement.

can be reduce to:

$$[M]\{\ddot{x_A}\} + [C]\{\dot{x_A}\} + [K]\{x_A\} = \{f_A\} \tag{2.23}$$

Mode shape $[\Psi]$, mass-normalised mode shape $[\Phi]$, and natural frequency ω_n for each mode can be derived from the eigen solution of Equation 2.23. Mass-normalisation of mode shape is accomplished through:

$$[\Phi_r] = \frac{1}{\sqrt{m_r}}[\Psi_r] \tag{2.24}$$

where r is the mode number and m_r is the modal mass.

The spatial model can be translated into modal model [78, 84] by establishing link between real displacement and mode shape (mass-normalised):

$$\{x_A\} = [\Phi]\{q\} \tag{2.25}$$

where $\{q\}$ is the modal displacement. Thus, Equation 2.23 can be rewritten as:

$$[\Phi]^T[M][\Phi]\{\ddot{q}\} + [\Phi]^T[C][\Phi]\{\dot{q}\} + [\Phi]^T[K][\Phi]\{q\} = [\Phi]^T\{f_A\} \tag{2.26}$$

The modal model possesses Orthogonality properties :

$$[\Psi]^T[M][\Psi] = \begin{bmatrix} \ddots & & \\ & m_r & \\ & & \ddots \end{bmatrix} \tag{2.27}$$

and

$$[\Psi]^T[K][\Psi] = \begin{bmatrix} \ddots & & \\ & k_r & \\ & & \ddots \end{bmatrix} = \begin{bmatrix} \ddots & & \\ & m_r & \\ & & \ddots \end{bmatrix}\begin{bmatrix} \ddots & & \\ & \omega_n^2 & \\ & & \ddots \end{bmatrix} \tag{2.28}$$

where r is the mode number. $\begin{bmatrix} \ddots & & \\ & m_r & \\ & & \ddots \end{bmatrix}$ is the modal mass diagonal matrix and

$\begin{bmatrix} \diagdown & & \\ & k_r & \\ & & \diagdown \end{bmatrix}$ is the modal stiffness diagonal matrix. The ratio between them is unique:

$$\begin{bmatrix} \diagdown & & \\ & \omega_n^2 & \\ & & \diagdown \end{bmatrix} = \begin{bmatrix} \diagdown & & \\ & m_r & \\ & & \diagdown \end{bmatrix}^{-1} \begin{bmatrix} \diagdown & & \\ & k_r & \\ & & \diagdown \end{bmatrix} \tag{2.29}$$

The mass-normalised mode shape has the property such that:

$$[\phi]^T [M] [\phi] = [I] \tag{2.30}$$

and

$$[\phi]^T [K] [\phi] = \begin{bmatrix} \diagdown & & \\ & \omega_n^2 & \\ & & \diagdown \end{bmatrix} \tag{2.31}$$

$[I]$ is the identity matrix and $\omega_n^2 = \frac{k}{m}$.

Under the assumption of proportional damping, the following equations hold true for each mode:

$$\zeta = \frac{C}{C_{critical}} = \frac{C}{2\sqrt{km}} \tag{2.32}$$

$$C = 2\zeta\sqrt{km} = 2\zeta m \omega_n \tag{2.33}$$

Applying Orthogonality properties to Equation 2.26, it transforms into:

$$\{\ddot{q}\} + \begin{bmatrix} \diagdown & & \\ & 2\zeta\omega_n & \\ & & \diagdown \end{bmatrix} \{\dot{q}\} + \begin{bmatrix} \diagdown & & \\ & \omega_n^2 & \\ & & \diagdown \end{bmatrix} \{q\} = [\Phi]^T \{f_A\} \tag{2.34}$$

Results from FE modelling will provide information about the two diagonal matrices on the left-hand side and the mass-normalised mode shapes on the right-hand side. The vector $\{f_A\}$ represents the aerodynamic forces acting on the blade and is obtained from the CFD solver. The term on the right-hand side of Equation 2.34 is the modal force [85] which is a measure of the correlation between the aerodynamic force and the mode shape in that particular mode. To be more specific, the matching between the pressure distribution on the blade surfaces and mode shape is assessed by the modal force. Thus, modal force indicates the strength of the unsteady forcing in a particular mode of vibration. Accordingly, for the rigid body motion mode such as blade plunging motion, modal force is equivalent to unsteady lift on the blade.

After obtaining the aerodynamic forces $\{f_A\}$ at time level n the aeroelastic solver computes the modal displacement q from Equation 2.34 which is used to calculate the real displacement $\{x_A\}$ on the blade surface mesh at time level $n+1$ from Equation 2.25. The mesh on blade surface is deformed every time step by the imposed modes using mode shapes and modal frequencies. Mesh deformation is executed through the Spring Network Analogy [78] where individual mesh node's displacement is inversely proportional to its distance to the blade surface. Boundary conditions at the fluid-structure interface are updated at each time step [78] as illustrated in Figure 2.4. Hence, the deformed mesh will be used in the next time step. The physical time step for aeroelastic computations is assigned as approximately 200 time steps per revolution. This time step setting was determined by performing a temporal convergence study. The results from this temporal convergence study is presented in Chapter 4.

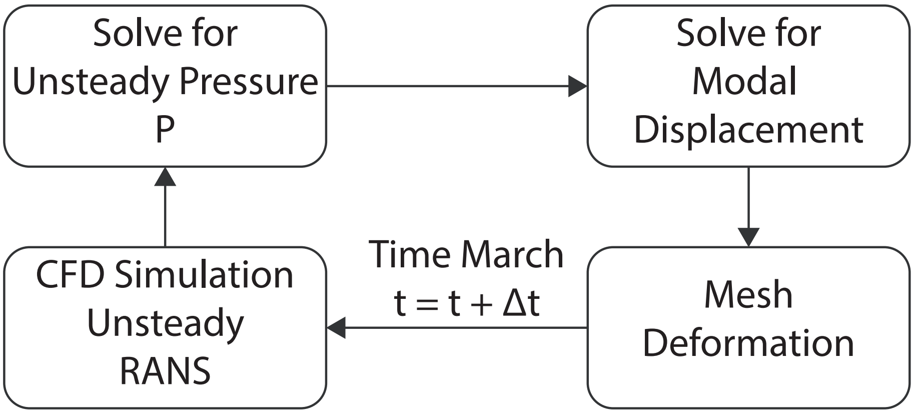

Figure 2.4: Aeroelastic Solver Scheme.

In essence, fluid domain and structural domain are solved alternately with information exchanged at the fluid-structure interface (i.e. blade surface) at each time step. Thus, there is a slight time lag (between the fluid domain and the structural domain) as compared to that of the fully coupled analysis where the two domains are solved simultaneously. The delay can be reduced to negligible magnitude through setting small time steps. Other than its advantage of lower computation requirement over fully coupled analysis, the closely coupled analysis does not impose any limit on the way the two domains are discretised.

The nominal running geometries (at speeds of interest) used in this study are either provided by the research partner or computed using the FE solver (Rolls-Royce SC03), which takes geometric non-linear effects into consideration. Rotor speed is kept constant during all the FSI computations. As the perturbation due to APD & NSV is relatively small, non-linear effects are not taken into account. It is important to acknowledge that geometric non-linear effect can become significant when the displacement is large, i.e. when attempting to derive running geometry from static geometry [86, 87].

2.4 Further Details on Mode Shape Derivation

As mentioned earlier, the mode shapes are obtained numerically through a FE solver (Rolls-Royce SC03). The first 3 mode shapes (in term of ascending natural frequency) for the two fans are shown in Figure 2.5 and 2.6. They are derived through blade-only model (i.e. zero displacement at blade root) with the assumption that there is no mechanical coupling of vibration through the blade root and disc (i.e. it is assumed that the disc is infinitely stiff). The mode shapes from the structural domain are then linearly mapped onto the fluid domain (i.e. mesh on the blade surface).

Critic [88] of this approach argues that this setup (i.e. mode shape derivation is conducted while excluding the disc and shaft) is not sufficient to capture the running geometry accurately and more mode shapes should be accounted for in the computation. However, the above argument is not practical given the context of the study (i.e. industrial application rather than pure academic research). At the same time, the critic does acknowledge the qualitative results (in particular, Chapter 4) derived through this approach. Though one concede with this argument regarding the accuracy [32, 88], it is important to note this approach is adopted as a compromise among accuracy, computation efficiency, and hence industrial relevance. Additionally, it is important to acknowledge that the main purpose of this study is to attempt to (1) model and understand the general behaviour of APD and NSV and (2) to find attenuating approach for the phenomena rather than to develop a perfect running geometry prediction approach. By adopting the above mentioned approach, more data can be derived to study the underlying physics.

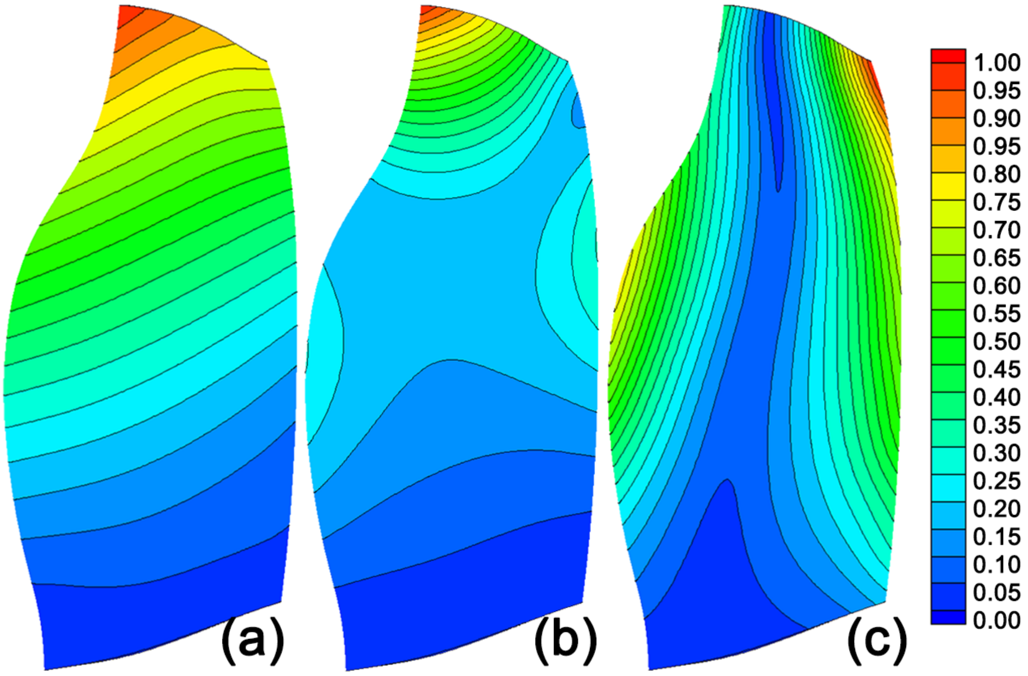

Figure 2.5: Mode shape deflection contour plots (normalised) for Fan 1. (a) First flapwise. (b) Second flapwise. (c) First torsional.

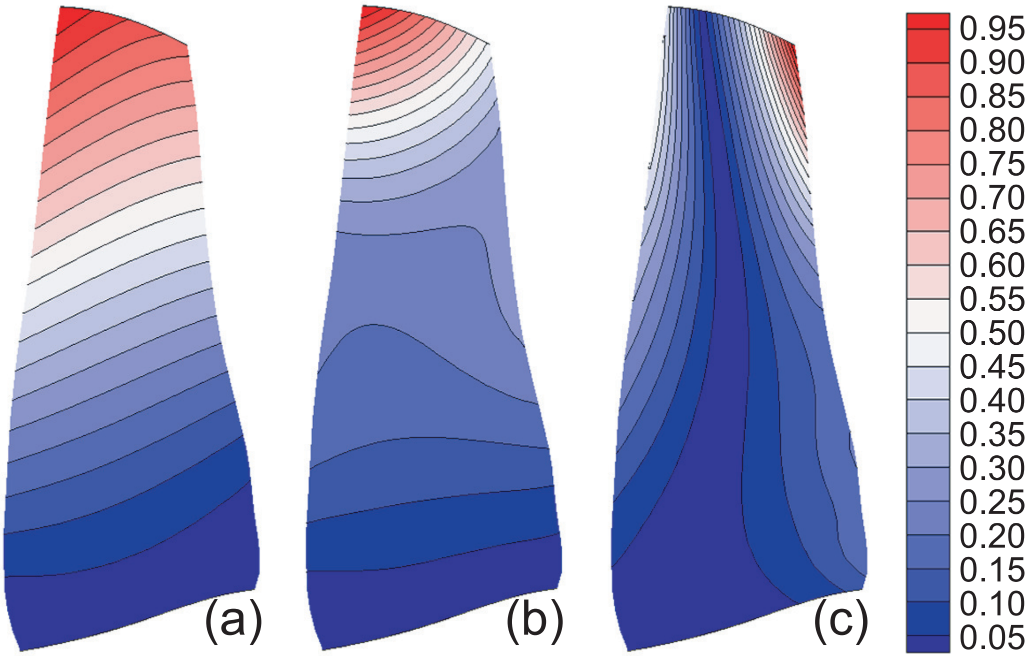

Figure 2.6: Mode shape deflection contour plots (normalised) for Fan 2. (a) First flapwise. (b) Second flapwise. (c) First torsional.

2.5 Mode Shape Expansion and Running Geometry Reconstruction

For full-annulus computation domain, mode shape expansion is required to expand the single blade mode shape onto every blade in the computation domain. Thus, the single blade mode shape is rotated to match the orientation of each additional blade according to Equation 2.35, 2.36, and 2.37. For a particular mode of interest, $\Phi_{1,x}$, $\Phi_{1,y}$, and $\Phi_{1,z}$ denote the x, y, and z component of the single passage mass-normalised mode shape respectively. $\Phi_{n,x}$, $\Phi_{n,y}$, and $\Phi_{n,z}$ denote the three components of expanded mode shape for blade n while N indicates the total number of blades in the assembly. Note that the underlying assumption for this process is that the disk is rigid [32] and the blades are only coupled through air.

$$\Phi_{n,x} = \Phi_{1,x} \tag{2.35}$$

$$\Phi_{n,y} = cos\left(\frac{2\pi\left(n-1\right)}{N}\right)\Phi_{1,y} + sin\left(\frac{2\pi\left(n-1\right)}{N}\right)\Phi_{1,z} \tag{2.36}$$

$$\Phi_{n,z} = cos\left(\frac{2\pi\left(n-1\right)}{N}\right)\Phi_{1,z} - sin\left(\frac{2\pi\left(n-1\right)}{N}\right)\Phi_{1,y} \tag{2.37}$$

The above mentioned expansion is repeated for each blade and then for each mode. While preparing the assembled mode shapes for the aeroelastic solver, modal frequency and consequently modal stiffness for each mode shape can be modified independently. Moreover, this type of mode shape expansion allows one to look at the effects of mistuning (i.e. blades in the same fan assembly have different modal frequencies) on the APD behaviour.

To reconstruct the running geometry from the aeroelastic computations. The blade motion captured by each mode is superimposed through the equations below.

For the i^{th} blade, the components (i.e. Cartesian coordinates) of its running geometry can be reconstructed as:

$$[X'_{i,x}] = [X_{i,x}] + \sum_{j=1}^{r} [\Phi_{i,x,j}]\left\{q_{i,j}\right\} \tag{2.38}$$

$$[X'_{i,y}] = [X_{i,y}] + \sum_{j=1}^{r} [\Phi_{i,y,j}]\left\{q_{i,j}\right\} \tag{2.39}$$

$$[X'_{i,z}] = [X_{i,z}] + \sum_{j=1}^{r} [\Phi_{i,z,j}] \{q_{i,j}\} \tag{2.40}$$

where X and X' are the blade geometry before and after aeroelastic computation respectively. j is the mode shape index. $q_{i,j}$ is the modal displacement for the i^{th} blade's j^{th} mode.

2.6 Computation Domains

The computational domains used for this study are shown in Figure 2.7. Figure 2.8 shows the relative position of the engine and the computation domain for Fan 1. The fan inlets are placed approximately 8 mid-span chord length away from the blade leading edges and the grids are gradually coarsened to minimise boundary reflection. As mentioned earlier, Sea-Level-Static (SLS) boundary condition prescribed at the inlet for its higher air density and ambient pressure than those at cruise condition. Near-wall flow is modelled through wall functions and a slip velocity is imposed at the wall. Wilson et al. [45] concluded that tip clearance only influences the untwist behaviour marginally and hence the domains used in this study do not include a tip clearance. Thus, tip and hub regions are modelled as inviscid walls. For studies involving a selection of passages, the two sides of the domain are modelled as periodic boundaries.

For Fan 1, shown in Figure 2.7(a), a mass flow boundary condition is prescribed at the inlet to the core compressor such that the correct by-pass ratio can be established. The bypass stream exit boundary is modelled as choked nozzle and is hence independent of the condition imposed at the exit. The area ratio of the nozzle is varied to control the flow condition. It was shown by Lee et al. [72] that this form of boundary condition leads to results which are in good agreement with measured data. To reduce computational effort and simplify post-processing, Engine Section Stators (ESS) and Outlet Guide Vanes (OGV) are not included in the domain. Since the splitter geometry is not available for Fan 2, the downstream geometry is modelled as a single convergent-divergent nozzle as shown in Figure 2.7(b). This is not expected to influence the untwist behaviour as Fan 2 is part of a high by-pass ratio engine and the deflection during untwist is highest at the blade tip (i.e. Figure 2.6).

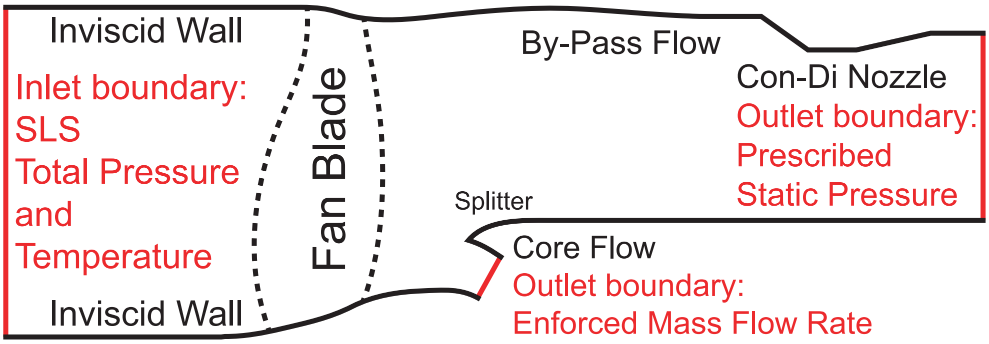

(a) Computation Domain for Fan 1.

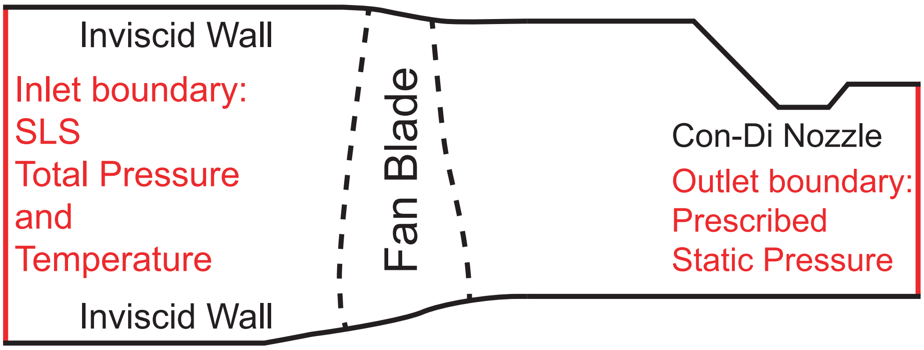

(b) Computation Domain for Fan 2.

Figure 2.7: Computation domains for the two fans. Meridional view. Not to scale.

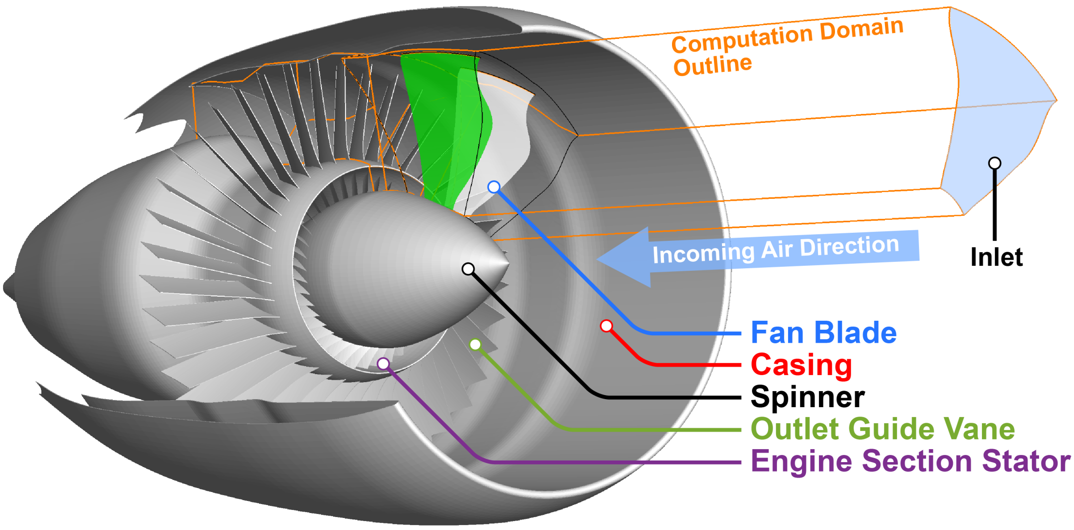

Figure 2.8: Computation domain position relative to the engine (Fan 1).

There are approximately 1.2 million mesh nodes per passage in the domains. This number is determined from a mesh convergence study based on both steady state computation on CF-only blade shape and time accurate blade untwist computation (i.e. CF+Aero blade shape). Given that the blade untwist is sensitive to the pressure distribution on the blade surface, and thus shockwave movement within the passage, the mesh nodes are distributed evenly around the blade on each radial section.

2.7 Untwist Computation on a Constant Speed Line

The approach for untwist calculation on a constant speed line can be broken into three steps. The first two steps are used to establish initial solutions for the blade at CF-only[3] and CF+Aero[4] condition through single passage computation. Blade variability is introduced into full annulus computational domain in the third step to observe the change in aeromechanical characteristics. In order to obtain the deflection due to CF loads for the first step, an in-house FE solver (Rolls-Royce SC03) is used. A single passage computation, which uses periodic boundaries to exploit the axisymmetric geometry, is performed on this geometry. At this stage, a constant speed line, shown in Figure 2.9 as the dashed line, is calculated using the same blade geometry and hence fluid-structure interaction is not taken into account. This also serves as the starting point for the untwist computations of the next step.

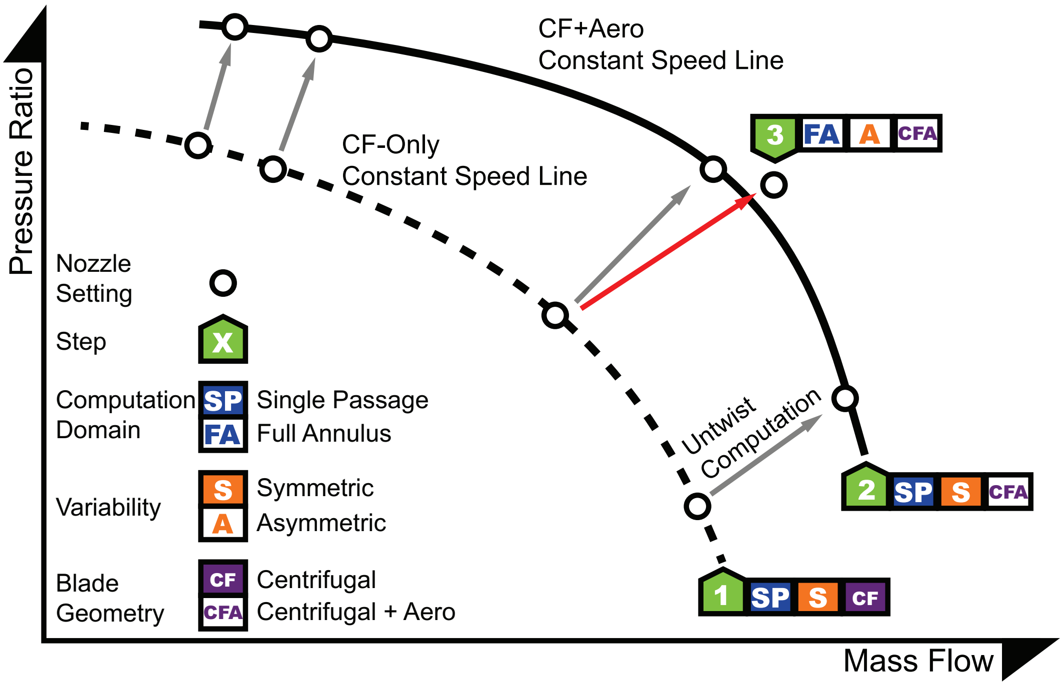

Figure 2.9: Aeroelastic computation approach for untwist and APD studies.

Coupling of fluid and structure is included in Step 2 where mode shapes are used to capture the motion of the blade during untwist. The mode shapes are captured by

---

[3] The fan blade geometry is only influence by the centrifugal force at the speed of interest.

[4] The fan blade geometry is influenced by both the centrifugal and aerodynamic force at the speed of interest.

the FE solver through zero-nodal-diameter[5] blade-only structural computation. The first 12 modes are used in the computation. This number is decided by a convergence study which shares the same conclusion as that presented by Wilson [32]. In essence, the first 3 modes, shown earlier in Figure 2.5 and 2.6, are dominantly important in capturing the untwist behaviour. The first mode, which is normally the first flapwise bending mode, is the most important for it accounts for 86% of the blade tip section untwist at the design point for the swept blade used in this study (i.e. Fan 1). The deflection contour from the blade untwist calculation at the CF+Aero peak efficiency condition is illustrated in Figure 2.10. Two observations can be drawn from the deflection contour. First, the pattern from the deflection contour (Figure 2.10) closely resembles that of the first flapwise mode (Figure 2.5), thus further highlighting its importance in untwist calculation. Secondly, the deflection is highest at the tip of the blade and hence current investigation focuses on the flow condition and untwist at the tip section. Similar to the first step, the untwist computation performed in Step 2 is based upon the assumption that the system is perfectly axisymmetric (both structural and geometrical).

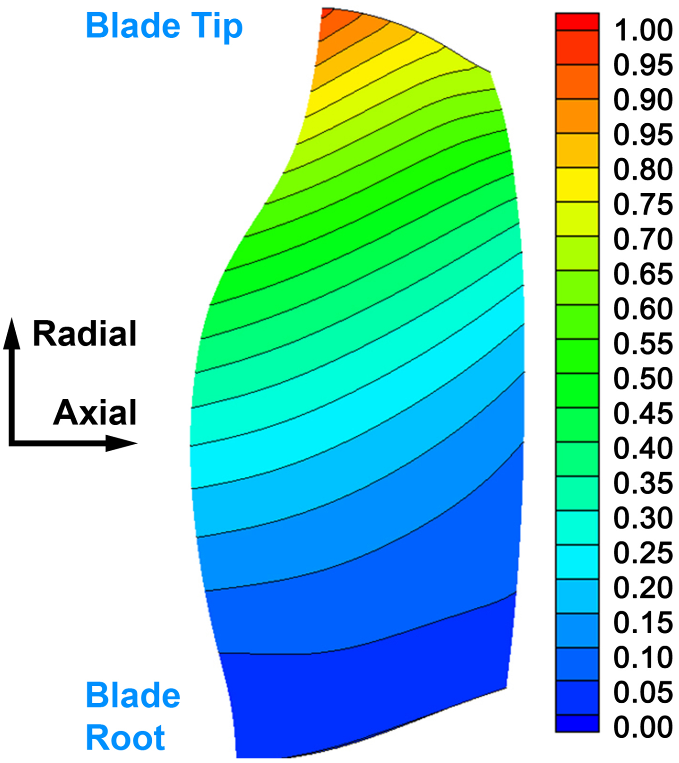

Figure 2.10: Fan 1's untwist deflection contour (normalised) at peak efficiency condition at the design speed.

The calculations completed in Step 2 provide the constant speed line and running geometry of the fan blade at the design speed. Different to the cases in Step 1, the

---

[5] The Nodal Diameter (ND) can be interpreted as the number of diameters on the fan assembly along which there is no displacement.

fan geometries presented on the CF+Aero speed line in Figure 2.9 varies with mass flow. Another important outcome from Step 2 is the determination of nozzle setting required for each operating point. In this way, the starting solution for full annulus aeroelastic computation in Step 3 could be determined from the CF-only constant speed line by identifying the correct nozzle setting.

Variability, geometric and/or structural, is taken into account in Step 3. Geometric variability is included through mis-staggering of the blades. It is applied linearly to the blade with respect to the geometric centre at each radial level with the highest magnitude at the tip section. Alternatively, structural variability is applied through mistuning (frequency-only). To be more specific, for each mode, the blades in the same assembly have slight difference in modal frequency. The single blade mode shapes deployed during Step 2 is then expanded onto each blade through the procedure discussed in Section 2.5. It is completed under the assumption that there is no mechanical coupling between the blade root and disc.

Through aeroelastic coupling, aerodynamic loading would amplify the variability introduced into the computation domain. Therefore, the final operating condition would deviate away from the operating conditions determined in Step 2 under ideal condition. This is illustrated by the red arrow shown in Figure 2.9. The extent of the resulting deviation is highly dependent on the aeroelastic operating condition of the blade and will be discussed in Chapter 3.

2.8 Notes on Reduced Computation Domain

As explained through Figure 2.10, the peak untwist deflection occurs at the blade tip and hence the main focus on the analysis will focus on the tip. Therefore, it is natural to question whether the computation domain can be reduced to included only the tip section or adopt a 2D approach while still achieving similar levels of accuracy. This demand becomes more prominent when the geometric variability which further increases the resource requirement is considered.

Unfortunately, this approach has been proven by Wilson [32] to be futile. In the previous study [32], a thin annulus approach based on the method introduced by Gliebe et al. [48] was attempted. In essence, Wilson concludes that the results from the thin annulus approach are sub-par compared to those from the fully 3D approach at operating conditions most susceptible to develop APD behaviour. Therefore, the approach with reduced computation domain is abandoned.

2.9 Chapter Summary

The test cases and aeroelastic coupling methodology employed in this study are presented in this chapter. The rationale behind many of these choices are elaborated with regard to the objective of the APD study. At the same time, certain compromises are made to ensure the initial investigation into APD & NSV are feasible and can yield useful insights in an industrial context. These highlighted compromises can serve as areas for improvement in future studies.

Chapter 3

APD Mechanism

> The numbers have no way of speaking for themselves.
> We speak for them. We imbue them with meaning.
>
> Nate Silver
> *The Signal and the Noise* [89]

3.1 Introduction

In this chapter, the APD mechanism is investigated using the approach discussed previously. Firstly, the nominal untwist behaviour where the fan assembly is perfectly symmetrical is discussed. The interaction among passage shock, aerodynamic loading, and tip stagger angle is examined across a constant speed line. To emphasis the importance of inclusion of untwist behaviour and hence Fluid-Structure-Interaction (FSI) in making performance[1] predictions, a comparison study is conducted to show the difference between the predicted fan characteristics from FSI calculation and CFD calculation.

Following the discussion of untwist behaviour in symmetric fan assemblies, the untwist behaviour in the presence of geometric variability and hence the APD mechanism are investigated. In particular, the mechanism in which FSI can amplify the initial mis-stagger and introduce the alternating pattern (in terms of tip stagger and passage shock positions) is explained. At the same time, the controlling parameters of APD are explored. The APD behaviour of two distinctly different fan designs (i.e. Fan 1 and Fan 2) are explored on their respective fan maps.

Given the nature of the research, a reduced order model designed to optimise the initial fan blade design stage is validated. The comparison between the peak APD

---

[1] In terms of efficiency, pressure ratio, and stability limit.

loci identified by the high-fidelity model which will be introduced in later sections and those identified by the reduced order model is conducted.

Lastly, the adverse effects of APD are explored. In particular, APD induced efficiency drop and the effect of mistuning over APD are investigated.

3.2 Fan Blade Untwist and APD Mechanism

The nominal untwist behaviour where there is no asymmetry on the fan assembly is first discussed in this section. This is followed by the investigation of the APD mechanism where geometric asymmetry is accounted for. The approach outlined in Chapter 2 is used in this section and results from Fan 1 are presented.

3.2.1 Fan Blade Untwist Mechanism

The shockwave structure within the blade passages influence the blade's aerodynamic untwist behaviour. In this study, the operating conditions across a constant speed line are divided into 3 types of flow regimes as illustrate in Figure 3.1(a). The corresponding pressure distributions on the tip of the fan and the operating regions on the fan map are presented in Figure 3.1(b) and Figure 3.2. The performance data are normalised against the corresponding quantities at the maximum efficiency condition. The aeromechanical data are normalised by the data range. For example, for the shock position data in Figure 3.2, 1.0 is used to denote the shock position on the leading blade's suction surface at the Type A condition (measured at the last stable operating condition before the fan blade stalls). At the same time, 0.0 represents the suction surface shock position when the shock is resting on the trailing edge of the blade.

Type A, unstarted flow, is characterised by the shockwave being expelled from the passage whereas Type C, started flow, can be easily identified by the swallowed passage shock. In between the two extremes is the Type B, intermediate flow, which is characterised by the shockwave being in close proximity of/resting on the leading edge of the trailing blade. Peak efficiency operating condition occurs in this type of flow regime [33, 34, 45], as will be demonstrated, the fan blade untwist behaviour is most sensitive to flow condition changes at this flow regime.

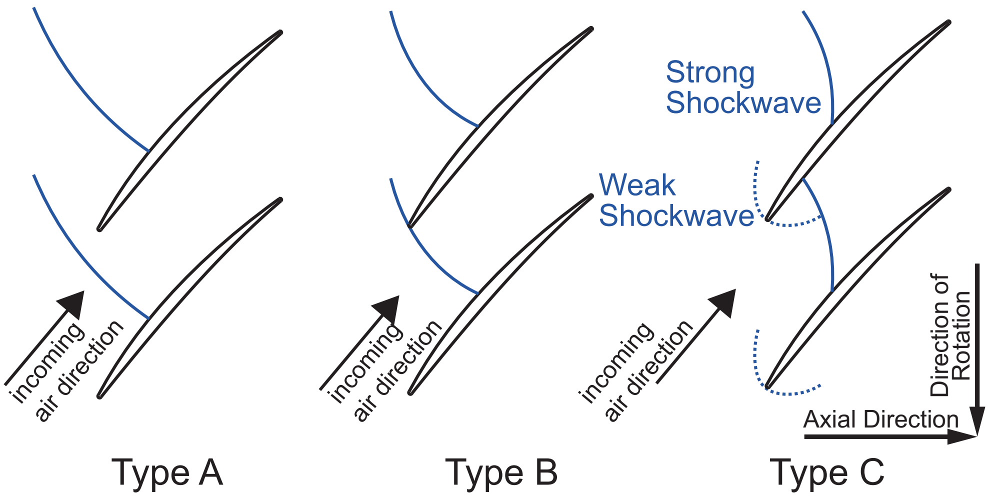

(a) 3 types of flow regime and the shockwave structure at blade tip.

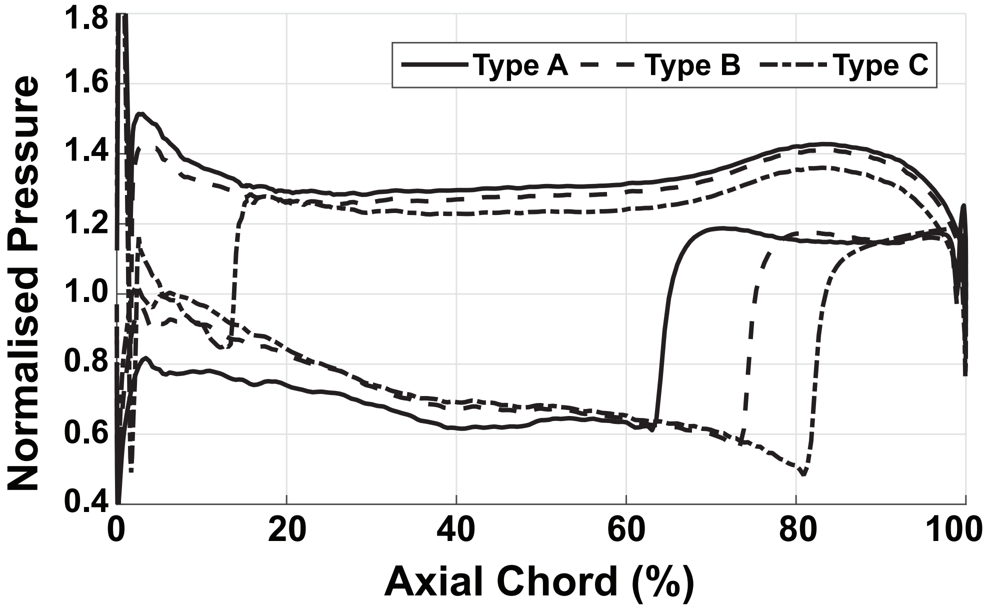

(b) Static pressure distribution at blade tip.

Figure 3.1: Three types of flow regimes and the corresponding pressure distributions at the blade tip (Fan 1).

As the operating point is shifted from the stall side (i.e. Type A) of the characteristics to the choked side (i.e. Type C), the shockwave is moved into the passages. Pressure distributions shown in Figure 3.1(b) demonstrate that such a passage shock displacement reduces the pitching moment on the blade section. Hence the aerodynamically induced moment counteracting the mechanical restoring moment is reduced. This trend could be clearly demonstrated through Figure 3.2 where the aeromechanical properties of the fan blade across a constant speed line are presented. All the performance data are normalised against those of the peak efficiency condition. The grey contours mark the region where each of the three types of flow regimes occur. Type B, intermediate flow, is marked by the white strip at the normalised mass flow rate slightly higher than 1.0. Type A resides at lower mass flow rate than Type B whereas Type C occurs with higher mass flow rate. Except for the pressure ratio, all parameters are calculated at the tip of the blade. The position of the passage shock on the suction surface is tracked for each point on the fan map and the data is normalised such that 1.0 represents the passage shock position near the stall condition (i.e. Type A flow regime) whereas 0.0 denotes position when the passage shock is at the extreme choked condition (i.e. Type C flow regime). The untwist moment is calculated with respect to the blade's centre of untwist (which is located downstream of the trailing edge in the axial direction) at the peak efficiency operating condition. High normalised untwist angle indicates low tip stagger angle (high incidence). As presented in Figure 3.1(b), the combination of a high pressure distribution on the pressure surface leading edge region and a forward passage shock on the suction surface lead to a greater untwist moment under started flow condition (Type A). As can be observed in Figure 2.5, the Fan 1 blade has backward sweep and hence the peak efficiency condition of this blade occurs with a slightly expelled passage shock at the tip. As a result, the Type B regime appears at a mass flow marginally higher than that of the peak efficiency condition.

The results illustrated in Figure 3.2 indicate that all the four parameters share the same type of behaviour across the constant speed line. Thus, at low mass flow up till peak efficiency, the parameters show a near horizontal behaviour as shown in Figure 3.2. In contrast, at high mass flow, a near vertical behaviour is observed. Thus, in the transition region (i.e. intermediate flow), the untwist behaviour and hence passage shock position are most sensitive to the change in mass flow region.

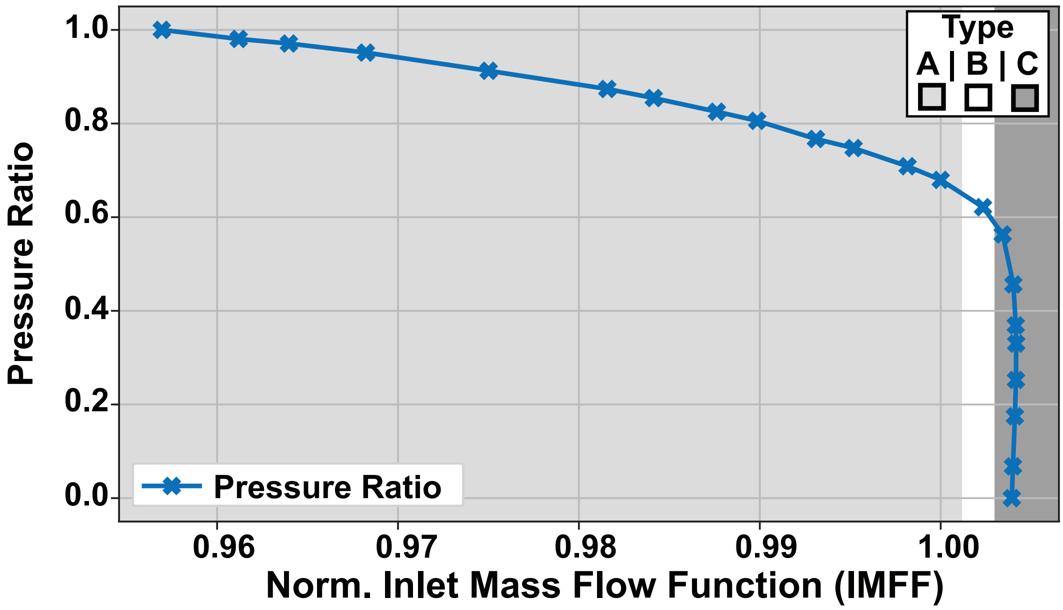

(a) Fan characteristics map.

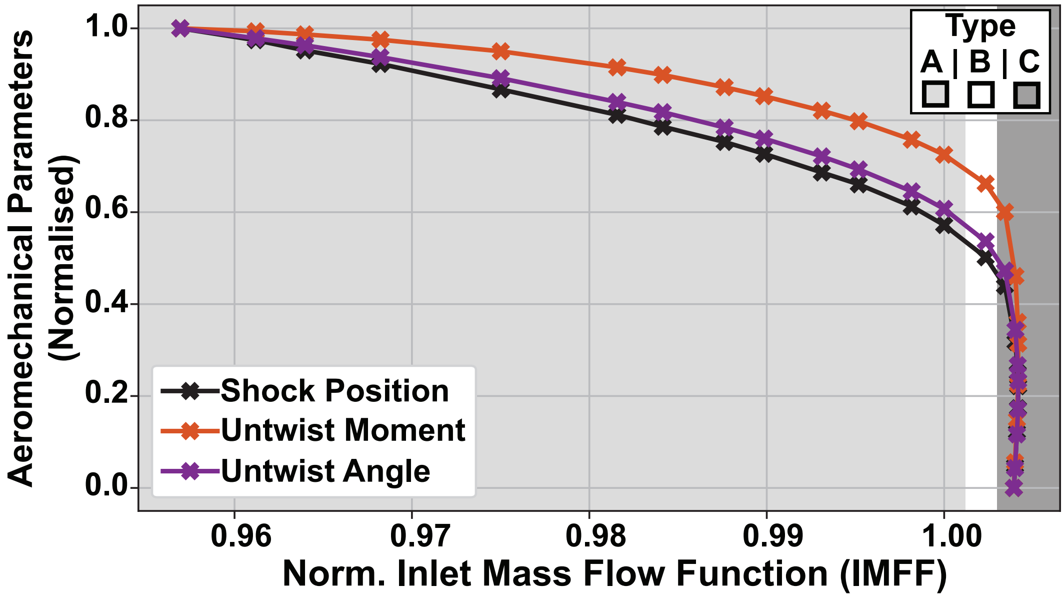

(b) Aeromechanical characteristics across a constant speed line.

Figure 3.2: Aeromechanical characteristics across a constant speed line (Fan 1).

3.2.2 The Importance of Aeroelastic Coupling in Running Geometry Prediction

To further demonstrate the coupling effect between the structural domain and the fluid domain, a comparison study is conducted on Fan 1. In this case, fan characteristics at high rotor speed (i.e. above design speed) are calculated first through the untwist calculation approach outlined in Section 2.7 and then through aerodynamic-only calculation. Note that geometrical variability is excluded in this study.

From the untwist calculation, the predicted fan characteristics are obtained as shown in Figure 3.3 (a) & (b)[2]. The data are normalised such that unity represents the performance metrics at the peak efficiency condition. The fan blade geometry at the peak efficiency condition, highlighted by Marker 2 in Figure 3.3 (a), is then used for the aerodynamic-only approach through which the predicted fan characteristics are presented as the orange data points in Figure 3.3 (a) & (b). In essence, the fan blade geometry varies along the constant speed line in the aeroelastic approach while the blade geometry is the same throughout constant speed line in the aerodynamic-only approach.

From the fan map comparison in Figure 3.3, it is obvious that the two approaches agree with each other at Marker 2 and their discrepancy grows as the operating point moves from the peak efficiency condition. The first observation originates from the fact that the blade shape at this point is the same for the two approaches by design. The second observation is rooted in the untwist mechanism explored earlier with Figure 3.1 and 3.2.

Towards stall, as illustrated in Figure 3.3 (a) & (c), the increased untwist moment reduces the tip stagger angle of the blade which in turn increases the incidence angle. At the same time, this leads to further increase in the untwist moment. Hence, the fan stalls at a higher mass flow rate in the aeroelastic computation as compared to the case where aeroelastic coupling is unaccounted for. The same symbiotic relationship between incidence change and untwist moment can be observed around the operating points towards choke (i.e. region bounded by Marker 3 in Figure 3.3 (a)). More importantly, as the tip stagger angle increases with the declining untwist moment towards choke, the passage gradually becomes ‘closed’. This restricts the mass flow which in turn manifests as the ‘backward’ bending (positive slope of the pressure versus mass flow curve) in Figure 3.3 (a).

As the discrepancy highlighted in Figure 3.3 show, aerodynamic-only calculation leads to over-prediction of the stability limit of the fan. Although the study is conducted at high rotor speed which amplifies such discrepancy, the phenomenon is still of high relevance to the fan designers given the current development trend of fan blades (i.e. longer and more flexible). Therefore, the observations from this study illustrates the necessity and significance of incorporating aeroelastic coupling while conducting numerical prediction of fan performance.

---

[2] Labelled as ‘aeroelastic computation’.

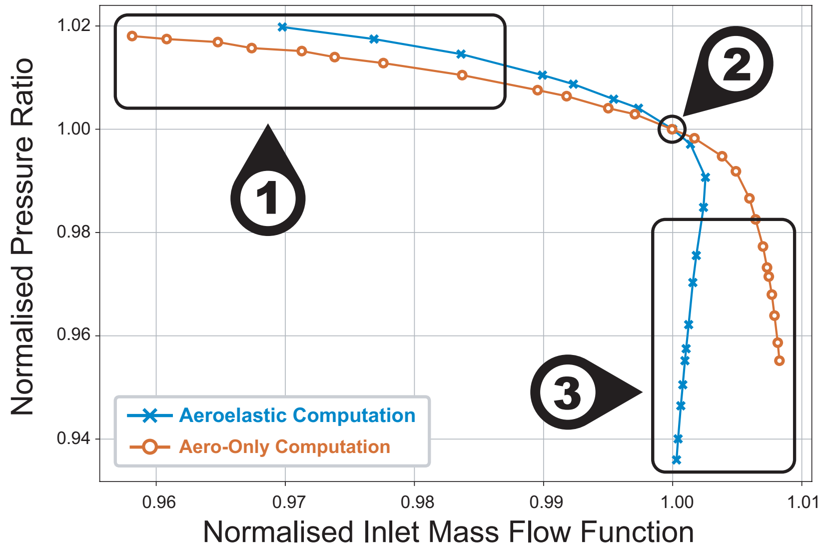

(a) Fan characteristics map: pressure vs. mass flow

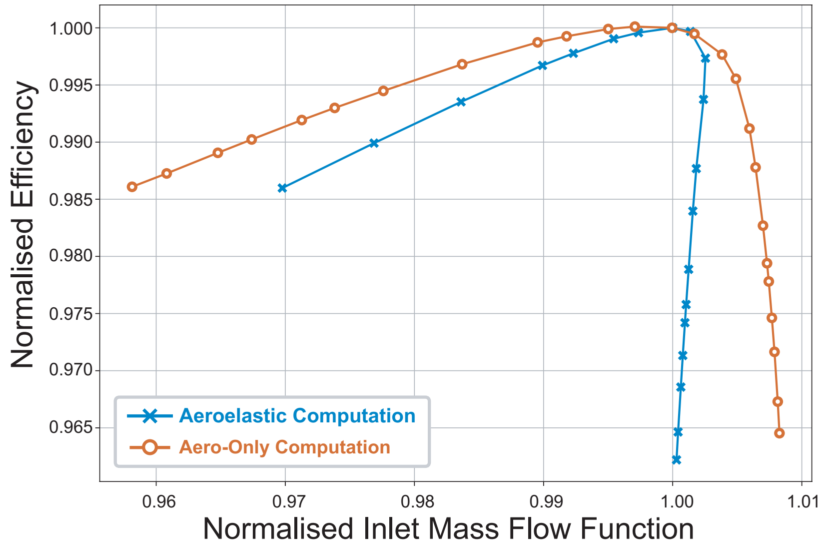

(b) Fan characteristics map: efficiency vs. mass flow

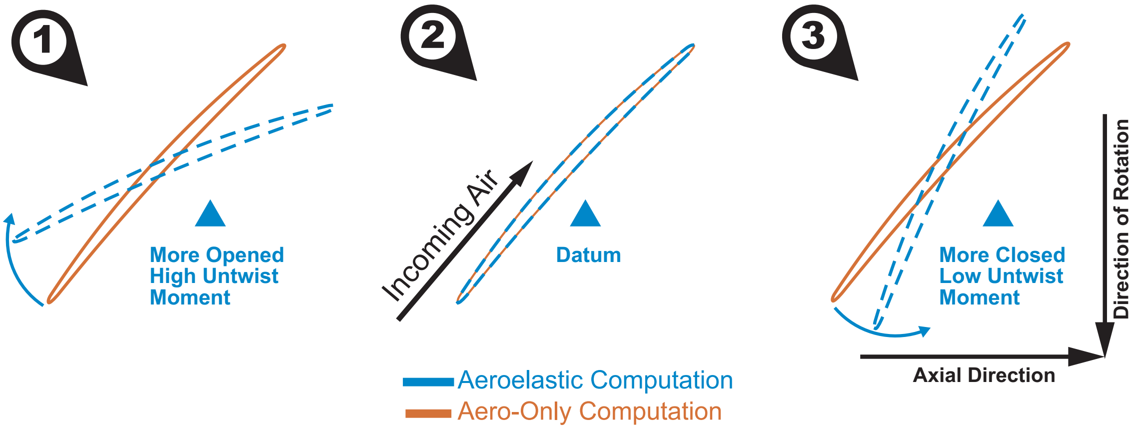

(c) Blade shape comparison (schematics) between the two approaches

Figure 3.3: Comparison of fan characteristic (Fan 1) prediction with aeroelastic approach and with aerodynamic-only approach.

3.2.3 The APD Mechanism

The above discussion on the untwist behaviour is under the scenario where the fan assembly is perfectly symmetric. In comparison, the introduction of geometric variability will bring disturbance to the passage shock structures in adjacent passages and the resulting fluid-structure-interaction could lead to the APD phenomenon. The presence of a mis-staggered blade in an otherwise uniform assembly will cause the geometry of the neighbouring passages to change, thus becoming either more divergent or convergent. Hence, as illustrated in Figure 3.4, where Blade 2's tip stagger is reduced (incidence is increased), the shockwaves in the adjacent passages are either expelled from the passage or swallowed into the passage. As a result, the adjacent blades (Blade 1 and 3) deflect and consequently change the passage geometry. In this case, Blade 1's suction surface passage shock and Blade 3's pressure surface leading edge shock are displaced. The difference in lever arm length (w.r.t. centre of untwist) and hence untwist moment leads to a large change in Blade 3's untwist behaviour whereas Blade 1 only experiences a marginal change. Therefore, under this scenario, the untwist moment on Blade 3 will decrease which results in an increase in Blade 3's stagger angle whereas Blade 1 will experience negligible stagger change. Likewise, forward passage shock displacement will be introduced onto the pressure surface of the blade trailing Blade 3 (i.e. Blade 4, not shown in Figure 3.4) as the tip stagger of Blade 3 deviates further from that of the nominal condition. In this case, an increase in pressure near the leading edge of the pressure surface would lead to a corresponding decrease in Blade 4's stagger angle.

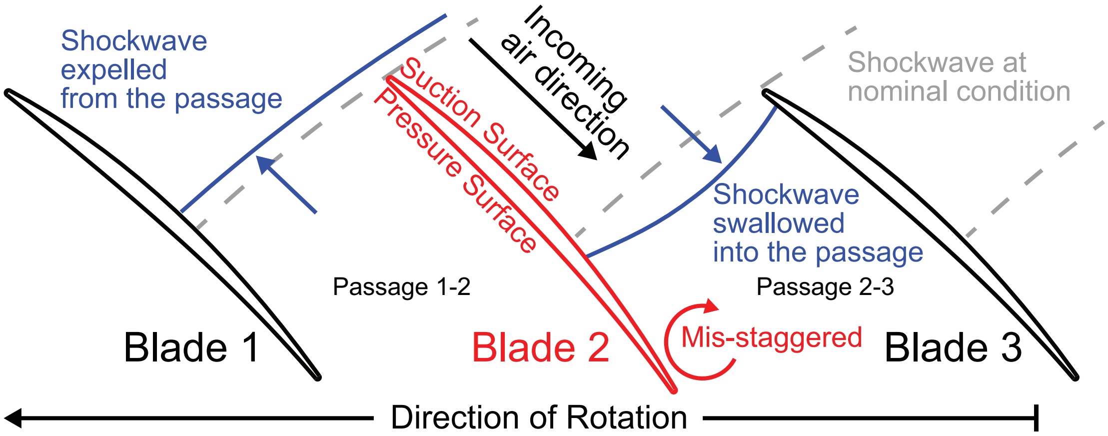

Figure 3.4: Schematic diagram illustrating the passage shock displacement at blade tip under APD condition.

The above mentioned APD propagation mechanism can be illustrated through the relative tip stagger history shown in Figure 3.5. The data are obtained from a coupled computation of Fan 2. The blade numbers are ascending in the direction opposite to rotation (i.e. same as in Figure 3.4). In this case, the initially mis-staggered Blade 2 (increased stagger) triggers the passage shock displacement on the trailing blades sequentially and eventually splits the blades into two groups, those with higher relative stagger and those with lower values. Thus, the APD stagger pattern is formed. This behaviour is consistent with that observed by Wilson et al. [45]. Note that in both studies, the fan design examined has even number of blades and it is reasonable to speculate that the fluid and structure might not reach an equilibrium condition for a design with odd number of blades.

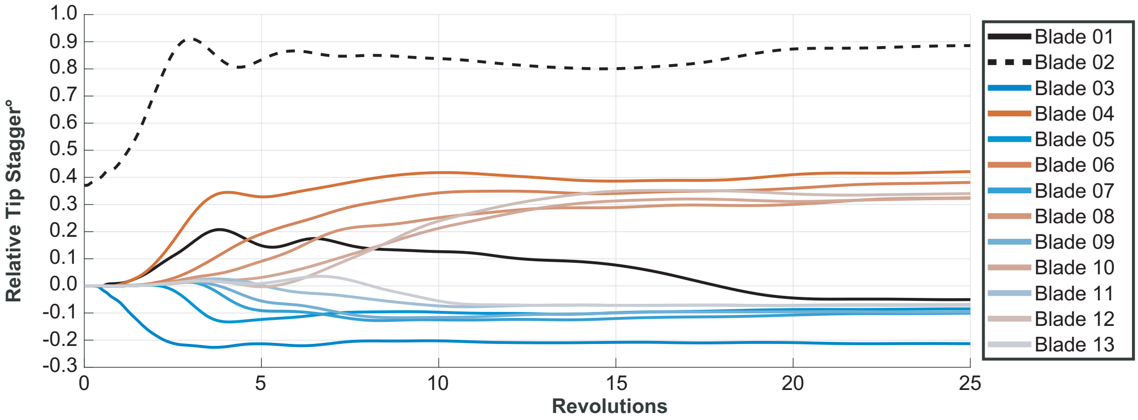

Figure 3.5: Fan 2's APD behaviour shown in term of relative tip stagger history.

The resulting deviant alternating tip stagger pattern has significant implication on the performance of the fan assembly. In the idealised case described above where one single mis-staggered blade forces the entire assembly to adopt the APD condition, half of the passages are pushed to operate in the unstarted flow regime whereas the other half operate with started flow regime. On the fan performance map shown in Figure 3.6, this means the passage operating points would be equally split between the 'APD closed' condition and 'APD opened condition' once APD phenomenon leads to their departure from the datum point. Consequently, this means there would be a net drop in efficiency for the assembly for shifting to either extremes during APD denotes a drop in efficiency. Hence, the designed peak efficiency condition will never be achieved. In comparison, the change in mass flow rate and pressure ratio may not be as significant as that for efficiency since the two sides tend to cancel out each other's offset.

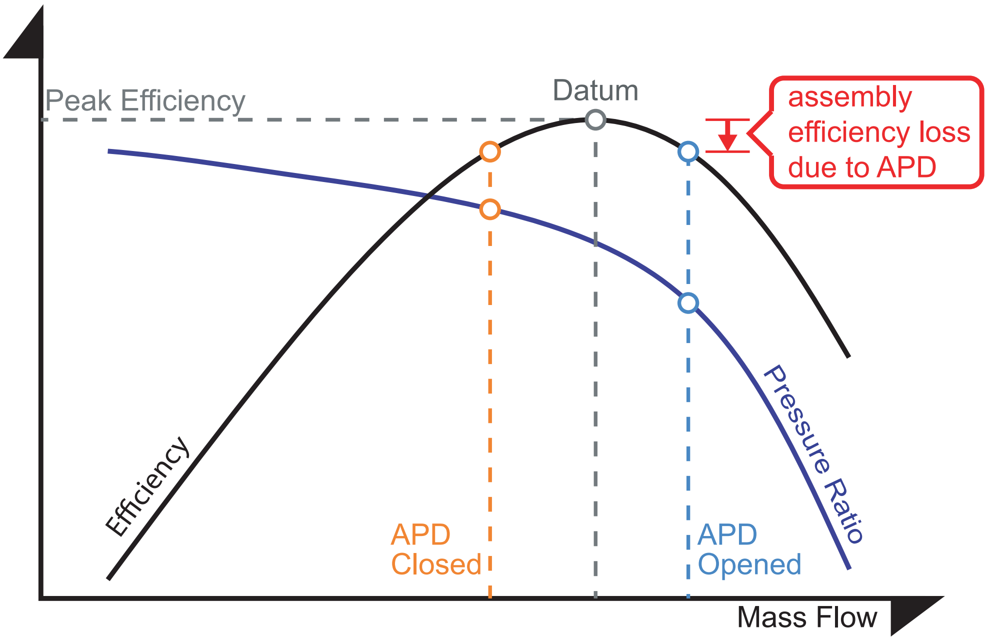

Figure 3.6: Schematic diagram illustrating the influence of APD over assembly efficiency.

3.2.4 Effect of Stiffness

With the method described earlier, full annulus untwist computation including geometric variability is performed at the peak efficiency operating condition at the design speed. However, for Fan 1, it is found that at the datum condition without stiffness reduction the mis-staggering could only introduce localised disturbance to the assembly instead of the macro change (on Fan 2) documented previously [32,45]. The highly localised change is illustrated through the blue line (labelled as 0% modal frequency reduction) in Figure 3.7. In this case, the mis-staggered Blade 16 (increased by 0.5°) can only alter the untwist behaviour of its immediate neighbours, namely Blade 17 and 18, through the aeroelastic coupling mechanism described previously. In order to investigate how APD behaviour is influenced by geometric features (i.e. by comparing the APD behaviour of Fan 1 to that of Fan 2) in the later part of the study, Fan 1's stiffness is artificially reduced to increase the blade deflection and hence the blade-to-blade coupling effect is augmented during untwist. In this case, a 10% and a 20% reduction in stiffness are applied. It is important to acknowledge that such modifications may not be realistic.

Under the coupling framework adopted by this study, the stiffness of the blade is modified by altering the individual frequencies of the vibration modes. By reducing the modal frequencies, the deflection of the blade is increased through the relationship described by Equation 2.34. For this study, modal frequencies of all the 12 natural modes are altered by the same percentage relative to their respective datum values. As illustrated in Figure 3.7, the influence of the initial geometric variability grows from a highly localised form to a full scale APD form as the modal frequencies are reduced. Note that for the three stiffness settings presented, the tip stagger results in Figure 3.7 are calculated relative to the single passage untwist results at the corresponding stiffness setting.

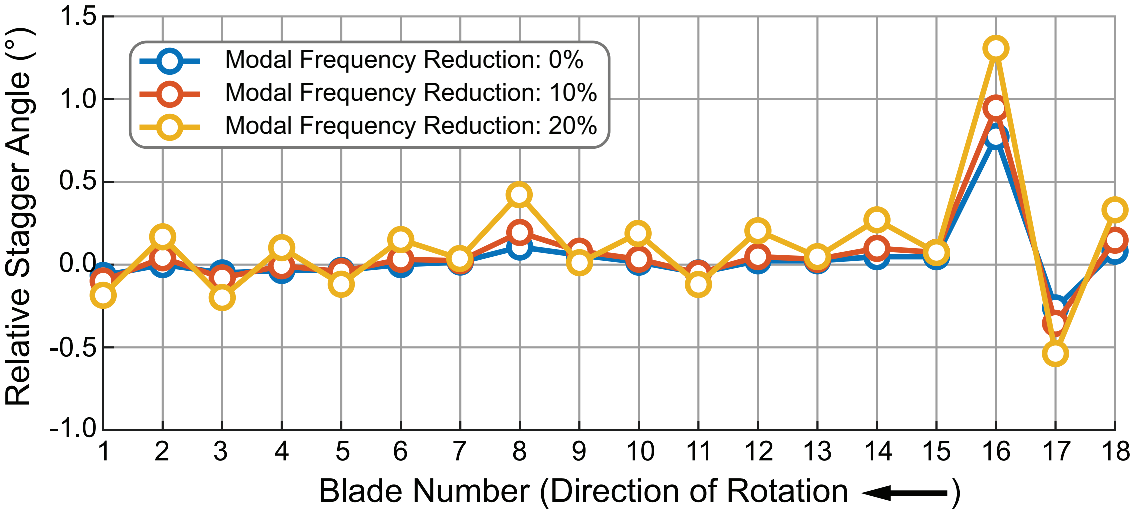

Figure 3.7: Effect of stiffness on the tip stagger pattern of the running geometry.

As evident from the data presented in Figure 3.7, it is undeniable that fan blade stiffness has a significant influence over the aeromechanical behaviour of the fan assembly. Reduced stiffness translates to greater deflection of the blade during untwist and hence empowers the influence of fluid over structure. In the context of APD research, the blade stiffness can also be used to determine the influence of geometric variability. Therefore, the remainder of this study is carried out with a 20% reduction of the modal frequencies (for Fan 1). Furthermore, as can be inferred from the investigation of the blade stiffness, the APD issue is expected to become a growing concern for longer and more flexible fan blade used in future high bypass ratio engines.

3.3 Results and discussion

3.3.1 APD Intensity Maps

In this study, the APD behaviour for the two fans is investigated across multiple speed lines. In order to obtain the APD geometry, time-accurate partially coupled computations (which is described in Chapter 2) are performed. The computations are started from the running geometry and blade-to-blade variability is introduced by mis-staggering a single blade. The mis-stagger is applied linearly from zero at the hub to 0.5°(i.e. within the manufacturing tolerance of 1° [37]) at the tip. The resulting tip stagger patterns are analysed through spatial FFT calculations. The amplitude of the 9th harmonic is used to define the APD intensity for Fan 1 (which has 18 blades) while the 13th harmonic signal is used for the 26-blade Fan 2. The amplitudes are then normalised against the data range and mapped onto the fan maps in Figure 3.8, where fill colour denotes the APD intensity. Note that the APD strength in Fan 1's APD behaviour (Figure 3.8(a)) is half of that in Fan 2's (Figure 3.8(b)). The dark grey lines represent the constant-speed characteristics for an idealised perfectly uniform fan assembly, which were obtained from steady single-passage computations.

Towards stall, the APD intensity levels are low and the operating points align with those of a uniform assembly. This indicates that a single mis-staggered blade has a minor effect on the aerodynamic characteristics of the fan. It causes tip stagger variations in a few adjacent blades but does not affect the overall performance significantly. Near choke condition, assemblies with APD achieve a higher mass flow than the uniform assembly because some of the passages are more open. Comparing the two blades, two main features can be observed: (1) Fan 2 exhibits more intense APD behaviour than Fan 1, and (2) the relative location between peak APD intensity and peak efficiency is different for the two fans.

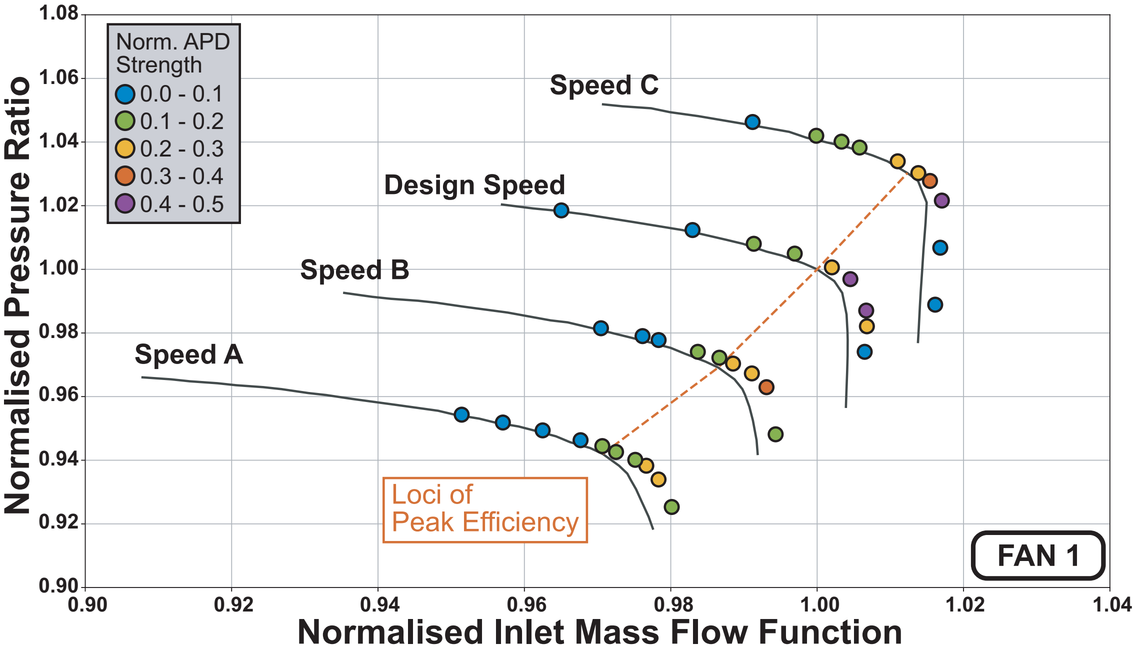

(a) APD intensity map for Fan 1.

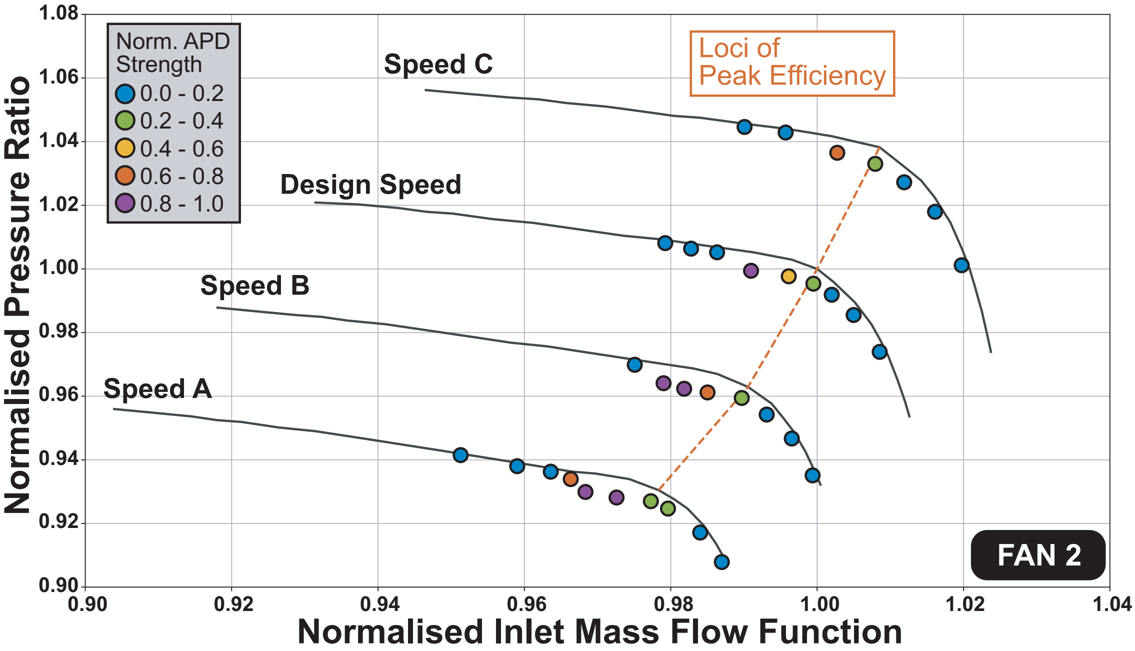

(b) APD intensity map for Fan 2.

Figure 3.8: APD intensity map comparison.

Firstly, the APD phenomenon is stronger on Fan 2 than on Fan 1. This can be explained from the differences in blade design and loading. As discussed earlier, the driving force for APD is the passage shock displacement and resulting change in untwist behaviour. The design feature governing this movement is the covered passage geometry, which is represented by the dashed lines in the sketch of Figure 3.9(a). The length of the covered passage is measured as the length between the leading blade's trailing edge and the foot in which the trailing blade's leading edge is projected onto the leading blade's chord line. At a given point in the covered passage, the covered passage width is measured as the distance between the suction surface of the leading blade and the pressure surface of the trailing blade in the direction perpendicular to the chord lines. This is plotted against chord for the two designs in Figure 3.9(b). It is clear that the Fan 1's covered passage is divergent, whereas Fan 2's covered passage is convergent-divergent with a minimum throat area at around 80% chord. This subtle geometric difference determines the smoothness of the shockwave displacement within the passage and consequently the strength of APD. Another distinct difference is that Fan 2 has twice the covered passage length as that of Fan 1. This is mainly due to the difference in the number of blades.

For Fan 2, the shock cannot be stabilised in the convergent region of the passage. A stable condition only exists if the shock is either resting on the leading edge of the tip or swallowed into the divergent section of the covered passage. This creates a discontinuity/step change in the shock structure of Fan 2's blades and consequently a discontinuity in aerodynamically induced untwist moment which creates strong blade-to-blade variations.

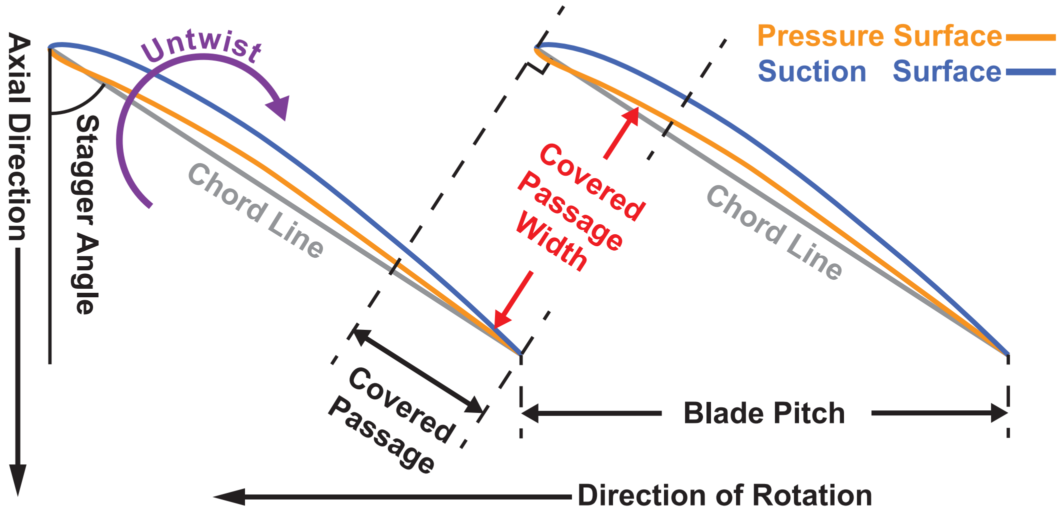

(a) Schematic diagram for covered passage geometry.

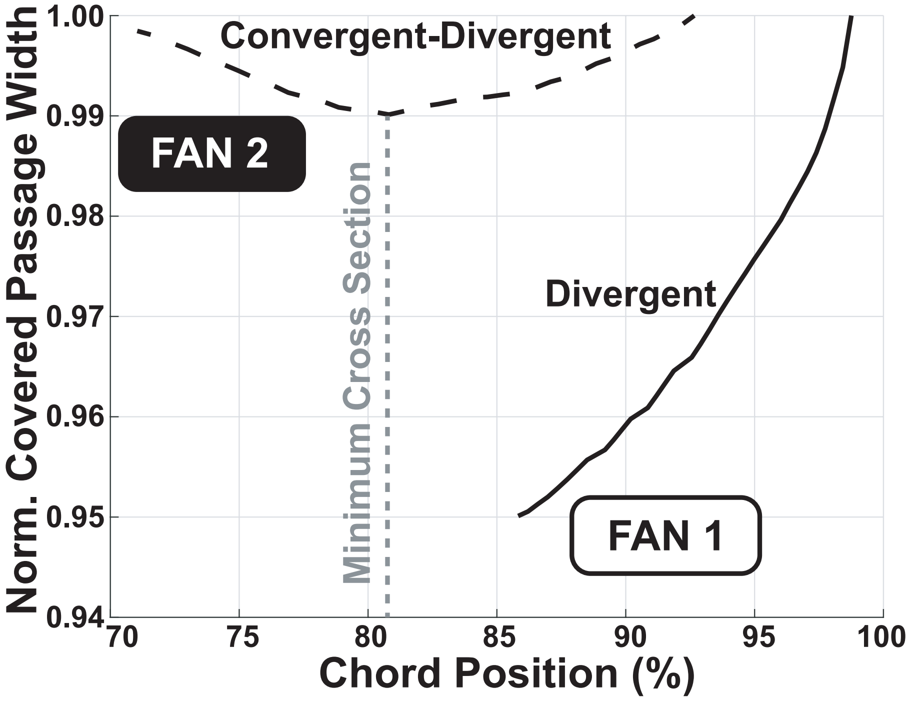

(b) Comparison of covered passage geometry between the two designs.

Figure 3.9: Covered Passage Geometry for nominal blade geometry.

The above explanation is supported by the differences in blade pressure distributions. Figure 3.10(a) shows the pressure profiles for individual blades at Fan 1's peak APD amplitude case at the design speed. Figure 3.10(b) shows the corresponding behaviour for Fan 2 (i.e. the peak APD amplitude case at the design speed). In both figures, the direction of rotation is represented by descending blade numbers and Blade 4 is initially mis-staggered. In Figure 3.10(a), small differences in leading edge pressure and suction surface shock position between the adjacent blades are visible. Such differences contribute to approximately 10% difference in untwist moment at the tip. This alternating pressure distribution thus introduces APD onto the assembly. In contrast, a more distinct difference can be observed in Figure 3.10(b) where pressure surface shock position on adjacent blades differ by approximately 20% of chord length. Consequently, this leads to almost 40% difference in untwist moment between blade pairs which makes Fan 2 highly prone to exhibit APD behaviour.

To summarise, the main geometry feature which determines the smoothness of the passage shock displacement is the absence /existence of the throat. A passage with a converging-diverging section results in a discontinuity in shock displacement which maximises the differences in loading and associated untwist between adjacent blades, creating a strong APD pattern.

Secondly, the maximum APD amplitude occurs close to the peak efficiency loci drawn in Figure 3.12 but is shifted towards choke for Fan 1 and slightly towards stall for Fan 2. The location of maximum APD intensity depends on the sweep of the blade. The backward sweep on Fan 1's blades (see Figure 2.10) dictates that its peak efficiency conditions is achieved when the shock is slightly expelled at the tip (i.e. Type A flow in Figure 3.1(a)). Thus the peak APD cases are located slightly towards choke for Fan 1. Conversely, Fan 2's distinct covered passage geometry prompts its peak efficiency condition to occur with passage shock right behind the throat (i.e. Type C flow in Figure 3.1(a)). Accordingly, the worst-case APD cases occur ahead of the peak efficiency loci with lower mass flow rate.

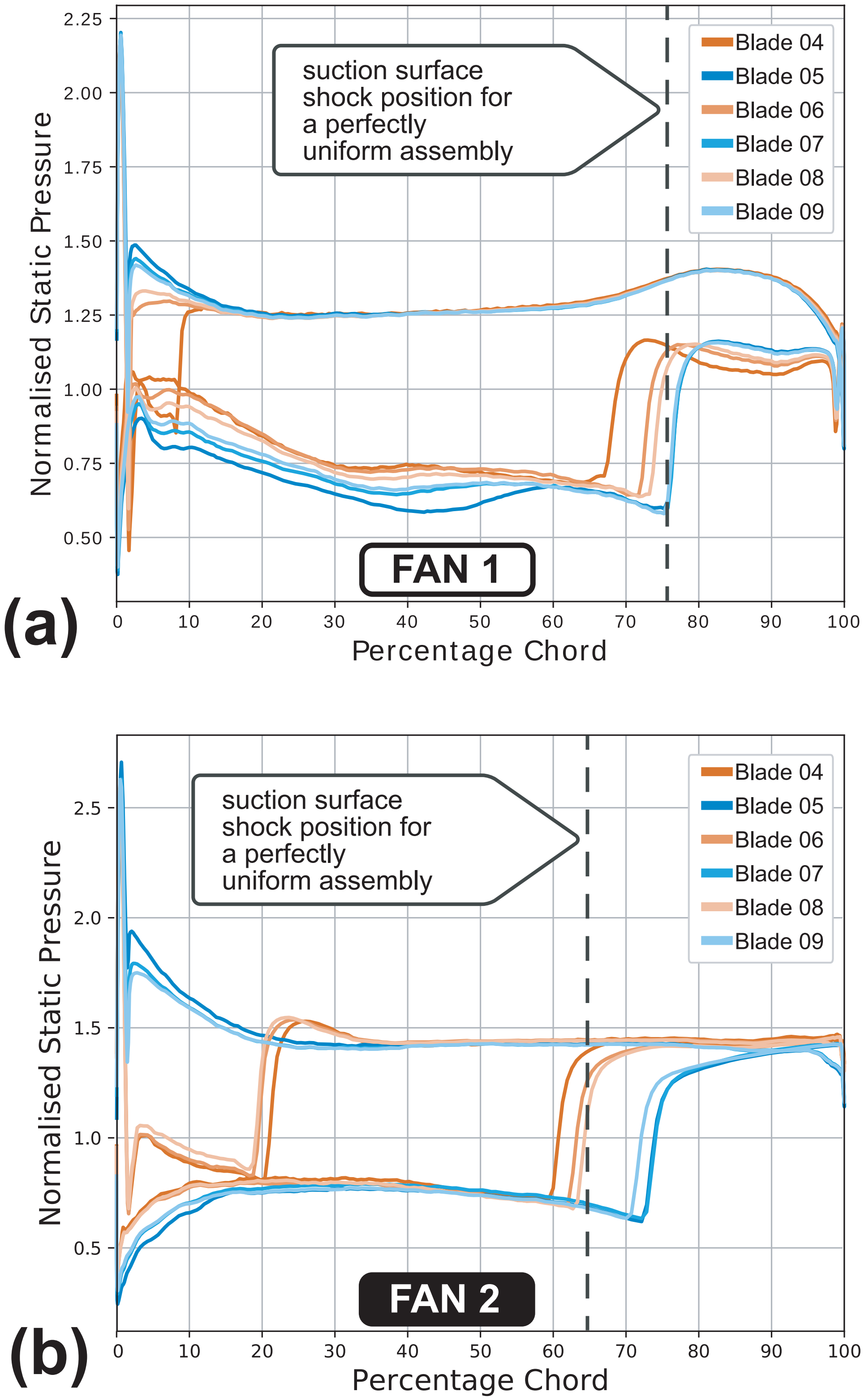

Figure 3.10: Pressure distribution at blade tips after a full annulus calculation.

3.3.2 Reduced Order Approach

The previous discussion showed how the passage shock is most sensitive to changes in flow condition when the shock sits near the leading edge (i.e. Type B in Figure 3.1(a)). Thus, APD is highly correlated to shock displacement. This can be further investigated through Figure 3.11(a) which shows the relative shock position against mass flow rate at Fan 1's design speed. The relative shock position is normalised such that 0 corresponds to near-stall while 1 corresponds to choke. Thus, the most sensitive/unstable operating condition can be identified by locating the peak value of the second derivative of the shock position with respect to mass flow rate (i.e. the 'acceleration' of the passage shock). In Figure 3.11(b), a peak can be clearly observed at the normalised mass flow above 1 (which corresponds to the peak efficiency condition). Note that the data for the extreme choke cases (cases in the blue rectangle in Figure 3.11(a)) are filtered out during the second derivative calculation.

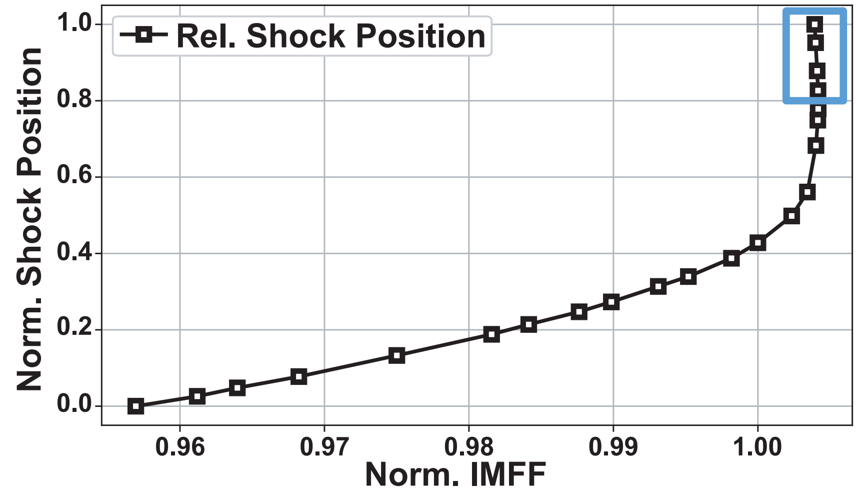

(a) Norm. Shock Position with respect to Mass Flow Rate.

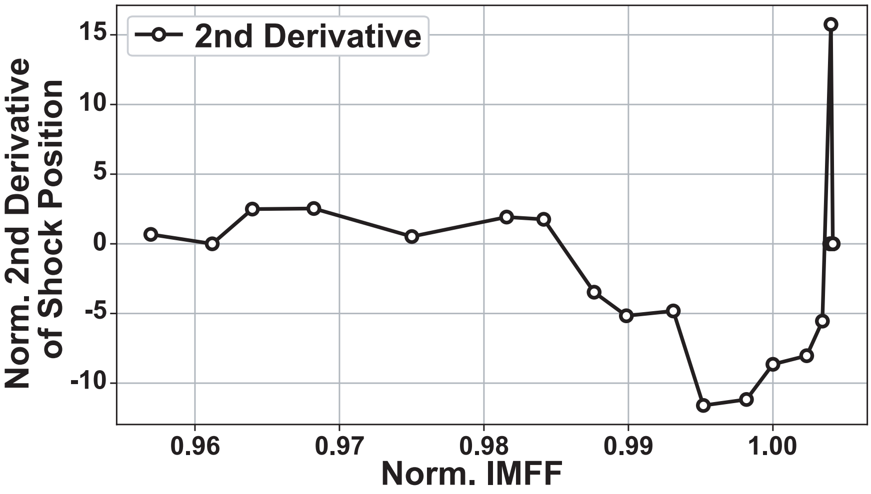

(b) Norm. 2nd Derivative of Shock Position with respect to Mass Flow Rate.

Figure 3.11: Relative shock displacement and its 2nd derivative.

This calculation was performed for each constant speed line and the operating points where the second derivative is at the highest for the particular speed line are mapped onto the APD map in Figure 3.12(a) and (b) as the blue dash-dot lines. From the plots, it is clear that the predicted peak APD intensity region has a strong correlation with the loci for peak shock displacement sensitivity for both blades. This reduced order approach can locate the worst-case APD condition in a computationally efficient fashion. Instead of performing full annulus coupled calculation to map the intensity map, the most undesirable case can be located through single passage untwist calculation and even uncoupled computation on the design blade geometry. With this approach, only a limited number of full annulus cases are required to gauge the strength of APD. For this study, the time required can be reduced from 400,000 CPU-hours to approximately 3,000 CPU-hours for each blade.

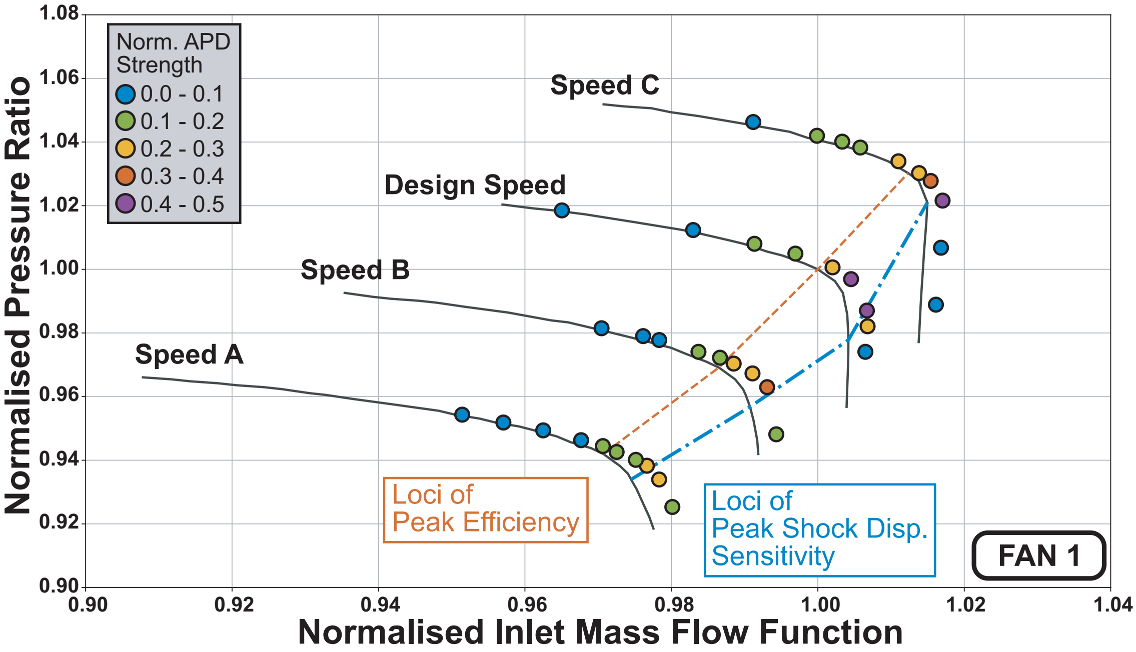

(a) APD intensity map for Fan 1.

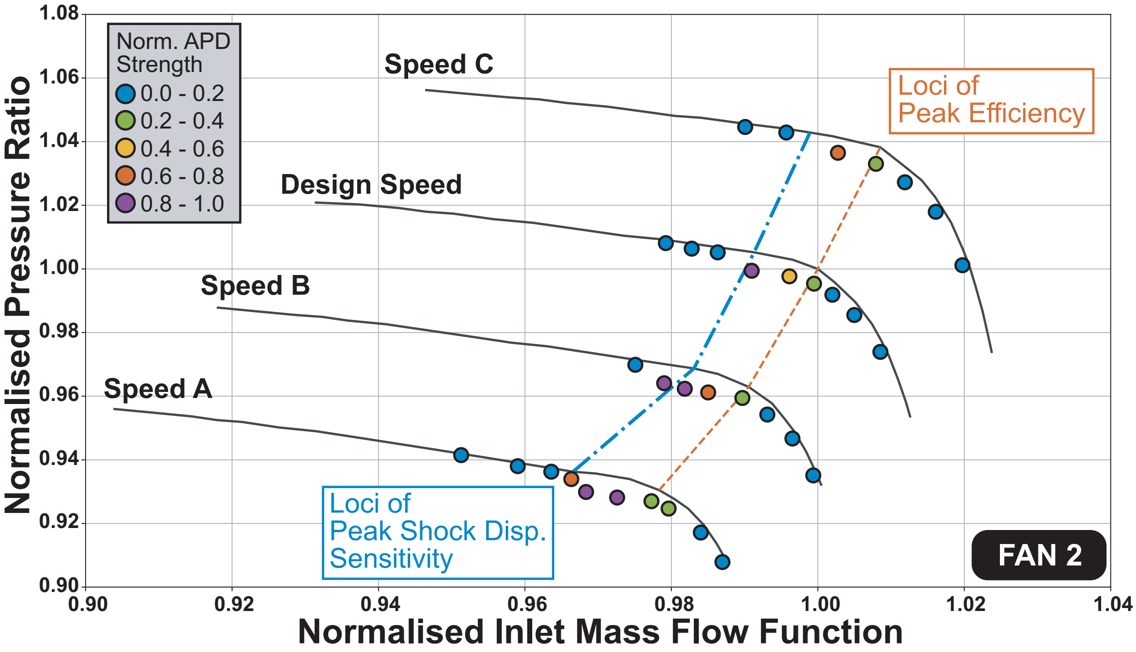

(b) APD intensity map for Fan 2.

Figure 3.12: APD intensity map comparison (incl. peak shock sensitivity loci).

3.4 Adverse Effects of APD

The adverse effects associated with APD are explored in this section through numerical studies on Fan 1.

3.4.1 Performance Deterioration

The previous discussion on performance is based on the highly idealised APD case where only one blade's CF-only geometry is different from the nominal CF-only geometry. For a real fan assembly, it is reasonable to expect all the blades will deviate away from the nominal /design geometry. Thus, based on the observation that geometric variability can trigger APD which could in turn introduce adverse effect to fan performance, it is important to explore whether forming the blades in a particular pattern on the assembly can minimise the performance drop. The secondary objective of this part of the study is to highlight the importance of including FSI during design. To do so, the aerodynamic computation and aeroelastic computation are started from the same CF+Aero blade geometry which gave the highest APD intensity at high speed. Three types of mis-staggering patterns, shown in Figure 3.13(a), are applied onto the fan assembly. The spatial Fourier decomposition of the pattern reveals that the most dominant signal in the random pattern is the 8ND pattern followed by the 2ND pattern. Additionally, three amplitude settings, 0.5°, 1.0°, and 1.5°are included in the study. The amplitude refers to the highest mis-stagger angle in the pattern.

Comparison of the tip stagger patterns shown in Figure 3.13(a) and (b) highlights how initial blade-to-blade variability can be augmented by aerodynamic forces. Of the three patterns, the 9ND pattern is enhanced the most, increasing the blade-to-blade variability from 1.0°to 2.5°. This is followed by the case with the random pattern. In addition to the magnified geometric variability, an APD pattern is almost formed. In contrast, the 1ND mis-stagger pattern results only demonstrate a marginally enhanced 1ND signal.

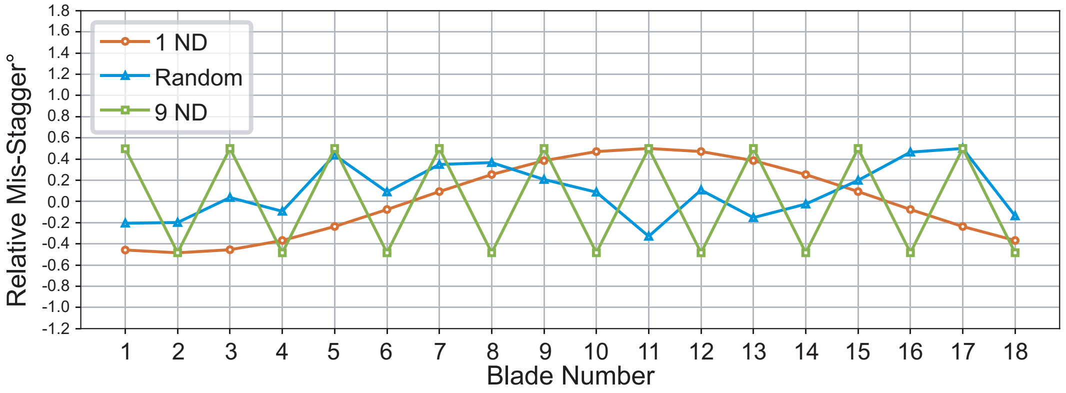

(a) 3 types of imposed mis-stagger patterns with amplitude of 0.5°.

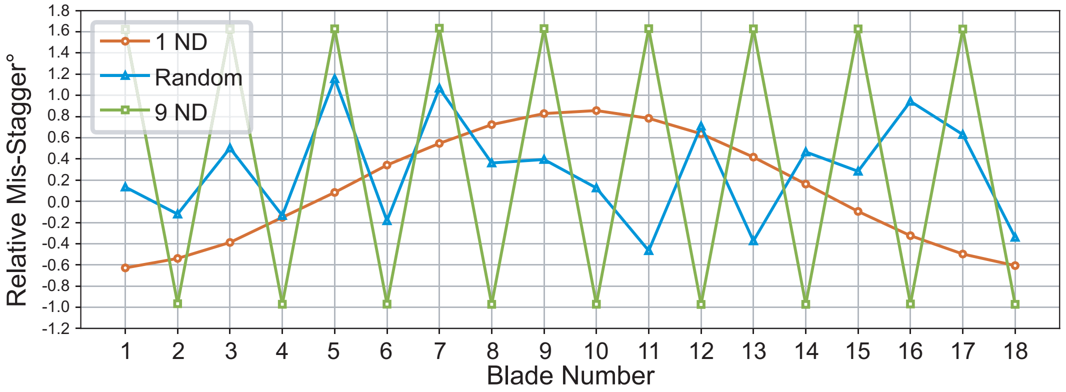

(b) Stagger pattern after aeroelastic computation. Initial pattern is shown in (a).

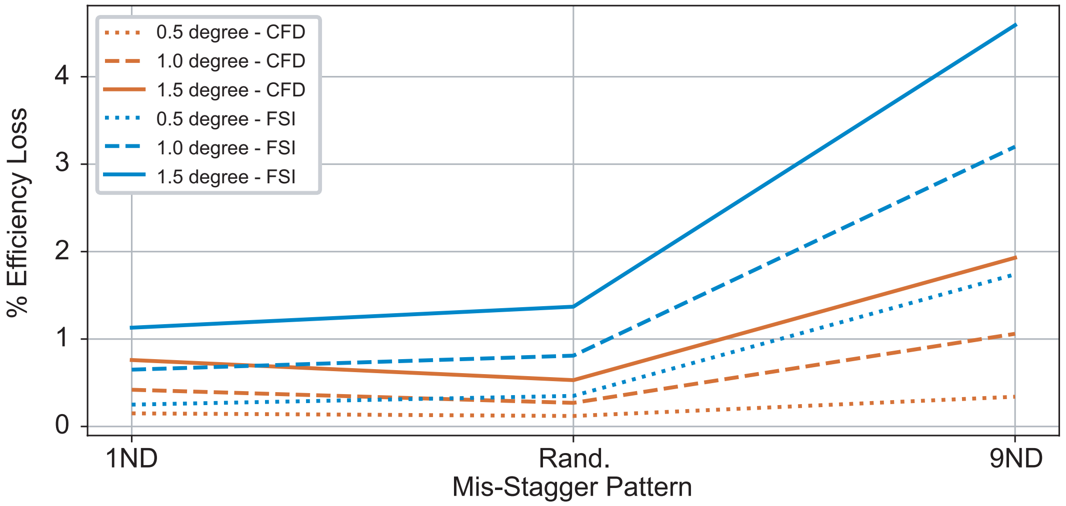

(c) Efficiency loss due to mis-staggering.

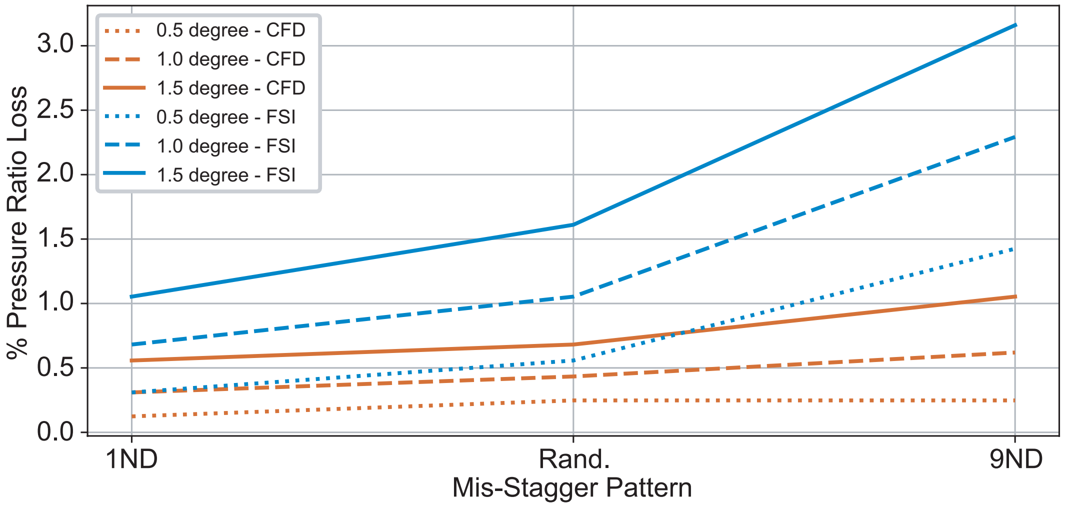

(d) Drop in pressure ratio due to mis-staggering.

Figure 3.13: Influence of blade variability on fan performance.

Performance results from the performance study are illustrated in Figure 3.13(c) and (d). Aeroelastic simulations are labelled as ‘FSI’ while the label ‘CFD’ denotes purely aerodynamic computations with fixed blade geometry. For both types of computation, the results reveal that the 9ND pattern is associated with the largest performance reduction while the 1ND pattern is accompanied by the smallest change. For all three mis-staggering amplitude explored in this study, it can be concluded that aeroelastic coupling can augment the performance deterioration significantly and the alternating 9ND pattern should be avoided.

It is important to note that the above performance reduction trend is derived through computation at Sea-Level-Static condition. It is reasonable to suggest that the reduction in performance is less significant at cruise altitude. However, the effect may become more important for future engines with longer, light-weight fan blades.

3.4.2 APD Introduction through Intentional Mistuning

Previous analyses are conducted under the assumption that the fan blades are structurally tuned. Given that intentional mistuning is sometimes used as a means to prevent fan flutter [90–92], it is interesting to explore whether mistuning alone can lead to APD behaviour. Therefore, a mistuning study is conducted for Fan 1. Frequency mistuning (of Mode 1/first flapwise mode) is introduced onto a perfectly symmetrical starting geometry. The starting operating condition is the one associated with the worst-case APD behaviour at the design speed.

As illustrated in Figure 3.14(a), a random mistuning pattern with amplitude of ±2% is used in the coupled untwist computation of a full-annulus geometrically tuned fan assembly. Fourier decomposition of the mistuning pattern, shown in Figure 3.14(c), reveals that the dominant signal is the 8th harmonic signal. Figure 3.14(b) shows the converged geometry in term of tip stagger. It should be noted that, without APD (i.e. not operating near the APD condition on the fan map), the final mis-stagger pattern follows the initial mistuning pattern and the magnitude of mis-staggering is significantly smaller than the APD case. Comparing Figure 3.14(a) to (b), it is evident that the final stagger pattern does not follow the initial mistuning pattern. The initially alternating mistuning pattern from Blade 8 to 18 has been translated into an alternating stagger pattern while a mild APD pattern is established between Blade 1 and 7 where the initial variability is not alternating in nature. Besides, as shown in Figure 3.14(c), aeroelastic coupling has shifted the dominant signal to the 9th harmonics and suppressed signals from all the other harmonics. By comparing the patterns in Figure 3.14(a) and (b), it is clear that mistuning can introduce APD behaviour into the system.

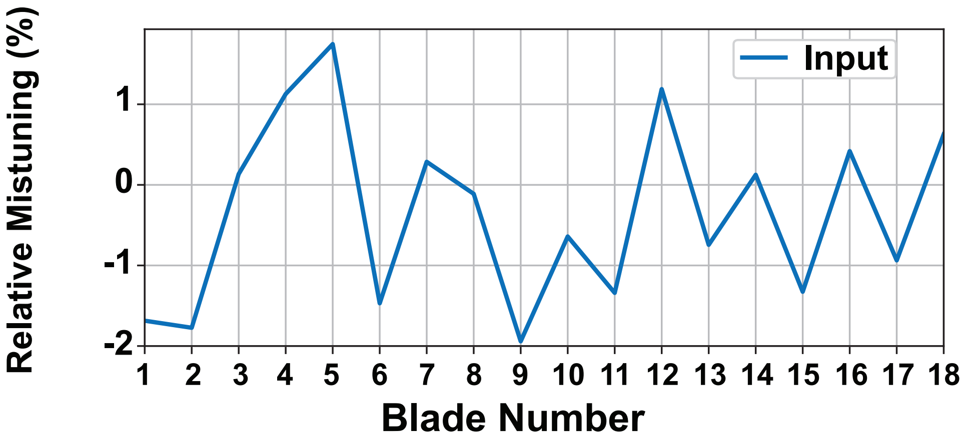

(a) Initial mistuning pattern.

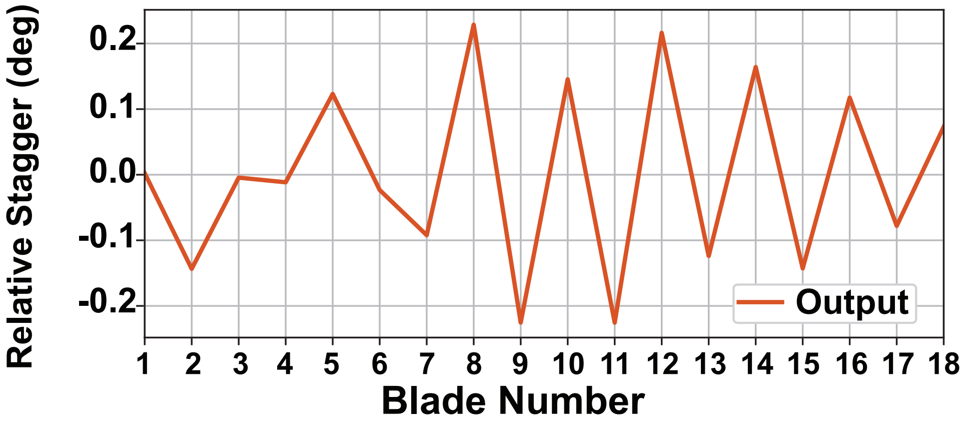

(b) Final tip stagger pattern.

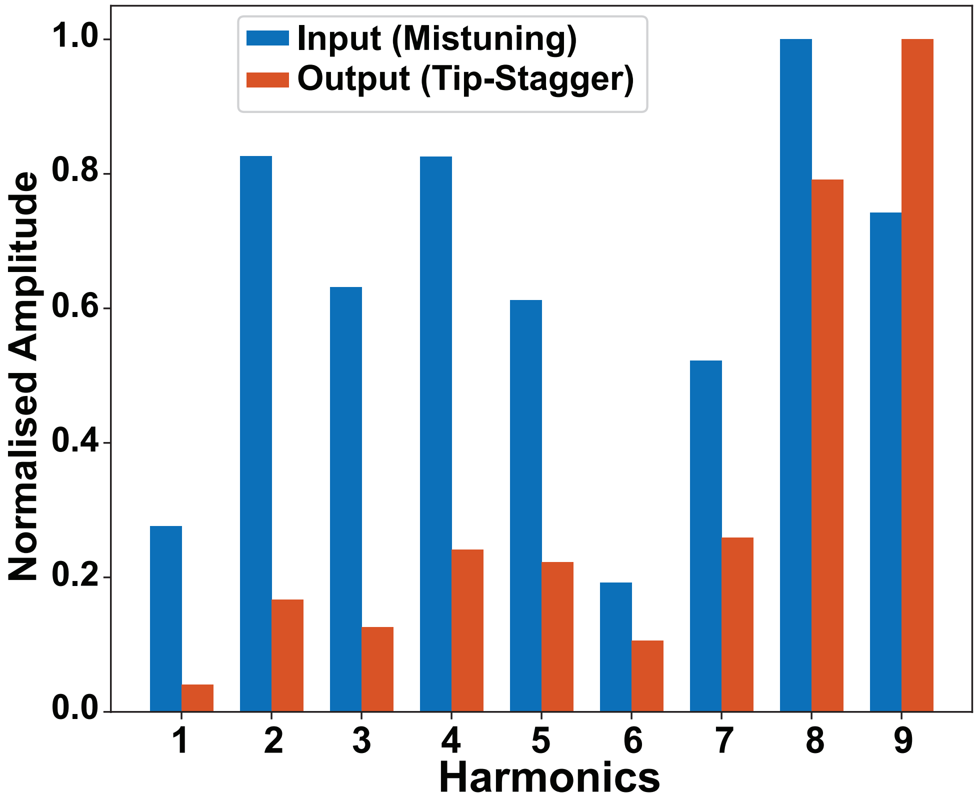

(c) Comparison of Fourier Decomposition results from the input and from the output.

Figure 3.14: Effect of mistuning on running geometry.

3.5 Chapter Summary

The findings revealed in this study lead us to the following conclusions and direction for further studies:

1. From results comparison between the aeroelastic approach and the aerodynamic-only approach in Section 3.2.2, it has been shown that the later approach leads to over prediction of the fan stability limit. This highlights the important of including aeroelastic coupling in running geometry and fan performance prediction.

2. Through the APD contour map and the loci of peak shock displacement sensitivity, it can be concluded that APD is closely related to the discontinuity /non-linearity in the untwist behaviour of the fan blades.

3. Results from the stiffness reduction study clearly indicates that APD behaviour is inversely related to the stiffness of the blade.

4. Comparison of the two blades' geometry and the corresponding difference in their APD behaviour reveals that a discontinuous /abrupt transition in the passage shock position exacerbates the APD behaviour. A spin-off idea from this observation is the convergent section of the covered passage (where the passage shock cannot be stabilised) on Fan 2 can introduce unsteadiness in the annulus because it prompts shock displacement and further aeromechanical change. In fact, it is previously observed that under certain conditions, APD can be accompanied by a travelling disturbance around the annulus. It is important to investigate the unsteady effect of APD because it can influence the fan blades' high cycle fatigue life.

5. From the results comparison between the reduced order model and the full annulus coupled computation, it is evident that the peak APD conditions at each constant speed line can be located by the reduced order model. This will result in the reduction in computation cost. Therefore, it would be interesting to investigate whether reduced order model can be used to quantify APD intensity such that it can be incorporated into fan blade design approach.

6. As demonstrated, APD occurs in close proximity to design point which sets it apart from other types of aeromechanical instabilities (such as flutter) which usually occur at off-design conditions and thus of relatively less concern to the engine manufacturers. This makes it paramount for the manufacturers to comprehend this phenomenon.

7. Given that intentional mistuning which is usually used to prevent flutter behaviour (i.e. at off-design conditions) can introduce APD behaviour (close to design condition), it is crucial for engine manufacturers to investigate the APD behaviour.

Chapter 4

Non-Synchronous Vibration and Running Geometry Prediction

> Seeing the big picture means much more than simply acquiring more information.We must see how the information is connected as well as how our own actions are connected.
>
> Garry Kasparov
>
> *How Life Imitates Chess* [93]

4.1 Chapter Introduction

This chapter focuses on the unsteady APD behaviour on Fan 2. As the unsteady behaviour is not linked to the multiples of engine shaft speed and thus, for brevity, the unsteady APD behaviour examined in this chapter will be termed Non-Synchronous Vibration (NSV). The NSV behaviour analysed here is similar to APD from the previous chapter. However, steady solution does not exist for NSV as the blades continue to switch from having higher than nominal tip stagger to lower ones, and vice versa.

This chapter is structured as follows. A general introduction to NSV behaviour is introduced first and the rationale for the major geometry related approximation is explained. Secondly, the results from the NSV temporal convergence are presented to establish the confidence in the temporal resolution used for the later calculations. Thirdly, a detailed discussion on the NSV mechanism is presented. Lastly, NSV computation results are presented and the key parameters influencing NSV behaviours are identified.

4.2 NSV Behaviour

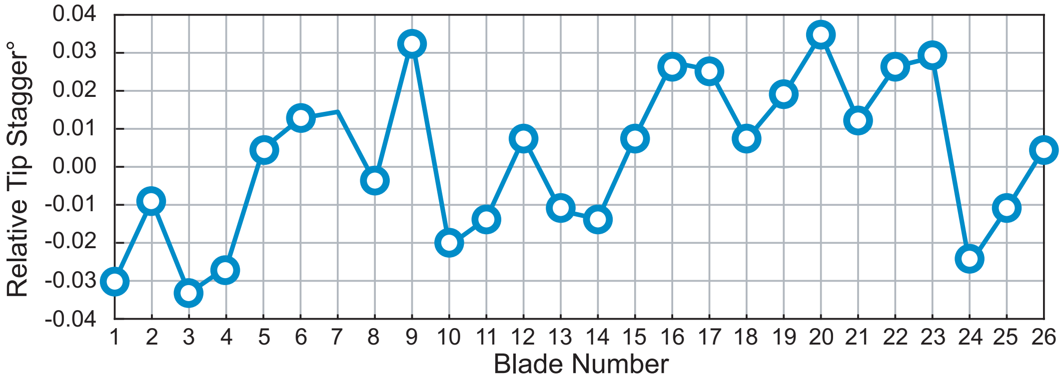

(a) Initial mis-stagger pattern.

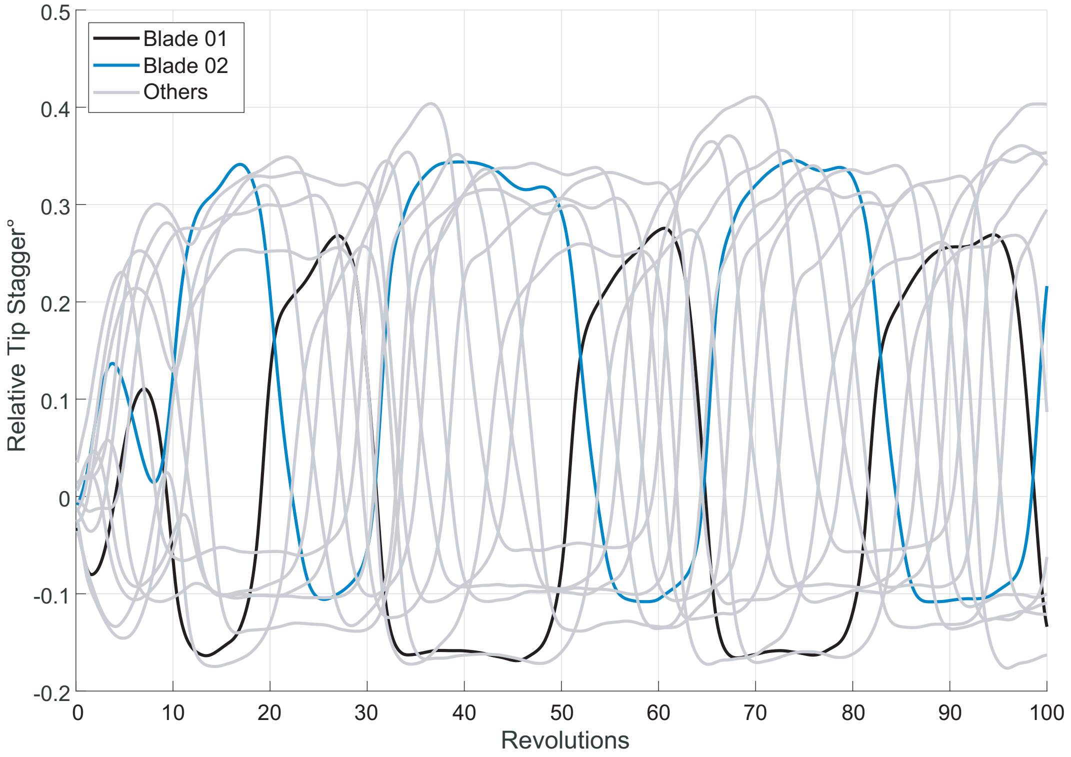

(b) Relative tip stagger history for the first 13 blades.

Figure 4.1: NSV on a randomly mis-staggered assembly.

An example of typical NSV behaviour is shown in Figure 4.1. The fan assembly is initially mis-staggered using the pattern shown in Figure 4.1(a) which can be representative of a real engine configuration. The resulting time history of tip stagger patterns shown in Figure 4.1(b) were obtained from a coupled aeroelastic simulation. For clarity, only half of the blades in the assembly are presented. The plots for two adjacent blades (i.e. Blade 1 and 2) are highlighted while the rest are plotted in grey. Here the typical NSV behaviour where the blades' tip stagger switches back and forth about the nominal condition is well represented. Additionally, it can be clearly seen that NSV is periodic. As illustrated in Figure 4.2, NSV's operating condition is in close proximity to that of the peak efficiency condition. In contrast to the other types of aeroelastic instability (i.e. stall flutter) which usually occur at off-design conditions, NSV behaviour occurs close to the design condition, away from the stability limit. Therefore, understanding the NSV behaviour is of great importance to the engine manufacturers.

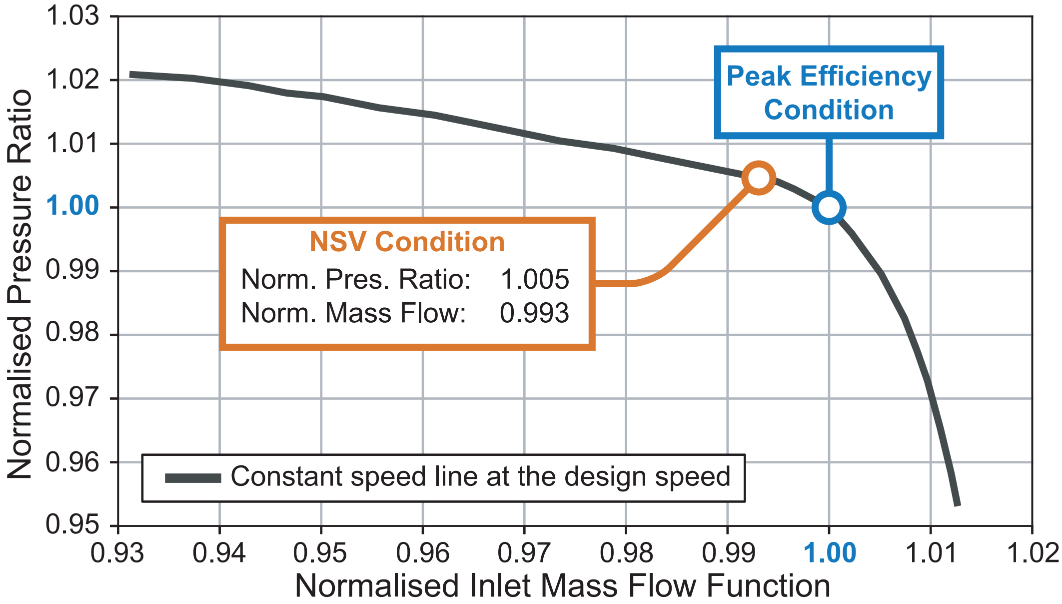

Figure 4.2: NSV operating condition on the fan map.

4.3 Temporal Convergence

Given that unsteady aeroelastic behaviour is being investigated, it is vital to ensure the temporal resolution is sufficient to capture the unsteady behaviour. Thus, a temporal convergence study is conducted to optimise the number of time steps per fan revolution required to capture the NSV behaviour. Three levels of temporal resolution are used to capture the running geometry under the influence of the travelling disturbance from NSV. The temporal resolutions are at 200, 400, and 800 time steps per revolution.

The random initial mis-stagger pattern, shown as the black line in Figure 4.3, is used to trigger the NSV behaviour. Aeroelastic computations are performed at the three temporal resolutions for 5 revolutions and the instantaneous running geometry, in term of tip stagger pattern, is captured at the end of the 5th revolution for each resolution level. The tip stagger patterns are presented in Figure 4.3 as the coloured lines. From the results, it is evident that the instantaneous tip stagger pattern is not sensitive to the temporal resolution in general. Therefore, all the NSV calculations are conducted at 200 time steps per revolution to reduce the computation resource requirements.

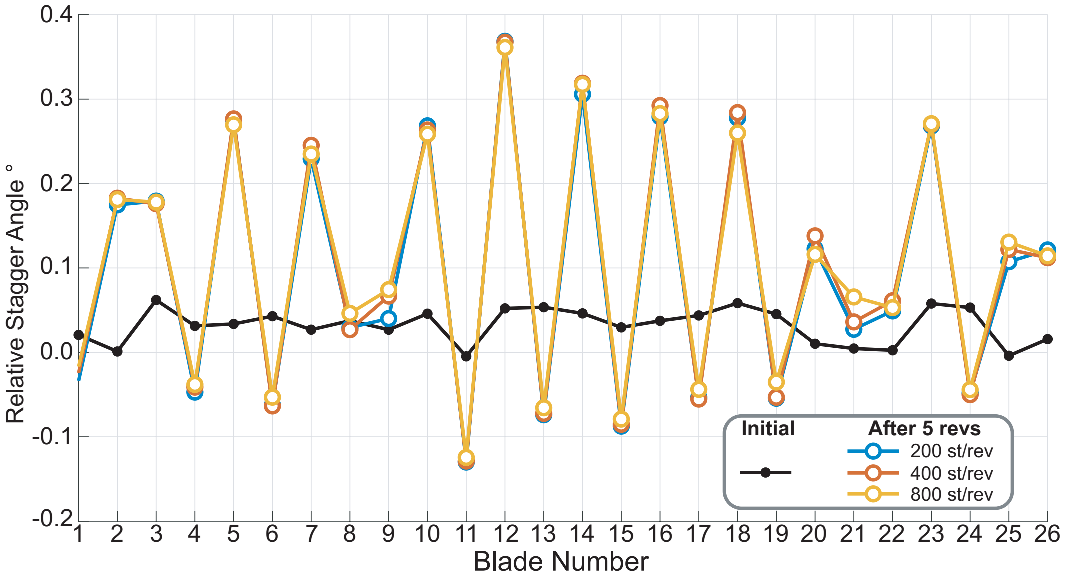

Figure 4.3: Temporal convergence study.

4.4 NSV Mechanism

4.4.1 NSV Mechanism: the NSV Transfer Window

The fundamental NSV mechanism is introduced below. This is to lay the foundation for the understanding of the NSV behaviour so that the parameters influencing NSV can be clearly distinguished in the later section.

The main geometric feature for APD and NSV behaviour on this blade, is the covered passage geometry at the tip, which is marked by the hatched region in Figure 4.4(a). The length of the covered passage is measured as the length between Blade 1's trailing edge and the foot in which Blade 2's leading edge is projected onto Blade 1's chord line. At a given point in the covered passage, the covered passage width is measured as the distance between the suction surface of the leading blade and the pressure surface of the trailing blade in the direction perpendicular to the chord lines. The measurement for this blade is plotted in Figure 4.4(b). The covered passage geometry is of a convergent-divergent shape with a minimum area/throat around 80% chord position. It was shown in Chapter 3 that this geometric feature has significant influence on the passage shock displacement and can enhance the APD mechanism.

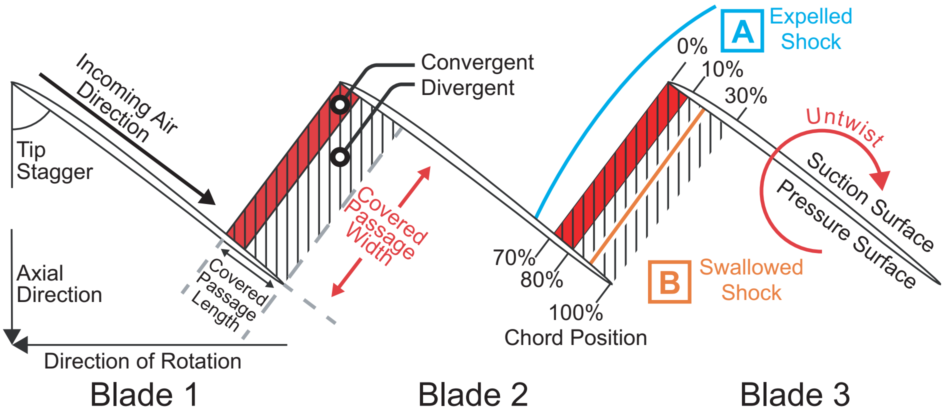

(a) Schematics of aeromechanical behaviour at blade tip.

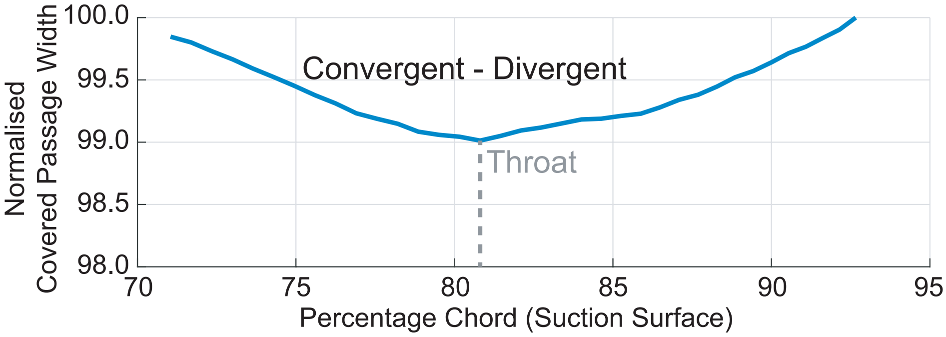

(b) Covered passage width measurement at blade tip.

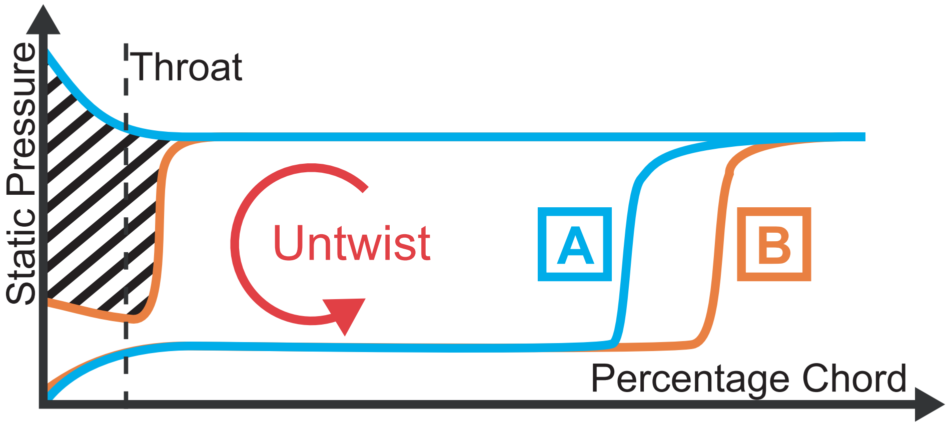

(c) Schematics for pressure distribution at blade tip.

Figure 4.4: Geometric features, shockwave structure, and pressure distribution at blade tip.

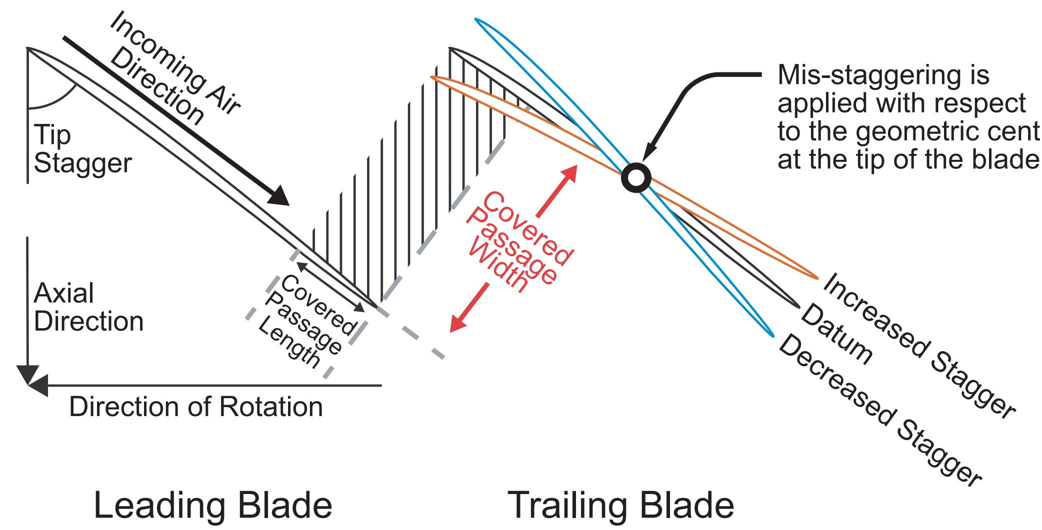

(a) Schematics for twin blade mis-staggering setup.

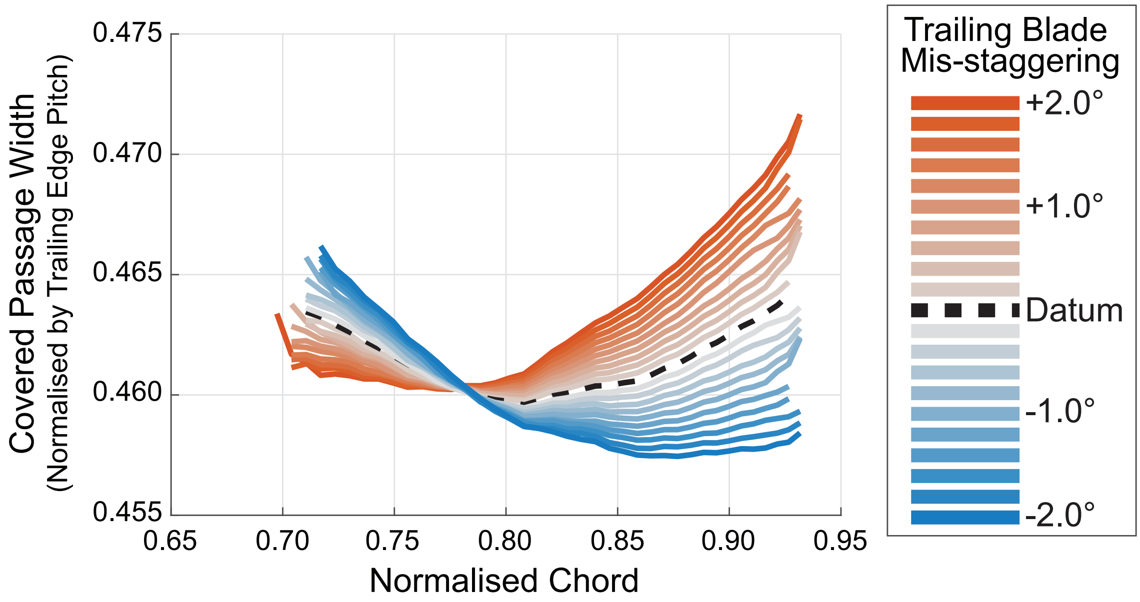

(b) Covered Passage geometry variation.

Figure 4.5: Covered passage shape variation with respect to initial mis-staggering.

It is important to note that the covered passage geometry in Figure 4.4(b) is measured from a pair of nominal fan blades. With the presence of geometric variability, such as mis-staggering, the position of the throat deviates from the nominal condition. In Figure 4.5, the covered passage geometry at various mis-staggering amplitudes are presented. Mis-staggering is applied with respect to te geometric centre of each radial section. The mis-staggering amplitude varies linearly along the radial direction with zero at the hub and peak mis-staggering amplitude at the tip. For all the mis-stagger amplitude, the convergent-divergent nature of the covered passage remains.

The passage shock cannot be stable inside the convergent part of the nozzle, resulting in an unstable region marked by the red hatched area in Figure 4.4(a) which ranges from the 70% to 80% chord position (Blade 2's suction surface) as shown in Figure 4.4(b). Therefore, the shockwave structure at the tip, as illustrated on the left side in Figure 4.4(a), has to adopt either Condition A - expelled from the passage or Condition B - swallowed into the passage and resting downstream of the throat. The corresponding pressure distribution patterns are illustrated in Figure 4.4(c). The pressure distribution determines the aerodynamic loading (i.e. pressure untwist) available to counteract the mechanical restoring force. Thus, in the case of Condition A, a high aerodynamically induced moment with respect to the centre of untwist which is situated downstream of the trailing edge in the axial direction leads to a reduction in tip stagger angle (i.e. high untwist). Similarly, in the case of Condition B where there is a region of low pressure around the leading edge on the pressure surface, low untwist moment translates to a high tip stagger angle.

For a fan assembly with an even number of blades, the initial APD signal introduced by a single mis-staggered blade needs to travel an even number of passages before hitting the initial mis-staggered blade. Due to its alternating nature, this means the blade leading the mis-staggered blade will deviate from its nominal tip stagger in the opposite direction as the mis-staggered blade. In the case shown in Figure 3.4, this means Passage 26-1 will have the same shock structure as that in Passage 2-3. The alternating shock structure on the adjacent passages stabilises Blade 1, essentially suppressing the initial APD travelling signal.

This behaviour, however, can transform into an unsteady form (i.e. NSV) when certain conditions are met. For an assembly with two mis-staggered blades, when the mis-staggering of 2nd blade is in-phase with the APD signal generated by the 1st blade (e.g. two mis-staggered blade polar opposite to each other on the 26 blade assembly), NSV behaviour will manifest after the APD pattern has been formed. This is under the assumption that the amplitude of mis-staggering is sufficiently small. The reason behind will be explained in the results section.

The NSV phenomenon can be better illustrated with the help of Figure 4.6. Grey outlines nominal conditions. The signs in brackets indicate the relative tip stagger to nominal condition. Tilde sign indicates negligible change. When the tip stagger of Blade 2 in Figure 4.6(a) is initially increased at time T_0, an APD signal will initiate in the direction opposite to that of rotation. As a result of the above mentioned symmetrical system (i.e. two mis-staggered blade polar opposite to each other on the 26 blade assembly), the number of passages the APD signal needs to advance prior to meeting another signal source is changed into an odd number. Thus, when the APD signal from Blade 2's 'twin' on the other side of the annulus (i.e. Blade 15) advances to Blade 1 at time T_1, the APD mechanism dictates that the passage shock

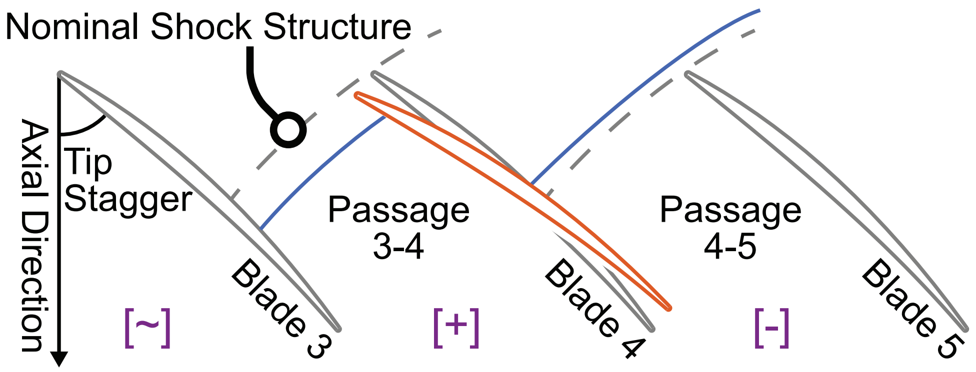

(a) Shock structure at T_0.

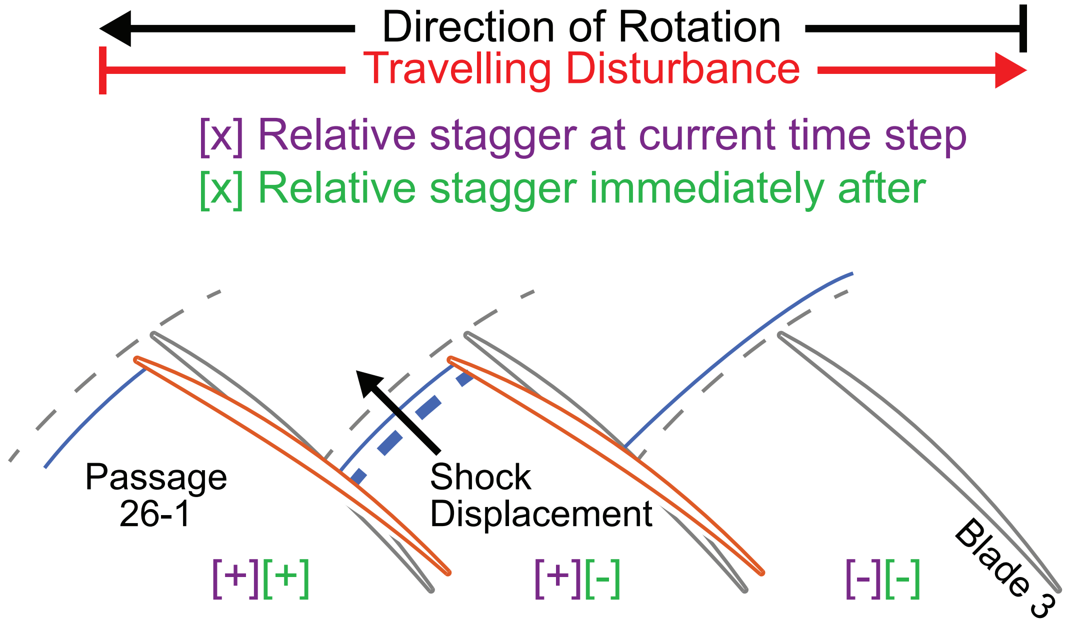

(b) Shock structure at T_1.

Figure 4.6: Schematic diagram showing shock structure at blade tip during NSV Transfer.

in Passage 26-1 should be swallowed. While the passage shock is being swallowed into Passage 26-1, the reduced aerodynamic untwist moment increases the tip stagger angle of Blade 1. Concurrently, the turning Blade 1 (from the grey shape to orange shape in Figure 4.6(b)) attempts to recover the covered passage geometry from a dominantly divergent shape at T_0 back to its original shape. This allows the shock in Passage 1-2 to move forward from the thick blue dashed line in Figure 4.6(b) (which is at the same position as the blue line in 4.6(a)) to the thin blue solid line. When this recovering shock in Passage 1-2 trespasses the 'unstable' zone in Figure 4.4(a), the shock displacement will be accelerated, pushing the shock away from the unstable zone. This eventually leads to the shock resting in a stable position outside the passage (i.e. Condition A in Figure 4.4). Such changes lead to a conflict, both passage shocks are expelled from the passage, between Passage 1-2 and 2-3 in the subsequent time step. This conflict and forced shock recovery will be termed ‘NSV Transfer Window’ in the later discussion. The propagation of this process causes blades to switch sign of their relative stagger angles sequentially and leads to NSV.

4.4.2 From APD to NSV

For clarity, schematics in Figure 4.7,4.8, and 4.9 are included to depict each phase of the APD & NSV behaviour. Figure 4.7 represents the initial idealised mis-stagger setup used in this study. The formation of APD behaviour in the assembly is depicted by the transition from Figure 4.7 to 4.8 in which the blades adopt the alternating mis-stagger pattern. Detailed explanation of this process is discussed previously in Chapter 3. The *NSV Transfer Window* mechanism discussed in the last section is depicted through the transition from Figure 4.8 to 4.9 during which Blade 4 and 17 switch from having higher (than nominal) stagger angles to lower ones. Detailed discussion of this mechanism is conducted in the next section.

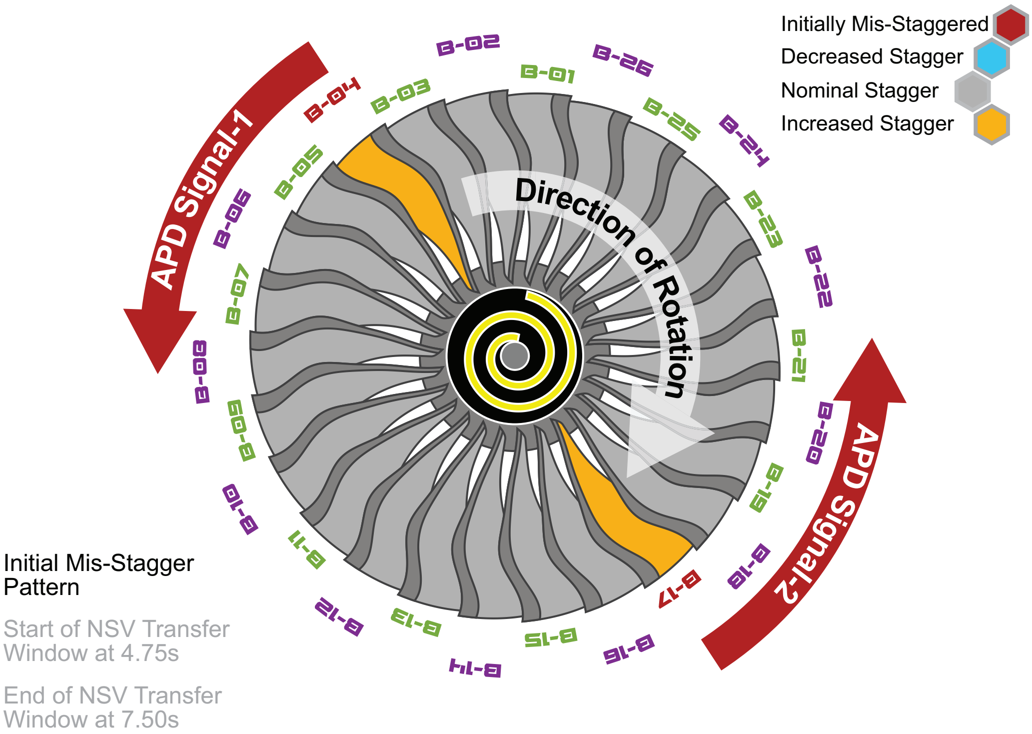

Figure 4.7: NSV stage 1 of 3: initial pattern.

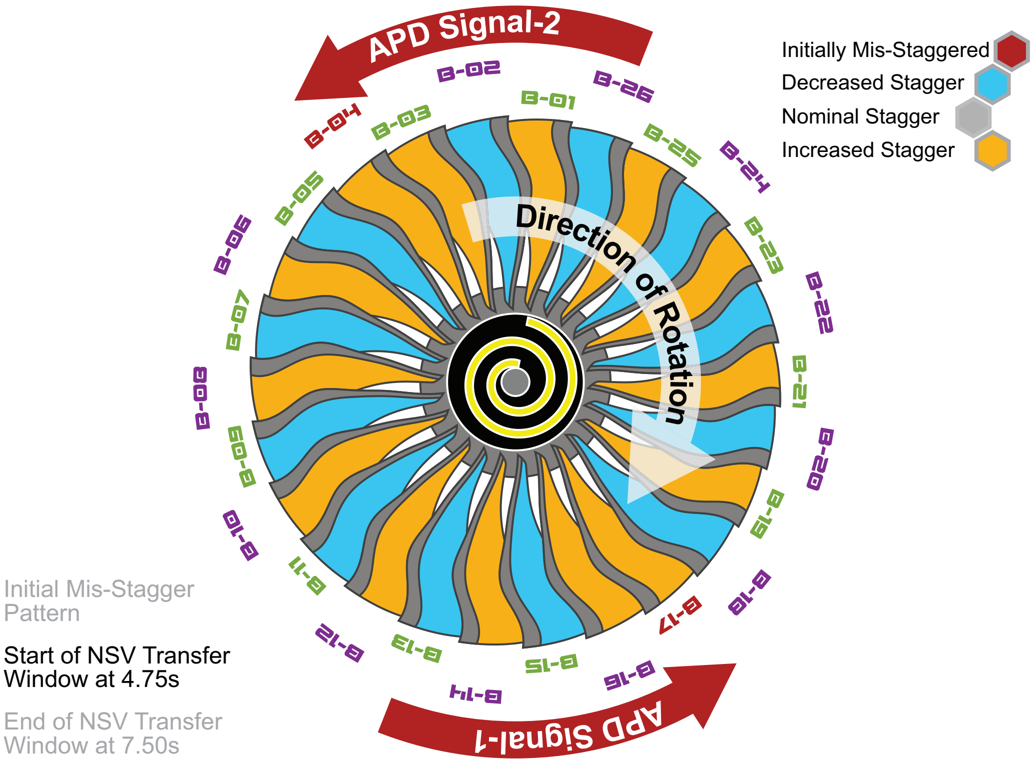

Figure 4.8: NSV stage 2 of 3: start of the NSV transfer window (Blade 3&4).

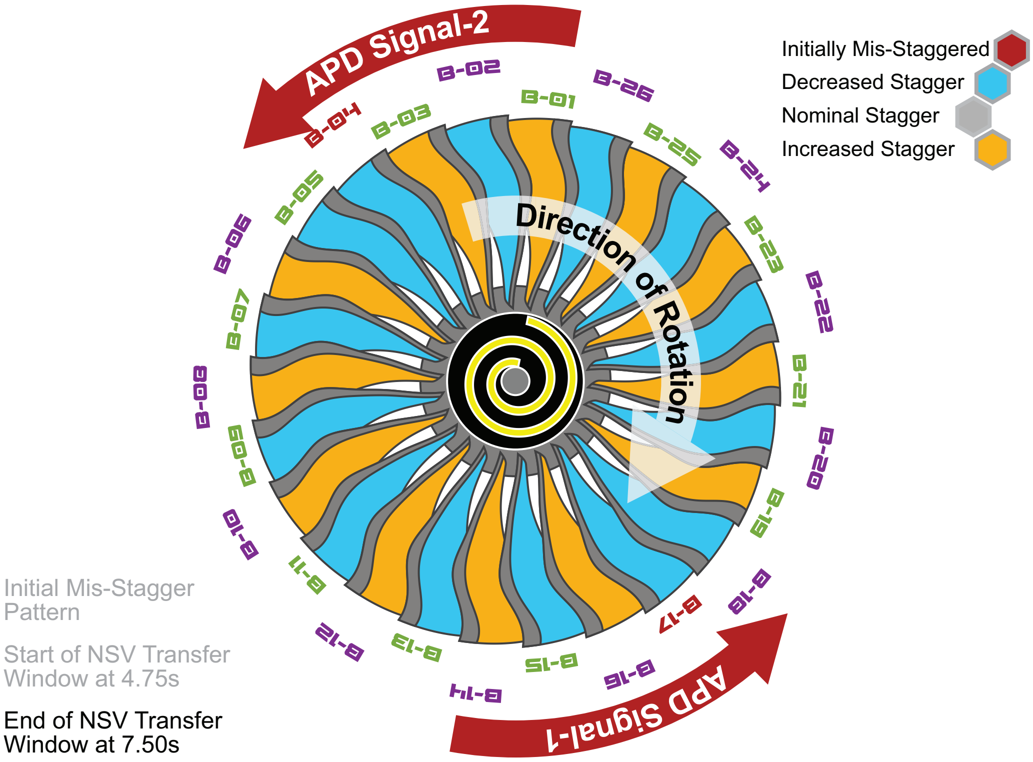

Figure 4.9: NSV stage 3 of 3: end of the NSV transfer window (Blade 3&4).

4.5 Results and Discussion

4.5.1 Typical NSV case and NSV Transfer Window

It was shown in Figure 4.1 that a randomly mis-staggered assembly (as generally observed on engines) can exhibit NSV behaviour. An idealised test case is used here to simplify the complex system to a more manageable one in order to investigate the NSV mechanism.

Single passage domain and mode shapes are expanded to a fully symmetric system first. Blade 4 and 17, which are polar opposite to each other on the annulus, are mis-staggered with 0.08° increase in tip stagger, resulting in a axisymmetric system. This mis-stagger amplitude is well within the Blade Tip Timing (BTT) technique's resolution limit [44] and is determined from a parameter study which will be presented later. As will be demonstrated in the later section, the sign of the initial mis-stagger does not have significant influence over the NSV behaviour. The mis-staggering is with respect to the centroid at each radial section and is applied linearly along the span with the highest change at the tip and the lowest at the root. The corresponding changes to mode shapes is negligible at this mis-staggering level. The structure assembly is perfectly tuned with the blades having exactly the same set of mode shapes and the same damping ratio (mechanical damping) of $\zeta = 0.05$ which is higher than what is typically expected in the fan blades (i.e. approx. $\zeta = 0.01$ [32]). Thus, the only asymmetry in the system is introduced through geometry. The tip stagger history is plotted in Figure 4.10. Only the time history for half of the blades is presented for one NSV cycle. Blades are numbered in the same sequence as in Figure 4.6 where ascending blade number is in the direction opposite to rotation.

From 0 to 4.5 revolutions, the blades diverges to two positions - approx. $+0.3°$ and $-0.1°$ under the APD mechanism. At approximately 4.75 revolution, the APD signal initiated by Blade 17 traverses across the annulus and reaches Blade 3, forming the tip stagger pattern presented in Figure 4.11(a). This activates the mechanism previously introduced as the *'NSV Transfer Window'* for Passage 3-4. Here, an alternative view of the transfer window is illustrated through the aeromechanical data at blade tips in Figure 4.11. The more detailed data during the same time period is presented through the pressure contour snapshots presented in Figure 4.12 and 4.13. The more targeted data, in term of the passage shock displacement tracking, is presented in Figure 4.14.

As seen in Figure 4.11(a), the APD pattern is not symmetrical about the nominal condition. Instead, the deviation is biased towards the side with increased relative tip stagger and this is, unsurprisingly, a direct consequence of its covered passage geometry. The starting solution corresponds to the condition where the shock at blade tip is resting on the leading edge (i.e. dashed line in Figure 3.4). All the tip staggers are calculated relative to the tip stagger at this condition. The shape of the covered passage dictates that the stabilised shock has to be on either side of the 'unstable zone'. In the expelled case, shown as Position A in Figure 4.4(c), this can be achieved with a slight forward displacement of the shockwave away from the initial solution. In contrast, in the other direction where the shock needs to the swallowed, the shock position needs to deviate more than 10% chord position away from the initial position, diminishing the untwist moment significantly. The resulting pressure distribution means the change in untwist moment and thus stagger angle change will not be symmetrical about the initial condition.

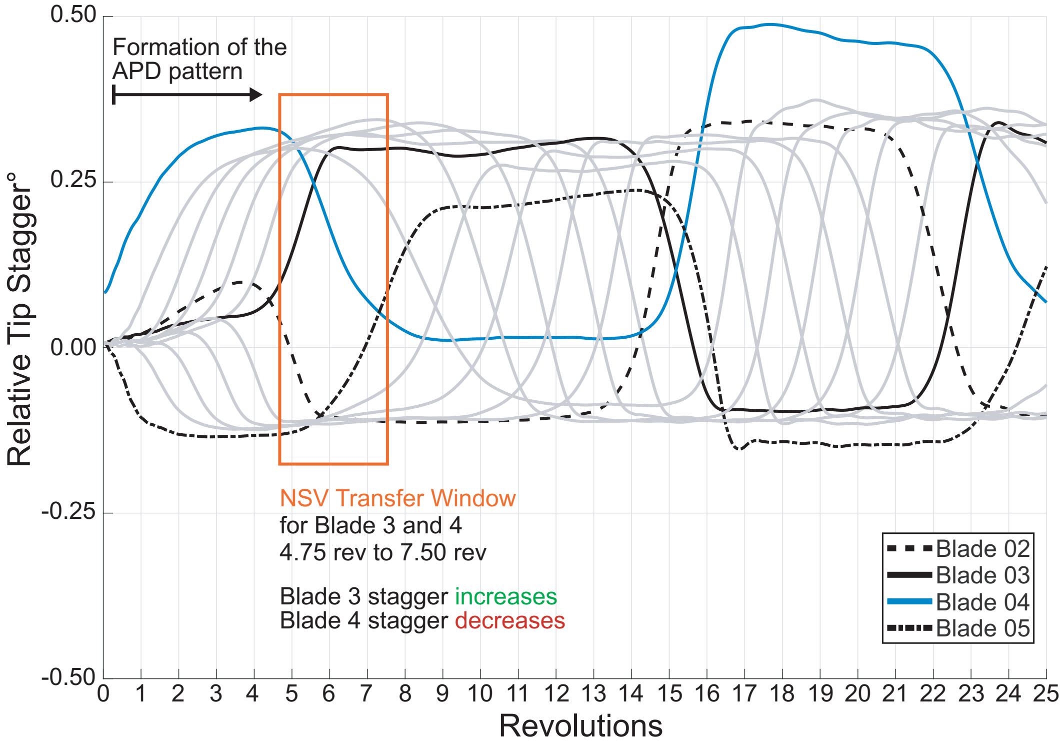

Figure 4.10: Blade tip stagger history for Blade 1-13.

As illustrated in Figure 4.11(a), when the signal from Blade 17 first reaches Blade 2, the APD pattern is forcing it to deviate from the nominal and adopt the −0.1° condition. This makes Passage 2-3 more divergent (similar to the behaviour illustrated in Figure 3.4) and the shock moves further into the passage which can be observed through the pressure surface shock displacement on Blade 3 illustrated in Figure 4.11(b). The chord positions in the figures are normalised such that 0% indicates the leading edge while 100% denotes the trailing edge. This shock displacement results in a significant decrease in the pressure distribution at the leading edge tip which is accompanied by a decrease in untwist moment shown in 4.14(c). The untwist moment is the aerodynamic moment measured with respect to the centre of untwist. Consequently, as shown in Figure 4.11(a), this pushes Blade 3 to switch from +0.1° to +0.3° condition where Blade 4 is at the beginning of the process.

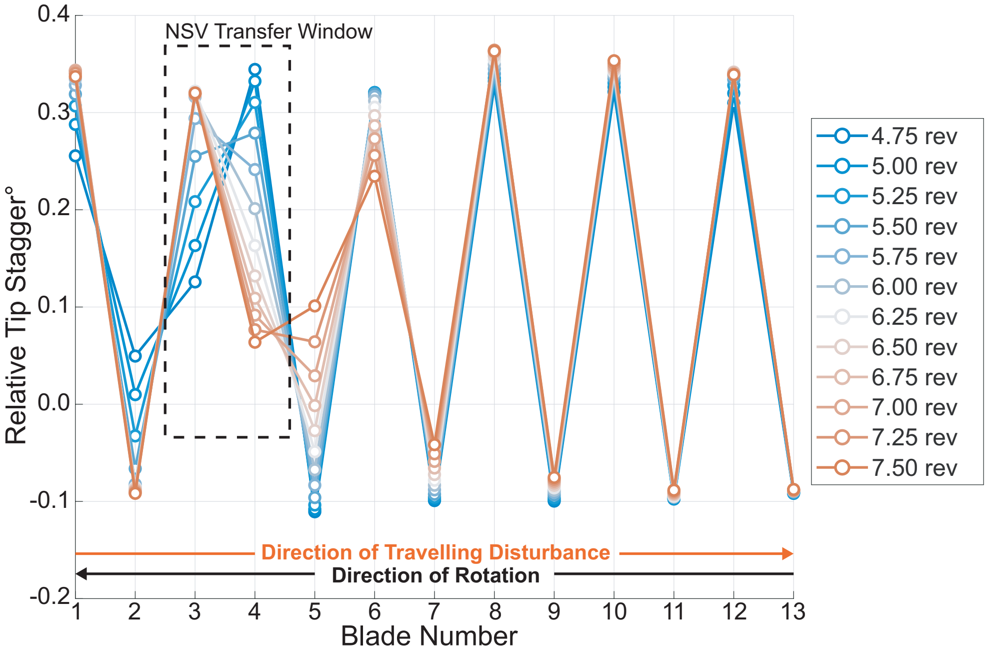

(a) Tip stagger pattern history.

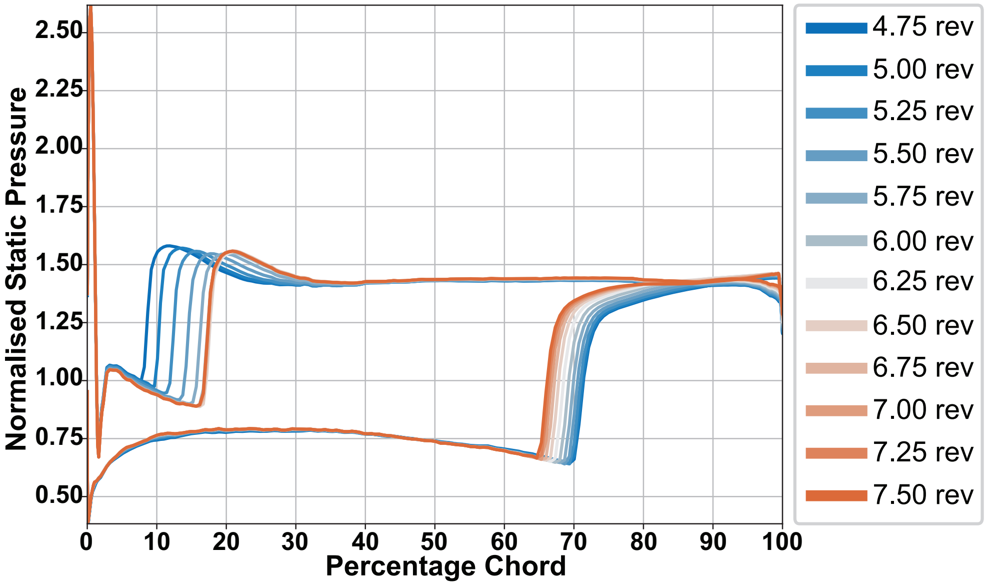

(b) Pressure distribution change on Blade 3.

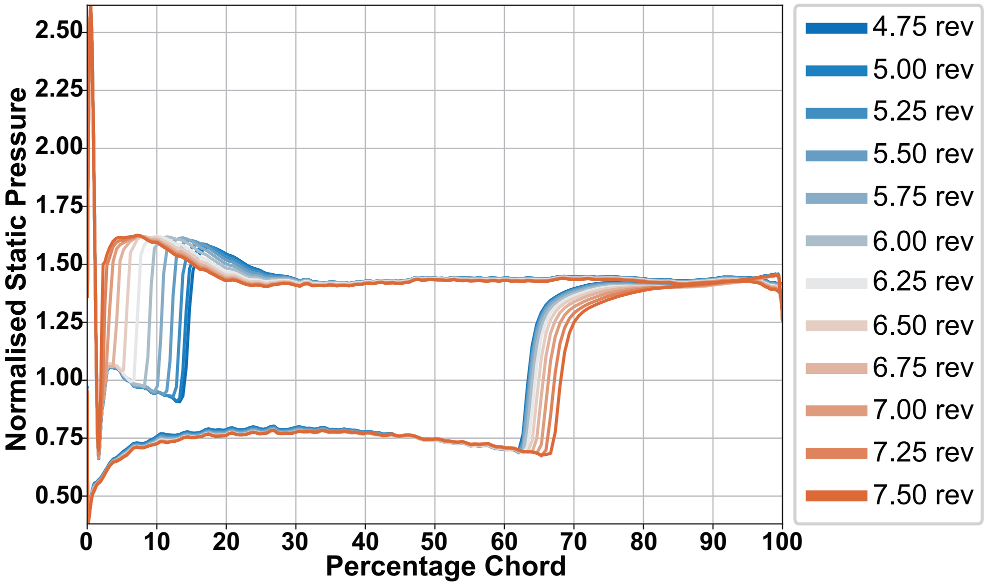

(c) Pressure distribution change on Blade 4.

Figure 4.11: Tip stagger and pressure distribution history during NSV transfer window.

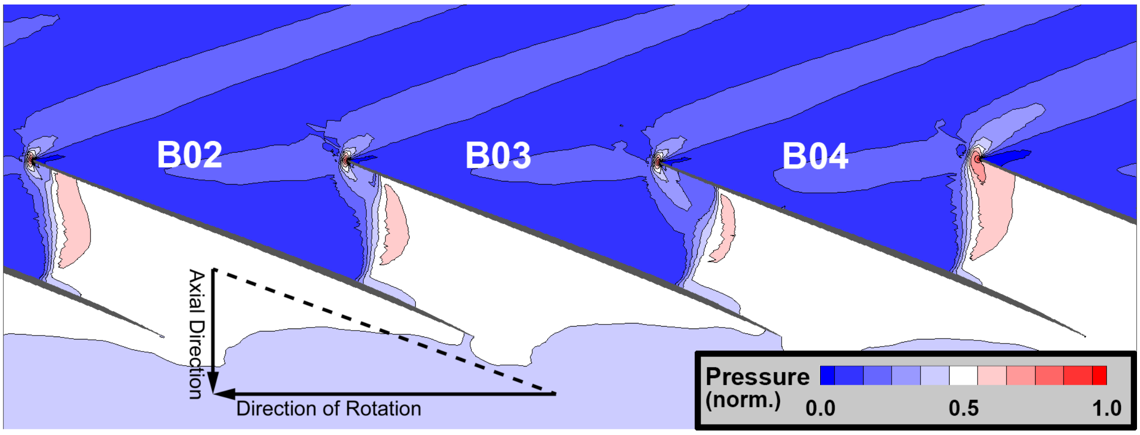

(a) At 4.75 revs.

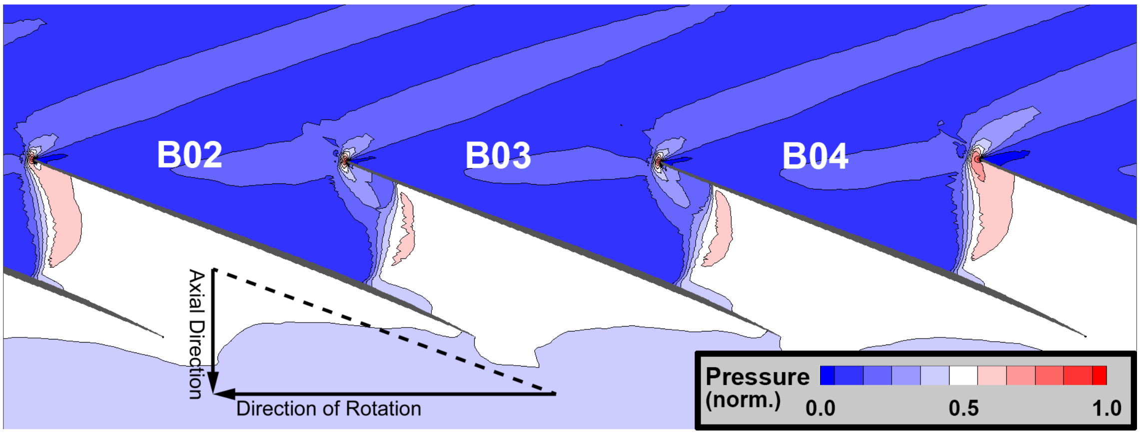

(b) At 5.25 revs.

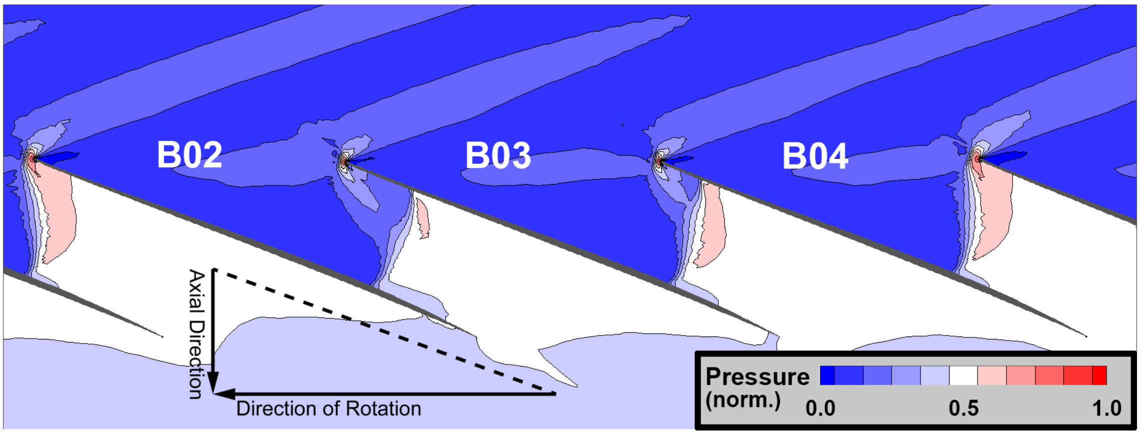

(c) At 5.75 revs.

Figure 4.12: Changes in pressure distribution during NSV transfer window (NSV case from 4.75 revs to 5.75 revs).

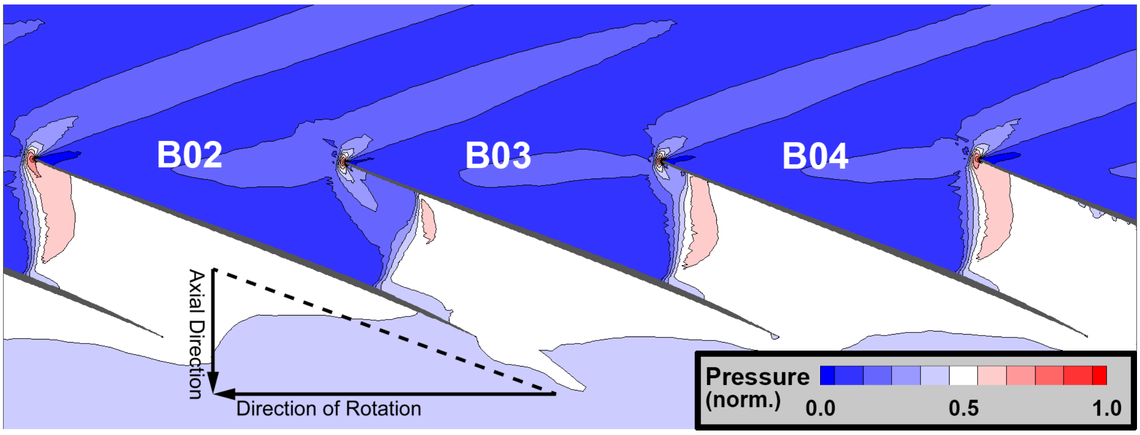

(a) At 6.25 revs.

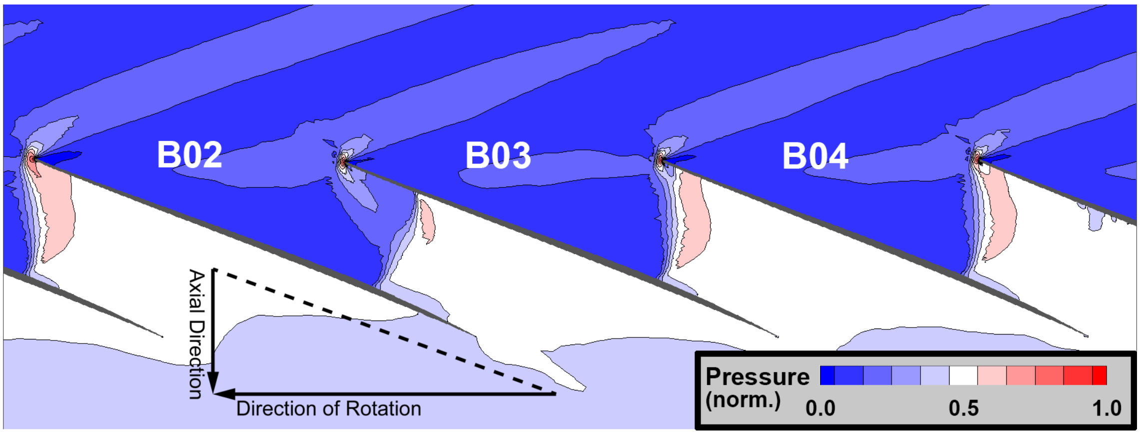

(b) At 6.75 revs.

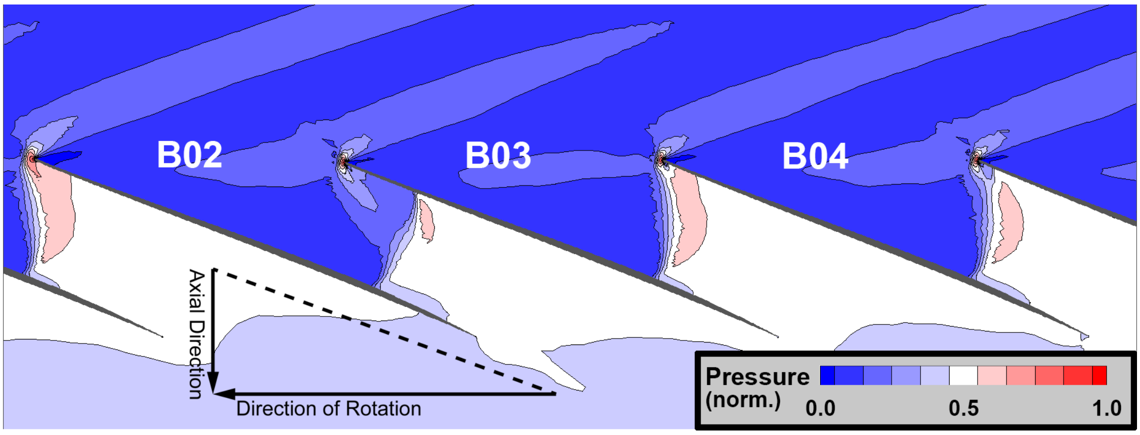

(c) At 7.25 revs.

Figure 4.13: Changes in pressure distribution during NSV transfer window (NSV case from 6.25 revs to 7.25 revs).

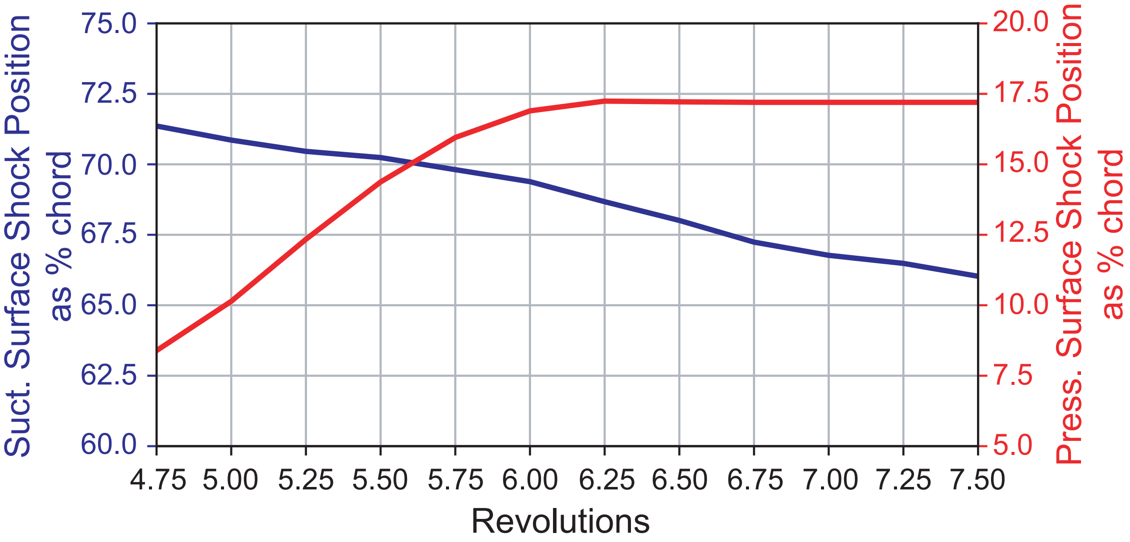

(a) Shock displacement on Blade 3.

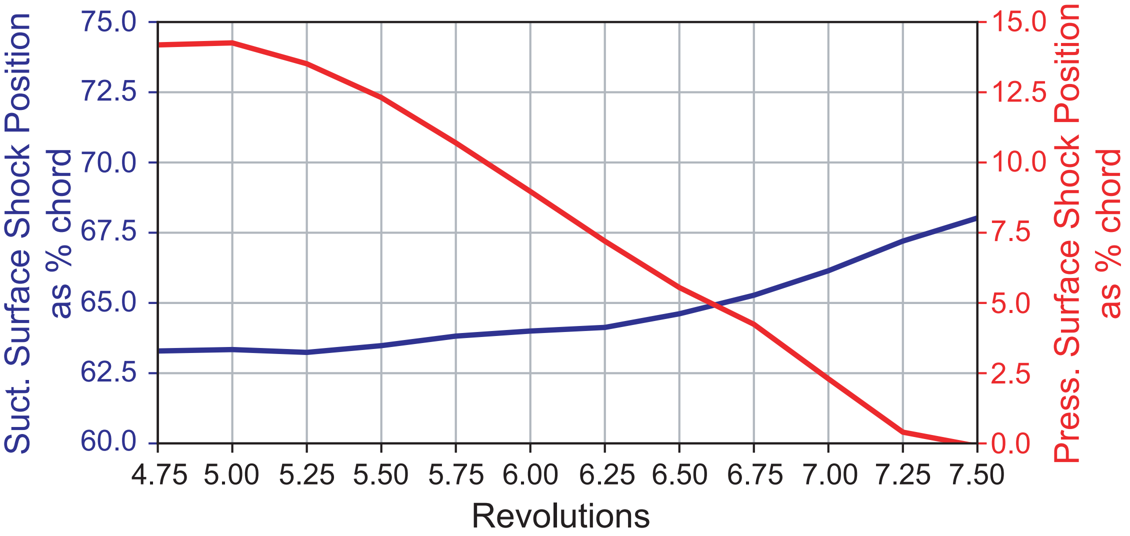

(b) Shock displacement on Blade 4.

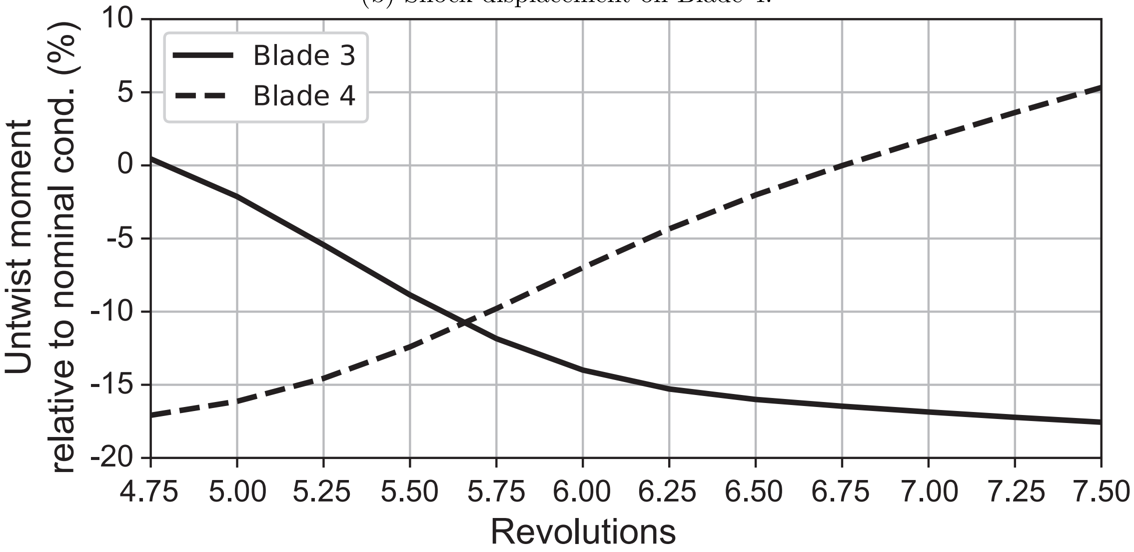

(c) Untwist moment changes on Blade 3 and 4

Figure 4.14: Aeromechanical changes during the NSV Transfer Window for Blade 3 and 4 (Alternative view).

Following the discussion regarding Figure 4.6, the passage shock 3-4 which can be tracked through Blade 4's pressure surface shock in Figure 4.11(c) is forced to recover from its swallowed position to the expelled position (i.e. $-0.1°$ condition). This recovery process is assisted by the 'unstable zone' which is positioned between 0% and 10% chord. Thus, when the passage shock captured in Figure 4.11(c) transits from a stable swallowed position forward towards leading edge and enters the 'unstable zone', the passage shock is forced to stabilise outside the passage resulting in an increase in pressure near the leading edge tip. Consequently, as shown in Figure 4.14(c), the untwist moment at the blade tip increases which translates to the decrease in Blade 4's tip stagger as illustrated in Figure 4.11(a). Additionally, by examining the shock position history in Figure 4.11(b) and 4.14(a), it can be seen that the shock on Blade 3's pressure surface (i.e. swallowed passage shock) is stabilised at the 6th revolution, ahead of Blade 4's pressure surface shock (Figure 4.14(b)) which is still being displaced by the changes on Blade 4 at 7.50 revolution.

Blade 4's behaviour during NSV can be further investigated with Figure 4.15 where the tip stagger rate of change (w.r.t. revolutions) is presented. These data can essentially be interpreted as the rate of change for aerodynamic loading which is dominated by shock position. From Figure 4.11(c) and 4.14(b), it can be seen that Blade 4's passage shock crosses the throat which is at approximately 10% chord and enters the 'unstable zone' slightly after 5.75 revs. This time coincides with the highest rate of change captured by Figure 4.15. After it crosses the throat, the passage shock maintains a relatively high displacement rate inside the 'unstable zone' and the shock starts to decelerate when it is about to be stabilised outside the passage. The same behaviour can be observed for Blade 5 during this transfer window. This further supports the view that the covered passage geometry of this blade amplifies the passage shock displacement whenever they crosses the unstable region, setting a series of chain reactions to further the divergence in aeromechanical behaviour.

As shown in Figure 4.11, from 6 to 15 revolutions, similar to the APD behaviour, the NSV Transfer Window shifts in the direction opposite to that of rotation. Thus, the trailing blades start experiencing the travelling disturbance and flip their relative tip stagger from one direction to another. This can be visualised by the following the tip stagger trace from $+0.3°$ group to $-0.1°$ group at regular intervals and vice versa. Note that, similar to the behaviour observed in Figure 4.11(a), only the blades immediately adjacent to the conflicting blade pair (i.e. Blade 3 and 4) would exhibit significant tip stagger change at this point in time while the other blades remain practically stationary.

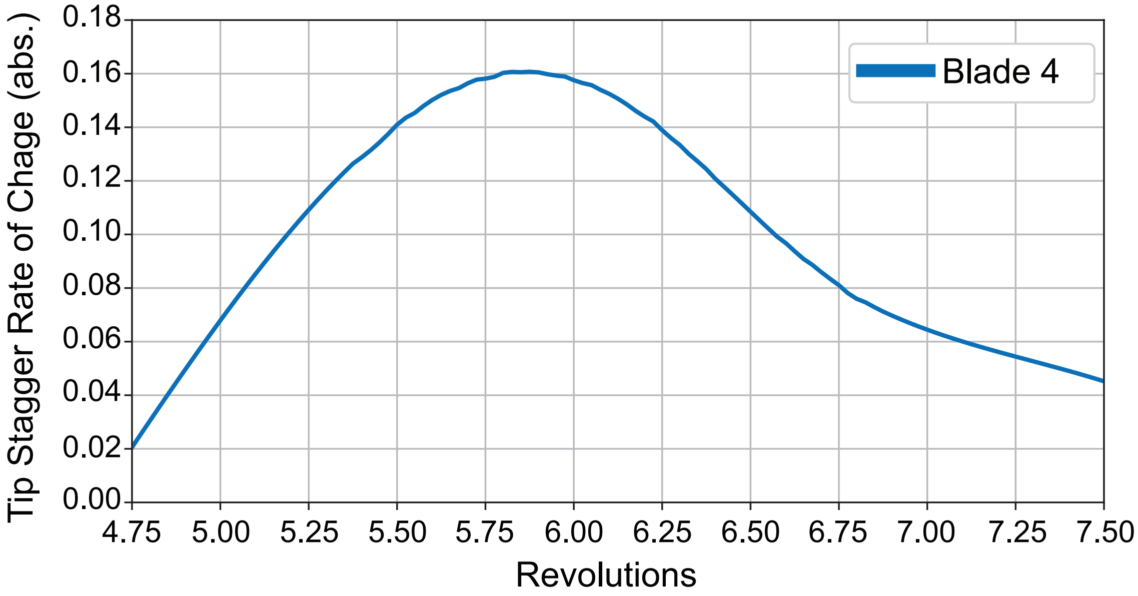

Figure 4.15: Stagger rate of change during NSV Transfer Window.

At approximately 15.5 revolutions, the travelling NSV Transfer Window initiated by Blade 4 at the very beginning would encounter itself, forcing its relative tip stagger to increase from near zero to approx. +0.5° through the NSV mechanism. This is then followed by standard NSV behaviour observed between 6 and 15 revolutions until the initial signal from Blade 17 travels across the annulus and hit Blade 4 once more at approx. 22 revolution. It is found that NSV has a period of 17.2 revolutions for the setup described earlier. It can be hypothesised from the 3 NSV periods shown in Figure 4.1 that NSV can continue perpetually and thus can potentially affect the fan blade's fatigue life adversely. Consequently, this further highlights the importance of understanding the blade design's NSV behaviour.

4.5.2 Factors Influencing the NSV behaviour

Following the discussion on the adverse effect of NSV, it is only natural to question whether there are parameters that can be manipulated to terminate the NSV behaviour. Two mis-staggering parameters have been found to fulfil this requirement: the amplitude and the phase. However, it is important to note that such measures are primarily linked to the idealised NSV case presented above.

Firstly, to assess the effect of initial mis-staggering amplitude over NSV behaviour, a comparison case is computed against the baseline case presented in Figure 4.10 to 4.15. In the comparison case, the initial mis-staggering level is increased from +0.08° to +0.16° while all other parameters remain the same. It has been found that this change terminates the NSV behaviour. The corresponding results from the baseline case (i.e. Figure 4.10 to 4.13) are illustrated in Figure 4.16 to 4.19.

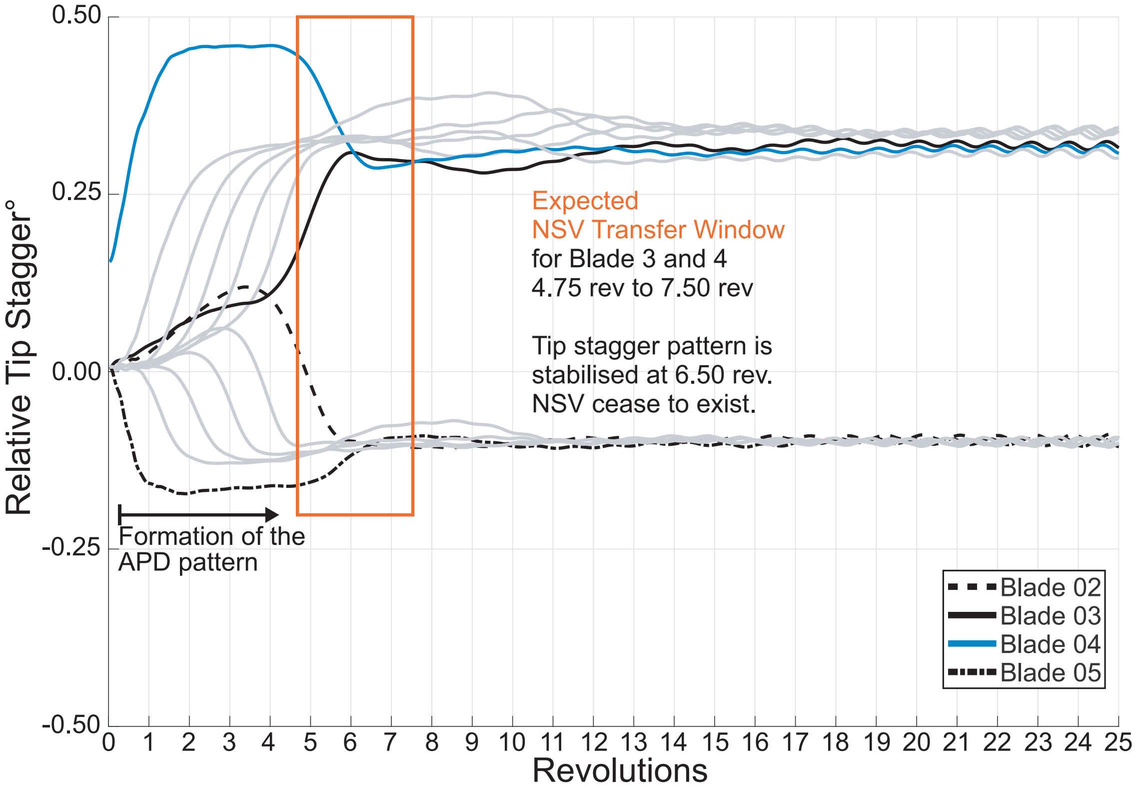

Figure 4.16: Blade tip stagger history for Blade 1-13 for the high mis-stagger amplitude (+0.16°) case.

Comparing the blade history plot in Figure 4.16 and the one in Figure 4.10, it can be clearly deduced that they share the same general APD behaviour until the 4th revolution and then the NSV behaviour on the comparison case fails to mature. Following Blade 4's tip stagger history in these two plots, it is evident that Blade 4 in the comparison case exhibits similar change as the one in the baseline case at the start of the expected NSV transfer window. However, it is not able to fully 'flip' from the higher relative tip stagger angle to the lower one which is illustrated in Figure 4.17(a). Additionally, from the comparison between Figure 4.11(a) and Figure 4.17(a), the behaviour suggests that Blade 3 is behaving in the similar fashion, increasing its tip stagger value. Thus, similar change introduced by the turning Blade 3 is not able to force Blade 4 into the lower tip stagger angle as observed in the baseline case. As a result, NSV behaviour fails to materialise. From the pressure contour shown in Figure 4.19 (a) to (c), it can be clearly seen that the assembly is stabilised after the passage shocks in Passage 2-3 and 3-4 are in the swallowed position.

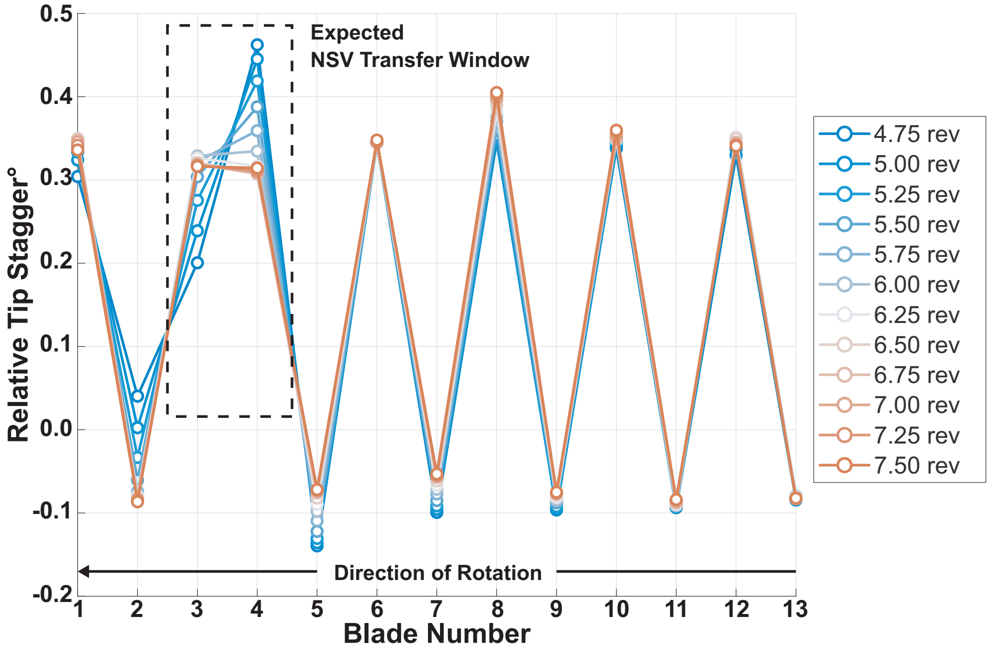

(a) Tip stagger pattern history.

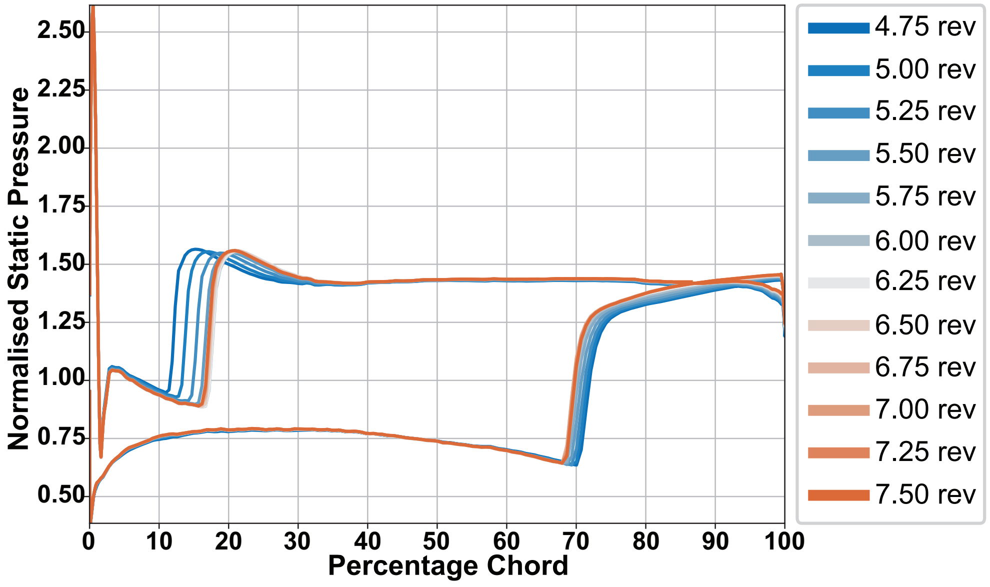

(b) Pressure distribution change on Blade 3.

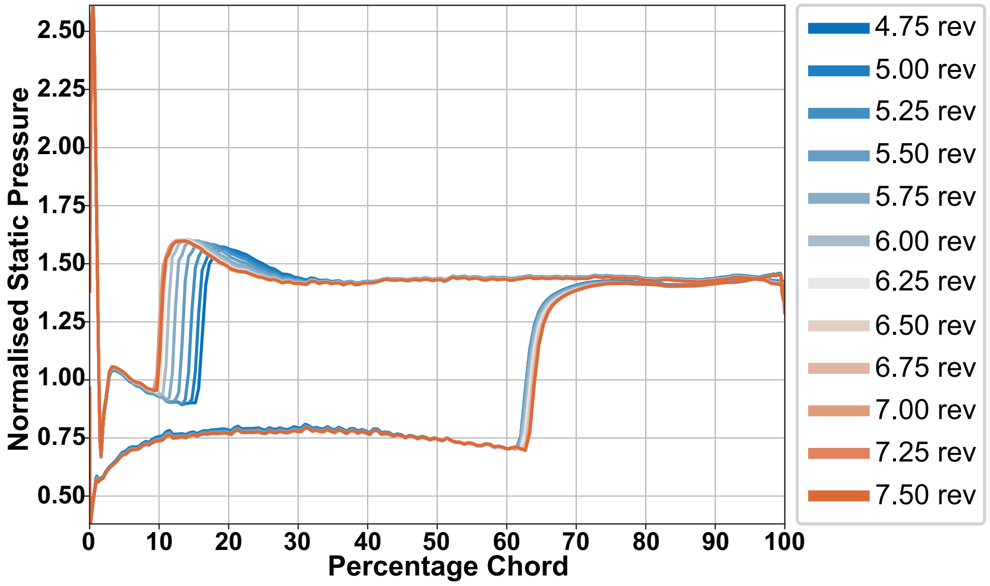

(c) Pressure distribution change on Blade 4.

Figure 4.17: Tip stagger and pressure distribution history during the expected NSV transfer window for the high initial mis-stagger level case.

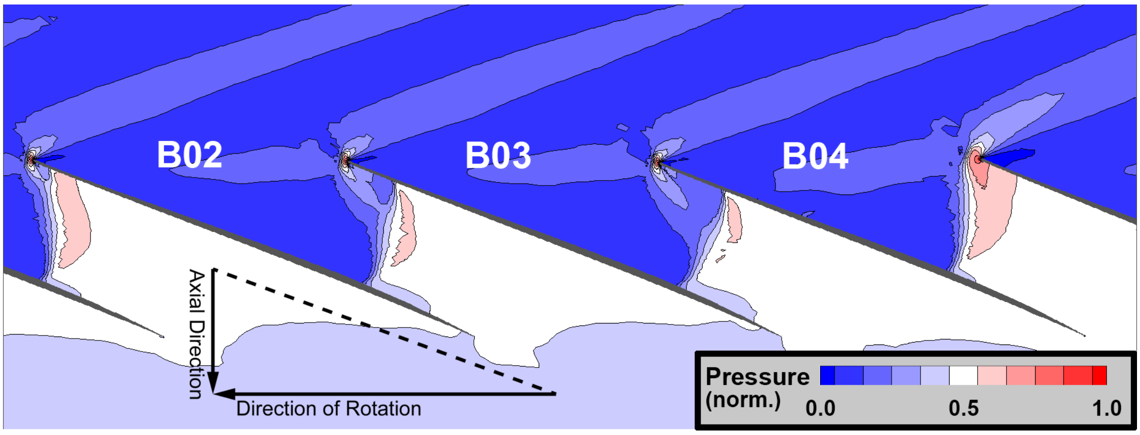

(a) At 4.75 revs.

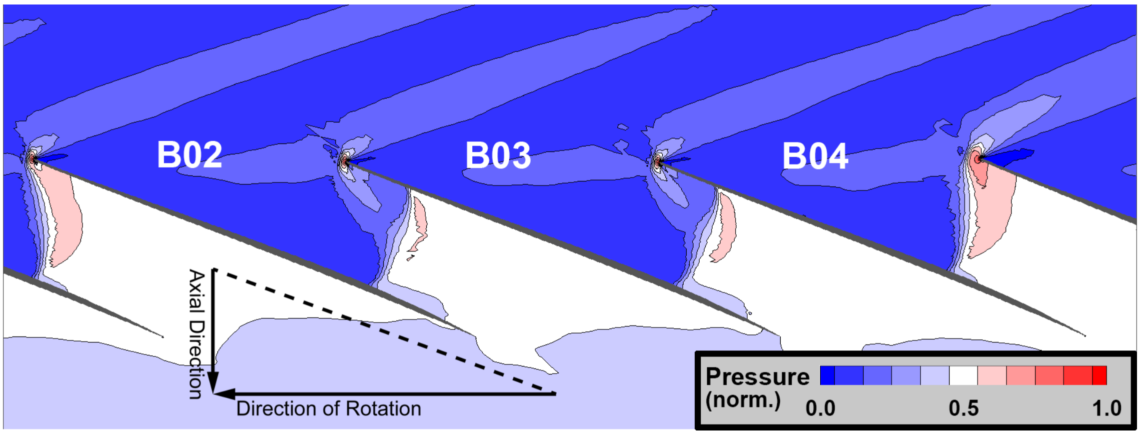

(b) At 5.25 revs.

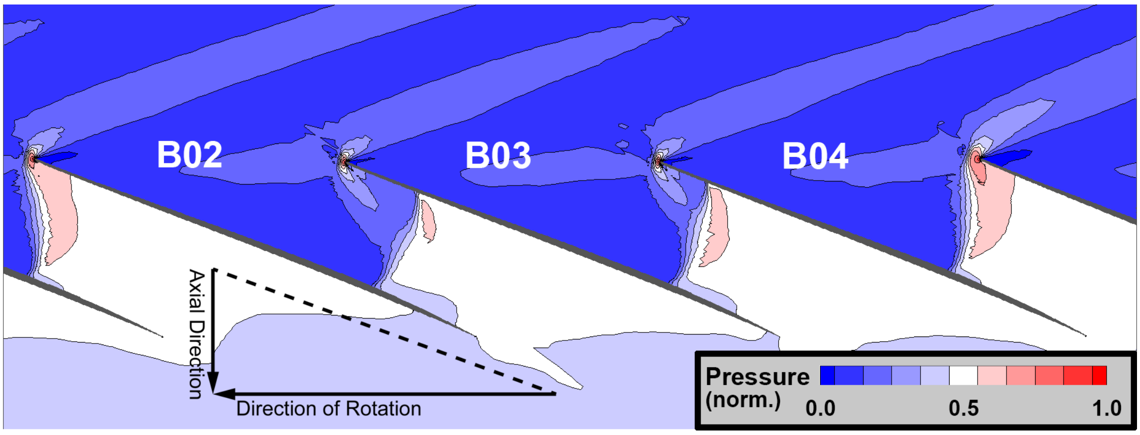

(c) At 5.75 revs.

Figure 4.18: Changes in pressure distribution during NSV transfer window (Non-NSV case from 4.75 revs to 5.75 revs).

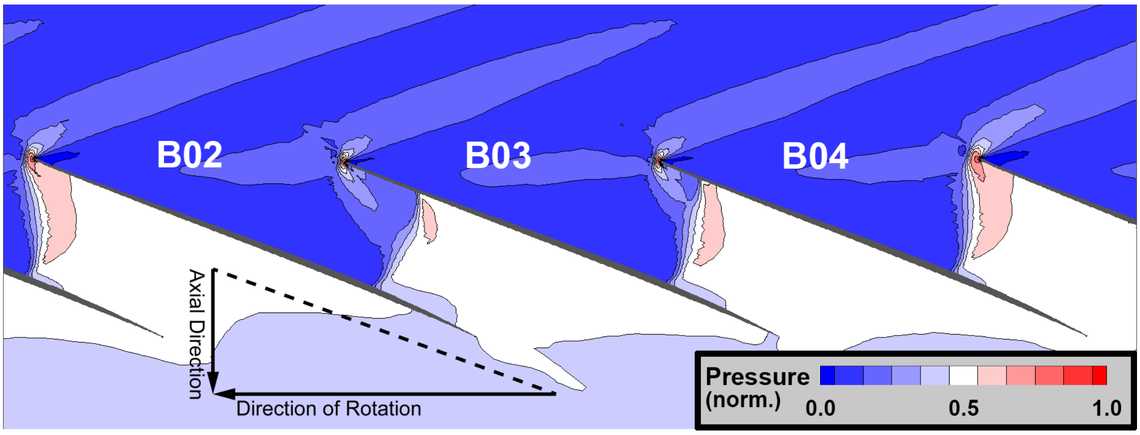

(a) At 6.25 revs.

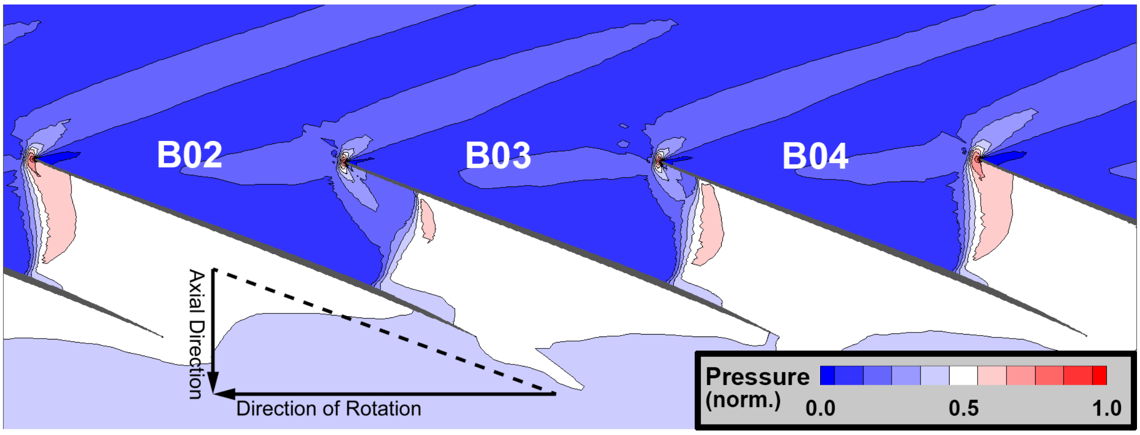

(b) At 6.75 revs.

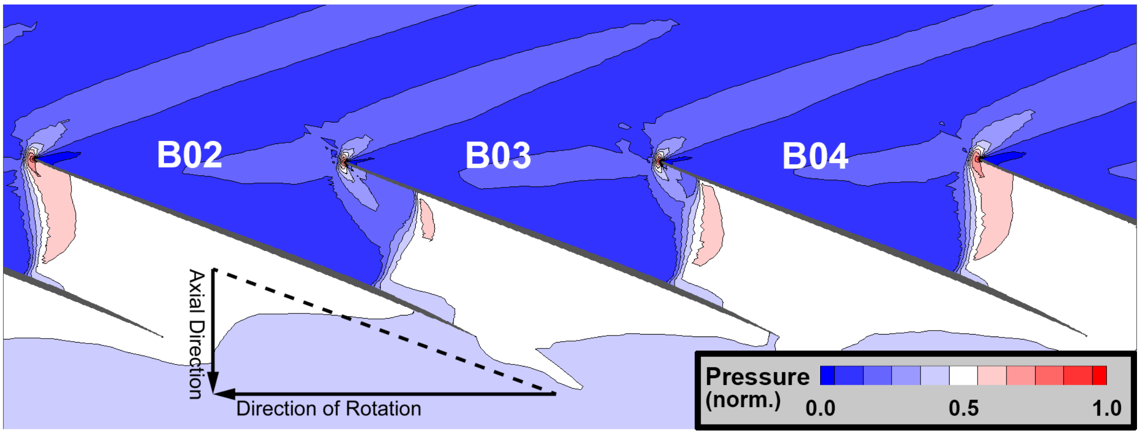

(c) At 7.25 revs.

Figure 4.19: Changes in pressure distribution during NSV transfer window (Non-NSV case from 6.25 revs to 7.25 revs).

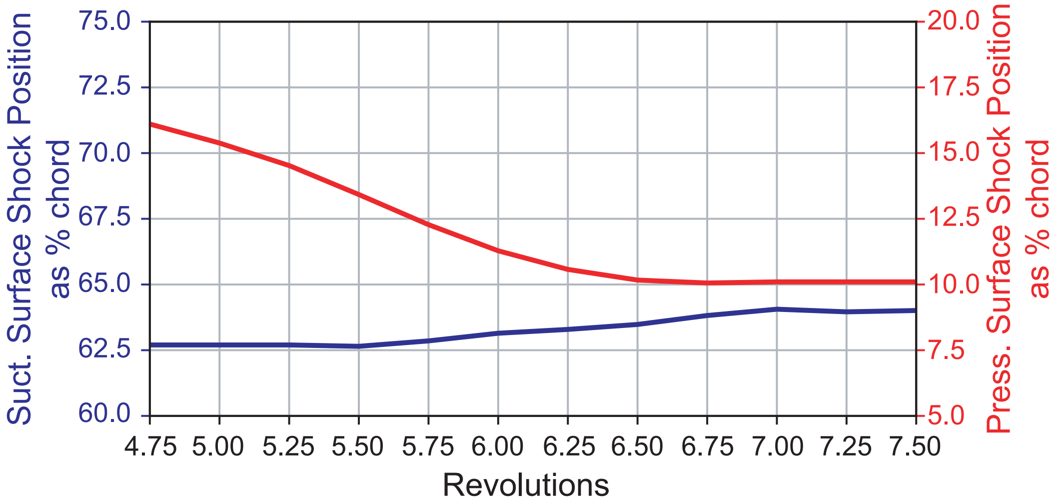

Figure 4.20: Shock displacement on Blade 4 for the high initial mis-stagger amplitude case.

The root cause of this difference lies in the fact that the amplitude of initial mis-staggering determines the starting position (at the beginning of the NSV Transfer Window) of the swallowed shock in Passage 3-4 relative to the throat in the covered passage. Comparison of the pressure distribution plots in Figure 4.11(c) and in Figure 4.17(c) reveals that the initial position of the passage shock at 4.75 revolution is approximately 14% (Figure 4.14(b)) for the baseline case and 16% (Figure 4.20)for the comparison case. From 4.75 to 6.25 revolutions, the pressure surface shock from both the baseline case and the comparison case have been displaced towards the leading edge by approximately 5% chord. From 6.25 revolutions onwards, the one in the baseline case continues to propagate forward while the other is stabilised at about 10% chord position which is where the cover passage throat is for a nominal assembly. This difference can be further highlighted by the data presented in Figure 4.21. Here, the distances between Blade 4's pressure surface shock and the covered passage throat for several initial mis-staggered settings are presented. The first point from the left represents the baseline case while the third point represents the comparison case. The solid line in Figure 4.21 is derived from numerical results while the the dashed line (excluding the NSV case) is estimated based on the measured shock position shift from the NSV case. It is evident from the plot that the distances and thus the resistance to NSV behaviour increase with the initial mis-staggering level. This implies that in the comparison case, the lack of support from the unstable region in the covered passage limits the shock displacement. In the other case, the unstable region amplifies the displacement. Thus, it can be speculated that the disturbance from Blade 3 serves as a trigger to start the shock displacement on Blade 4's pressure surface while its proximity to the covered passage throat determines whether the abrupt shock displacement occur to assist the motion.

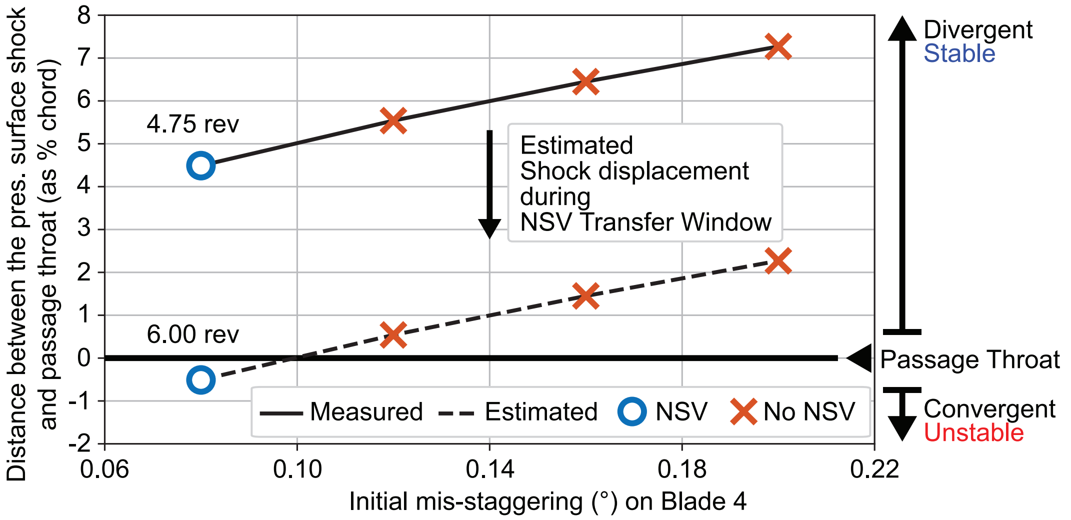

Figure 4.21: Relationship between initial mis-stagger amplitude and the distance between the displaced pressure surface shock and passage throat.

Secondly, as hinted by the underlying mechanism for both APD and NSV, under the current test configuration, the relative position of the two mis-staggered blades and their direction of mis-staggering can significantly influence NSV behaviour. To test this hypothesis, two other comparison cases are computed and their tip stagger patterns are presented in Figure 4.22. The corresponding tabulated data is presented in Table 4.1 where the changes made with respect to Case (a) is in red. Case (a) is the baseline case presented in Figure 4.10 to 4.15 whereas Case (b) correspond to the comparison case shown in Figure 4.16. In term of the computation setup, the 4 cases differ only in the way they are mis-staggered. Case (a) is the only case exhibiting NSV behaviour while the other three only show APD behaviour with tip staggers stabilised in the same fashion as that in Figure 4.17(a).

Case (c) differs from Case (a) in term of the position of the second mis-staggered blade. By switching the second mis-staggered blade from Blade 17 to Blade 16, the number of passages that the two travelling disturbances need to cover prior to hitting another source (i.e. mis-staggered blade) has changed from an odd number (i.e. 13) to a even number (i.e. either 12 or 14). In this way, when the signal from Blade 16 first travel to Blade 4 after traversing 14 passages, it would lead to an out-of-phase blade pair, Blade 3 and 4. In contrast to the behaviour observed in Case (a), the passage shock 3-4 will be further stabilised and thus disturbances cease to exist. An alternative approach for this is through reversing the sign of the mis-staggering on the second blade, i.e. Case (d). In fact, excluding the local effect of mis-staggered blade from Blade 15 to 18, the stabilised tip stagger pattern is practically the same for Case (c) and (d).

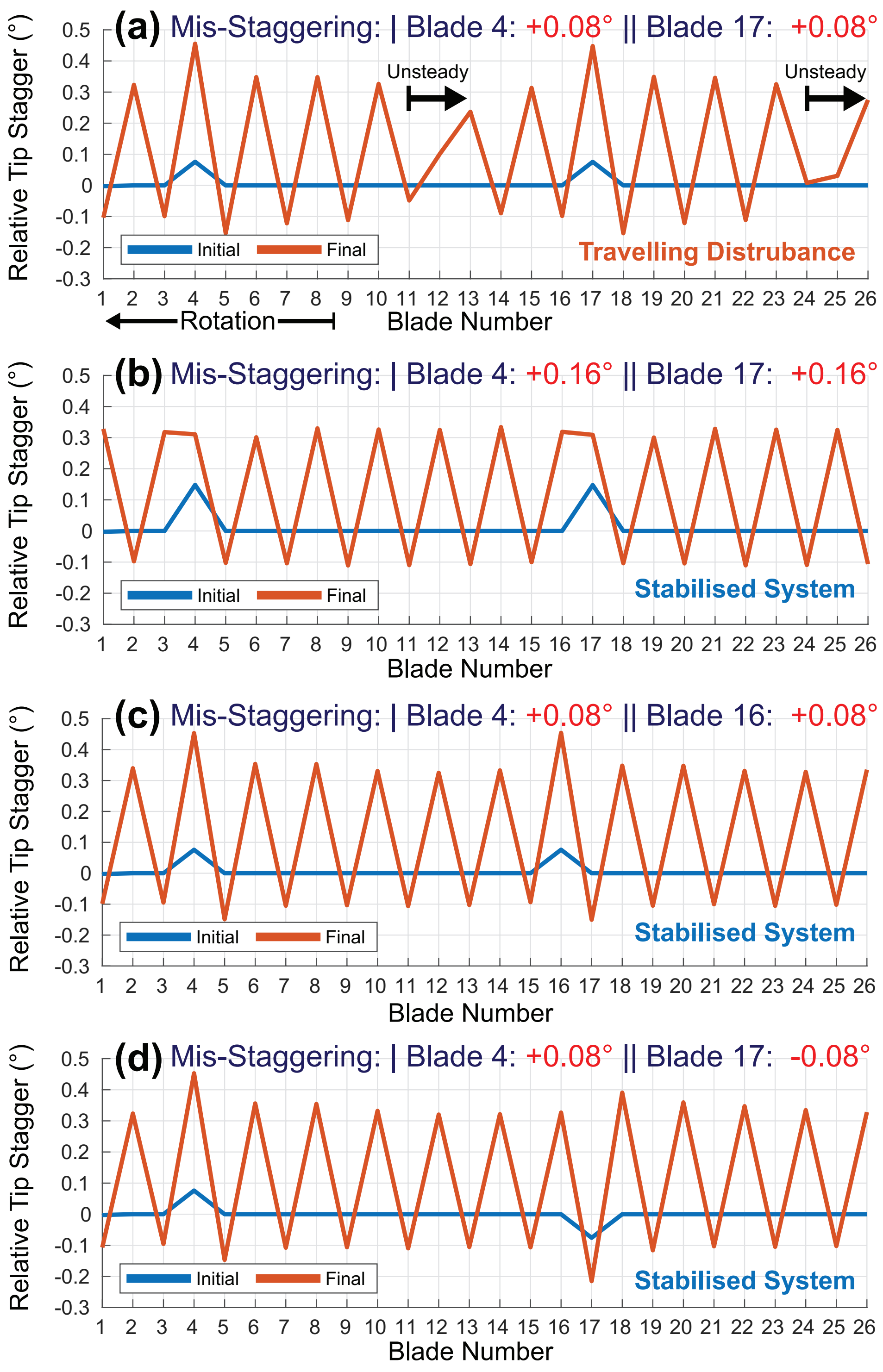

Figure 4.22: Comparison of tip stagger patterns (at 20th rev).

Case	Initial Mis-Stagger	Amplitude	APD Phase	NSV Behaviour
(a)	Blade 4 (+) and Blade 17 (+)	0.08	In-Phase	NSV
(b)	Blade 4 (+) and Blade 17 (+)	0.16	In-Phase	Non-NSV
(c)	Blade 4 (+) and Blade 16 (+)	0.08	Out-of-Phase	Non-NSV
(d)	Blade 4 (+) and Blade 17 (-)	0.08	Out-of-Phase	Non-NSV

Table 4.1: NSV and Initial Mis-Stagger Phase.

4.5.3 Fan Designs with an Odd Number of Blades

Previous discussion on NSV is focused on the Fan-2 design which has an even number of blades. From the decision tree classifier, it is demonstrated that fan assemblies with a strong $\frac{N}{2}$ th harmonic initial mis-stagger pattern (N is the number of blades and is even) tend not to exhibit NSV. Naturally, this gives rise to the question of how does NSV interacts with fan designs with an odd number of blades.

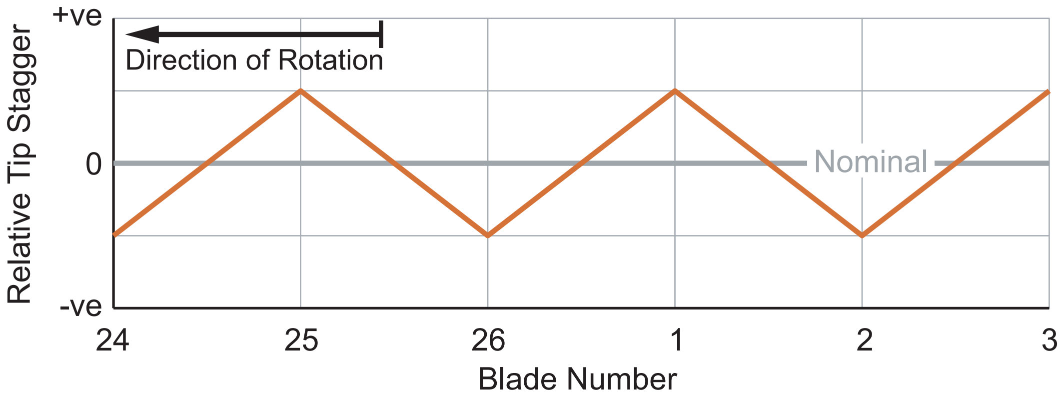

(a) Original Fan-2 (26 Blades)

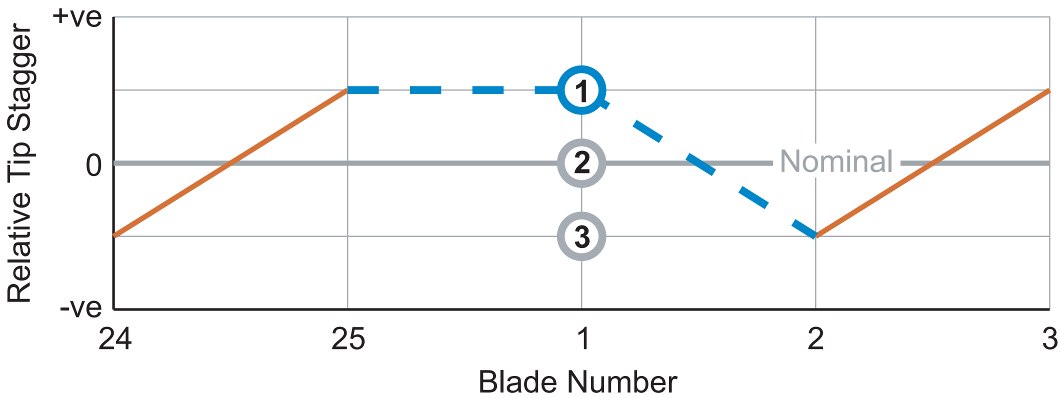

(b) Hypothetical fan design (25 Blades)

Figure 4.23: NSV behaviour on a fan with an odd number of blades.

The above question can be addressed with the aid of the schematics in Figure 4.23. Figure 4.23(a) denotes Fan-2 with a saturated APD pattern while Figure 4.23(b) denotes a hypothetical fan (with 25 blades) exhibiting a partially established APD pattern. Later discussion is based upon the following assumptions. Firstly, it is assumed that the only difference (with respect to NSV) between the two designs is the number of blades. Secondly, it is assumed that both assemblies satisfy NSV's blade-to-blade mis-stagger threshold. However, the case shown in Figure 4.23(a) has higher 13th ND amplitude than the NSV threshold and hence is stabilised as an alternating pattern.

In both cases, the rest of the assembly (i.e. Blade 2 to 25) has established the alternating stagger pattern. For Blade 1 on the hypothetical fan, its stagger angle has to adopt one of the three marked conditions: (1) higher than nominal, (2) nominal, and (3) lower than nominal. Based on the discussion in Chapter 3, condition (2) is not feasible as the disturbances introduced by the neighbouring blades will change the aerodynamic moment on the blade and force its stagger angle to deviate away from the nominal. Although the other two conditions are feasible in this regard, they are transient states and cannot be stabilised. As explained in Section 4.5.1 and more specifically the discussion regarding Figure 4.11, either condition can lead to unstable passage shocks and the blades need to adjust to a new equilibrium condition. Thus, for condition (1), the conflict between Blade 25 and 1 will force Blade 1's tip stagger to decrease, shifting from condition (1) to condition (3). Similarly, condition (3) will cause Blade 2's tip stagger to increase. As this process repeats in the downstream direction (i.e. opposite to rotation), NSV behaviour propagates. Hence, the hypothetical fan design cannot reach the stabilised APD condition as compared to that of the original blade (i.e. Figure 4.23(a)).

4.6 Chapter Summary

Based on the findings presented, the following conclusions and future directions for APD & NSV research can be drawn:

1. A typical NSV behaviour where travelling disturbances cause the blade tip staggers to oscillate about the nominal condition was captured in the study. It was demonstrated that it is closely related to the interaction between the passage shock displacement and the covered passage geometry. The mis-staggering phasing and amplitude were shown to determine whether APD behaviour transits into unsteady NSV behaviour after the alternating stagger pattern was fully formed.

2. As demonstrated by Figure 4.1 and 4.2, NSV behaviour was observed on a randomly mis-staggered assembly operating near the peak efficiency. This makes NSV distinct from other types of aeroelastic instability which generally occur at off-design conditions. Consequently, this makes the understanding of NSV crucial to the engine manufacturers. In addition, based on the blade history comparison between Figure 4.1 and Figure 4.10, it can be concluded that the fan assembly of an idealised symmetric mis-stagger setup can be used to capture the bulk behaviour of a more realistic fan assembly. This means that the assessment of NSV can be performed at the early design stage which makes the discovery highly relevant to the engine designers.

3. As demonstrated in the results section, the NSV mechanism can simply be explained by the interaction between shock position and passage geometry. Based on the physical reasoning, it is reasonable to deduce that the NSV behaviour is not limited to the numerical cases presented in this study or this particular blade.

4. The NSV behaviour was initiated on an assembly with 26 blades when there are two polar opposite sources. A comparison of four different initial mis-stagger patterns' NSV response were investigated, it showed that having an odd number of passages to cover before encountering the other source is vital for NSV to occur. Therefore, it could be hypothesised that NSV behaviour can be activated with a single mis-staggered blade for an assembly with an odd number of blades. Alternatively, it would be interesting to investigate the NSV behaviour on a design with total blade number divisible by 4 (i.e. 24). In this way, the polar mis-staggering would leave the initial signals even number of passages to cover and thus can potentially suppress NSV behaviour.

Chapter 5

NSV Behaviour Prediction using Machine Learning Techniques

> My two main conclusions are that technology develops cumulatively, rather than in isolated heroic acts, and that it finds most of its uses after it has been invented, rather than being invented to meet a foreseen need.
>
> Professor Jared Diamond
> *Guns, Germs, and Steel: the Fates of Human Societies* [94]

5.1 Chapter Introduction

In Chapter 4, an idealised mis-stagger setup was used to gain an initial understanding of the NSV phenomenon. However, random mis-staggering patterns due to manufacturing variability complicate the evolution of NSV significantly, making it difficult to draw general conclusions from parametric studies. Thus, machine learning techniques are used to analyse mis-stagger patterns to identify patterns that can lead to NSV and thus help avoid it. Numerical results from 1.6 million CPU hours of computation are used to train and test the classifiers. Machine learning techniques are used in this part of the study to explore the correlations between features in mis-stagger patterns and the corresponding NSV behaviours.

The machine learning component of this study is conducted through the open source library scikit-learn [95]. Three machine learning algorithms are used: logistic regression classifier, support-vector machine classifier, and decision tree classifier. The decision tree classifer is specifically chosen for its interpretability and is implemented through the *Classification And Regression Tree* (CART) [96] algorithm. The data used for the training of the machine learning models are obtained through the same computation approach outlined in Chapter 2 and 4. Fan 2 is used in this part of the study.

5.2 The Use of Machine Learning in Engineering

In recent years, the improvement in computing power and rise in availability of data have led to the rapid development and adoption of machine learning techniques. It is proven useful in various applications [97–103]. The purpose of machine learning, in short, is to build a computer algorithm that can discover useful structures /correlations hidden in existing the data and make predictions to improve future performance.

In engineering, machine learning techniques have been widely adopted for vibration diagnostics in rotating machinery [100–102, 104] where machine learning techniques are employed to determine the origin of the fault based on its symptoms. This type of problem is referred to as the *supervised learning* problems. In this case, the purpose is to discover the mapping from the input variables (i.e. symptoms of the fault) to the target variables (i.e. source of the fault). As the mapping leads to one of the finite number of target variables, it is also termed the *classification problem*.

Among the commonly used algorithms, the decision tree model [96, 105, 106] is well known for its interpretability [107, 108]. In contrast, it is generally difficult to understand the logic behind the decision-making of the ‘black box models’ such as artificial neural networks. In addition, the decision tree algorithm automatically selects features that are useful in making predictions [104, 109, 110] and hence can help to discover insights that are otherwise unreachable through more traditional methods.

5.3 Motivation and Objective of the Study

5.3.1 Motivation of the Study

In the last chapter, NSV behaviour was investigated through aeroelastic computations of idealised mis-stagger patterns. Naturally, to advance the study further, NSV investigations should be conducted on more realistic mis-stagger patterns which are of greater industrial relevance. This can potentially unearth additional NSV control factors under the more realistic systems.

To bridge the gap between the idealised setup and the randomly mis-staggered setup, a few intermediary cases are investigated and their initial mis-stagger patterns are illustrated in Figure 5.1 and 5.2. Similar to the cases in Chapter 4, only half of the blades in the symmetric system are presented. The setup and observed NSV behaviour of these cases are tabulated in Table 5.1. Case A and B are the idealised cases investigated in Chapter 4. As compared to Case A and B which have one pair of polar-opposite mis-staggered blades, these intermediary cases (i.e. Case C to E) have three pairs.

In Chapter 4, the investigation of the difference between Case A and Case B led to the conclusion that the amplitude of the mis-staggering determines whether NSV behaviour will occur. To be more specific, it is deduced that the initial mis-stagger amplitude needs to be sufficiently low to allow the activation of the NSV Transfer Window mechanism. However, the comparison among Case A, C, D, and E leads to the conclusion that it is in fact the amplitude of the blade-to-blade relative mis-staggering difference that ultimately determines the NSV behaviour. This discovery does not invalidate the conclusion reached in Chapter 4 since the two terms, amplitude of absolute mis-staggering and relative mis-staggering, is the same in the system with one pair of polar-opposite mis-staggered blades. Thus, it enhances the understanding from Chapter 4.

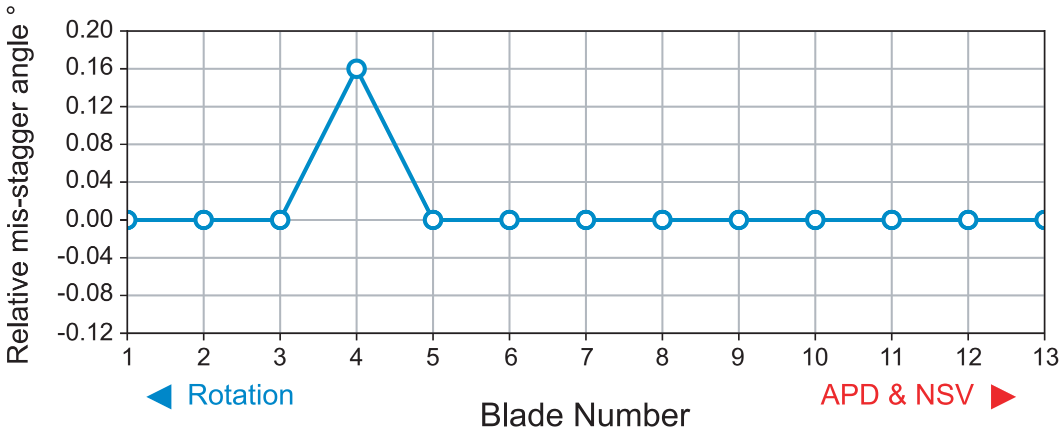

(a) Case A. No NSV behaviour.

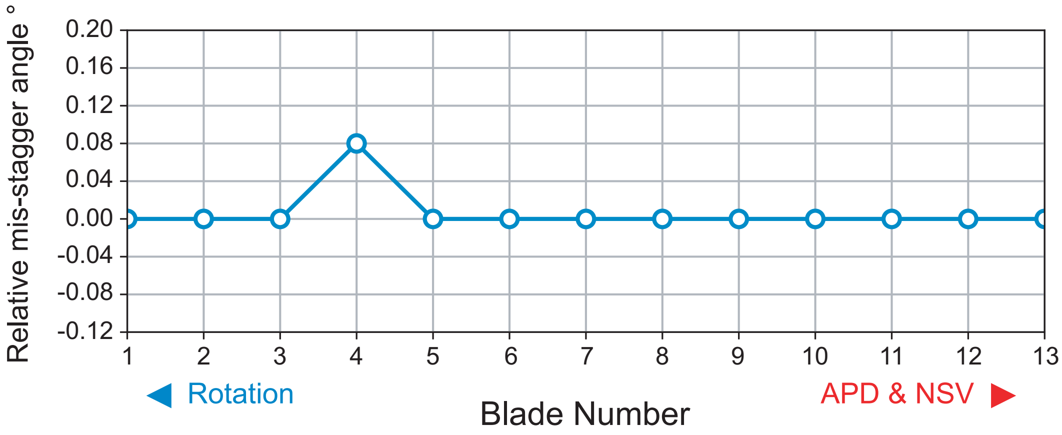

(b) Case B. NSV behaviour.

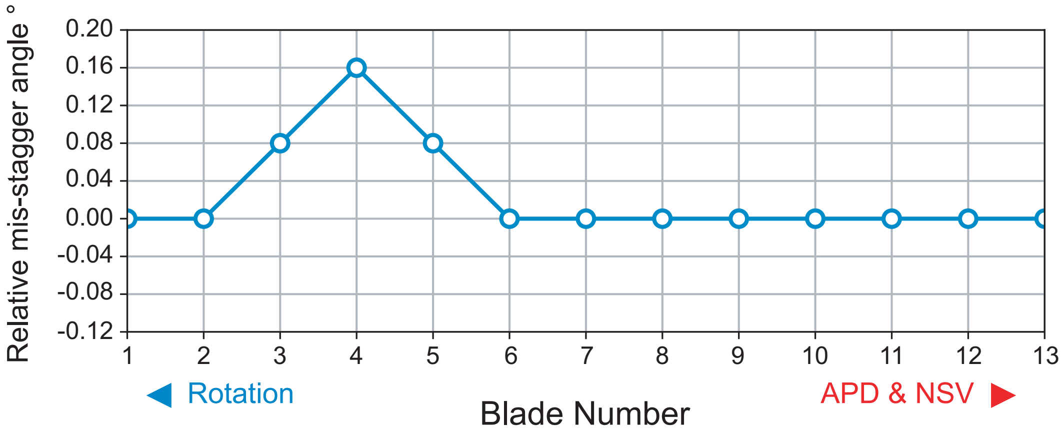

(c) Case C. NSV behaviour.

Figure 5.1: Relative mis-stagger study. Case A-C.

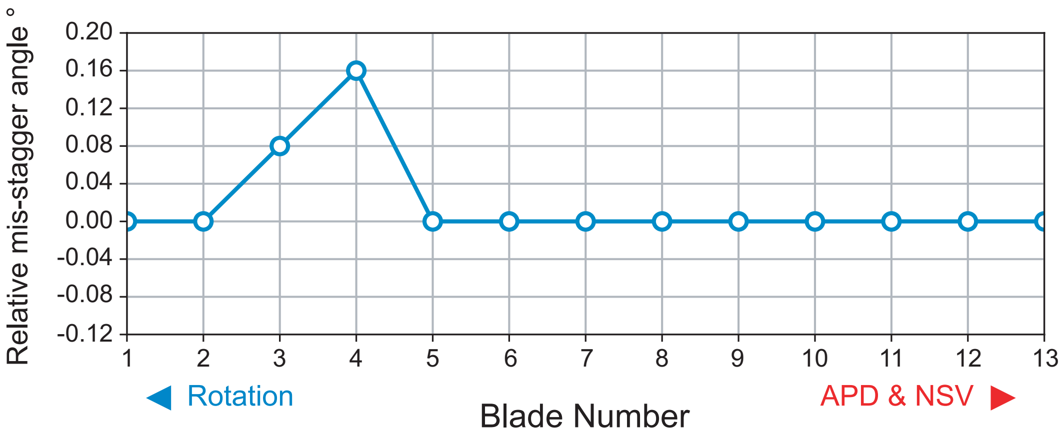

(a) Case D. NSV behaviour.

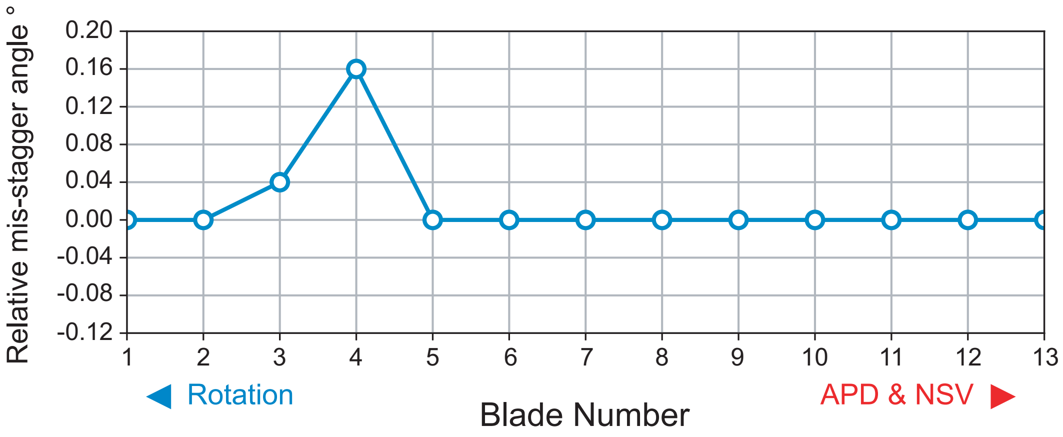

(b) Case E. No NSV behaviour.

Figure 5.2: Relative mis-stagger study. Case D and F.

Case	Initial Mis-Stagger Pattern (°)			Max Delta	NSV
	B-03/B-16	B-04/B-17	B-05/B-18	Mis-Stagger (°)	Behaviour
A	0.00	0.16	0.00	0.16	Non-NSV
B	0.00	0.08	0.00	0.08	NSV
C	0.08	0.16	0.08	0.08	NSV
D	0.08	0.16	0.00	0.08	NSV
E	0.04	0.16	0.00	0.12	Non-NSV

Table 5.1: Mis-Stagger patterns and the corresponding NSV behaviour.

This discovery is important from the industry perspective. The main argument against the previous conclusion (i.e. the absolute amplitude is important) is that the tolerance of the fan blades is likely to be higher than the threshold for NSV and thus inhibits it. This means it is far from being a major concern to the industry. The tide has turned under the new discovery. Thus, the inherent unsteadiness during jet engine operation can easily attain the required low relative mis-staggering level for NSV behaviour to occur.

To further the understanding of the NSV behaviour, cases with randomly mis-staggered patterns are investigated. The initial pattern for two of them are illustrated in Figure 5.3. The computation reveals that one of them exhibits NSV while the other one does not. The corresponding tip stagger history plots (for half of the assembly) are presented in Figure 5.4. In Figure 5.3, the correlation between the initial patterns and the NSV behaviours reveals that the pattern with the higher relative mis-stagger level (above 0.10°) shows NSV behaviour while the one with lower amplitude (0.06°) does not. This is in direct contradiction with the understanding so far and suggests there are more than one control factor for NSV. One of the potential factors is the phasing of the mis-stagger pattern which is discussed in the parametric study in Chapter 4. However, in contrast to the idealised case where there are only a few mis-staggered blades, it is less feasible to study the phasing aspect on randomly mis-staggered pattern.

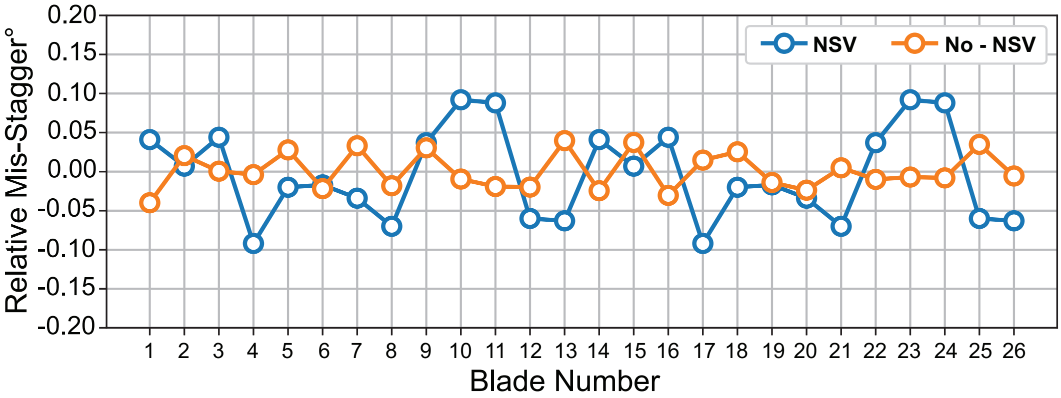

Figure 5.3: Two initial mis-stagger patterns.

As it is apparent from the discussion in Chapter 4 where only idealised patterns are studied, analysing NSV behaviour on a randomly mis-staggered pattern with the same level of thoroughness as Section 4.5.1 is not practical. To be more specific, as the assembly is fully mis-staggered, the NSV mechanism need to be studied in every single passage which posses unrealistic computation and time requirement. Thus, it is vital to find an alternative approach to examine NSV behaviour on randomly mis-staggered assemblies. As mentioned in the literature review section, machine learning techniques have been proven useful in the field of vibration diagnostics in rotating machinery [100–102, 104]. In essence, the machine learning algorithms are used to determine the source of the fault based on the symptoms. In this study, the objective is to investigate the correlation between NSV behaviours and the features in the mis-staggering patterns. It is important to acknowledge that the effectiveness of the approach is limited as additional experimental data are required to validate the findings from the machine learning models.

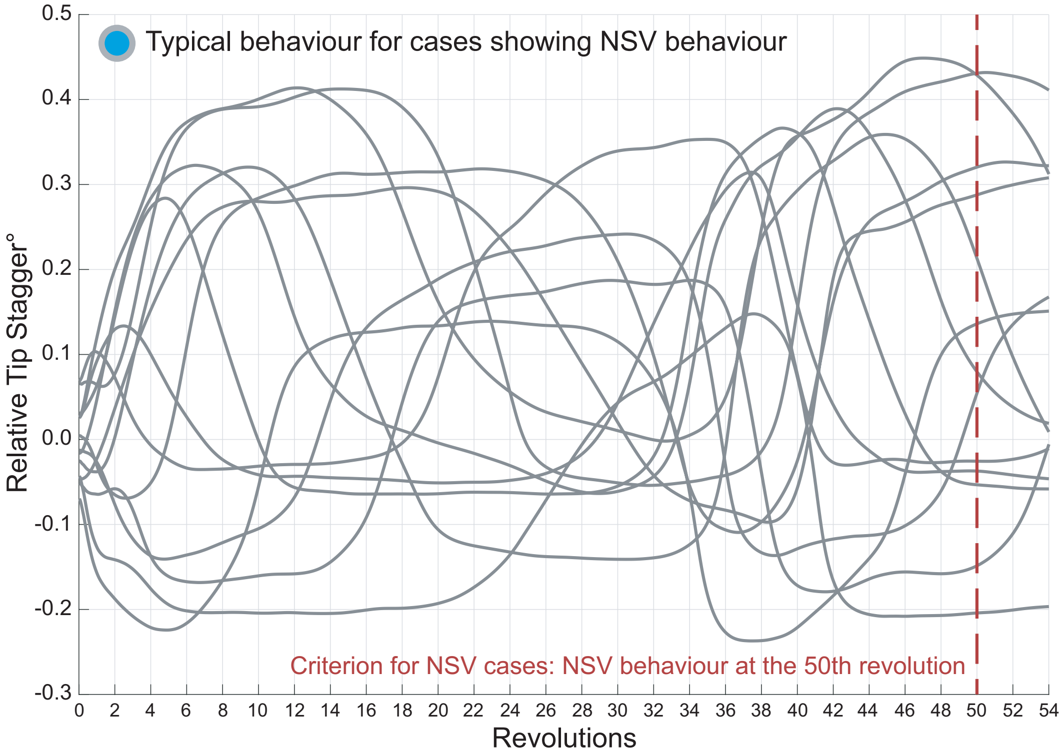

(a) NSV case.

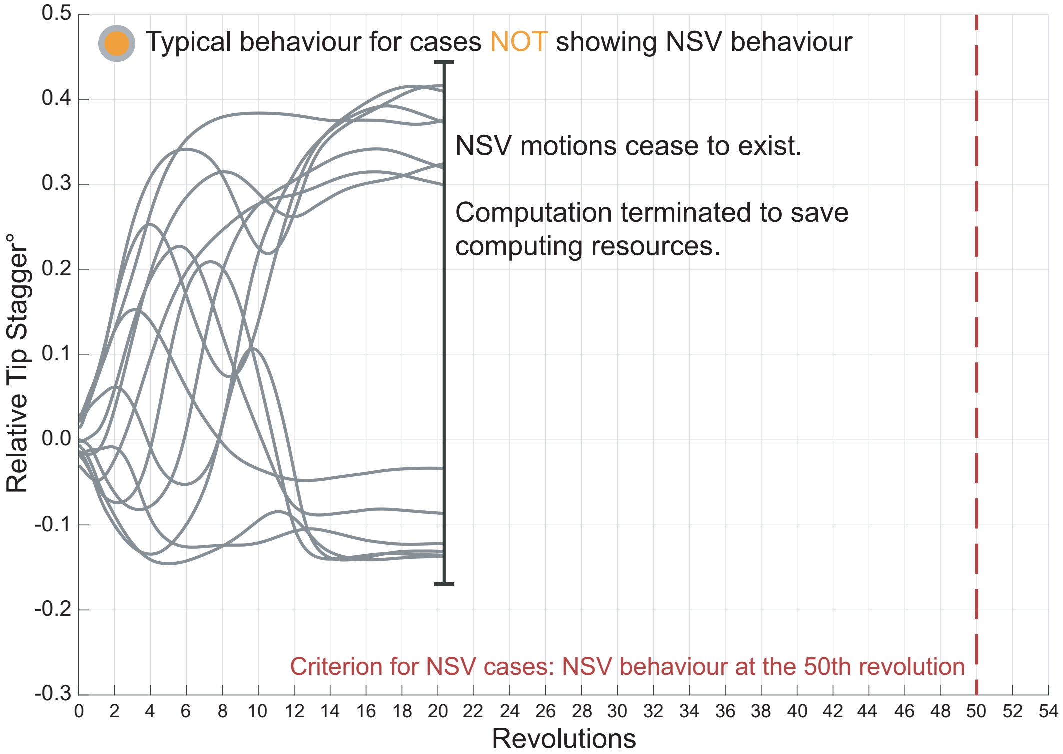

(b) Non-NSV case.

Figure 5.4: Typical NSV behaviour and typical Non-NSV behaviour for randomly mis-staggered cases.

5.3.2 Objective and Structure of the Study

The long term objective of this study is to be able to determine whether a particular mis-stagger (denoted as MSTG in later discussion) pattern would lead to NSV behaviour by evaluating the features of the pattern through machine learning algorithms. While evaluating the machine learning models , the relative importance of the features would also provide insights on the features and allows one to better understand the controlling mechanism behind NSV. At the current stage, the objective is to explore the potential of adopting machine learning techniques for NSV behaviour prediction. Experimental data, which can be expensive to obtain, are required to validate the findings from this initial investigation.

Development of such classifier is useful from the engine operators' point of view for the following reason. With the inherent manufacturing tolerance [37] and in-service wear, the fan blades available for a fan assembly possess inevitable geometric variability. As demonstrated previously in Chapter 3 and 4, this can potentially lead to APD and NSV which have various adverse aerodynamical and aeromechanical effects on the fan operation. In the worst case scenario, NSV can lead to High Cycle Fatigue (HCF) which, as discussed in Chapter 1, can potentially lead to significant loss to both the engine manufacturer and operators [5, 10].

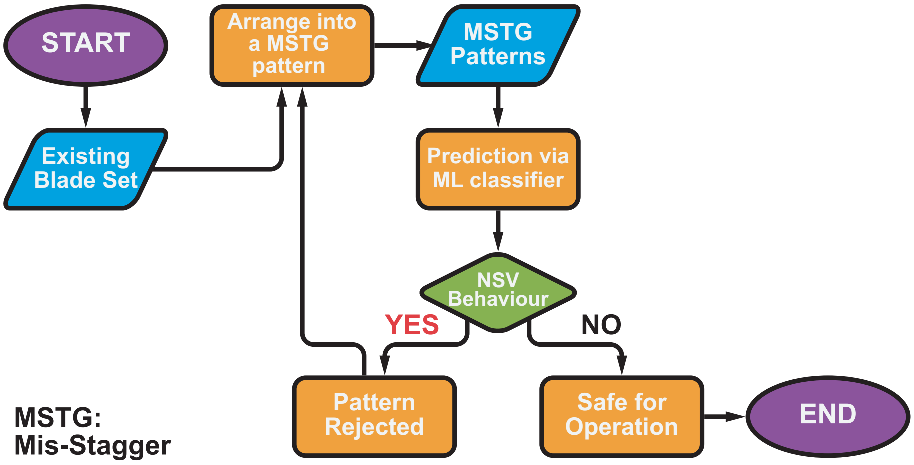

(a) Application of this method in operation.

Figure 5.5: Implementation of Machine-Learning-assisted NSV detection during operation.

The usefulness of the classifier can be demonstrated through the schematic diagram in Figure 5.5. There are many ways a given set of mis-staggered fan blades can be arranged into on an assembly. Based on the discussion so far, it is clear that there are a small number of the arrangement (i.e. the sequence of the blades on the assembly) that will lead to the NSV behaviour. Though the probability is small, the resulting damage is enormous and hence it is vital to identify the defect patterns and remove them from operation. This goal can be achieved via a machine learning model which can predict whether the pattern will exhibit NSV behaviour based on its features (i.e relative mis-staggering level). The patterns deemed to exhibit NSV behaviour is then rejected while those considered safe can be used for operation. The above mentioned process can be completed within seconds which is important from the operation perspective. This is in contrast to alternative of doing FSI analysis which is both time and resource demanding.

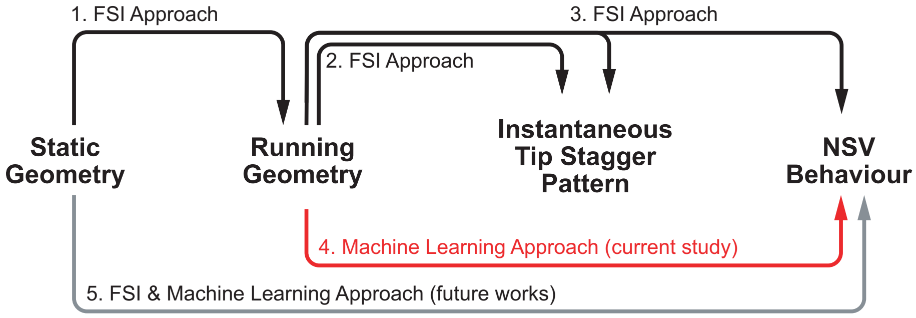

Figure 5.6: Current stage of Machine-Learning-assisted NSV detection study.

It is important to note that, the current stage of the study focuses on predicting NSV behaviour through mis-staggered running geometry[1] instead of through static geometry. This can be further illustrated through the schematics in Figure 5.6 where different stages (from static geometry to NSV behaviour) of prediction are presented. Step 1 which predict nominal running geometry from nominal static geometry is routinely done in the industry [36] and can readily be accomplished by the FSI approach adopted by this study. The feasibility of predicting running geometry in the presence of geometric variability and prediction of the NSV behaviour (i.e. Step 2 and 3 in Figure 5.6) has been proved by previous studies in Chapter 3 and 4. The current machine learning study (i.e. Step 4) uses the results from Step 3 as training data for NSV classification. The scope of the current study can also be extended to predict instantaneous tip stagger pattern through regression analysis.

To reach the full potential of the study (i.e. Step 5) and thus to be able to predict NSV behaviour from mis-staggered static geometry, FSI study should be conducted first to provide training data for the later machine learning approach. The current study is meant to be a proof of concept for the machine learning aspect of the future study. As discussed earlier, experimental data are required to validate the overall approach.

In term of the structure, this chapter starts with outlining the overall approach for the machine learning assisted NSV study. This is followed by discussion on two of

---

[1] For this study, the nominal running geometry at Fan-2's design speed is used.

the most commonly used machine learning algorithms, the Decision Tree Classifier and the Logistic Regression Classifier. A greater emphasis will be spent on the Decision Tree model as its interpretability makes it extremely useful from the industry perspective. Its usefulness will be demonstrated through a mini study on classifying the species of flowers through certain traits. Evaluation criteria are presented for evaluating machine learning models. Based on the context of the study, the reasoning behind the criterion choice is elaborated. Lastly, the prediction performance of the classifiers are compared. As will be demonstrated, the trained decision tree model yields important understanding of the NSV criteria. More importantly, insights from the model offers answer to the questions revolved around Figure 5.3.

5.4 Approach for Machine-Learning assisted NSV detection

5.4.1 Overall Approach

The overall approach for this study is outlined in Figure 5.7. Firstly, 113 test cases /instances with distinct mis-stagger patterns are evaluated using the same FSI approach demonstrated in Chapter 4. The mis-stagger patterns are generated randomly with the maximum mis-stagger amplitude limited to 0.5°. The mis-staggering is applied in the same way as described in Section 3.3.1. In the early phase of the study, the patterns are generated randomly with an uniform distribution of the mis-stagger angles (i.e. ±0.5°). Based on the earlier discussions in Chapter 4 and Section 5.3.1, it is deduced that the NSV behaviour tends to occur at low relative blade-to-blade mis-stagger levels. Therefore, more cases are placed at the lower end of the range. The initial mis-stagger range of ±0.5° is reduced to ±0.2°. Their corresponding NSV behaviour (i.e. exhibiting /not exhibiting NSV) can be determined through the tip stagger history plots in the same fashion as illustrated in Figure 5.4. To be more specific, the pattern will be classified as not exhibiting NSV (labelled as OOO/0 in the dataset) if the rate of change on all the blades' stagger angle is sufficiently small (e.g. Figure 5.4(b)). Otherwise, the case is deemed as exhibiting NSV (labelled as NSV/1 in the dataset). In contrast to the case in Figure 5.4(b) where the blades motion stabilised within 20 revolutions, it has been observed in both the previous study [32] and the current one that it can take significantly longer time (i.e. close to 100 revolutions) for the pattern to stabilise. Therefore, an arbitrary limit on the number of revolutions to observe is chosen. In this study, to optimise the use of computation resource, the case will be labelled as exhibiting NSV if the blades are still experiencing the switching in their relative tip stagger angles (i.e. from higher to lower, vice versa) at the 50th revolution. Based on this criteria, 34 of the 113 cases are labelled as NSV cases.

At the same time, the mis-stagger patterns are analysed and various features (such as mean mis-stagger amplitude and maximum mis-stagger amplitude) are extracted. This reduces the excessive level of complexity in a mis-stagger pattern (i.e. the sequence and amplitude of 26 mis-stagger angles) into slightly more manageable dimensions. These arbitrarily defined features, which will be discussed in details later, include relative blade-to-blade mis-stagger amplitude[2], peak mis-stagger value, and dominant nodal diameter (ND)/circumferential harmonics etc. The derived features and the labels (i.e. exhibiting/ not exhibiting NSV) determined from FSI calculation are combined into the dataset. As an example, Figure 5.8 illustrates the breakdown of the dataset /cases based on the dominant ND in the mis-stagger patterns. The data is first presented in term of the total number of cases tested for each nodal diameter and then the data is segmented to show the number of NSV and Non-NSV cases tested for each nodal diameter.

The full data set is randomly split into two subsets, the training set and the test set. The former has 88 cases /instances while the later has 25 cases. The composition of the datasets is kept the same throughout the study such that the performance of different machine learning models can be compared. The split is used to avoid overfitting the machine learning models such that they predict well on the existing set yet performs poorly when exposed to new data. At the same time, having an independent test set can help to evaluate the performance of the models on new data and in turn facilitates its optimisation. As the names suggest, the training set is used to train the machine learning models while the test set is used to evaluate their performance. To be more specific, the machine learning models are trained and optimised in an iterative process. The trained models are then used to make predictions on the test dataset which is independent of the training data set and has not been used in tuning the models. Their predictive performances are then used to determine whether they are fit for the objective of this study, i.e. to predict the NSV behaviour of a mis-stagger pattern based only on the arrangement and mis-stagger amplitude of the blades.

---

[2] For brevity, this term is shortened to relative mis-stagger amplitude or RDelta (Relative Delta) in future discussion.

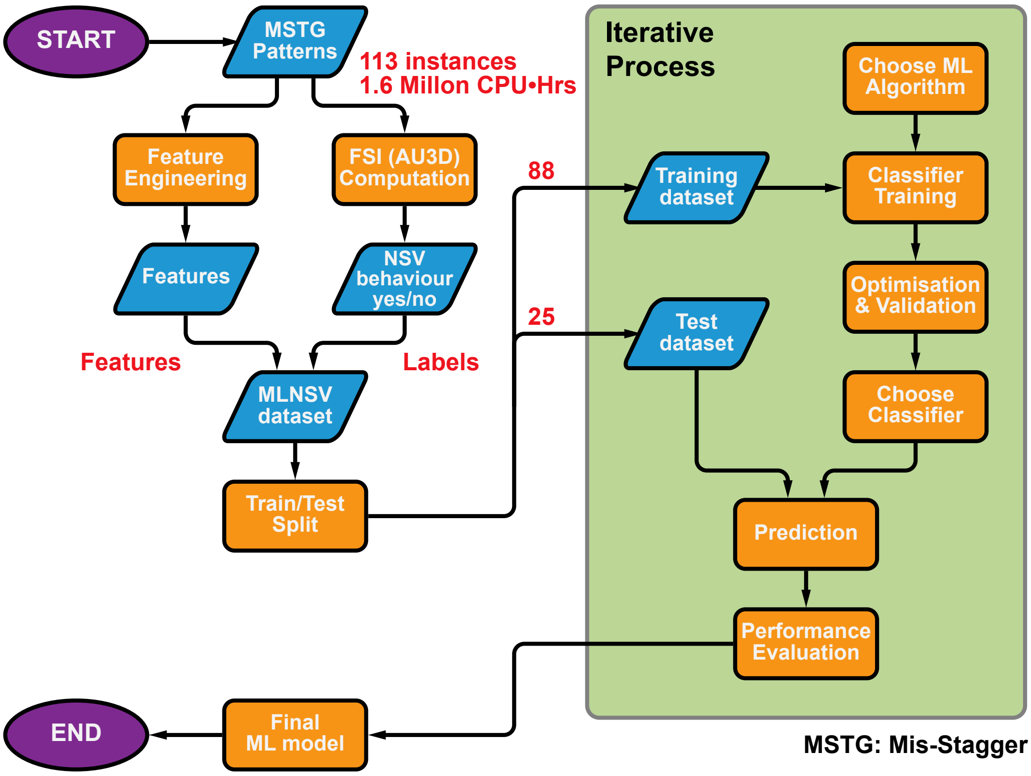

Figure 5.7: Overall approach for Machine-Learning-assisted NSV detection.

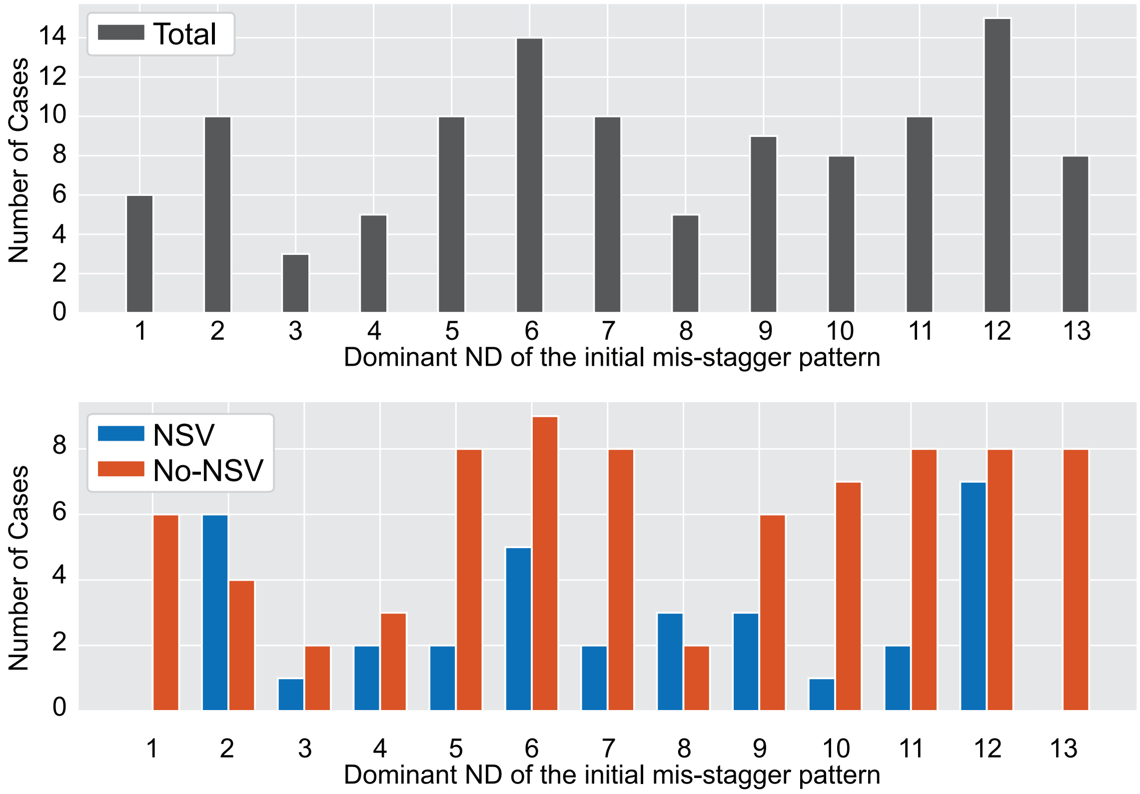

Figure 5.8: Test cases categorised by the dominant Nodal Diameter.

5.4.2 Features Used

As mentioned earlier, various arbitrarily derived features are used to train the machine learning models. The derived features for the two cases shown in Figure 5.3 are tabulated in Table 5.2 to facilitate the interpretation of the features.

		NSV case	Non-NSV case
Features	AmpAbs	0.092	0.040
	AmpPlus	0.092	0.040
	AmpMinus	-0.092	-0.040
	MeanMSTG	-0.004	0.001
	Variance	0.003	0.001
	RDelta	0.107	0.062
	Rdelta(ABS)	0.148	0.068
	DominantND	6	13
	WeakestND	1	4
	APDsignalND	6.31E-17	2.10E-02
Label	NSV behaviour	1	0

Table 5.2: Comparison of the features in the two patterns presented in Figure 5.3.

Features used:

1. AmpAbs, AmpPlus, AmpMinus:
   AmpAbs is the maximum absolute mis-staggering amplitude within the initial pattern. In contrast, AmpPlus only accounts for peak mis-staggering amplitude whereas AmpMinus only accounts for the minimum values. These features are used based on the discussion in Chapter 4 where amplitude of the mis-stagger in the idealised cases determines the resulting NSV behaivour.

2. MeanMSTG, Variance:
   Mean and variance of the mis-stagger amplitudes of the blades in the initial pattern.

3. RDelta, RDelta(ABS):
   RDelta is the maximum value of the relative blade-to-blade stagger difference in the direction of NSV travel. In comparision, RDelta(ABS) accounts for the maximum absolute stagger difference between adjacent blades. As demonstrated through the discussion about Figure 5.2, this feature can effectively differentiate NSV from Non-NSV behaviours in idealised mis-stagger patterns.

4. DominantND, WeakestND:
   Through Fourier decomposition, the amplitude of each harmonics /ND can be ranked. The one with the highest amplitude will be taken as the DominantND value while the one with the lowest value is taken as the WeakestND value.

As Fan 2 has 26 blades, the highest observable harmonic/ND is the 13th. The two features are thus discrete values ranging from 1 to 13.

5. APDsignalND:
   Amplitude of the 13th harmonic/ND when the initial mis-stagger pattern is de-constructed by Fourier decomposition. Fan 2 has 26 blades in the assembly and thus ND corresponding to APD is the 13th.

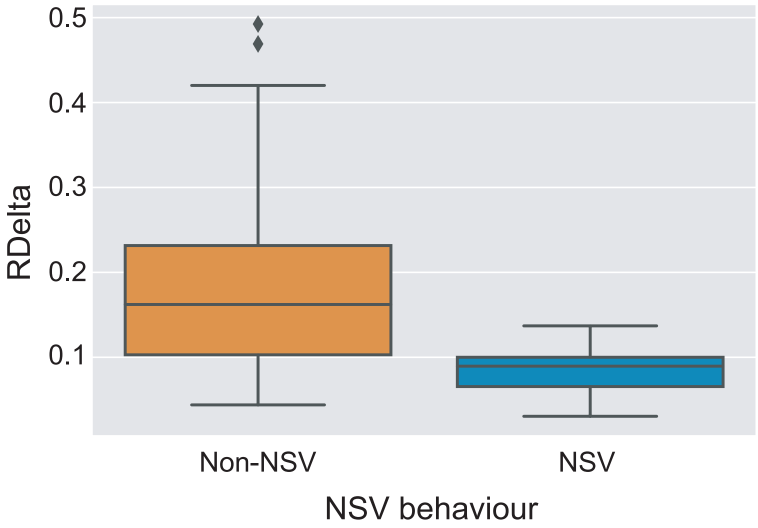

Figure 5.9: Box-and-whisker plot for the feature *RDelta*.

Initial investigation indicates that none of the features, by itself, can be used to distinguish mis-stagger patterns that exhibit NSV behaviour from those that don't. The feature closest to achieving this objective is the RDelta value and its predictive performance is illustrated through the box-and-whisker plot[3] in Figure 5.9. Here the entire dataset is analysed and the variations of RDelta in both the NSV cases and the Non-NSV cases are presented. From the box plot, it is evident that the 3rd quartile of the NSV cases is at approximately the same value (approx. 0.1) as the 1st quartile of the Non-NSV cases. Though this comparison indicates that the NSV cases tend to have lower relative mis-staggering amplitude than the Non-NSV cases do, it does not separate the two classes. This agrees with the conclusion reached about the data in Figure 5.3. On the bright side, however, the discovery indicates the relative mis-staggering amplitude will be an important feature for the later machine learning model. In fact, as will be demonstrated in the results section, the RDelta feature is one of the most important features for both the decision tree model and the logistic regression model.

---

[3] Also known as the box plot or the box-and-whisker diagram.

5.5 Methodology

In this study, the machine learning models are implemented through the open source library scikit-learn (version 0.20.1) [95]. Discussion on the algorithm for the decision tree model and the logistic regression model is included in Appendix B.

As mentioned earlier, the decision tree classifier is chosen specifically for its interpretability [107, 108]. This aspect of the model contributes to its trustworthiness which is vital from the industry perspective. In general, machine learning models utilise the correlation between features and behaviours for classification. This can result in models that establish irrelevant associations between the two [111, 112]. This is particularly true for the artificial neural networks which are commonly referred to as 'black box' models as they do not explain how the decisions are reached. In fact, as demonstrated by Ribeiro et al. [112], a neural network based classification model incorrectly used the snow in the background (or light background at the bottom) as a dominating feature in the classification of photos of wolves and huskies (a type of sled dog).

Without understanding how and why the model does the classification, it is difficult to establish trust of the model. In the context of canine photo classification, this is nothing of concern. However, in the context of civil aviation where safety concern is fundamental to most of the decision making, the lack of understanding how the model operates would be extremely troubling.

5.6 Evaluating Classifier Performance

The results of a binary classification problem can be summarised through a *Confusion Matrix* which is illustrated in Figure 5.10. More specifically, the matrix highlights how accurate the classifier is performing and what type of errors it is making. Inside the confusion matrix, positive and negative are used to mark whether a case belongs to a class. In the context of the study, positive means the case is exhibiting NSV behaviour and vice versa. The columns in the confusion matrix represent the actual behaviour of the case which, in this study, is determined through the aeroelastic computations. The rows represent the behaviour predicted by the classification model. The entries in the matrix describe the nature of the predictions. For example, *True Positive* is used to label outcomes where the cases from a particular class is correctly classified by the model and predicted to be from that class. In contrast, *False Negative* labels outcomes where cases from a class is falsely predicted to be from the other class.

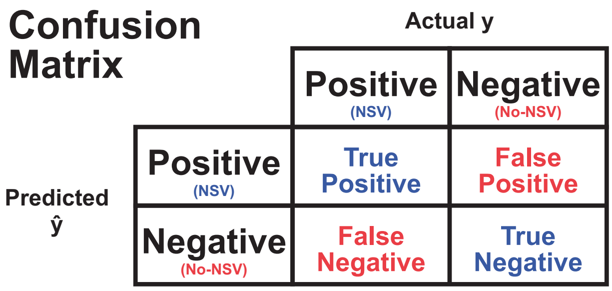

Confusion Matrix		Actual y	
		Positive (NSV)	Negative (No-NSV)
Predicted ŷ	Positive (NSV)	True Positive	False Positive
	Negative (No-NSV)	False Negative	True Negative

Figure 5.10: Confusion matrix for binary classification.

The performance of a classification can be further reduced to a single metric. The equations for the most commonly used performance metrics are shown in Equation 5.1 to 5.9.

$$Accuracy = \frac{True\,Negative + True\,Positive}{Total} \tag{5.1}$$

$$Accuracy = \frac{\sum_i^n 1_{[y_i = \hat{y}_i]}}{n} \tag{5.2}$$

$$Precision = \frac{True\,Positive}{True\,Positive + False\,Positive} \tag{5.3}$$

$$Precision = \frac{\sum_i^n 1_{[y_i = \hat{y}_i\, and\, y_i > 0]}}{\sum_i^n 1_{[\hat{y}_i > 0]}} \tag{5.4}$$

$$True\,Positive\,Rate(Recall) = \frac{True\,Positive}{True\,Positive + False\,Negative} \tag{5.5}$$

$$True\,Positive\,Rate\,(Recall) = \frac{\sum_i^n 1_{[y_i = \hat{y}_i\, and\, y_i > 0]}}{\sum_i^n 1_{[y_i > 0]}} \tag{5.6}$$

$$True\,Negative\,Rate = \frac{True\,Negative}{True\,Negative + False\,Positive} \tag{5.7}$$

$$True\,Negative\,Rate = \frac{\sum_i^n 1_{[y_i = \hat{y}_i\, and\, y_i < 0]}}{\sum_i^n 1_{[y_i < 0]}} \tag{5.8}$$

$$F_1\,score = 2 \cdot \frac{Precision \times Recall}{Precision + Recall} \tag{5.9}$$

Each of the five metrics introduced above offers a peek into the strength and more importantly the weakness of the classification model. The necessity of such evaluation can be perfectly summarised by the quote from George E.P. Box FRS, *'Since all models are wrong the scientist must be alert to what is importantly wrong. It is inappropriate to be concerned about mice when there are tigers abroad'* [68]. Therefore, the prioritisation of the five metrics introduced depends on the nature of the study.

In general, accuracy which is shown in Equation 5.1 is not a useful metric. This particularly true for the binary NSV classification study which has class imbalance in the dataset. The full dataset consist of the FSI analysis of 113 mis-stagger patterns. 79 of the 113 do not exhibit NSV behaviour while the remaining 34 do. A naïve classifier that simply predict every case available as non-NSV will have an accuracy of 69.9% and the 34 NSV cases will be falsely labelled. Additionally, evaluating model performance through this measure offers little information on how the two classes are separated and hence offers little insights to the understanding of NSV behaviour. Therefore, it is evident that this metric is not fit for the purpose of this study.

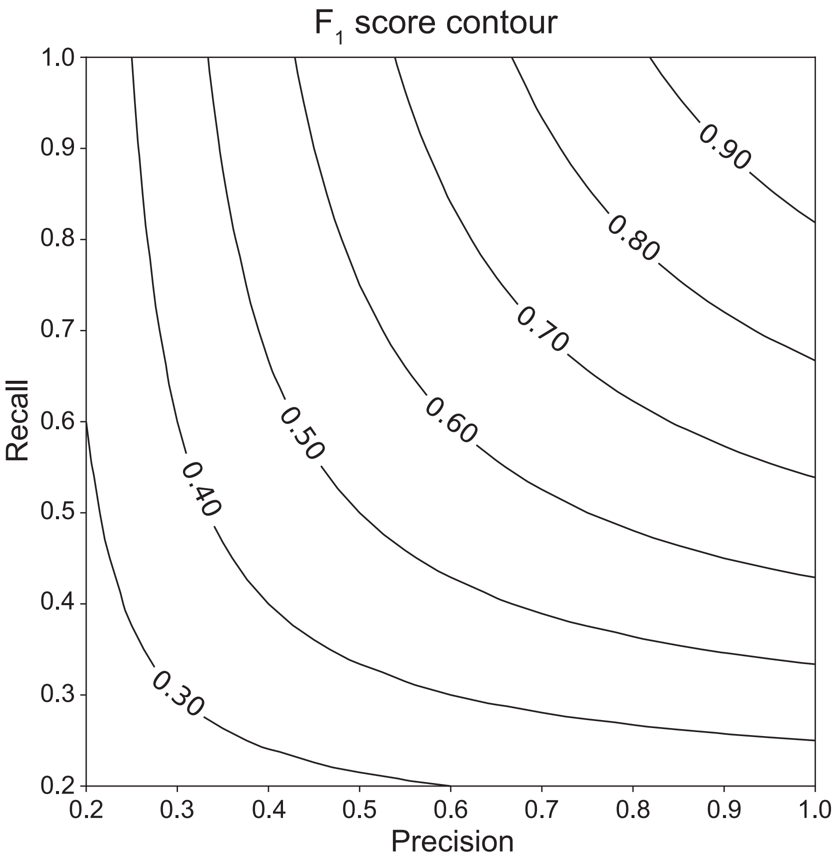

Figure 5.11: F1 score contour. Truncated to only included independent variable range between 0.2 and 1.0.

The F_1 score, also known as the F-score, is the harmonic mean between precision and recall. The F_1 score peaks at 1 when both the precision and recall value are equal to 1. As illustrated in Figure 5.11, this metric gives equal weight to its two component metrics and introduces heavy penalty to low values. In practice, a high F_1 score generally implies the classification model is performing well [110].

Given that the ultimate goal for this study is to reduce operation down time by identifying NSV-inducing and thus fatigue-damage-inducing stagger pattern, the *False Negative* classification error should be avoided at all costs. In the case when a true NSV-inducing stagger pattern is falsely categorised as non-NSV-inducing and installed on the fan assembly, the potential damage is high. In contrast, when a non-NSV-inducing pattern is falsely classified as unsafe for operation, the only cost incurred is the insignificant effort required to find another safe blade arrangement. Therefore, the *False Positive* classification error is of much less concern compared to the *False Negative* type. The performance metric relevant to the *False Positive* classification error is the *True Positive Rate*, also known as *Recall*, shown in Equation 5.5. Therefore, maximising the Recall performance is a major objective in optimising the models.

5.7 Results and Discussion

5.7.1 Decision Tree Classifier

Using the approaches mentioned previously in Figure 5.7, the optimised decision tree classifier is illustrated in Figure 5.12. Its performance is evaluated on the test set and the *confusion matrix* is shown in Figure 5.13.

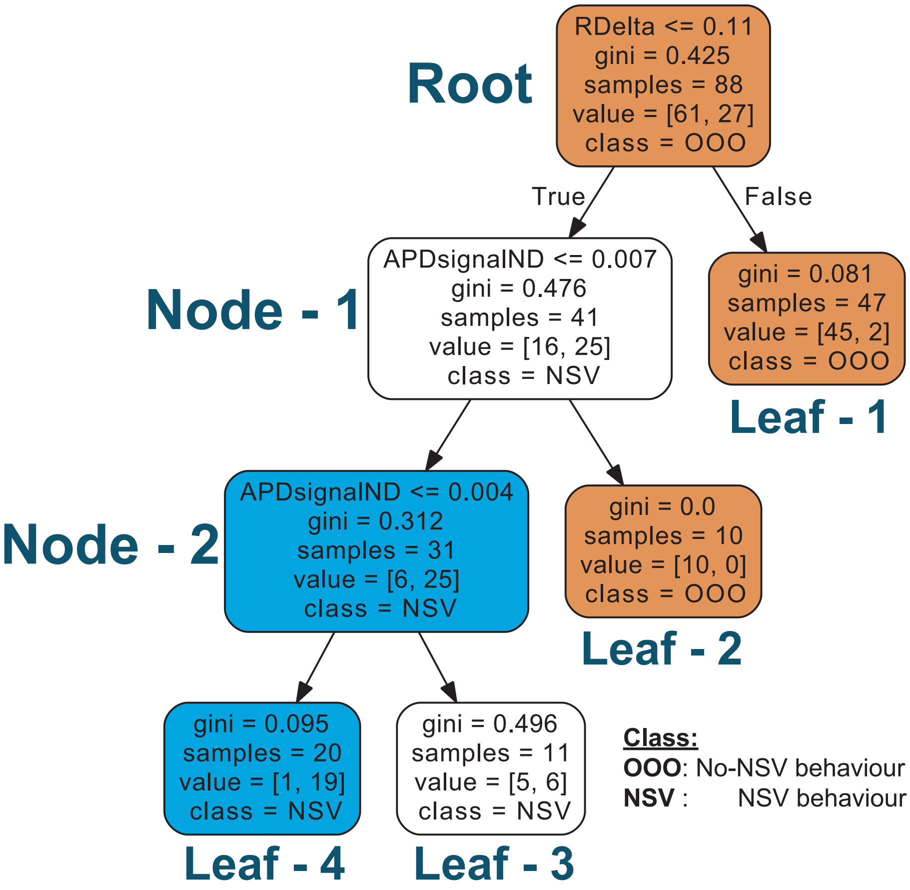

Figure 5.12: Decision Tree Classifier for NSV behaviour prediction.

The trained decision tree model in Figure 5.12 uses two features of the initial mis-stagger pattern for NSV behaviour prediction. Unsurprisingly, the first one is the relative blade-to-blade stagger angle difference (i.e. RDelta). This agrees with the conclusion discovered through the analytical method. In fact, using these features together with a threshold value of 0.11°, the Root node is able to identify and separate more than half of the Non-NSV cases from the full dataset. This leads to a relatively pure (i.e. gini index = 0.081) Leaf-1 in Figure 5.12. The amplitude of the 13th harmonics/ND from the Fourier decomposition of the initial mis-stagger value (i.e. APDsignalND) is used by subsequent nodes to make predictions on the remaining cases. Lastly, a further split based on the same feature is conducted by Node-2, resulting a relatively pure Leaf-4 node and impure Leaf-3 node. This further highlights the significance of this feature to NSV classification.

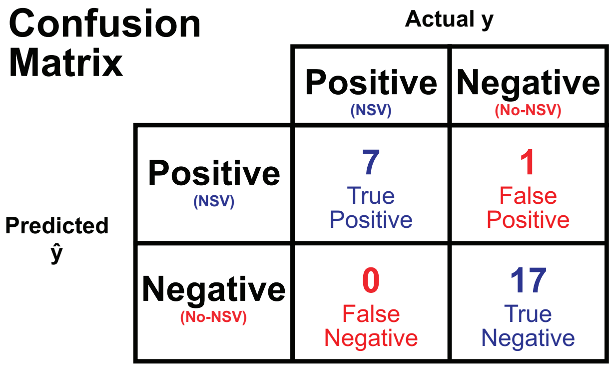

Confusion Matrix

		Actual y	
		Positive (NSV)	Negative (No-NSV)
Predicted ŷ	Positive (NSV)	7 True Positive	1 False Positive
	Negative (No-NSV)	0 False Negative	17 True Negative

Figure 5.13: Confusion matrix of the CART classifier's performance on the test set.

The decision tree model is evaluated on the 25 test cases to gauge its performance on new data. The confusion matrix in Figure 5.13 illustrates the more than satisfactory classification performance[4] of the decision tree model which has a true positive rate of 1.00, a precision value of 0.88, and a F1 score of 0.93. At the same time, the only misclassification error belongs to the false positive category. Thus, a NSV-free mis-stagger pattern is misclassified as a NSV-inducing one. As previously discussed, the penalty for this type of error is negligible in operation and it only results in minimal time loss in searching for a NSV-free mis-stagger arrangement.

To further demonstrate the effectiveness of this classifier, its decision boundary is illustrated in Figure 5.14. The figure is presented in terms of the two important features identified by the decision tree. The entire NSV dataset, including both the training set and the test, is presented in Figure 5.14 and the true behaviour [5] of each case is colour coded. The solid and dashed line represent the classification criteria of the Root and Node-1 respectively. The grey scale contour maps the decision boundary for the two above mentioned node.

As revealed by the decision boundary, the model leaves two false negative cases as highlighted in Figure 5.14(b). These two cases come from the training set and end up on the Leaf-1 node in Figure 5.12. Despite this, it is important to acknowledge that the combination of features and threshold values can separate almost all of the NSV cases from the rest. This is important from the industry perspective since the cost of having NSV-inducing mis-stagger patterns in operation is significant.

It is important to note that, in Figure 5.14, the origin represents the scenario with no stagger variability in the assembly. Thus, under the conditions investigated in this study, neither NSV nor APD behaviour can manifest since there is no initial

---

[4] All the performance metrics peak at 1.00.

[5] Which, as mentioned earlier, is investigated through FSI computation.

mis-stagger to trigger initialise the passage shock displacement. However, it is important to note that this is an unrealistic scenario due to the inherent manufacturing tolerance and hence is not considered in this study.

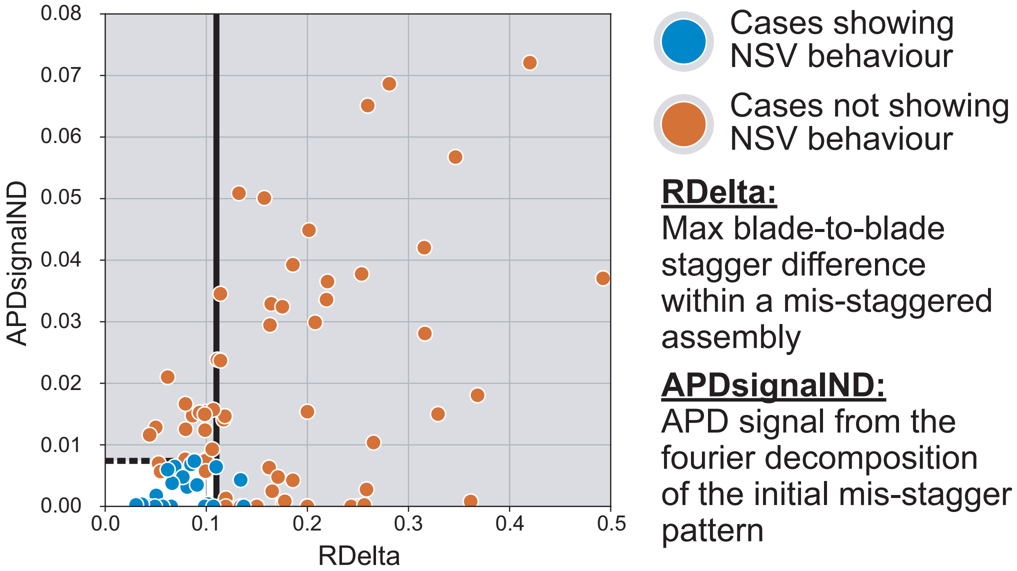

(a) Full data range.

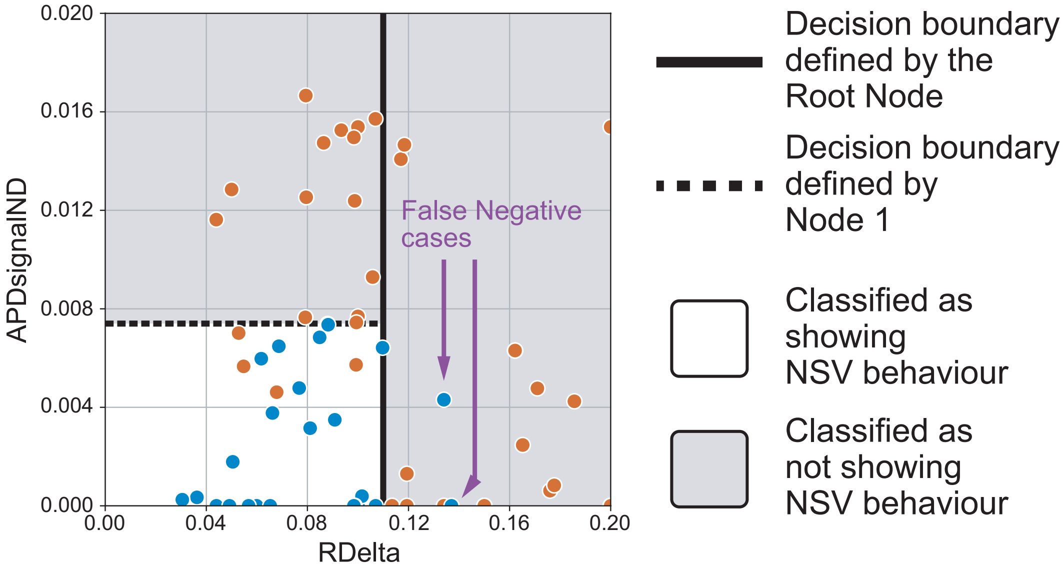

(b) Zoomed view.

Figure 5.14: Decision boundary of the tree classifier. Illustrated on the full dataset.

5.7.2 Application of the Decision Tree Classifier

From the trained decision model, it is found that there are two features in a mis-stagger pattern that determines whether the assembly will exhibit NSV behaviour: (a) mis-stagger amplitude between adjacent blades (i.e. RDelta), and (b) amplitude of the 13th ND/harmonics[6]. As the decision boundary in Figure 5.14 demonstrates, NSV behaviour will manifest when both values are sufficiently small. The analysis of the former is previously completed in Chapter 4 and further reinforced in the beginning of this chapter.

The earlier question revolved around Figure 5.3 can now be answered by the new insights offered by the decision tree model. The features of the two cases are reproduced in Table 5.3 with the important features highlighted. Though the Non-NSV case has a significantly higher relative mis-stagger amplitude between adjacent blades (i.e. RDelta) than the NSV case does, both fulfil the Root node's criteria of $RDelta \leq 0.11$ shown in Figure 5.12 and 5.14. The property that distinguish the two case from each other, in term of NSV behaviour, is the amplitude of the 13th harmonics /ND (i.e. APDsignalND). The NSV case satisfy both Node-1's and Node-2's requirement on the low amplitude and hence ends up on the Leaf-4 node in Figure 5.12. In contrast, the Non-NSV case has higher APDsingalND value than the Node-1's threshold value of 0.007 and hence is sorted into Leaf-2. Thus, this further highlights the decision tree classifier's strength in interpretability which is important from the industry perspective.

		NSV case	Non-NSV case
Features	AmpAbs	0.092	0.040
	AmpPlus	0.092	0.040
	AmpMinus	-0.092	-0.040
	MeanMSTG	-0.004	0.001
	Variance	0.003	0.001
	RDelta	**0.107**	**0.062**
	Rdelta(ABS)	0.148	0.068
	DominantND	6	13
	WeakestND	1	4
	APDsignalND	**6.31E-17**	**2.10E-02**
Label	NSV behaviour	**1**	**0**
Prediction		True Positive	True Negative

Table 5.3: Comparison of the features in the two patterns presented in Figure 5.3.

---

[6] For the 26-blade Fan 2.

5.7.3 Logistic Regression Classifier

Unlike the decision tree algorithm, logistic regression classifier does not identify the important features automatically and hence feature selection is required prior to training the model. In this study, feature selection is completed manually since the physical interpretation of the features is important to understand the NSV behaviour. Alternatively, more advanced techniques can be found in literature [108, 109]. The combination of features used in training some of the Logistic Regression Classifiers (LRC) and the corresponding performance when applied against the test dataset is tabulated in Table 5.4. The performance comparison of these classifiers against the test dataset[7] is visualised in Figure 5.15.

ML Model		LRC-1	LRC-2	LRC-3	LRC-4	LRC-5
Features Used	AmpAbs	Y	-	-	-	-
	AmpPlus	Y	-	-	-	-
	AmpMinus	Y	-	-	-	-
	MeanMSTG	Y	-	-	-	-
	Variance	Y	-	-	-	-
	RDelta	Y	Y	-	Y	Y
	RDelta_ABS	Y	-	-	-	-
	DominantND	Y	Y	Y	Y	-
	WeakestND	Y	Y	Y	Y	-
	APDsignalND	Y	Y	Y	-	Y
Metrics	Accuracy	0.760	0.920	0.600	0.760	0.840
	Precision	0.556	0.778	0.364	0.600	0.667
	TPR	0.714	1.000	0.571	0.429	0.857
	TNR	0.778	0.889	0.611	0.889	0.833
	F1 score	0.625	0.875	0.444	0.500	0.750

Table 5.4: Comparison of the five LRC Models and their performance metrics.

From Table 5.4 and Figure 5.15, it is immediately clear that employing all the available features does not lead to the best classification performance. In particular, LRC-1's accuracy score of 0.76 is only marginally better than the proportion of Non-NSV cases in the entire dataset[8] which is 0.70. In other words, in term of accuracy, LRC-1 slightly outperforms a dummy classifier that classifies all the cases to the Non-NSV class. Thus, through an iterative process, different combinations of features are tested and the subset deployed for LRC-2 is found to offer the best performance against the test set. The corresponding confusion matrix for LRC-2's performance against the test set is shown in Figure 5.16. Note that, during this process, the two features identified by the decision tree classifier, RDelta and APDsignalND, are always present in the combination.

---

[7] The same test case combination used to evaluate the decision tree classifier.

[8] As mentioned earlier, 79 of the 113 cases do not exhibit NSV behaviour.

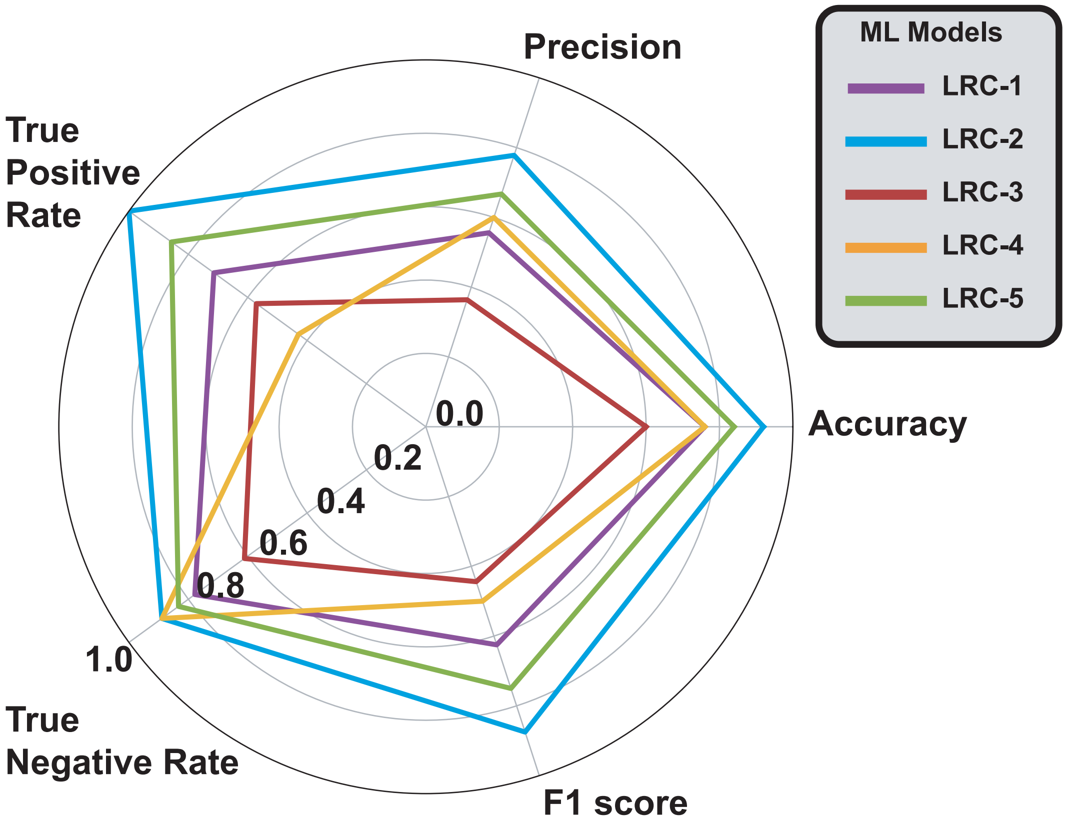

Figure 5.15: Comparison of the five LRC model's performance metrics.

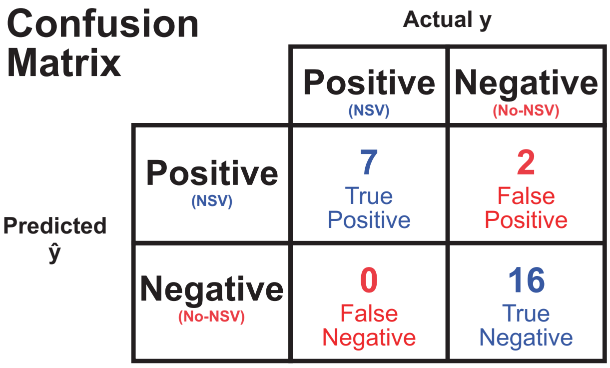

Confusion Matrix		Actual y	
		Positive (NSV)	Negative (No-NSV)
Predicted ŷ	Positive (NSV)	7 True Positive	2 False Positive
	Negative (No-NSV)	0 False Negative	16 True Negative

Figure 5.16: Confusion matrix of the LRC-2's performance on the NSV test set.

To investigate the influence of the two features identified by the decision tree classifier over the LRCs, subsets of LRC-2's feature combination are tested. This leads to classifier LRC-3 to LRC-5 in Table 5.4. Evidently, as illustrated by the performance metrics comparison in Figure 5.15, lacking either one of the two features can lead to significant classifier performance deterioration. Comparing the performance between LRC-2 and LRC-5, it is undeniable that the two newly identified features, DominantND and WeakestND, have strong influence over the classifiers' predictive capability. Evidently, both have strong correlation with the APDsignalND feature identified by the decision tree classifier. Thus, with all other factors held constant, a domiant 13th ND/harmonic mis-stagger tends to lead to a high amplitude of the

13th ND after Fourier decomposition. The same argument holds true for the weakest ND feature.

5.7.4 Support Vector Machine Classifier

Another commonly used machine learning algorithm is the *Support Vector Machine (SVM)* [102,104,113,114]. An optimised Support Vector Machine Classifier (SVC) is tested against the NSV test dataset and the confusion matrix is shown in Figure 5.17. As its predictive performance on the NSV dataset is inferior when compared to the two models discussed above, discussion of its algorithm is not included in this thesis. Detailed discussion of the SVM algorithm can be found in literatures [108, 109].

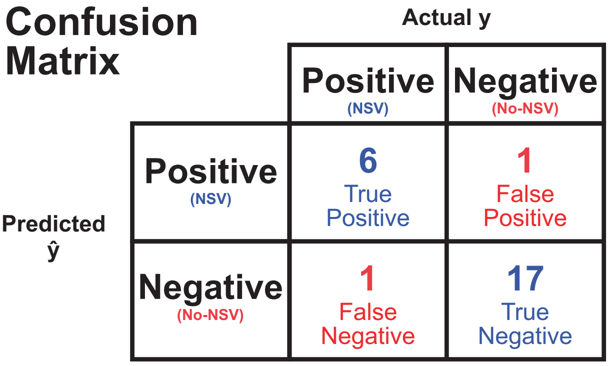

Confusion Matrix

Predicted ŷ	Actual y: Positive (NSV)	Actual y: Negative (No-NSV)
Positive (NSV)	6 True Positive	1 False Positive
Negative (No-NSV)	1 False Negative	17 True Negative

Figure 5.17: Confusion matrix of the SVC classifier's performance on the test set.

5.7.5 Comparison of the Three Classifiers

The performance metrics of the three classifier against the test dataset are tabulated in Table 5.5 and key performance metrics are illustrated on the F1 score contour in Figure 5.18. As discussed previously, though adequate on its own, the SVC classifier demonstrates inferior performance as compared to the other two. This view is further enhanced when the types of misclassification errors made by the classifiers are taken into account. Comparing the three models' misclassification errors through the confusion matrices in Figure 5.13, 5.16, and 5.17, it is immediately evident that all three incur false positive errors yet only SVC results in false negative error. This leads to the SVC's compromised Recall (i.e. True Positive Rate in Equation 5.5) score in Figure 5.18. Based previous discussion, the context of this study dictates that false negative error is significantly more alarming than false positive ones. In short, the consequence of the former can potentially lead to high unscheduled maintenance cost whereas the later, at its worst, results in a short time-loss. Thus, this criterion alone invalidates the feasibility of using the SVC.

ML models		LRC-2	CART	SVC
Metrics	Accuracy	0.920	0.960	0.920
	Precision	0.778	0.875	0.857
	TPR	1.000	1.000	0.857
	TNR	0.889	0.944	0.944
	F1 score	0.875	0.933	0.857

Table 5.5: Comparison of the performance metrics for the three machine learning models.

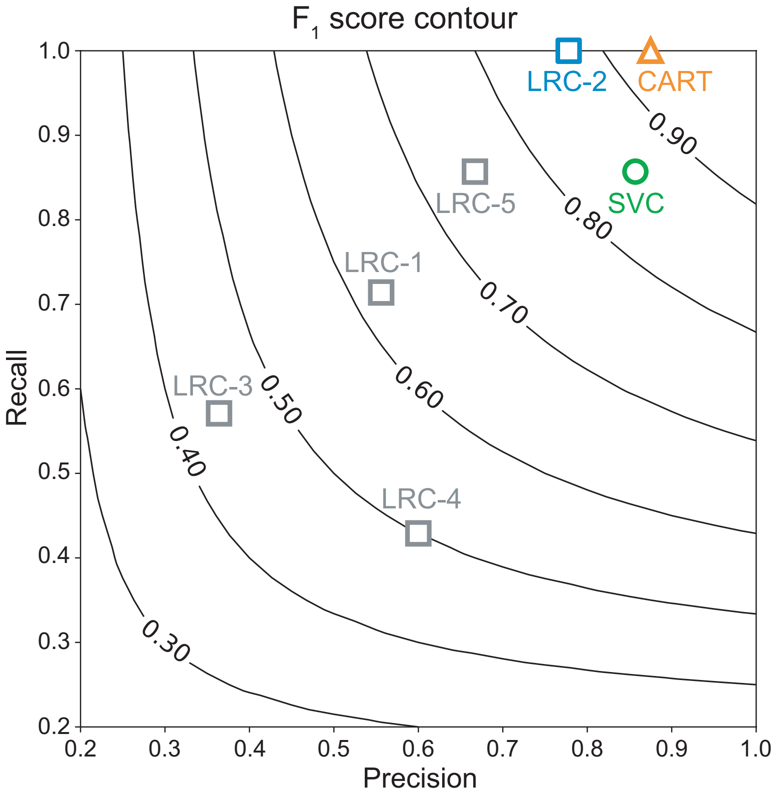

Figure 5.18: Comparison of the models' performance metrics.

As evident from the confusion matrices, the logistic regression classifier is comparable with the decision tree classifier in predictive capability. In fact, their predictions only disagree on one case in the NSV test dataset[9]. Given the overlap between their subsets of useful features and significant difference in their underlying algorithm, it can be concluded that the two key features identified, RDelta and APDsingalND, can be trusted in differentiating NSV-inducing mis-stagger patterns from the benign ones.

---

[9] Detailed breakdown of the three classifiers' predicted behaviour of the test cases is tabulated in Table C.2 in Appendix C.2.

5.8 Chapter Summary

Following the discussion on the use of machine learning techniques in the NSV study, the findings and future direction can be summarised below:

1. The classification outcome from the machine learning models used in this study demonstrates that machine learning techniques are viable for the purpose of NSV behaviour identification. This potentially allows NSV-inducing and hence HCF-inducing mis-stagger patterns to be eliminated from operation, thus avoiding the high cost incurred by unscheduled maintenance. It is also important to acknowledge the limit of this initial investigation and experimental data are required to validate the findings from the machine learning models.

2. As mentioned at the beginning of the chapter, though the current machine learning based method is showing promising results, its effectiveness is limited by the availability of data and can be further improved. In particular, the full untwist history (i.e. from static geometry to running geometry) is not accounted for in the dataset. Instead, the mis-staggering is applied with respect to the nominal running geometry. Thus, the industry relevance of this study can be significantly enhanced by extending the level of complexity (i.e. the inclusion of static mis-stagger patterns) in the dataset.

3. A NSV identification method is developed under the assumption that the fan blade design is fixed. Thus, it is best suited for blade designs that are in active service. Though approach does not remove the root cause of the NSV issue, it can effectively identify and eliminate NSV-inducing mis-stagger pattern from operation, thus minimising the occurrence of the NSV behaviour. In this regard, the method is considered as a passive NSV attenuation method since it does not completely resolve the problem from the root. Naturally, to cover the entire life cycle of a fan blade design, more active NSV attenuation method that can achieve this objective should be explored. In Chapter 6, a redesign approach that can serve as the active NSV attenuation approach is explored.

4. The scope of the current project can be further extended to predict other aerodynamic and aeroelastic behaviours (e.g. stall margin and aeroacoustics noise) by analysing the initial mis-stagger pattern. This involves using the FSI approach adopted by this study (discussed in Chapter 2) to compute training data for machine learning models and perform regression analysis.

Chapter 6

Fan Blade Redesign to Attenuate NSV Behaviour

> All things change in a dynamic environment. Your effort to remain what you are is what limits you.
>
> Puppet Master, *Ghost in the Shell (1995)* [115].

6.1 Chapter Introduction

In the previous chapters, the focus of the study is on the identification of the vibration mechanism and passive control of the NSV behaviour. In this chapter, active NSV control through design modification is demonstrated.

As discussed in Chapter 4, the convergent-divergent covered passage geometry on Fan 2's blades, shown in Figure 6.1, is determined to be the dominating factor in forming the *NSV Transfer Window*. Additionally, it has been hypothesised that the idealised mis-stagger setup can be used for design evaluation at early design stages. Thus, in this part of the study, the design modification approach is targeted at the covered passage geometry and focused on removing the convergent-divergent nozzle inside the covered passage. Two redesigned blades with modified covered passage geometry are evaluated. It can be demonstrated through the aeromechanical comparison of the original blade (i.e. Fan 2) and the fully modified blade that such redesign approach can eliminate NSV behaviour completely. Additionally, as a by-product, the redesign approach is capable of efficient attenuation of APD behaviour. This further supports the discovery from Chapter 3 that the presence of the nozzle in the covered passage makes the APD intensity more prominent on Fan 2 than on Fan 1. Thus, a simple redesign approach targeting the NSV behaviour is investigated in this chapter in order to prove the hypothesis from the previous chapters.

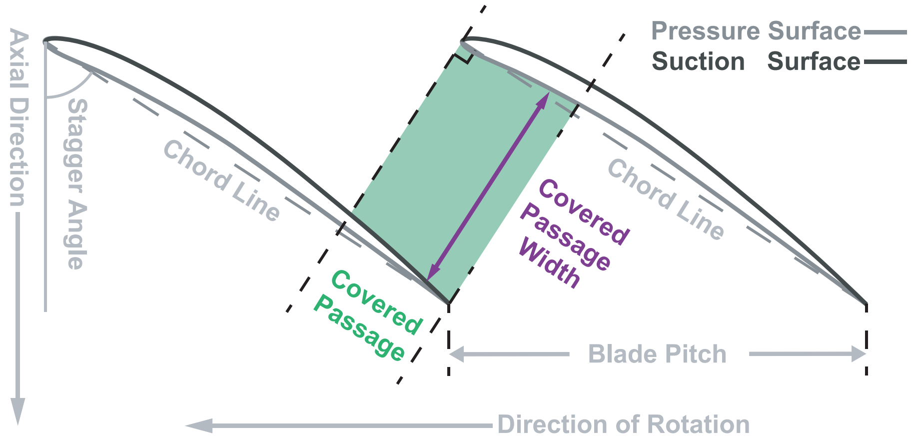

(a) Schematic diagram for covered passage geometry.

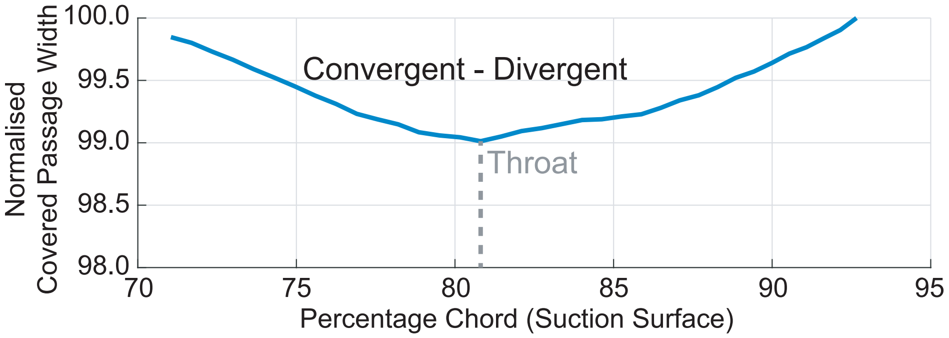

(b) Covered passage width measurement at blade tip.

Figure 6.1: Covered passage geometry of the original Fan-2 blade.

This chapter is structured as follows. The geometric modification approach embedded in the redesign method is first outlined. This is followed by the results section. The first half of the results section focuses on the changes introduced by the redesign on the nominal geometry (i.e. no geometric variability present). The second half focuses on the difference in NSV behaviour between the original design and the modified design when geometric variability is present in the fan assembly. This is succeeded by investigating the NSV attenuating mechanism leading to such differences.

6.2 Blade Redesign Approach

The discussion in Chapter 3 and 4 demonstrates strong correlation between APD & NSV behaviour and the presence of the covered passage throat. Therefore, it is reasonable to hypothesis that the NSV induced vibration can be attenuated by removing the throat from the covered passage geometry. There are infinite types of fan blade modification that can fulfil this requirement. For example, it can be achieved through changing the radial section profile of the fan blade or changing the number of blades. The objective of this transonic fan blade redesign study is to develop a simple approach to alleviate the NSV phenomenon such that it can be integrated into a more sophisticated blade design approach. Thus, minimising changes to the operating conditions is an implicit objective. To meet both criteria, the redesign method focuses on making small changes to trailing edge of the blade at high spanwise locations (i.e. close to the tip of the blade) where the NSV mechanism dominates.

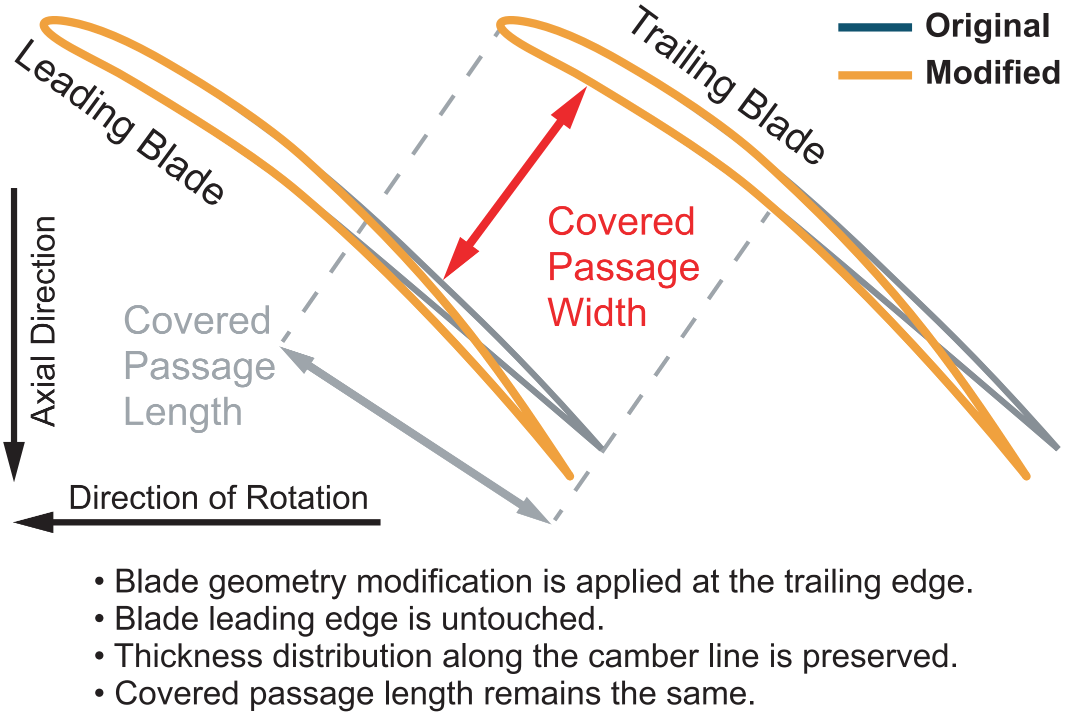

- Blade geometry modification is applied at the trailing edge.
- Blade leading edge is untouched.
- Thickness distribution along the camber line is preserved.
- Covered passage length remains the same.

Figure 6.2: Schematics for fan blade redesign approach.

The redesign method can be illustrated through the schematics in Figure 6.2. In essence, the trailing edge of the blade is ‘bent’ towards the leading blade /in the direction of rotation. As illustrated by the covered passage region in Figure 6.2, the ‘bending’ modification makes the covered passage geometry more divergent. Thus, it can change the convergent-divergent covered passage geometry into a fully divergent shape. Ultimately, it removes the controlling geometric feature for the NSV phenomenon and thus attenuates the vibratory behaviour. At the same time, the leading edge shape and the thickness distribution along the camber of the blade is unchanged. As the changes applied to the trailing edge region is sufficiently small, the corresponding changes to the covered passage length can be deemed negligible. More importantly, this preserves the incidence angle and thus minimises the change to the operating condition.

A more detailed demonstration of the method is illustrated in Figure 6.3. Firstly, the camber line of the airfoil at the span location of interest is isolated and the thickness distribution along the camber line is calculated. The variation of camber line angle, which is defined as the angle formed between the camber line and the axial direction, together with its rate of change with respect to the axial position are calculated. To modify the blade, the camber line angle's rate of change is magnified at high axial chord positions. The magnifying factor varies linearly with respect to the axial chord position. Thus, the magnifying factor is 1.0 (i.e. no change) at the start of the modification which is at low axial locations and the factor reaches the desired level at the trailing edge, thus allowing a gradual modification. In this study, the highest magnifying factor value used is 1.8. This modification to the camber line angle variation is demonstrated through Figure 6.3(b) where the deviation between the two camber lines increases along the axial direction.

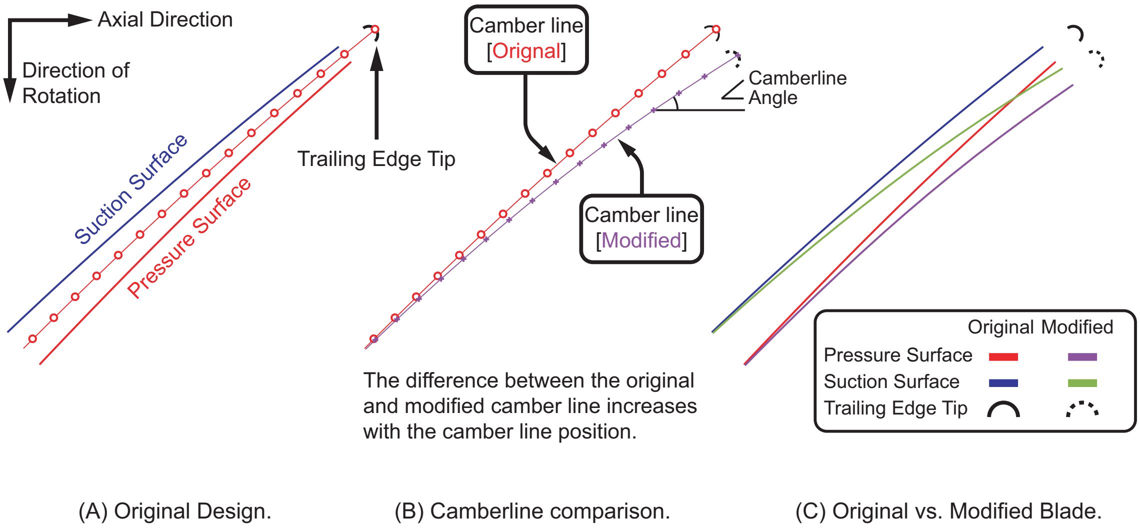

(A) Original Design. (B) Camberline comparison. (C) Original vs. Modified Blade.

Figure 6.3: Schematics for fan blade modification. Detailed view.

Once the modified camber line is determined, the original thickness distribution of the original blade is applied onto the new camber line, as demonstrated in Figure 6.3(c). Thus, the thickness distribution along the camber line is preserved. The shape of the trailing edge tip, as highlighted in Figure 6.3, is also preserved during the modification and is simply oriented clockwise by the change in the camber line angle applied to the last camber line segment. It is important to note that the incidence angle remains the same.

6.3 Results and Discussion

6.3.1 Comparison of Modified Geometries

The redesign approach is applied onto the fan blade geometry linearly from 100% span position to 80% span position with the highest level of modification applied at the tip (i.e. 100% span position) while the geometry below 80% span position remains unchanged. The effect of such modification is illustrated in Figure 6.4 where the differences in span-wise stagger variation between the original design and the two modified designs are presented. It can be observed that the linearly applied modification imposes a gradual deviation from the nominal condition from 80% to 100% span position with the maximum stagger angle change being relatively small (i.e. within the manufacturing tolerance of 1° [37]).

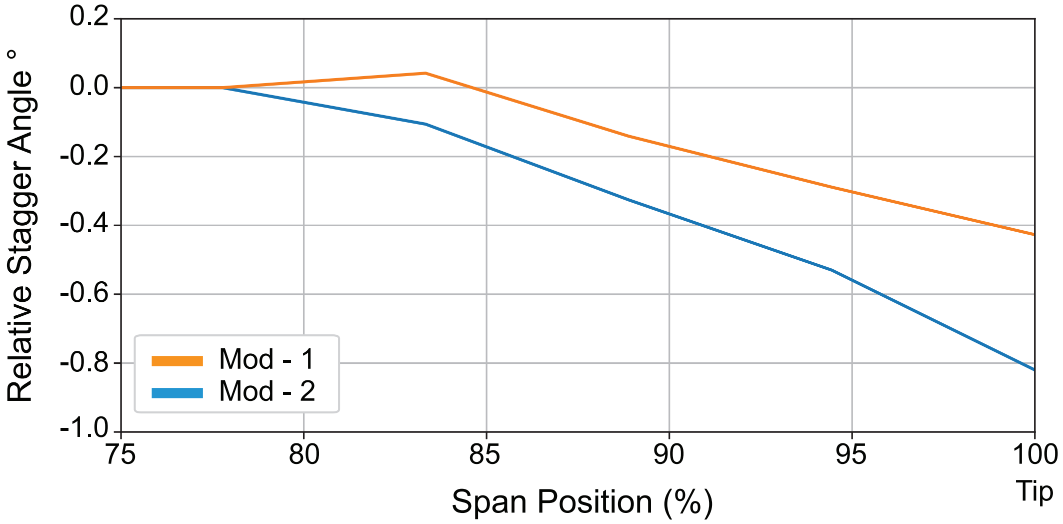

Figure 6.4: Differences in stagger angle variation (relative to the original design).

The comparison of the covered passage geometry among the three blades is presented in Figure 6.5. The covered passage widths are normalised by the maximum value on the Mod-2 blade. Evidently, it can be observed that the blade modification makes both Mod-1 and Mod-2' covered passage geometry more divergent while preserving the length of the covered passage.

On the Mod-1 blade, though the redesign effort makes the geometry more divergent, the minimum area (i.e. the nozzle) remains in the middle of the nozzle. In other words, the modification has not moved the throat out of the covered passage. Instead, the throat is only moved slightly forward towards the entrance of the covered passage and rests in-between the 75% to 80% chord position. Therefore, based on the previous understanding of APD & NSV, it can be expected that the presence of the nozzle will lead to NSV behaviour. At the same time, the forward-displaced throat allows the passage shock to be stabilised closer to entrance and hence the intensity of the APD behaviour is expected to reduce. In contrast, on the Mod-2 blade, the blade modification has achieved the intended effect of removing the throat and made the covered passage fully divergent. As will be demonstrated in the later section, as a result of the throat's absence, the NSV behaviour cannot manifest on the Mod-2 blade.

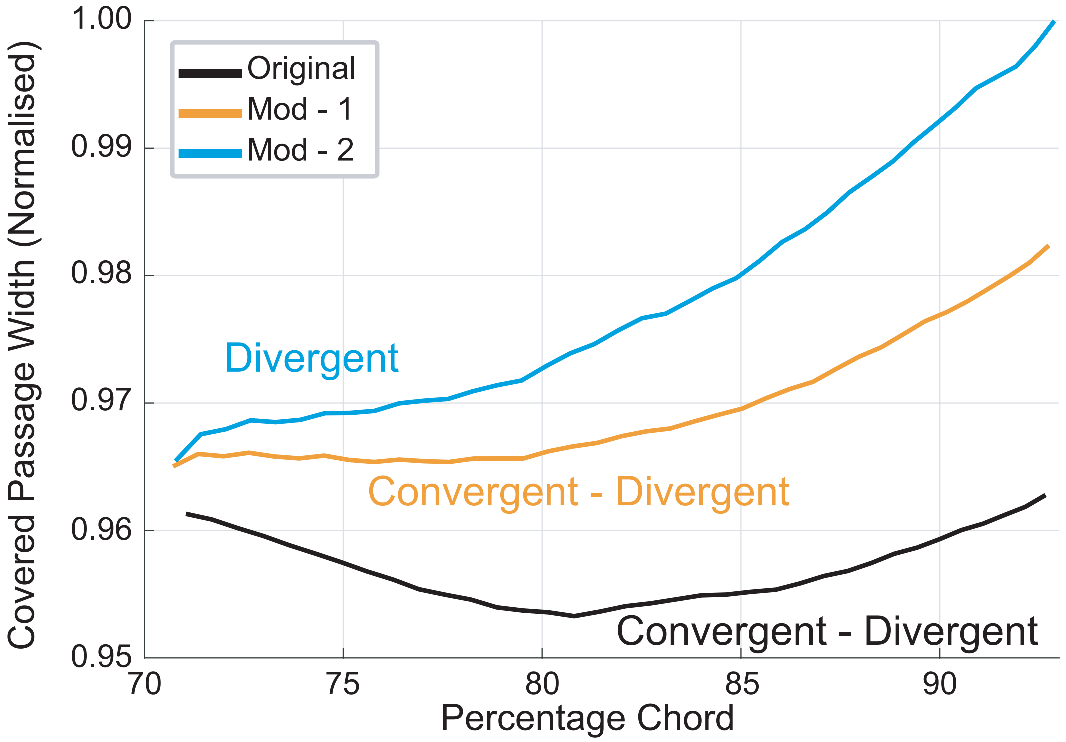

Figure 6.5: Covered passage geometry comparison for the three blade designs.

6.3.2 Comparison of Aerodynamic Properties at the Nominal Condition

Figure 6.6 shows the fan performance comparison of the three blade designs at the design speed. The results are captured using perfectly symmetric fan assemblies. Variation of pressure ratio against the inlet mass flow is shown on the left while the variation for efficiency is shown on the right. The data are normalised such that unity is used to correspond to the conditions at Mod-2's peak efficiency condition (at design speed). Unsurprisingly, the modified blades operate at different operating conditions as compared to that of the original blade. As the objective of the study is to demonstrate the redesign approach's effectiveness in NSV attenuation, the relatively small difference in the three designs' operating conditions is accepted.

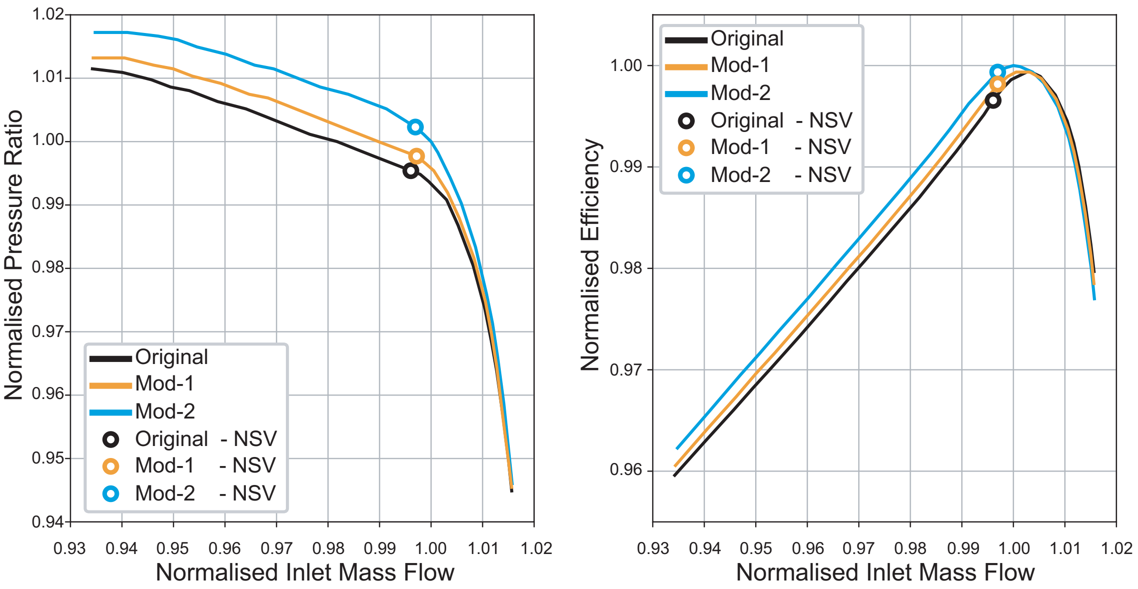

Figure 6.6: Fan map for the three blade designs.

For the original blade and the Mod-1 blade, the circles mark the operating condition where NSV behaviour is the most intense and also where the ideal APD condition is (i.e. Figure 6.7). In contrast, in the case of the Mod-2 blade, the circles only mark the operating condition with the most intense APD behaviour since NSV behaviour is not observed. These operation conditions are located using the same approaches discussed in Chapter 3 and 4. It is also interesting to point out that the blade modification introduces negligible change to the mass flow rate where the APD behaviour peaks. Results from full annulus NSV calculations at the circled conditions are discussed in the next section.

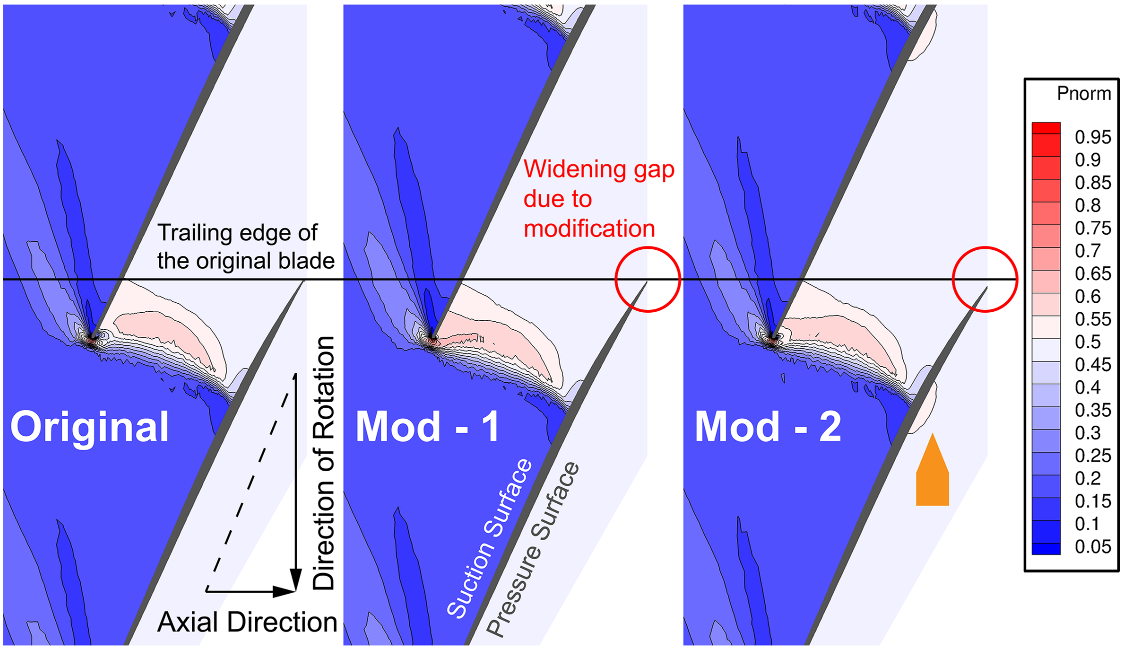

Figure 6.7: Comparison of the pressure contour plots for the three blades at their respective initial conditions.

The aerodynamic properties at the above mentioned marked locations are presented in Figure 6.7 and Figure 6.8. Figure 6.7 illustrate the normalised pressure contour at the blade tips. A line is drawn to highlight the geometric difference due to the blade modification. Evidently, the difference between the three blades is barely noticeable from the contour except the small zone with raised pressure on Mod-2 blade's pressure surface (i.e. refer to the marker in 6.7).

Further comparison of the three blade's operating condition is presented through Figure 6.8 where the pressure distributions at the blade tips are shown. Similar to the conclusion drawn about Figure 6.7, the difference in the operating conditions is small and the two modified blades do not deviate away from the original design in a significant way.

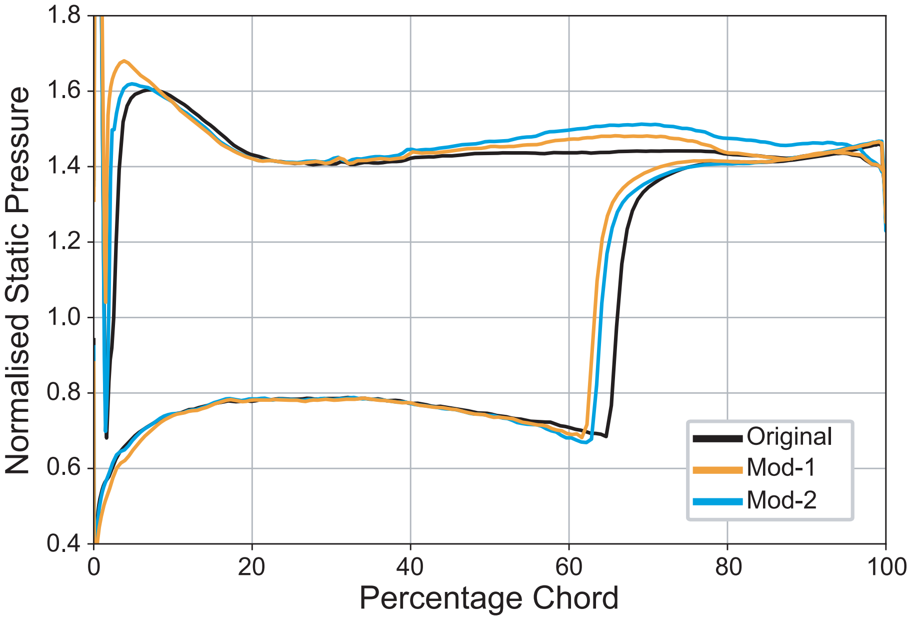

Figure 6.8: Tip loading for the three blade designs.

6.3.3 NSV Behaviour Comparison

In the presence of geometric variability, the three blades exhibit distinctly different behaviour in terms of APD and NSV.

In this redesign study, geometric variability is introduced in the same fashion introduced previously in Section 4.5.1. Single passage domain and mode shapes are expanded to a fully symmetric fan assembly first. Then the two blades polar opposite[1] to each other are mis-staggered in the same direction and with the same amplitude. To match configuration of the typical NSV case in Section 4.5.1 (i.e. the original Fan 2 blade), the two chosen blades are mis-staggered with 0.08° increase in tip stagger. The mis-staggering is applied at the centroid at each radial section in a linear fashion. Therefore, this setup is used to validate the hypothesis in Chapter 4

---

[1] Blade 4 and 17 on the 26-blade Fan 2 assembly are mis-staggered

which states the idealised mis-stagger pattern can be used for design assessmment. In the structural domain, the mode shapes are prescribed with the same arbitrary damping ratio of $\zeta = 0.05$ as that of the baseline case.

The tip stagger history plots of the three blade designs are presented in Figure 6.9. Selected results from the original blade which are previously presented in Section 4.5.1 are reproduced for clarity. Due to the symmetry of the setup, the tip stagger histories are presented for only half of the assembly and the tip stagger history for the initially mis-staggered blade (Blade 4) is shown in blue.

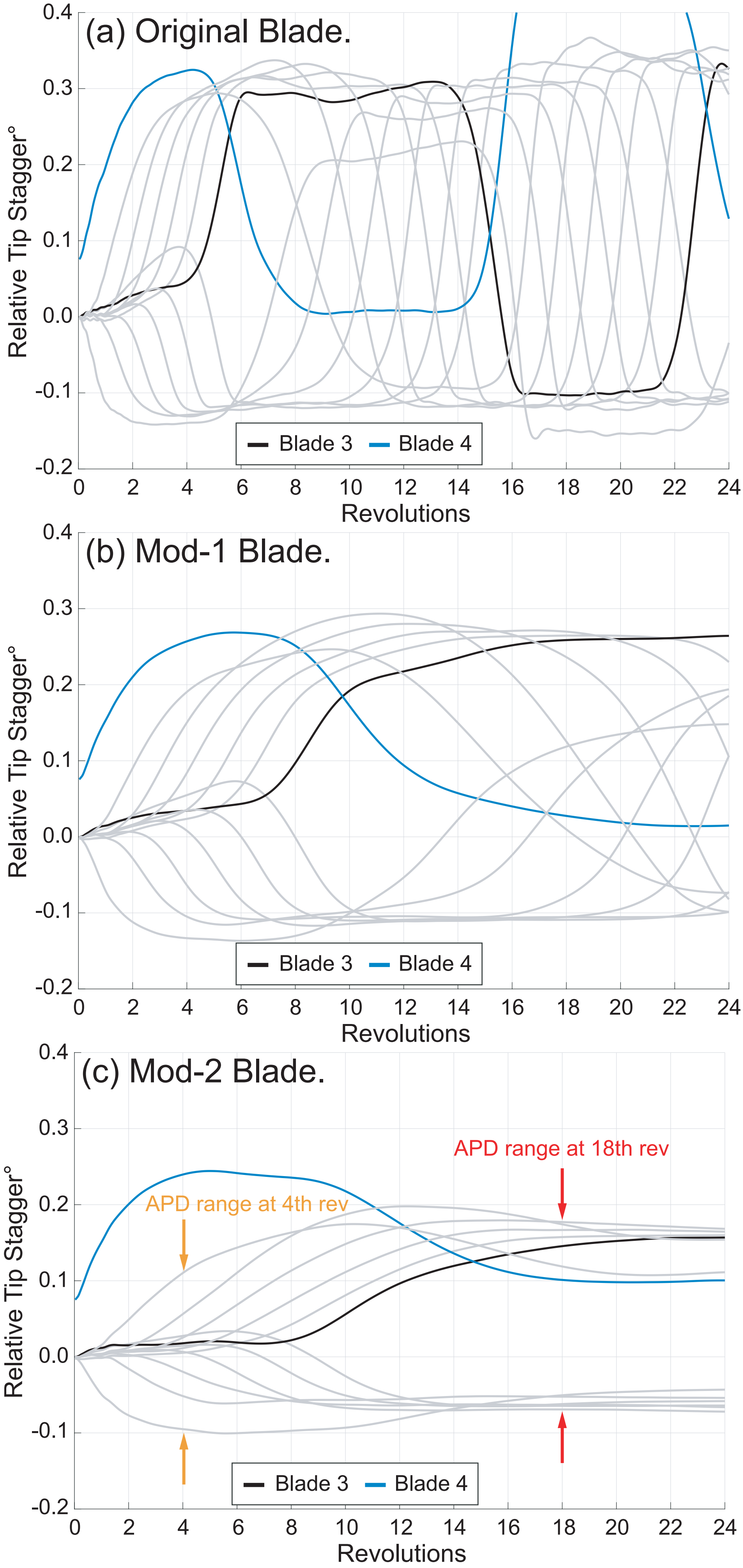

Figure 6.9: Blade tip stagger history for the original and fully modified blade.

A few interesting observations can be made from Figure 6.9. Firstly, in term of the steadiness of the plots, it is evident that both the original blade and the partially modified Mod-1 blade exhibit NSV behaviour where blades switches from the group with higher relative stagger angle to lower ones, and vice versa. In contrast, the Mod-2 blades only exhibit the initial APD behaviour and is stabilised after 20 revolutions. Secondly, by observing the range of the relative tip stagger, it is clear that the original blade demonstrates a much greater range than the two modified blade. In this part of the study, the range of relative tip staggerd in a given instant is termed the *APD range*. As annotated in Figure 6.9(c), this quantity does not take the tip stagger angle of the initially mis-staggered blade into consideration. Thus, the APD range is independent of the amplitude of the initial mis-staggering and hence can potentially be used as a factor in assessing different blade designs' APD performance. Thirdly, by tracking the time for the blades to be grouped into the two groups, one with higher tip stagger and one with lower tip stagger, the time required for the three blade designs to establish the APD behaviour can be compared. For the original blade shown in Figure 6.9(a), the APD pattern first emerges at the 6th revolution whereas the pattern only emerges in Figure 6.9(c) at approximately the 20th revolution. In essence, the time for the initial APD signal to travel around the annulus is extended after the modification. The reason behind such differences will be explained in the next section. The above observations and geometric difference of the blade designs are tabulated in Table 6.1.

Blade Design	Original	Mod-1	Mod-2
Modification	-	Partial	Complete
Covered Passage Throat	Present	Present	Removed
Max APD Range	0.52°	0.47°	0.28°
Time to form APD pattern	6 revs	12 revs	20 revs
NSV Behaviour	NSV	NSV	No NSV

Table 6.1: APD and NSV behaviour of the redesigned blades.

From the table, it can be concluded that Mod-1's behaviour falls in-between that of the other two. Consequently, the following discussion will focus primarily on the two extremes. Comparing the APD & NSV behaviour of the original blade and the Mod-2 blade, it can be deduced that the original blade is the interior design based on the discussion in Chapter 1, 3, and 4. In particular, the large APD range of the original blade makes it inferior in term of aeroacoustic noise. More importantly, the elimination of the NSV behaviour in Mod-2 can significantly alleviate the NSV-induced HCF damage to the fan blade. Furthermore, from the table, the time required to form the initial APD pattern correlates strongly with the level of modifications applied to the blade design. To be more specific, with modification, the speed of travelling disturbance has been significantly reduced and requires twice the time to form on the Mod-1 blade. This alone helps to alleviate the HCF problem introduced by NSV as it reduces the number of NSV cycles per unit time.

To conclude, the above results demonstrate that the described blade redesign technique can achieve the intended effect of attenuating the NSV behaviour, effectively eliminating it from the fan assembly. As a by-product, the redesign effort also brings the additional benefit of alleviating the APD behaviour.

6.3.4 Mechanism to attenuate NSV

The reason behind the effectiveness of the redesign approach can be explained through Figure 6.10 and Figure 6.11. The aeromechanical change associated with NSV are compared between the original blade and the Mod-2 blade through the figures. The corresponding pressure contour plots for the original blade are previously presented in Figure 4.12 and 4.13. The same plots for the Mod-2 blade are illustrated in Figure 6.12 and 6.13.

It is important to note that the time scale for the plots in Figure 6.10 is different from that in Figure 6.11. In the case of the original blade (Figure 6.10) which exhibit NSV behaviour, the aeromechanical property changes during the its NSV transfer window (i.e. from 4.75 revs to 7.50 revs) are presented. In contrast, in the case of Mod-2 blade (Figure 6.11) where the NSV behaviour is exterminated, the changes prior to its stabilised form are presented.

Absence of NSV on the Mod-2 Blade

The reason behind the original blade's NSV behaviour is explained previously in Section 4.5.1. In contrast to the original blade's response, the Mod-2 blade shows no signs of NSV and has significantly reduced APD range. These are direct results of the removal of the covered passage throat. The reasoning behind these differences can be explained clearly by isolating the steady behaviour from the dynamic behaviour.

1. **Differences in the steady behaviour:**

   As it has been demonstrated on the original blade which has a convergent-divergent covered passage geometry, the passage shock experiences a binary position change near the convergent section. Thus, to reach equilibrium, the passage shock has to be either expelled from the passage or swallowed and stabilised downstream of the throat. On the original blade, the distance between the positions is at least 10% of the tip chord length. As discussed earlier in

Chapter 3, this translates to almost 40% difference in aerodynamic moment and hence results in a significant difference in stagger angles between the two groups of blades during APD (i.e. blades with increased relative stagger and blades with decreased relative stagger).

On the Mod-2 blade, the passage shock can move smoothly inside the fully divergent covered passage instead of undergoing the binary position change described above. This reduces the difference in aerodynamic moment on the two groups of blades during APD and simultaneously removes the mechanism vital for NSV disturbance to continue. By comparing pressure distribution plots in Figure 6.10 and 6.11. i.e. (b)s and (c)s, it is evident that the removal of the covered passage throat allows the passage shocks to stabilise much closer to the leading edge. In the case of Figure 6.11(b) and (c), the passage shocks' starting position is within 10% chord length from the leading edge.

At the same time, comparing the loading conditions at blade tips between the two blade designs, it can be deduced that the difference between adjacent blades is significantly smaller for the Mod-2 blade as compared to that of the original blade. To be more specific, the distance between the pressure surface shocks on adjacent blades is below 10% chord length for the Mod-2 blade whereas it is above 15% chord length for the original blade. Thus, the convergent section of the original blade's covered passage forces the swallowed passage shock which cannot be stabilised within this region to be stabilised far away from the leading edge. In contrast, the absence of the convergent section on the Mod-2 blade reduces the distance between the swallowed shock and the leading edge. Therefore, for blades with swallowed passage shock on their pressure surface, the original design has significantly less aerodynamically induced moment than the Mod-2 blade does. Thus, as it is evident from the comparison between Figure 6.10(a) and 6.11(a), the original design exhibits higher tip stagger angle than the Mod-2 blade does. Consequently, this explains the significant difference in APD range shown in Table 6.1.

2. **Differences in the dynamic behaviour:**

   On the original blade, the unstable convergent section assists the displacement of the passage shock after it enters the section and initiates the *NSV Transfer Window* process. In the absence of this assistance, such as the case on the Mod-2 blade, it takes significantly longer time for the displaced passage shock to stabilise. In fact, from Figure 6.10 and 6.11, the number of revolutions required for Blade 4's pressure surface shock to traverse the 10% chord length is approximately 2.75 on the original blade and 14 on the Mod-2 blade. Similarly, the same reasoning holds true when examining the significant time difference required for APD condition to establish on the two designs.

As elaborated in Chapter 4, the original blade's covered passage geometry enforces the sharp transition of passage shock positions which leads to significant change in the aerodynamically induced loading. This causes the relative tip stagger angle to switch between the two extremes. As the passage shock can move smoothly inside Mod-2 blade's fully divergent covered passage, the initial disturbance to the passage shock is not amplified and only a small displacement is required for the passage shock to reach the new equilibrium. As a result, the mild change in aerodynamic moment cannot switch the relative tip stagger angle from the slightly higher values to the slightly lower ones, and vice versa. Therefore, NSV cannot manifest on the modified design.

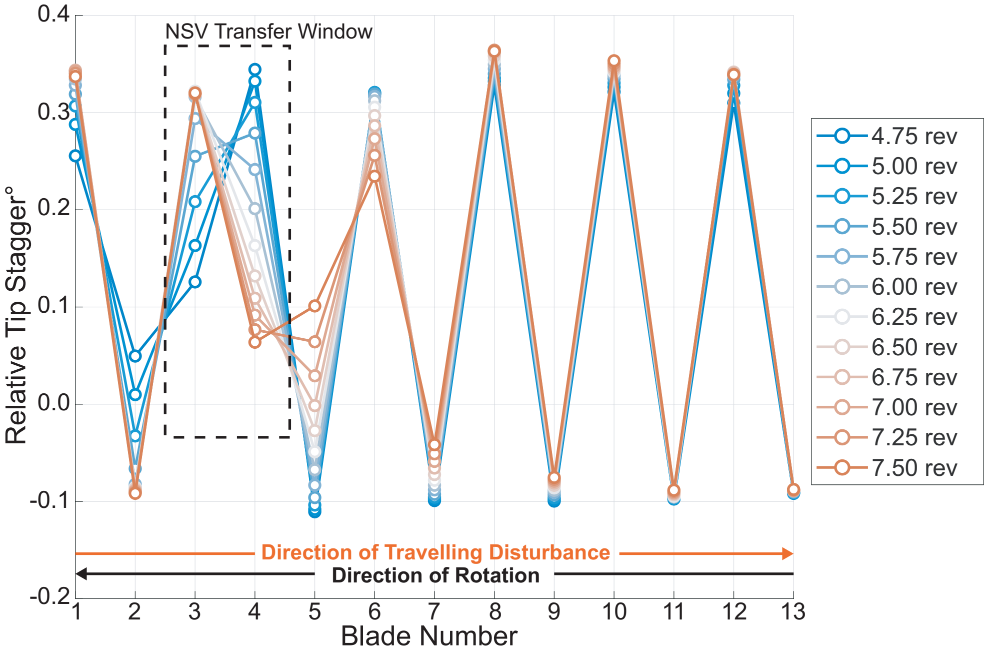

(a) Tip stagger pattern history.

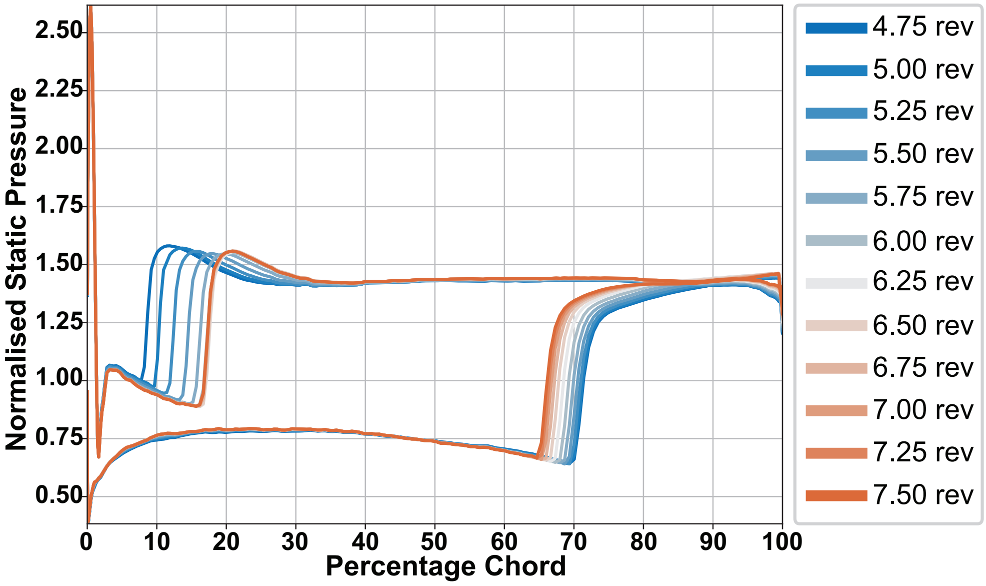

(b) Original - Blade 3.

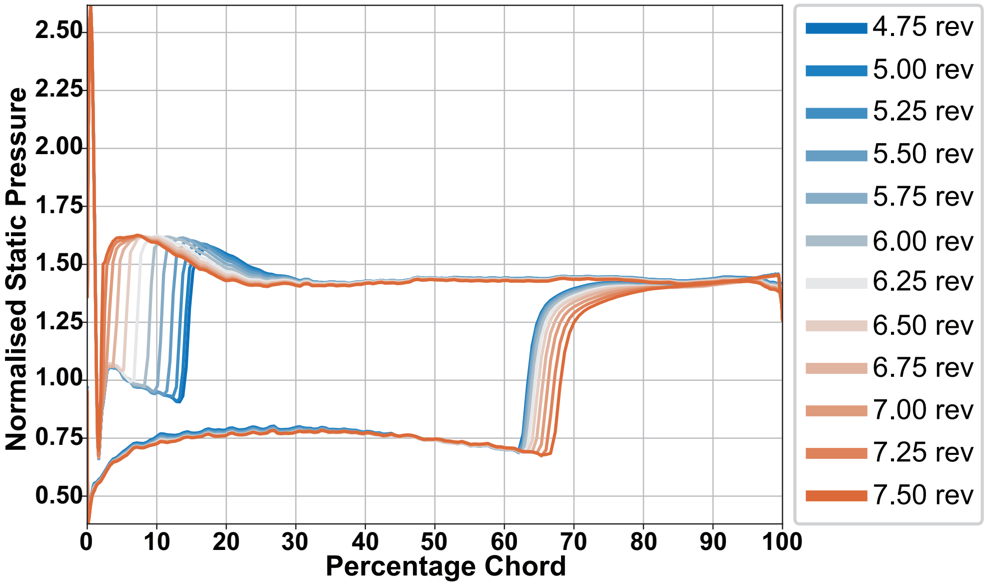

(c) Original - Blade 4.

Figure 6.10: Tip stagger and pressure distribution history for original blade during NSV transfer window. Reproduced from Figure 4.11.

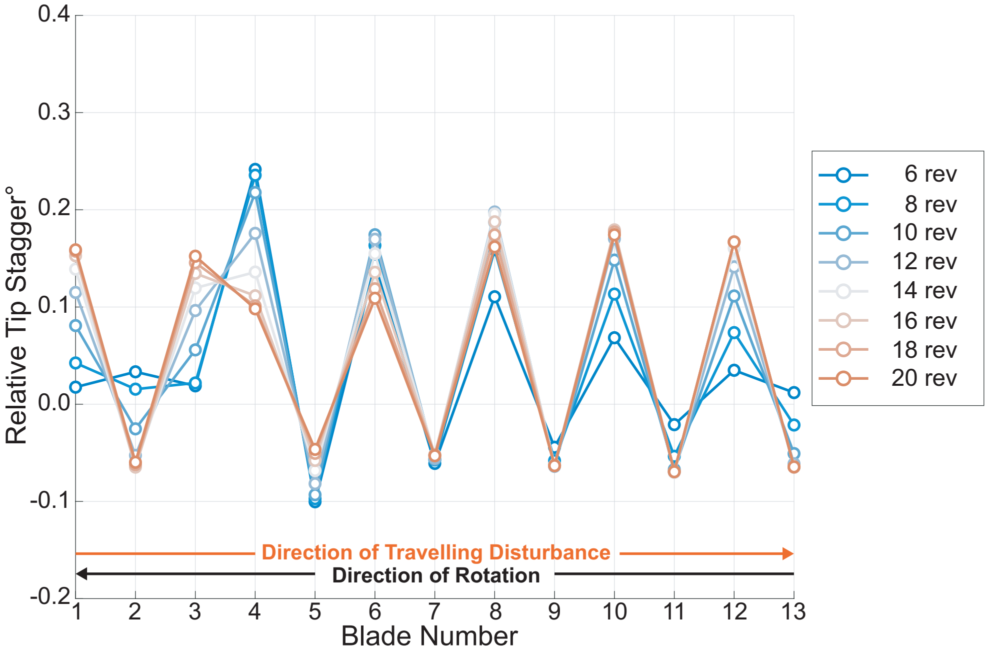

(a) [Tip stagger pattern history.

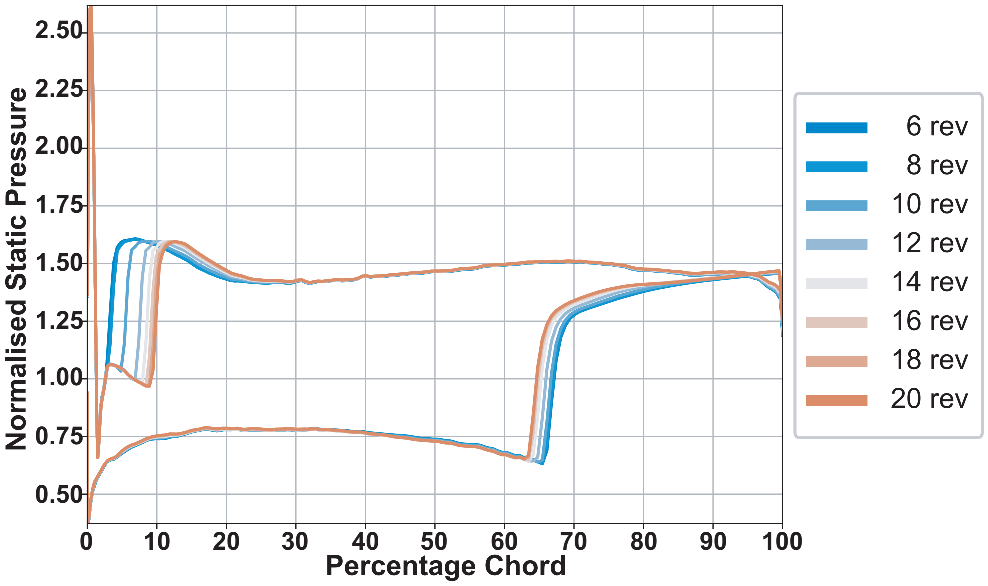

(b) Mod-2 - Blade 3.

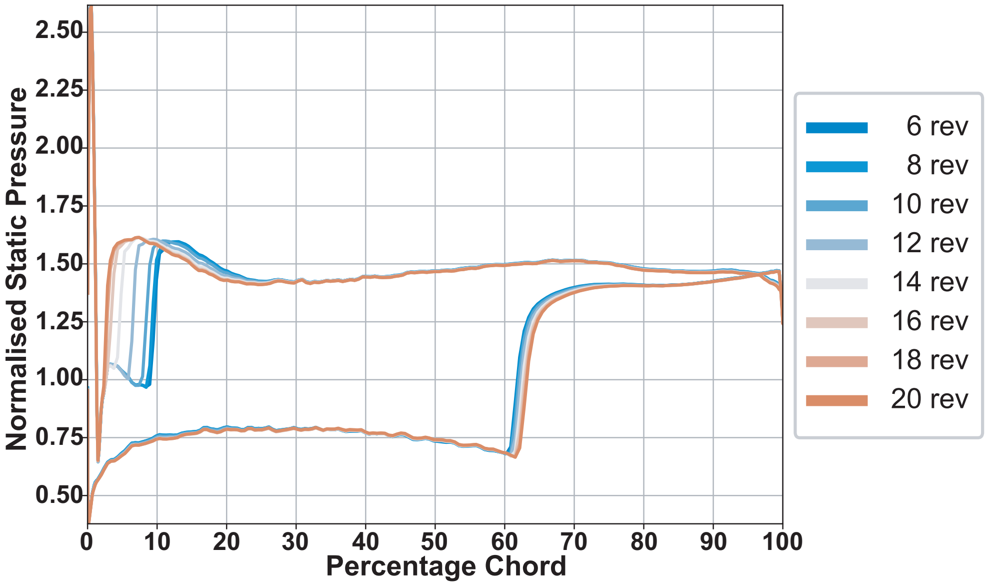

(c) Mod-2 - Blade 4.

Figure 6.11: Tip stagger and pressure distribution history for Mod-2 Blade as the NSV motion ceases.

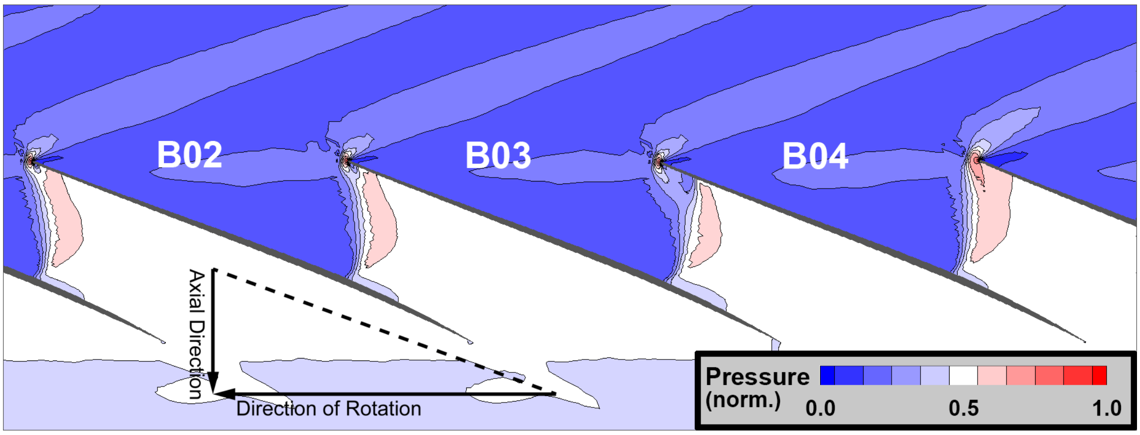

(a) At 8 revs.

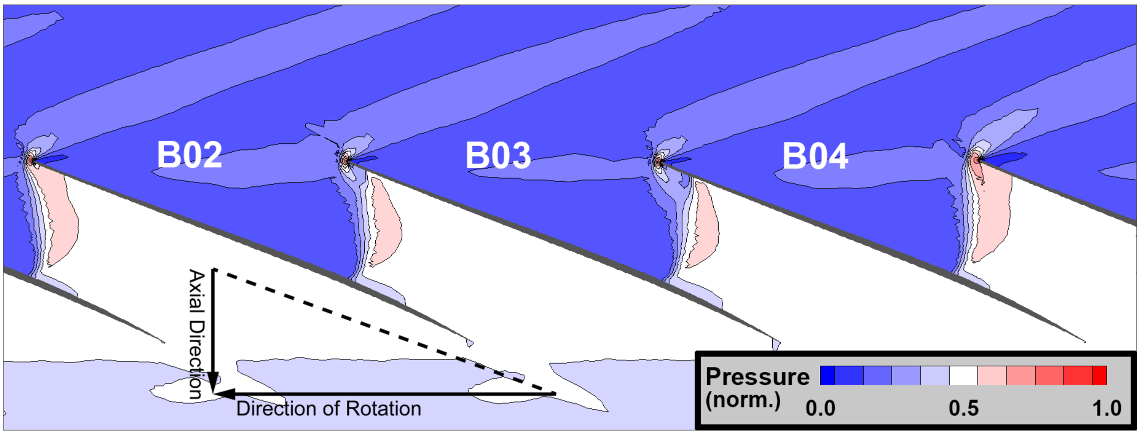

(b) At 10 revs.

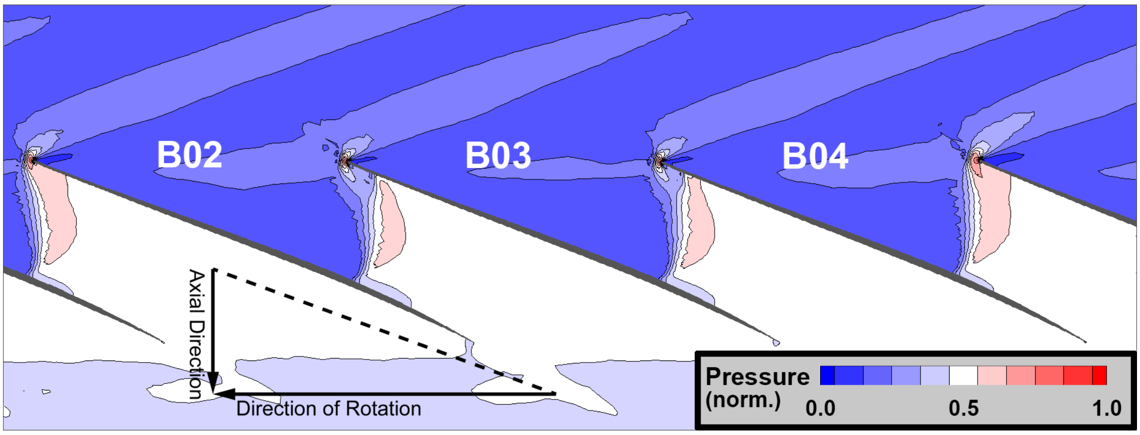

(c) At 12 revs.

Figure 6.12: Changes in pressure distribution as the NSV behaviour ceases to exist on Mod-2 Blades (from 8 revs to 12 revs).

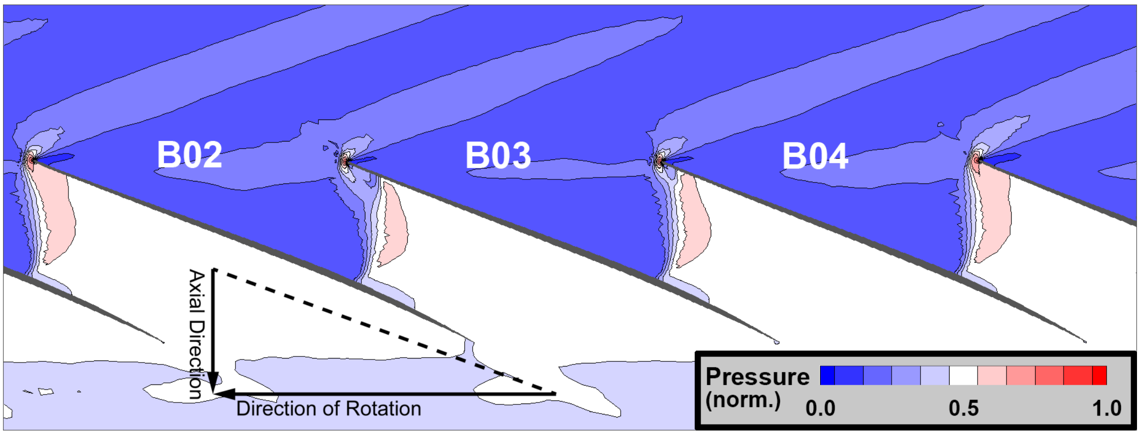

(a) At 14 revs.

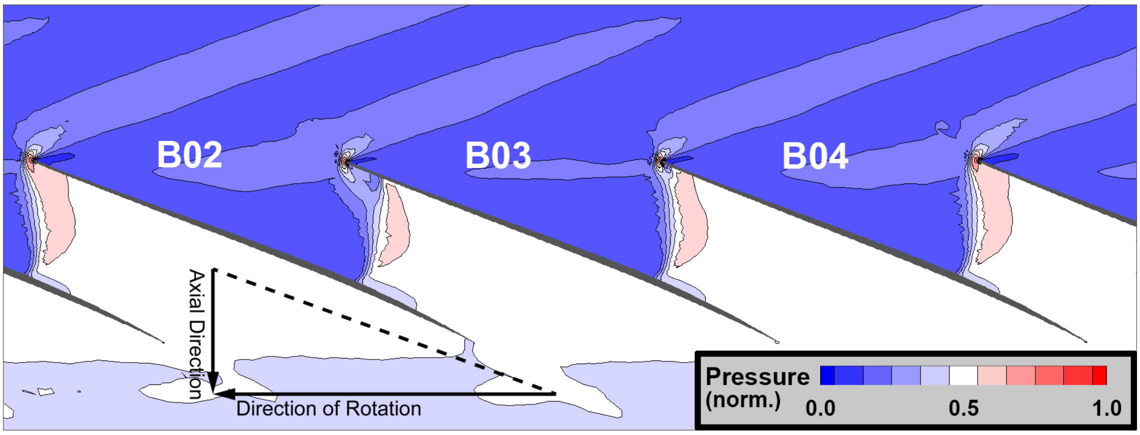

(b) At 16 revs.

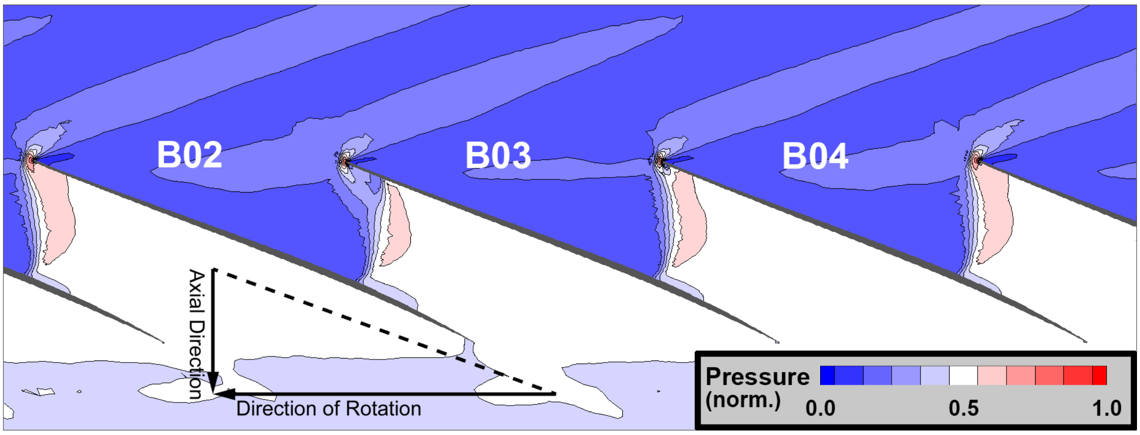

(c) At 18 revs.

Figure 6.13: Changes in pressure distribution as the NSV behaviour ceases to exist on Mod-2 Blades (from 14 revs to 18 revs).

6.4 Chapter Summary

Through the aeromechanical comparison among the blade designs, the following conclusions and future directions can be identified:

1. In Chapter 4, it was hypothesised that NSV behaviour can be assess through the idealised mis-staggering pattern with two polar-opposite blades being mis-staggered in the identical fashion. The hypothesis is validated in this chapter through the assessment of three fan blade designs. Thus, this suggests the simplified approach can be used in the early design stages to streamline the initial design and assessment process.

2. The key idea behind the proposed NSV-attenuating redesign approach is to eliminate the core geometric factor behind NSV, the covered passage throat. In this study, it is implemented through the Mod-2 blade where the throat and consequently the binary switching mechanism propelling the NSV are completely removed. The comparison between the original blade and the Mod-2 blade demonstrates that such approach is highly effective against NSV as it can no longer manifest on the Mod-2 blade. Simultaneously, this reinforce the understanding of NSV that was previously discussed in Chapter 4.

3. At the same time, by pushing the covered passage throat forward (i.e. Mod-1 blade) or by eliminating the covered passage throat (i.e. Mod-2 blade), the new equilibrium condition for the swallowed passage can be slightly closer to the leading edge. This alleviates the APD range significantly as it minimises the untwist moment difference between the two extreme APD conditions (i.e. the more opened blades and the more closed blades). Thus, the proposed redesign approach is efficient in attenuating APD phenomenon.

4. The blade geometry modifications explored in this chapter is applied in an empirical way. Thus, it would be worthwhile to use a systemic approach to isolate and quantify the effect of blade geometry changes on the final APD intensity and the speed of the APD signal around the annulus. Following the discussion in Chapter 5, it would be useful to explore whether machine learning technique can be used to map these relationships (i.e. regression).

5. Based on above discussion, it is evident that an active NSV-attenuating redesign approach is found and the approach can be used in the early design stages to streamline the process. However, it is important to note, the redesign approach presented here is only meant to be an initial approach targeting the NSV phenomenon and should be integrated into more sophisticated fan blade

design methodologies to meet other requirements (i.e. stall margin, stability limit, and performance etc.).

Chapter 7

Conclusions and Future Works

> But dreams are meaningful when you work toward them in the real world. If you merely live within the dreams of other people it's no different from being dead.
>
> Motoko Kusanagi, *Ghost in the Shell: S. A. C.* [116]

7.1 Chapter Introduction

In this chapter, the main achievements of this research are summarised and the answers to the guiding questions are presented. The findings are discussed further in the context of the civil aviation industry. Lastly, recommendations are also made regarding future works.

7.2 Conclusions

7.2.1 Summary of Thesis Achievements

The first half of the study focuses on the static APD phenomenon and has expanded the understanding of its mechanism from the previous study. The comparison of fan characteristics predicted by aeroelastic approach and the aerodynamic-only approach in Section 3.2.2 accentuate the necessity of incorporating aeroelastic coupling in fan performance and running geometry prediction. The investigation into the influence of blade stiffness and APD reveals strong correlation between the two. As can be inferred from the results, APD issue is expected to become a growing concern for longer and more flexible fan blade used in future high bypass ratio engines.

Intensity maps for the APD behaviour on two transonic fan designs have been derived through high-fidelity full annulus computations. The data from the maps reveal that the APD behaviour is most pronounced at/near the peak efficiency condition at the design speed. This proximity proves that the APD behaviour is an important design issue and hence is highly relevant to the civil aero engine industry. Evidently, it is vital to develop APD assessment methods that can be used in early design stages. Therefore, a reduced order model that can locate the worse case scenario for APD on a fan map is developed. The results from the reduced order model are then validated against those from the high-fidelity model. The reduced order model can decrease the computation resource requirement by a factor of 100 and hence is both useful and feasible for application at early design stages.

The comparison of APD behaviour between the two fan designs indicates that the throat inside the covered passage shape plays an important role in determining the amplitude of APD. To be more specific, the presence of a convergent-divergent nozzle inside the covered passage geometry provides a resting position for the passage shock rather than allowing a smooth displacement for the shock. Hence, the nozzle significantly intensifies the APD behaviour. It can also be hypothesised that removal of the nozzle can minimise the APD behaviour. The hypothesis is validated in the second half of the study.

The adverse effects of the APD behaviour are also evaluated in the study. Efficiency reduction during APD, which is of most concern to the engine designers and operators, is evaluated and the results prove that APD is strongly correlated with efficiency drop when the fan is operating at/near peak efficiency condition. In addition, given that intentional mistuning is commonly used by the industry to attenuate flutter, the interaction between intentional mistuning and APD is clarified in the study. It is proven that the intentional mistuning can introduce APD behaviour alone, without the presence of geometric variability in the fan. These further highlight the importance of APD study from the industry perspective.

NSV behaviour, which is the dynamic phase of APD, is investigated in the second half of the study. NSV behaviour is first evaluated through idealised mis-staggering patterns to gain initial insights into the vastly complex fluid-structure-interaction phenomenon. The mechanism and controlling factors are identified through the study. To be more specific, the presence of a nozzle inside the covered passage geometry present a binary switching mechanism for passage shocks, facilitating their displacement inside and out of the passages. Coupled with the in phase travelling disturbances generated by initial mis-staggering, the switching mechanism introduced NSV behaviour into the fan assembly, resulting in travelling disturbances inside the system. Consequently, the travelling disturbances can lead to high cycle fatigue issues.

As discussed in the introduction, high cycle fatigue is extremely alarming and undesirable for the engine operators. Therefore, it is important to investigate the behaviour further and develop attenuating methods for it. This objective is accomplished in two stages. Firstly, the NSV progresses onto evaluating more realistic mis-staggering patterns using machine learning techniques. This has yield both deeper understanding of the underlying mechanism for NSV and a passive attenuating methods. Secondly, a redesign approach, which serves as an active attenuating method, is attempted. Analysis from both APD and NSV study identifies the nozzle inside the covered passage geometry as an important controlling factor. Therefore, the redesign approach revolves around removing the nozzle, thus eliminating the mechanism for NSV. Additionally, the redesign method has the bonus effect of significantly alleviating APD behaviour.

Both the passive and active attenuating methods are proven effective in attenuating the NSV phenomenon. From the industry's point of view, the two methods collectively cover the entire life cycle of fan blades, both at design stage and during service. Unsurprisingly, it is evident that the methods developed can potentially lead to significant cost and risk reduction for both the fan designers and engine operators.

7.2.2 Answers

Through the data and analysis presented in the thesis, the guiding questions presented in Chapter 1 can now be addressed.

- ***Where does APD/NSV occur on the fan performance map?***

  Results presented in Chapter 3, i.e. Figure 3.12(a) and 3.12(b), show that the peak APD condition occurs where the passage shock displacement is most sensitive to changes in geometry and operating conditions. In most cases, this occurs in close proximity to the peak efficiency condition at the design speed. NSV, which is essentially the unsteady form of APD occurs at the same locations as the peak APD loci.

- ***What type of influence do APD and NSV have on performance and life expectancy of blades?***

  The discussion in Section 3.4.1 illustrates that APD can introduce performance deterioration, in terms of both efficiency and pressure ratio, through the magnified variability in the assembly. Through the travelling disturbance and the 'switching' of the mis-staggered blades, NSV can introduce the additional effect of making the fan blades susceptible to high cycle fatigue.

- ***What triggers NSV?***

  As presented in Chapter 4, with in-phase APD signals and sufficiently small initial mis-stagger amplitude, NSV behaviour can be triggered when the APD signal from an upstream source travels downstream and meet an in-phase mis-staggered blade.

- ***What is the speed /frequency of the NSV propagation around the assembly?***

  As illustrated in Figure 4.10, with the mechanical damping ratio at $\zeta = 0.05$, the blade tip stagger time history for the idealised NSV case show that the initial APD/NSV signal takes approximately 17.2 revolutions to travel around the annulus. Given its direction of travel is in the direction opposite to rotation and the data is presented in the rotor frame of reference, this translates to a propagation speed of $(1 - 1/17.2) \approx 0.942$ times the rotation speed (in the direction of rotation). Thus, it occurs just below 1EO (Engine Order) and is below the frequency of the first flapwise mode.

- ***What is the amplitude of APD and NSV (in term of stagger angle)? Is there a limit?***

  Through the data presented in Chapter 3 and 4, the maximum APD/NSV amplitude is found on Fan 2 with the range of approximately $-0.1°$ to $+0.3°$. Based on the discussion on fan blade differences in Chapter 3, it can be seen that the upper limit (i.e. positive mis-stagger for when the passage shock in the pressure surface side passage is swallowed) is set by the position of the throat within the covered passage. Additionally, the removal/modification of the convergent section inside the covered passage, as shown in Chapter 6, can significantly reduce the instantaneous mis-stagger range.

- ***What are the blade geometric characteristics that make the blade exhibit APD and NSV behaviour?***

  This question can only be answered through the collective effort from Chapter 3 and 4. Through the analysis of APD mechanism in Chapter 3, it is clear that APD is inherent in fan assemblies through the aeroelastic coupling and the inevitable geometric variability. Comparison of the fan blade designs in Fan 1 and Fan 2 reveals that the convergent-divergent covered passage geometry (i.e. a throat) can facilitate the diverging of blades into two groups and thus APD. In contrast, the blade redesign study conducted in Chapter 6 indicates that the convergent-divergent section inside the covered passage is crucial for the NSV behaviour to manifest. Therefore, it can be concluded that the throat inside the covered passage is important for both the APD and the NSV behaviour — beneficial to the former while crucial to the later.

- ***What are the controlling factors? Which of them are controllable and which of them are not?***

  Five controlling factors for NSV can be identified through the studies in Chapter 4, 5, and 6: **(1) covered passage geometry**, **(2) phasing of the initial APD signals**, **(3) relative mis-stagger amplitude between adjacent blades**, **(4) frequencies of the mode shapes**, and **(5) amplitude of APD signal of the initial mis-stagger pattern**.

  1. Covered passage geometry:

     The controllability of this parameter is highly flexible. For a fan blade in early design stages, this parameter can be considered as controllable. However, the ultimate decision depends on whether the alternative designs with the convergent-divergent section come with aeromechanical benefits and how the fan blade designers compromise and balance these factors. In essence, it can be deemed to have limited controllability at this stage.

     Alternatively, for a finalised fan blade design, this factor is not controllable in the short term at all. The only solution to attenuate NSV at this stage is either to adopt the passive NSV control explored in Chapter 5 or to redesign the fan blades as demonstrated in Chapter 6.

  2. Phasing of the initial APD signals:

     In the idealised NSV case presented in Chapter 4, two APD signal of equal strength originate from the symmetrical setup. In this case, the phasing of initial APD signals can be quantified through the passages between the initially mis-staggered blades. However, due to the complex evolution of NSV within a randomly mis-staggered assembly, it is difficult to determine the phasing of APD signals and therefore it is justifiable to conclude that the APD signal phasing is not controllable except in the idealised case.

3. Relative mis-stagger amplitude between adjacent blades:

   This is a fully controllable parameter. The easiest arrangement to avoid NSV is to arrange them in alternating pattern. However, as illustrated through the results in Figure 3.13, this arrangement tends to receive a high performance penalty.

4. Frequencies of the mode shapes:

   As demonstrated by the results from Chapter 3, APD behaviour increases with decreasing modal frequencies. The frequencies of the mode shapes can be effectively controlled by adding/removing mass from the tip of the blade. However, this might also result in changes in the mode shapes and performance penalties.

5. Amplitude of APD signal of the initial mis-stagger pattern:

   Similar to the previous one, this parameter can be controlled. In fact, it is interconnected with the blade-to-blade relative mis-stagger amplitude—a zig-zag mis-stagger pattern is correlated with a strong APD signal. Therefore, based on findings revealed by the machine learning classifiers in Chapter 5, the best approach would be to optimise the two parameters simultaneously while minimising the performance penalty.

7.3 The Importance of APD: An Industry Perspective

The discussion on APD in this chapter up to this point focuses on examining it as a physical phenomenon. Here the conversation transitions into investigating its implications through an industry perspective. Three findings that are of most concern to the industry are listed here:

1. The study conducted in Chapter 3 yields the conclusion that APD behaviour occurs in close proximity to the peak efficiency point in general. This behaviour sets it apart from other types of aeroelastic instabilities, which generally occur at/near stability boundary (i.e. off-design conditions), as shown in the schematics in Figure 7.1[1]. Thus, its nature of being a design point problem alone is sufficient to make understanding of such behaviour a top priority for

---

[1] Reproduced from Figure 1.12 for clarity.

engine manufacturers. More importantly, given that unsteady APD /NSV can lead to high cycle fatigue near /at the design point at which the fans are expected to be operating most of the time, it is evident that the fan designers should conduct the assessment of this behaviour first before moving onto other types of off-design instabilities such as forced response (which can be easily removed with the aid of a Campbell diagram).

2. The majority of gas turbine engines used for civil aviation, with the exception of the Olympus engine used for Concorde Supersonic Transport [35], have a fixed exhaust nozzle and hence the working line in Figure 7.1 only meet the loci of peak efficiency at the design speed. Thus, the absence of Variable Area Nozzle (VAN) [117] prohibits the fan from adjusting its operating point along the constant speed line. By following such relationship and mapping dummy working line onto the APD contour maps obtained in Chapter 3, as shown in Figure 7.2 and 7.3, it can be inferred that the APD behaviour during operation would be distinctly different for the two fans.

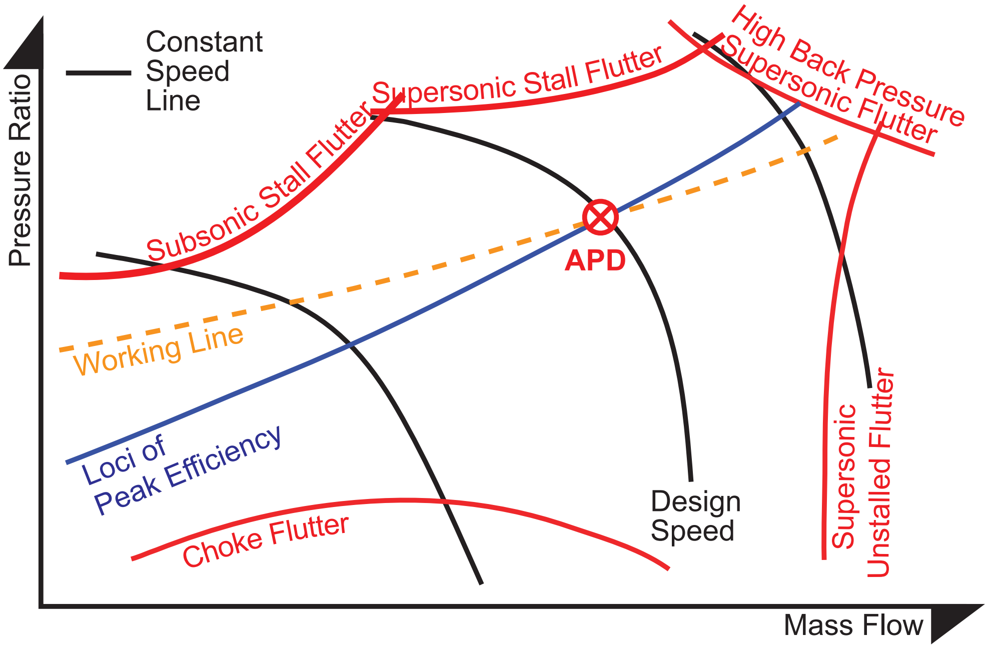

Figure 7.1: Aeroelastic instability boundaries on a fan map.

In the case of the swept blade (i.e. Fan 1), where the peak APD conditions occurs at higher mass flow rate than the peak efficiency condition on the same constant speed line, the peak APD condition and the working line intersect at speed above the design speed. In contrast, for Fan 2, the crossing at lower speed due to the reversed relative position between peak efficiency condition and peak APD condition. In other words, during operation, the actual worst case APD for Fan 1 occurs above design speed while Fan 2 experiences it at lower speed. It is more desirable to encounter the point of interception at lower speed than at higher ones since the lower aeroelastic coupling effect will limit the APD behaviour intensity. This discovery brings both a challenge and an opportunity for APD study.

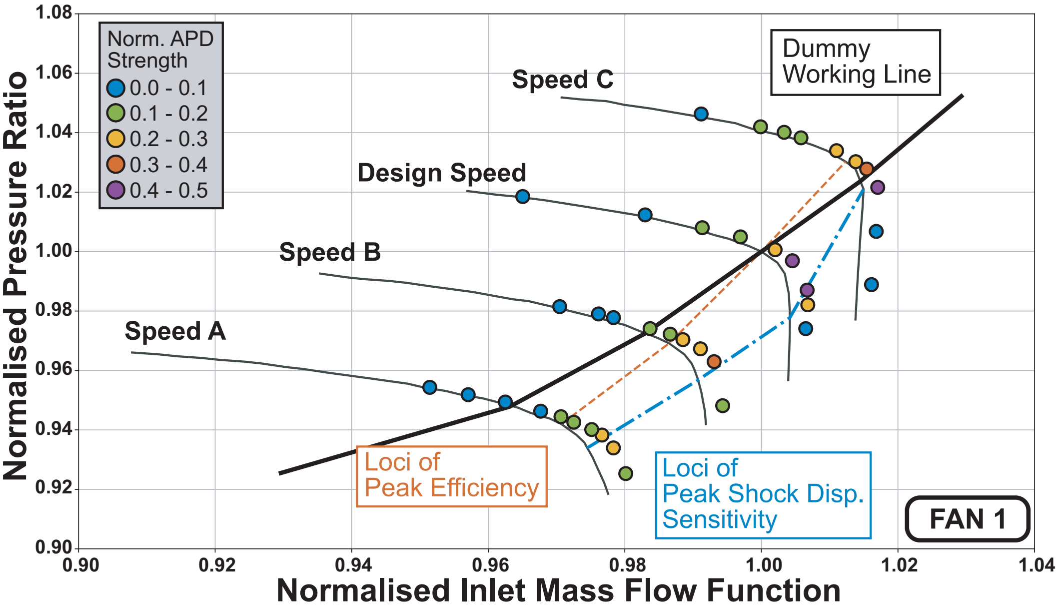

Figure 7.2: APD contour for Fan 1.

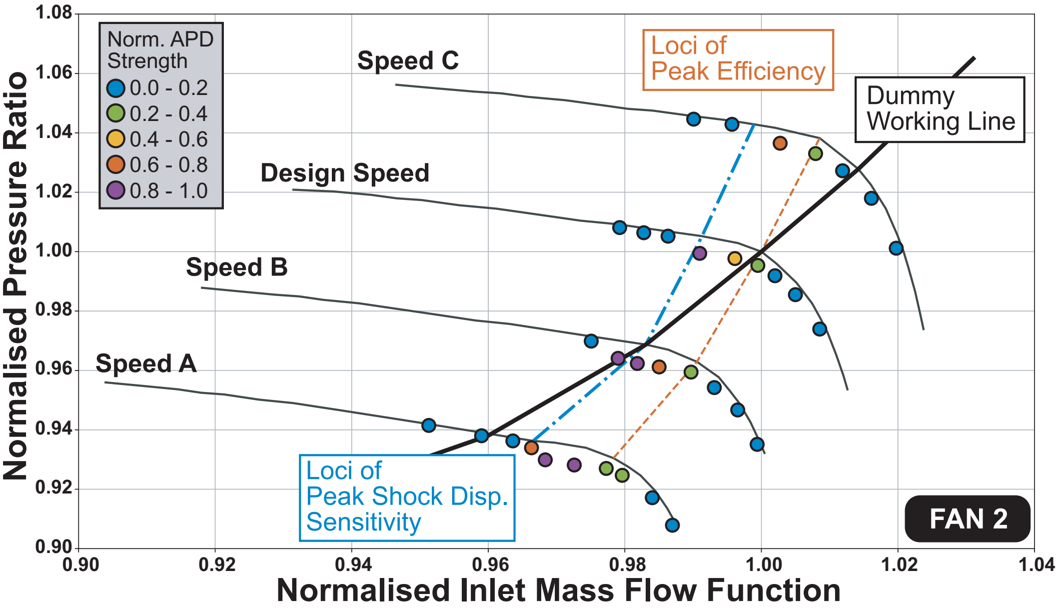

Figure 7.3: APD contour for Fan 2.

Firstly, this discovery means the fan designers need to take the relative position of working line into account when performing APD & NSV assessment for fan blade designs. Inevitably, this raises the level of complexity involved. At the same time, the previous discussion in Section 3.3.2 implies that the reduced order approach which allows the peak APD loci to be revealed without computationally intensive calculations can help locate the intersection point between the working line and the peak APD loci. Thus, it allows the fan designers to estimate the speed where the worst APD behaviour occurs during operation and thus can prioritise computation effort accordingly. Assessment of the full working line is beyond the scope of this study and hence the discussion ends here.

3. The discussion above is based on the simplified view where the working line behaves as a thin 'line' on the fan map and APD occurrence on a constant speed line is only of concern at its peak intensity condition.

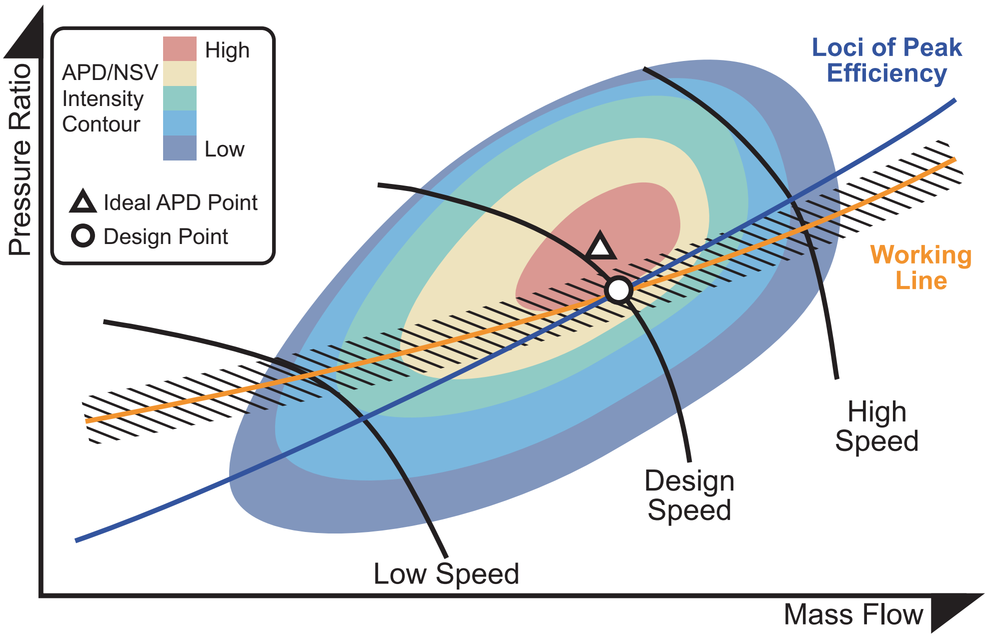

Figure 7.4: Interaction between working line and APD intensity contour.

In reality, the inherent transient behaviour and uncertainty during operation means the working 'line' will behave like a band on the fan performance map such as the one shown in Figure 7.4. In other words, the fan's operating point will swing back and forth between loci of high APD behaviour and those of low intensity. As such, the gradient of the APD contours also becomes important when conducting APD assessment on a fan blade design.

7.4 Future Works

From the jet engine manufacturers' perspective, given the importance of the phenomena, it is vital for the assessments and optimisation work to be incorporated into the existing fan blade design workflow. Though the study has sufficiently addressed the guiding questions, the research into APD & NSV is not yet exhaustive with many uncharted territory left to explore. Further research is required to help construct a more comprehensive understanding fo APD & NSV. Below is a list of research areas that may help to bridge the gap between the theoretical understanding of the phenomena and their physical implications.

- **Inlet distortion**

  Due to the novelty of the APD & NSV study, the inlet condition is confined to be axisymmetric to reduce the number of variables under investigation. Thus, the effect of asymmetrical inlet condition (i.e. introduced either by inlet distortion [118–120] or by the asymmetric engine intake) is not explored in this study.

  In the computations conducted in this study, the axisymmetric inlet condition keeps all the blades/passages operating at exactly the same operating condition prior to APD. However, during operation, the inevitable inlet distortion will force a few blades to work at operating conditions away from that of the rest at any given instant in time. From the understandings gained in Chapter 3 and 4, the ideal starting operating conditions for APD & NSV is relatively narrow on a constant speed line and this segregation of operating conditions can potentially inhibit the initiation/propagation of NSV.

  With inlet distortion, e.g. the asymmetric inlet pressure distribution shown in Figure 7.5, the blades are divided into two groups instantaneously: (1) those operating at/near the ideal APD condition (i.e. in the clean flow region) and (2) the rest of the assembly (i.e. in the 'dirty' flow region). The effect of such segmentation has two folds. Firstly, when the blades rotate and transit between the two states, the operating condition difference makes the blades at either side of the operating condition interface (i.e. Marker 1 in Figure 7.5(b)) adopt different stagger pattern. Thus, the transition inherently leads to mis-staggering in the assembly which can serve as trigger for APD.

  Secondly, in contrast to the case with axisymmetric inlet condition and all the blades are operating at /near ideal APD condition, the lack of symmetry prohibits the propagation of APD signal from being carried into the zone with unfavourable conditions. In the schematics in Figure 7.5(b), this means when the signal from the upstream of Marker 2 enters (clockwise) the distorted region, the unfavourable operating condition prevent the passages from transmitting the signal further.

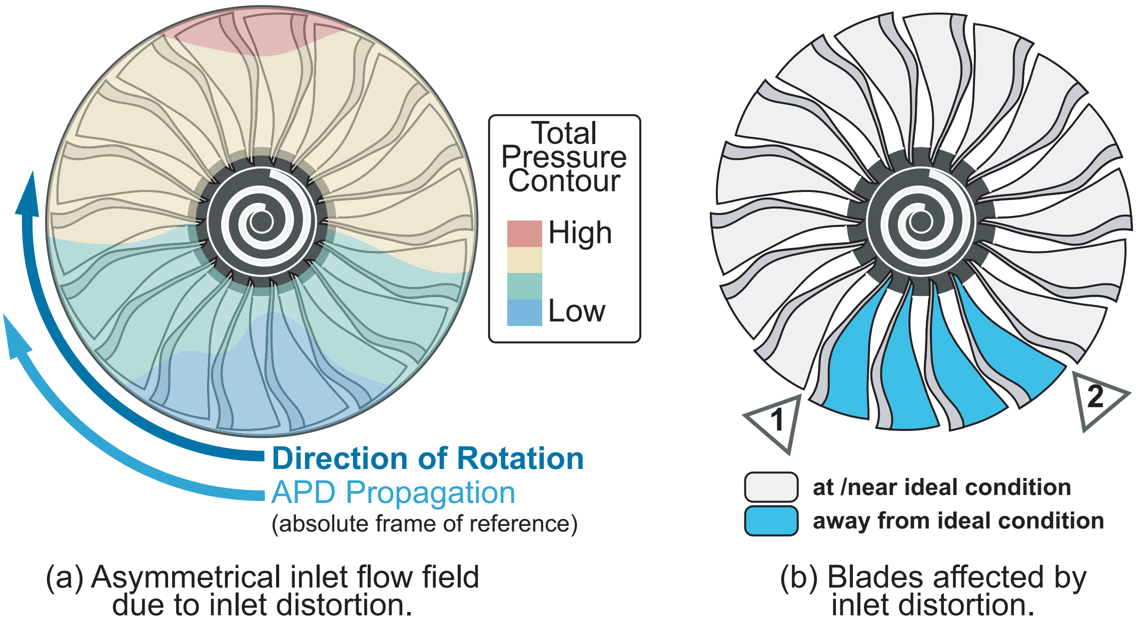

(a) Asymmetrical inlet flow field due to inlet distortion.

(b) Blades affected by inlet distortion.

Figure 7.5: Effect of Inlet Distortion on APD.

As discussed earlier, the NSV signal has a period of approximately 17.2 revolutions[2]. This is significantly longer than the time required for a blade to traverse the clean flow region (i.e. from Marker 1 to Marker 2 clockwise in Figure 7.5(b)). Thus, when mis-staggering is introduced at Marker 1, the resulting NSV signal can only influence a few passages before the blade rotation moves it into the 'dirty' region. Based on the above discussion of the two effects, it can be hypothesised that the NSV signal cannot propagate in the annulus since the distorted region will force the passages to operate in a condition unfavourable for NSV, thus terminating the NSV signal.

The underlying assumption of the above hypothesis is that the distorted region can shifts the operating condition of the blades under influence sufficiently away from the ideal APD conditions. It is expected that the extent of the required distortion is highly correlated with the APD contour (e.g. Figure 7.4). Additionally, it is expected that the required distortion will be influenced by the time a blade is inside the distorted zone. Thus, the investigation of the hypothesis is highly worthwhile as it will expand the understanding of both APD and inlet distortion.

- **Machine learning assisted blade design approach**

  In Chapter 5, novel machine learning techniques are incorporated into the study for vibration classification and the predicting capability is proven to be

---

[2] With mechanical damping ratio at $\zeta = 0.05$. Refer to Figure 4.10 for further details.

more than satisfactory. To be more specific, a statistical approach (i.e. supervised learning) is used to analyse known cases and map the stagger patterns' characteristics to their corresponding NSV behaviour. The trained decision tree classifier can identify the key NSV-inducing features and helps to eliminate stagger patterns prone to vibration.

In Chapter 6, a basic redesign approach focusing on the covered passage geometry is proven useful in alleviating the APD behaviour. Through a series of empiricist redesign effort, a new fan blade design is found and its APD behaviour is reduced[3] to 54% of the original design's.

Therefore, it becomes natural to question whether the two techniques can be coupled to optimise fan blade shapes such that the amplitude of APD (i.e. the APD range in Figure 6.9) can be reduced in operation. Therefore, it would be useful to derive design features, such as covered passage width rate of change, from a database of modified blade designs and map them onto their corresponding APD range values, thus developing APD-oriented redesign approach with machine learning regression technique. Eventually, it can be integrated into more sophisticated design guidelines to meet other requirements (i.e. efficiency and aerodynamic stability).

- **APD & NSV at cruise altitudes**

  As explained earlier in Chapter 2, all the calculation are performed at the Sea-Level-Static conditions such that the fan blades experience the maximum possible aerodynamic loading. Thus, this study is primarily concerned with capturing the worst case scenario.

  From the engine operators' perspective, the operating condition of most concern is at the cruise altitudes where the engine operates at most of the time. Given the current trend of increasingly long and light fan blades, where the influence from aerodynamics increases with respect to inertial effects, it is not yet certain whether the reduced ambient pressure and air density at the cruise altitudes could magnify the initial geometry non-uniformity to a noticeable extent and make the fan exhibit APD & NSV behaviour. Additionally, the working line at cruise altitude differs from that of the Sea-Level-Static condition and this adds complexity to the analysis. Therefore, further study in altitude effects would provide substantial insights to the fan designers and is thus of significant relevance to the aviation industry.

  Additionally, it is useful to investigate the influence of altitude over APD &

---

[3] In term of the APD range. Detailed data can be found in Table 6.1.

NSV and to determine at which altitude the phenomena becomes completely negligible. This would offer guidance to the fan designers to avoid the onset of APD & NSV when the aircraft is in a holding pattern (i.e. lower altitude than at cruise conditions [121]).

- **Aeroacoustics of APD & NSV**

  Continuing from the buzz-saw noise discussion in Chapter 1, it is natural for the research to progress into studying APD-induced aeroacoustics. However, in order to capture the axial and circumferential acoustic modes, the mesh density has to be improved from approximately 1.2 million points per passage to approximately 19.6 million points per passage [122, 123]. Though feasible with the current aeroelastic solver, the colossal computation requirement for APD and aeroacoustics calculations voids the cost viability of this study. Nonetheless, it is useful for the fan designers to assess the influence of NSV's travelling disturbances over buzz-saw noise numerically once the computation requirement can be fulfilled.

- **A more accurate yet still practical structural model**

  As discussed in Chapter 2, there is untapped potential for improving the accuracy and meticulousness of the computation in the structural domain. The current structural model for the static untwist analysis is deemed fit for the core purpose of this APD & NSV path-finding study and more accurate structural models should be adopted for future studies. However, given that the NSV calculations are computationally demanding[4], it is important to keep the computational requirement practical for engineering application while pursuing more complex and accurate structural computation techniques, rather than adopting a doctrinaire approach.

---

[4] The NSV cases analysed in Chapter 4 require tens of thousands CPU hours per case.

Bibliography

[1] Hadfield, C., 2013. *An Astronaut's Guide to Life on Earth.* Pan Macmillan.

[2] International Civil Aviation Organization, 2019. Civil Aviation Statistics of the World and ICAO staff estimates. Air trasnport, freight (million ton-km). https://data.worldbank.org/indicator/IS.AIR.GOOD.MT.K1 [Online. Accessed: 2019-05-11].

[3] International Civil Aviation Organization, 2019. Civil Aviation Statistics of the World and ICAO staff estimates. Air trasnport, passengers carried. https://data.worldbank.org/indicator/IS.AIR.PSGR [Online. Accessed: 2019-05-11].

[4] European Commission, 2013. Annual Analyses of the EU Air Transport Market 2012. https://ec.europa.eu/transport/sites/transport/files/modes/air/internal_market/observatory_market/doc/annual-2012-summary.pdf [Online. Accessed: 2019-05-11].

[5] Rolls-Royce Holdings plc, 2018. 2018 Annual Report.

[6] Cooper, T., Reagan, I., Porter, C., and Precourt, C., 2019. Global Fleet and MRO Market Forcast Commentary 2019-2029. Oliver Wyman.

[7] Rolls-Royce Holdings plc, 2015. 2015 Annual Report.

[8] Rolls-Royce Holdings plc, 2016. 2016 Annual Report.

[9] Rolls-Royce Holdings plc, 2017. 2017 Annual Report.

[10] Grous, A., 2018. Global Fleet and MRO Market Forcast Commentary. London School of Economics and Political Science.

[11] Whurr, J., 2013. Future Civil Aeroengine Architectures and Technologies. Rolls-Royce plc. http://www.etc10.eu/mat/Whurr.pdf [Online. Accessed: 2019-05-09].

[12] Cumpsty, N., 2019. Private Communication. London, United Kingdom.

[13] GE Aviation, 1995. GE90 Fact Sheet. https://www.geaviation.com/press-release/ge90-engine-family/ge90-fact-sheet [Online. Accessed: 2019-05-08].

[14] GE Aviation, 2001. GE90-115B Fan completing blade testing; On schedule for first engine to test. https://www.geaviation.com/press-release/ge90-engine-family/ge90-115b-fan-completing-blade-testing-schedule-first-engine-test [Online. Accessed: 2019-05-08].

[15] GE Aviation, 2013. The GEnx Commercial Aircraft Engine. https://www.geaviation.com/commercial/engines/genx-engine [Online. Accessed: 2019-05-08].

[16] MTU Aero Engines, 2018. GP7000 Turbofan Engine. https://www.mtu.de/fileadmin/EN/7_News_Media/2_Media/Brochures/Engines/GP7000.pdf [Online. Accessed: 2019-05-08].

[17] MTU Aero Engines, 2014. CF6. https://www.mtu.de/engines/commercial-aircraft-engines/widebody-jets/cf6/ [Online. Accessed: 2019-05-08].

[18] Pratt & Whitney, 2003. Pratt & Whitney's JT9D. http://newsroom.pw.utc.com/download/ce_jt9d_fact.pdf [Online. Accessed: 2019-05-08].

[19] Pratt & Whitney, 2003. Pratt & Whitney's PW4000 112-inch-fan. http://newsroom.pw.utc.com/download/ce_pw4000_112_fact.pdf [Online. Accessed: 2019-05-08].

[20] Pratt & Whitney, 2009. PW4000-100" Engine Product Card. http://newsroom.pw.utc.com/download/ce_pw4000_100_pCard.pdf [Online. Accessed: 2019-05-08].

[21] Charles Alcock, 2013. GE Pushes Envelope With GE9X for New Boeing 777. https://www.ainonline.com/aviation-news/air-transport/2013-06-16/ge-pushes-envelope-ge9x-new-boeing-777 [Online. Accessed: 2019-05-08].

[22] Safran Aircraft Engines, 2002. Commercial Aircraft Engines CFM56-5B. https://www.safran-aircraft-engines.com/sites/snecma/files/fiche_cfm56-5b_ang.pdf [Online. Accessed: 2019-05-08].

[23] Rolls-Royce plc, 2007. Civil Aerospace. https://web.archive.org/web/20071023084910/http: /www.rolls-royce.com/media/packs/200702-civilaerospace.pdf [Online. Accessed: 2019-05-08].

[24] Rolls-Royce plc, 2015. Trent 800. https://www.rolls-royce.com/~/media/Files/R/Rolls-Royce/documents/ civil-aerospace-downloads/trent-800-infographic.pdf [Online. Accessed: 2019-05-08].

[25] Rolls-Royce plc, 2015. Trent 900. https://www.rolls-royce.com/~/media/Files/R/Rolls-Royce/documents/ civil-aerospace-downloads/trent-900-infographic.pdf [Online. Accessed: 2019-05-08].

[26] Rolls-Royce plc, 2017. Trent 1000. https://www.rolls-royce.com/~/media/Files/R/Rolls-Royce/documents/ civil-aerospace-downloads/280717-Trent\%201000\%20infographic.pdf [Online. Accessed: 2019-05-08].

[27] Rolls-Royce plc, 2018. Trent XWB. https://www.rolls-royce.com/~/media/Files/R/Rolls-Royce/documents/ civil-aerospace-downloads/trent-xwb-infographic.pdf [Online. Accessed: 2019-05-08].

[28] Rolls-Royce plc, 2017. The Rolls-Royce Trent 7000 engine. https://www.airbus.com/content/dam/corporate-topics/publications/ backgrounders/RollsRoyceTrent7000factsheet.pdf [Online. Accessed: 2019-05-08].

[29] Clean Sky, 2018. The UHBR engine flight testing programme gathers momentum. https://www.cleansky.eu/ the-uhbr-engine-flight-testing-programme-gathers-momentum [Online. Accessed: 2019-05-08].

[30] Norris, G., 2014. Rolls-Royce Details Advance And UltraFan Test Plan. https://aviationweek.com/commercial-aviation/ rolls-royce-details-advance-and-ultrafan-test-plan [Online. Accessed: 2019-05-08].

[31] Norris, G., 2019. Rolls-Royce Runs First Composite Fan And Case Combo On Trent 1000. https://www.mro-network.com/manufacturing-distribution/

rolls-royce-runs-first-composite-fan-and-case-combo-trent-1000 [Online. Accessed: 2019-05-08].

[32] Wilson, M. J., 2007. "The Effects of Blade Variability in Gas Turbine Fan Assemblies". PhD thesis, Imperial College London.

[33] Denton, J. D., and Xu, L., 2002. "The Effects of Lean and Sweep on Transonic Fan Performance". In ASME Turbo Expo 2002: Power for Land, Sea, and Air, American Society of Mechanical Engineers, pp. 23–32.

[34] Calvert, W., and Ginder, R., 1999. "Transonic Fan and Compressor Design". *Proceedings of the Institution of Mechanical Engineers, Part C: Journal of Mechanical Engineering Science,* ***213***(5), pp. 419–436.

[35] Hooker, S., 1985. *Not Much of an Engineer.* Crowood Press UK.

[36] Schuff, M., Lengyel-Kampmann, T., and Forsthofer, N., 2017. "Influence of the Steady Deformation on Numerical Flutter Prediction for Highly Loaded and Flexible Fan Blades". In ASME Turbo Expo 2017: Turbomachinery Technical Conference and Exposition, American Society of Mechanical Engineers, pp. V07BT36A011–V07BT36A011.

[37] Rugg, D., 2010. Trends and Issues - Titanium Alloy use in Gas Turbines. Rolls-Royce plc. https://goo.gl/Hxzj6j [Online. Accessed: 2018-07-02].

[38] Brandstetter, C., 2019. Private Communication. Lausanne, Swtizerland.

[39] Brandstetter, C., Paoletti, B., and Ottavy, X., 2019. "Compressible Modal Instability Onset in An Aerodynamically Mistuned Transonic Fan". *Journal of Turbomachinery,* ***141***(3), p. 031004.

[40] Geer, A., 2019. Update on Ultrafan Programme. Rolls-Royce Mechanical UTC Partnership Annual Review, Derby.

[41] Cumpsty, N. A., 1989. *Compressor Aerodynamics.* Longman Scientific & Technical.

[42] Mikolajczak, A., Arnoldi, R., Snyder, L., and Stargardter, H., 1975. "Advances in Fan and Compressor Blade Flutter Analysis and Predictions". *Journal of Aircraft,* ***12***(4), pp. 325–332.

[43] Jousselin, O., 2016. Blade Tip Timing Uncertainty. US Patent 9,494,491 B2.

[44] Lad, B., 2018. Private Communication. London, United Kingdom.

[45] Wilson, M. J., Imregun, M., and Sayma, A. I., 2007. “The Effect of Stagger Variability in Gas Turbine Fan Assemblies”. *Journal of Turbomachinery,* ***129***(2), pp. 404–411.

[46] Stapelfeldt, S. C., and Vahdati, M., 2018. “On the Importance of Engine-Representative Models for Fan Flutter Predictions”. *Journal of Turbomachinery,* ***140***(8), p. 081005.

[47] Stratford, B., and Newby, D., 1977. “A New Look at the Generation of Buzz-Saw Noise”. In AIAA 4th Aeroacoustics Conference, AIAA Paper 77-1343, AIAA.

[48] Gliebe, P., Mani, R., Shin, H., Mitchell, B., Ashford, G., Salamah, S., Connell, S., and Huff, D., 2000. Aeroacoustic Prediction Codes. the National Aeronautics and Space Administration (NASA).

[49] McAlpine, A., Fisher, M., and Tester, B., 2006. “‘Buzz-Saw’ noise: A Comparison of Measurement with Prediction”. *Journal of Sound and Vibration,* ***290***(3-5), pp. 1202–1233.

[50] Han, F., Sharma, A., Paliath, U., and Shieh, C., 2014. “Multiple Pure Tone Noise Prediction”. *Journal of Sound and Vibration,* ***333***(25), pp. 6942–6959.

[51] Srinivasan, A., 1997. “Flutter and Resonant Vibration Characteristics of Engine Blades”. *Journal of Engineering for Gas Turbines and Power,* ***119***(4), pp. 742–775.

[52] Castanier, M. P., and Pierre, C., 2006. “Modeling and Analysis of Mistuned Bladed Disk Vibration: Current Status and Emerging Directions”. *Journal of Propulsion and Power,* ***22***(2), pp. 384–396.

[53] Vahdati, M., and Salles, L., 2015. “The Effects of Mistuning on Fan Flutter”. In Proceedings of the 14th International Symposium on Unsteady Aerodynamics, Aeroacoustics and Aeroelasticity of Turbomachines.

[54] Kielb, R. E., Feiner, D. M., Griffin, J. H., and Miyakozawa, T., 2004. “Flutter of Mistuned Bladed Disks and Blisks with Aerodynamic and FMM Structural Coupling”. In ASME Turbo Expo 2004: Power for Land, Sea, and Air, American Society of Mechanical Engineers, pp. 573–579.

[55] Cowles, B., 1996. “High Cycle Fatigue in Aircraft Gas Turbines—An Industry Perspective”. *International Journal of Fracture,* ***80***(2-3), pp. 147–163.

[56] El-Aini, Y., deLaneuville, R., Stoner, A., Capece, V., El-Aini, Y., deLaneuville, R., Stoner, A., and Capece, V., 1997. “High Cycle Fatigue of Turbomachinery Components - Industry Perspective”. In 33rd Joint Propulsion Conference and Exhibit, p. 3365.

[57] Australian Transportation Safety Board, 2001. Examination of a Failed Fan Blade Rolls-Royce RB211 Trent 892 Turbofan Engine. Available at: https://www.atsb.gov.au/publications/2001/tr200100445.aspx [Online. Accessed: 2018-08-30].

[58] National Transportation Safety Board, 2016. Investigative Update Provides Initial Findings in Investigation of Uncontained Engine Failure. Available at: https://www.ntsb.gov/news/press-releases/Pages/PR20160912.aspx [Online. Accessed: 2018-08-30].

[59] National Transportation Safety Board, 2018. DCA18MA142 SWA1380 Investigative Update. Available at: https://www.ntsb.gov/investigations/Pages/DCA18MA142.aspx [Online. Accessed: 2018-08-30].

[60] Sayma, A., Vahdati, M., Lee, S., and Imregun, M., 2003. “Forced Response Analysis of A Shaft-Driven Lift Fan”. *Proceedings of the Institution of Mechanical Engineers, Part C: Journal of Mechanical Engineering Science,* ***217***(10), pp. 1125–1137.

[61] Seinturier, E., 2007. “Forced Response Computation for Bladed Disks Industrial Practices and Advanced Methods”. In Proceedings of the 12th IFToMM World Congress, p. 1–17.

[62] Chan, K. S., Enright, M. P., Golden, P. J., Naboulsi, S., Chandra, R., and Pentz, A. C., 2012. “Probabilistic High-Cycle Fretting Fatigue Assessment of Gas Turbine Engine Components”. *Journal of Engineering for Gas Turbines and Power,* ***134***(6), p. 062502.

[63] Lu, Y., Green, J., Stapelfeldt, S. C., and Vahdati, M., 2019. “Effect of Geometric Variability on Running Shape and Performance of a Transonic Fan”. *Journal of Turbomachinery*, 09, pp. 1–9.

[64] Lu, Y., Lad, B., Vahdati, M., and Stapelfeldt, S. C., 2019. “Nonsynchronous Vibration Associated with Transonic Fan Blade Untwist”. In ASME Turbo Expo 2019: Turbomachinery Conference and Exposition, Phoenix AZ, USA, American Society of Mechanical Engineers.

[65] Lu, Y., Lad, B., Green, J., Vahdati, M., and Stapelfeldt, S. C., 2019. "Effect of Geometry Variability on Transonic Fan Blade Untwist". *International Journal of Turbomachinery, Propulsion and Power,* ***4***(3).

[66] Lu, Y., Green, J., Vahdati, M., and Stapelfeldt, S. C., 2018. "Effect of Geometry Variability on Fan Performance and Aeromechanical Characteristics". In 15th International Symposium on Unsteady Aerodynamics, Aeroacoustics and Aeroelasticity of Turbomachines, Oxford, UK, pp. 24–27.

[67] Lu, Y., Zhao, F., Salles, L., and Vahdati, M., 2017. "Aeroelastic Analysis of NREL Wind Turbine". In ASME Turbo Expo 2017: Turbomachinery Technical Conference and Exposition,Charlotte NC, USA, American Society of Mechanical Engineers, pp. V009T49A002–V009T49A002.

[68] Box, G. E., 1976. "Science and Statistics". *Journal of the American Statistical Association,* ***71***(356), pp. 791–799.

[69] Box, G. E., Luceno, A., and del Carmen Paniagua-Quinones, M., 2009. *Statistical Control by Monitoring and Adjustment*, Vol. 700. John Wiley & Sons.

[70] Vahdati, M., Simpson, G., and Imregun, M., 2011. "Mechanisms for Wide-Chord Fan Blade Flutter". *Journal of Turbomachinery,* ***133***(4), p. 041029.

[71] Choi, M., Smith, N. H., and Vahdati, M., 2013. "Validation of Numerical Simulation for Rotating Stall in A Transonic Fan". *Journal of Turbomachinery,* ***135***(2), p. 021004.

[72] Lee, K.-B., Wilson, M., and Vahdati, M., 2017. "Numerical Study on Aeroelastic Instability for A Low-Speed Fan". *Journal of Turbomachinery,* ***139***(7), p. 071004.

[73] Stapelfeldt, S. C., Parry, A. B., and Vahdati, M., 2016. "Investigation of Flutter Mechanisms of A Contra-Rotating Open Rotor". *Journal of Turbomachinery,* ***138***(5), p. 051009.

[74] Lee, K.-B., Wilson, M., and Vahdati, M., 2018. "Validation of a Numerical Model for Predicting Stalled Flows in a Low-Speed Fan — Part I: Modification of Spalart-Allmaras Turbulence Model". *Journal of Turbomachinery,* ***140***(5).

[75] Sayma, A. I., Vahdati, M., Sbardella, L., and Imregun, M., 2000. “Modeling of Three-Dimensional Viscous Compressible Turbomachinery Flows using Unstructured Hybrid Grids”. *AIAA Journal,* ***38***(6), June, pp. 945–954.

[76] Swanson, R. C., and Turkel, E., 1992. “On central-difference and upwind schemes”. In *Upwind and High-Resolution Schemes.* Springer, pp. 167–181.

[77] Spalart, P., and Allmaras, S., 1992. “A One-Equation Turbulence Model for Aerodynamic Flows”. In 30th Aerospace Sciences Meeting and Exhibit, p. 439.

[78] Sayma, A., Vahdati, M., and Imregun, M., 2000. “An Integrated Nonlinear Approach for Turbomachinery Forced Response Prediction. Part I: Formulation”. *Journal of Fluids and Structures,* ***14***(1), pp. 87–101.

[79] Sayma, A., Vahdati, M., Sbardella, L., and Imregun, M., 2000. “Modeling of Three-Dimensional Viscous Compressible Turbomachinery Flows Using Unstructured Hybrid Grids”. *AIAA journal,* ***38***(6), pp. 945–954.

[80] Gao, F., Poujol, N., Chew, J. W., and Beard, P. F., 2018. “Advanced Numerical Simulation of Turbine Rim Seal Flows and Consideration for RANS Turbulence Modelling”. In ASME Turbo Expo 2018: Turbomachinery Technical Conference and Exposition, American Society of Mechanical Engineers Digital Collection.

[81] Kim, S., Pullan, G., Hall, C., Grewe, R., Wilson, M., and Gunn, E., 2019. “Stall Inception in Low-Pressure Ratio Fans”. *Journal of Turbomachinery,* ***141***(7).

[82] Rumsey, C., 2020. Turbulence Modeling resource. NASA Langley Research Centre. https://turbmodels.larc.nasa.gov [Online. Accessed: 2020-03-11].

[83] Mayorca, M. A., 2011. “Numerical Methods for Turbomachinery Aeromechanical Predictions”. PhD thesis, KTH Royal Institute of Technology.

[84] Marshall, J., and Imregun, M., 1996. “An Analysis of the Aeroelastic Behaviour of a Typical Fan-Blade with Emphasis on the Flutter Mechanism”. In ASME 1996 International Gas Turbine and Aeroengine Congress and Exhibition, American Society of Mechanical Engineers, pp. V005T14A009–V005T14A009.

[85] Vahdati, M., Breard, C., Simpson, G., and Imregun, M., 2008. “Forced response assessment using modal force based indicator functions”. In ASME

Turbo Expo 2008: Power for Land, Sea, and Air, American Society of Mechanical Engineers, pp. 665–672.

[86] Timon, V. P., and Corral, R., 2014. “A Study on the Effects of Geometric Non Linearities on the Un-running Transformation of Compressor Blades”. In ASME Turbo Expo 2014: Turbomachinery Technical Conference and Exposition, American Society of Mechanical Engineers.

[87] Yang, H., and Zheng, Y. “A Fluid-Structure Coupling Method for Rotor Blade Unrunning Design”. In ASME Turbo Expo 2013: Turbomachinery Technical Conference and Exposition, American Society of Mechanical Engineers.

[88] Petrov, E., 2019. Private Communication. Phoenix, AZ, US.

[89] Silver, N., 2012. *The Signal and the Noise: Why So Many Predictions Fail - but Some Don’t.* Penguin.

[90] V. Kaza, K. R., and Kielb, R. E., 1982. “Flutter and Response of a Mistuned Cascade in Incompressible Flow”. *AIAA Journal,* ***20***(8), pp. 1120–1127.

[91] Salles, L., and Vahdati, M., 2016. “Comparison of Two Numerical Algorithms for Computing the Effects of Mistuning of Fan Flutter”. In ASME Turbo Expo 2016: Turbomachinery Technical Conference and Exposition, American Society of Mechanical Engineers, pp. V07BT34A018–V07BT34A018.

[92] Figaschewsky, F., Kühhorn, A., Beirow, B., Nipkau, J., Giersch, T., and Power, B., 2017. “Design and Analysis of An Intentional Mistuning Experiment Reducing Flutter Susceptibility and Minimizing Forced Response of a Jet Engine Fan”. In ASME Turbo Expo 2017: Turbomachinery Technical Conference and Exposition, American Society of Mechanical Engineers, pp. V07BT36A020–V07BT36A020.

[93] Kasparov, G., 2008. *How Life Imitates Chess.* Random House.

[94] Diamond, J., 1997. *Guns, Germs, and Steel: the Fates of Human Societies.* W.W. Norton & Company.

[95] Pedregosa, F., Varoquaux, G., Gramfort, A., Michel, V., Thirion, B., Grisel, O., Blondel, M., Prettenhofer, P., Weiss, R., Dubourg, V., Vanderplas, J., Passos, A., Cournapeau, D., Brucher, M., Perrot, M., and Duchesnay, E., 2011. “Scikit-learn: Machine Learning in Python”. *Journal of Machine Learning Research,* ***12***, pp. 2825–2830.

[96] Breiman, L., Friedman, J., Olshen, R., and Stone, C., 1984. *Classification and Regression Trees.* The Wadsworth Statistics/Probability series. Belmont, Calif. : Wadsworth International Group.

[97] Silver, D., Huang, A., Maddison, C. J., Guez, A., Sifre, L., Van Den Driessche, G., Schrittwieser, J., Antonoglou, I., Panneershelvam, V., Lanctot, M., et al., 2016. “Mastering the game of Go with deep neural networks and tree search”. *Nature,* ***529***(7587), p. 484.

[98] Vinyals, O., Babuschkin, I., Chung, J., Mathieu, M., Jaderberg, M., Czarnecki, W. M., Dudzik, A., Huang, A., Georgiev, P., Powell, R., Ewalds, T., Horgan, D., Kroiss, M., Danihelka, I., Agapiou, J., Oh, J., Dalibard, V., Choi, D., Sifre, L., Sulsky, Y., Vezhnevets, S., Molloy, J., Cai, T., Budden, D., Paine, T., Gulcehre, C., Wang, Z., Pfaff, T., Pohlen, T., Wu, Y., Yogatama, D., Cohen, J., McKinney, K., Smith, O., Schaul, T., Lillicrap, T., Apps, C., Kavukcuoglu, K., Hassabis, D., and Silver, D., 2019. AlphaStar: Mastering the Real-Time Strategy Game StarCraft II. https://deepmind.com/blog/alphastar-mastering-real-time-strategy-game-starcraft-ii/ [Online. Accessed: 2019-03-12].

[99] Parkhi, O. M., Vedaldi, A., Zisserman, A., and Jawahar, C., 2012. “Cats and Dogs”. In 2012 IEEE Conference on Computer Vision and Pattern Recognition, IEEE, pp. 3498–3505.

[100] Yang, B.-S., Lim, D.-S., and Tan, A. C. C., 2005. “VIBEX: an expert system for vibration fault diagnosis of rotating machinery using decision tree and decision table”. *Expert Systems with Applications,* ***28***(4), pp. 735–742.

[101] Yang, B. S., Park, C. H., and Kim, H. J., 2000. “An Efficient Method of Vibration Diagnostics for Rotating Machinery using a Decision Tree”. *International Journal of Rotating Machinery,* ***6***(1), pp. 19–27.

[102] Widodo, A., and Yang, B.-S., 2007. “Support Vector Machine in Machine Condition Monitoring and Fault Diagnosis”. *Mechanical Systems and Signal Processing,* ***21***(6), pp. 2560–2574.

[103] Podgorelec, V., Kokol, P., Stiglic, B., and Rozman, I., 2002. “Decision Trees: An Overview and Their Use in Medicine”. *Journal of Medical Systems,* ***26***(5), pp. 445–463.

[104] Saimurugan, M., Ramachandran, K., Sugumaran, V., and Sakthivel, N., 2011. “Multi Component Fault Diagnosis of Rotational Mechanical System

based on Decision Tree and Support Vector Machine". *Expert Systems with Applications,* ***38***(4), pp. 3819–3826.

[105] Quinlan, J. R., 1986. "Induction of Decision Trees". *Machine learning,* ***1***(1), pp. 81–106.

[106] Quinlan, J. R., 2014. *C4. 5: Programs for Machine Learning.* Elsevier.

[107] Kotsiantis, S. B., Zaharakis, I., and Pintelas, P., 2007. "Supervised Machine Learning: A Review of Classification Techniques". *Emerging Artificial Intelligence Applications in Computer Engineering,* ***160***, pp. 3–24.

[108] Bishop, C. M., 2007. *Pattern Recognition and Machine Learning.* Springer.

[109] Géron, A., 2017. *Hands-on Machine Learning with Scikit-Learn and TensorFlow: Concepts, Tools, and Techniques to Build Intelligent Systems.* O'Reilly Media, Inc.

[110] Elston, S., and Rudin, C., 2018. Principles of Machine Learning. https://www.edx.org/course/principles-of-machine-learning [Online. Accessed: 2019-01-06].

[111] Spiegelhalter, D., 2019. *The Art of Statistics: Learning from Data.* Pelican Books. Penguin Books Limited.

[112] Ribeiro, M. T., Singh, S., and Guestrin, C., 2016. "Why Should I Trust You?: Explaining the Predictions of Any Classifier". In Proceedings of the 22nd ACM SIGKDD international conference on knowledge discovery and data mining, ACM, pp. 1135–1144.

[113] Cortes, C., and Vapnik, V., 1995. "Support-Vector Networks". *Machine learning,* ***20***(3), pp. 273–297.

[114] Vapnik, V., 2013. *The Nature of Statistical Learning Theory.* Springer Science & Business Media.

[115] Oshii, M., 1995. Ghost in the Shell. Film.

[116] Kamiyama, K., 2002. Ghost in the Shell: Stand Alone Complex. Animated series.

[117] Michel, U., 2011. "The Benefits of Variable Area Fan Nozzles on Turbofan Engines". In 49th AIAA Aerospace Sciences Meeting including the New Horizons Forum and Aerospace Exposition, p. 226.

[118] Zhang, W., Vahdati, M., and Stapelfeldt, S. C., 2019. “Stall and Recovery Process of a Transonic Fan with Inlet Distorition”. In 13th European Turbomachinery Conference, Lausanne, Switzerland, European Turbomachinery Society.

[119] Longley, J., and Greitzer, E., 1992. “Inlet Distortion Effects in Aircraft Propulsion System Integration”. *AGARD Lecture Series 183.*

[120] Hall, D., Greitzer, E., and Tan, C., 2017. “Analysis of Fan Stage Conceptual Design Attributes for Boundary Layer Ingestion”. *Journal of Turbomachinery,* ***139***(7), p. 071012.

[121] Federal Aviation Administration, 2017. Aeronautical Information Manual. US Department of Transportation, Washington, DC.

[122] Sureshkumar, P., Vahdati, M., Parry, A., Blanchi, S., and Doherty, M., 2017. “Towards A Holistic Prediction of Fan Stage Tone Noise Mechanisms”. In 12th European Turbomachinery Conference, Stockholm, Sweden, European Turbomachinery Society.

[123] Rolls-Royce plc, 2015. Buzz-Saw noise: Mesh Quality Criteria.

[124] Quinlan, J. R., 2019. Information on See5 /C5.0. RuleQuest Research. https://www.rulequest.com/see5-info.html [Online. Accessed: 2019-08-10].

[125] Fisher, R. A., 1936. “The Use of Multiple Measurements in Taxonomic Problems”. *Annals of Eugenics,* ***7***(2), pp. 179–188.

[126] Willems, K., 2018. Machine Learning in R for Beginners. https://www.datacamp.com/community/tutorials/machine-learning-in-r [Online. Accessed: 2019-05-01].

[127] Rokach, L., and Maimon, O., 2005. “Top-Down Induction of Decision Trees Classifiers - A Survey”. *IEEE Transactions on Systems, Man, and Cybernetics, Part C (Applications and Reviews),* ***35***(4), pp. 476–487.

[128] scikit-learn developers, 2018. Documentation of scikit-learn 0.20.3. https://scikit-learn.org/stable/documentation.html# [Online. Accessed: 2019-05-01].

Appendix A

Global MRO Market Forecast 2019-2029

A.1 Commercial Aircraft Fleet Forecast

Region	Fleet Size			Average Age	
	2019	2029	Growth Rate	2019	2029
Africa	1125	1325	1.6%	15.5	14.7
Asia Pacific	4410	6629	4.2%	9.7	10.3
China	3376	7209	7.9%	6.4	9.0
India	604	1547	9.9%	7.1	10.7
Middle East	1440	2277	4.7%	9.3	9.6
Latin America	1771	2387	3.0%	11.4	9.9
North America	8033	9247	1.4%	14.1	12.1
Eastern Europe	1414	1743	2.1%	11.6	12.6
Western Europe	5319	6811	2.5%	11.4	10.6
World	27492	39175	3.6%	11.3	10.7

Source: Cooper et al., 2019 [6].

Table A.1: Commerical aircraft fleet forecast by region 2019-2029.

A.2 Commercial Aircraft MRO Market Forecast

Region	MRO by component				Total MRO			
	Engine		Others		Total			
	2019	2029	2019	2029	2019	2029	Growth	Growth Rate
Africa	0.9	1.3	1.7	2.1	2.6	3.4	0.8	2.7%
Asia Pacific	7.1	8.5	8.2	11.8	15.3	20.3	5.0	2.9%
China	2.2	7.3	5.0	11.0	7.2	18.3	11.1	9.7%
India	0.7	1.6	1.3	2.4	2.0	4.0	2.0	7.1%
Middle East	5.6	8.0	3.4	5.1	9.0	13.1	4.1	3.9%
Latin America	1.5	2.3	2.6	3.3	4.1	5.6	1.5	3.2%
North America	7.8	10.3	12.7	14.2	20.5	24.5	4.0	1.8%
Eastern Europe	1.6	2.0	2.7	3.2	4.3	5.2	0.9	2.0%
Western Europe	6.0	8.7	10.9	12.8	16.9	21.5	4.6	2.5%
World	33.4	50.0	48.5	66.0	81.9	116.0	34.1	3.5%

Unit: Billions USD.

Source: Cooper et al., 2019 [6].

Table A.2: Commerical aircraft MRO forecast by conponent and region 2019-2029.

Appendix B

Machine Learning Algorithms

B.1 Decision Tree Algorithm

There are various Decision Tree algorithms including ID3 (Iterative Dichotomiser 3) [105], C4.5 [106], C5.0 [124], and CART (Classification And Regression Tree) [96]. C4.5 and C5.0 are successors of the ID3 algorithm. The optimised CART algorithm implemented in the scikit-learn library [95] is used in this study. To illustrate its algorithm, the decision tree model is applied onto a simple dataset, the *Iris Dataset* [125]. The mathematics formulation behind the model is then introduced to explain how the model is trained.

B.1.1 The Iris Dataset

The *Iris Dataset* contains measurements for 3 species of iris which are illustrated in Figure B.1 (Image source: Williams, 2018 [126]). Evidently, it is not possible for someone from a different discipline[1] to distinguish the three types of plant visually. Within the dataset, there are 50 sets of sepal and pedal measurements for each class/species (i.e. 150 sets in total). Sepal and petal are labelled in Figure B.1. The measurements (i.e. features) are in terms of sepal length, sepal width, petal length, and petal width.

Two ways of visualising this dataset are presented in Figure B.2 and B.3. Different types of marker are used to distinguish the data points based on their labels. It is clear that one of the classes, iris-setosa, is linearly separable from the other two which are linearly inseparable from each other. Fortunately, the decision tree algorithm can be applied here to optimise the classification approach. For simplicity, the algorithm

---

[1] Despite having a strong interest in felinology, the author does not hold an academic degree in biology or related fields.

is applied onto a subset of the dataset, containing only the petal measurements (visualised in Figure B.3). The decision tree shown in Figure B.4[2] is grown and its corresponding decision boundary is visualised in Figure B.5[3]. Note that, the maximum number of split is limited to 2 in this case.

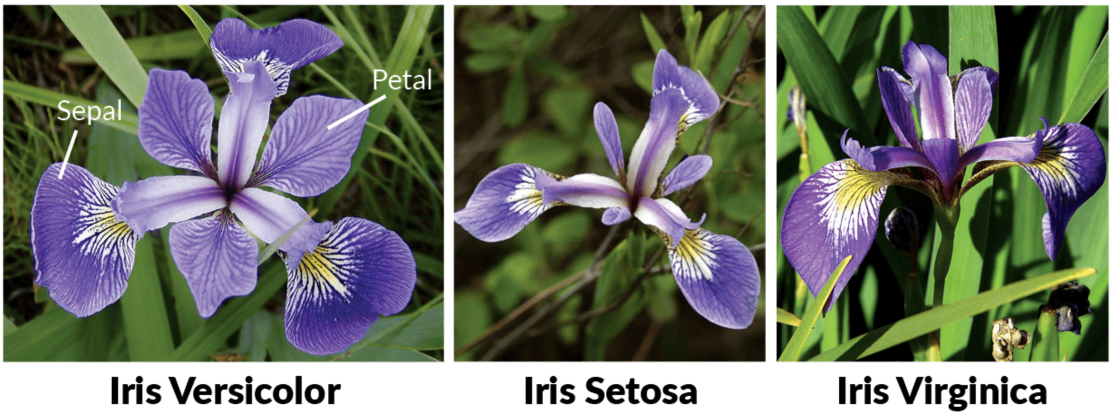

Figure B.1: Three species of Iris.

---

[2] Source: Géron, 2017 [109]

[3] Adapted from Gèron [109].

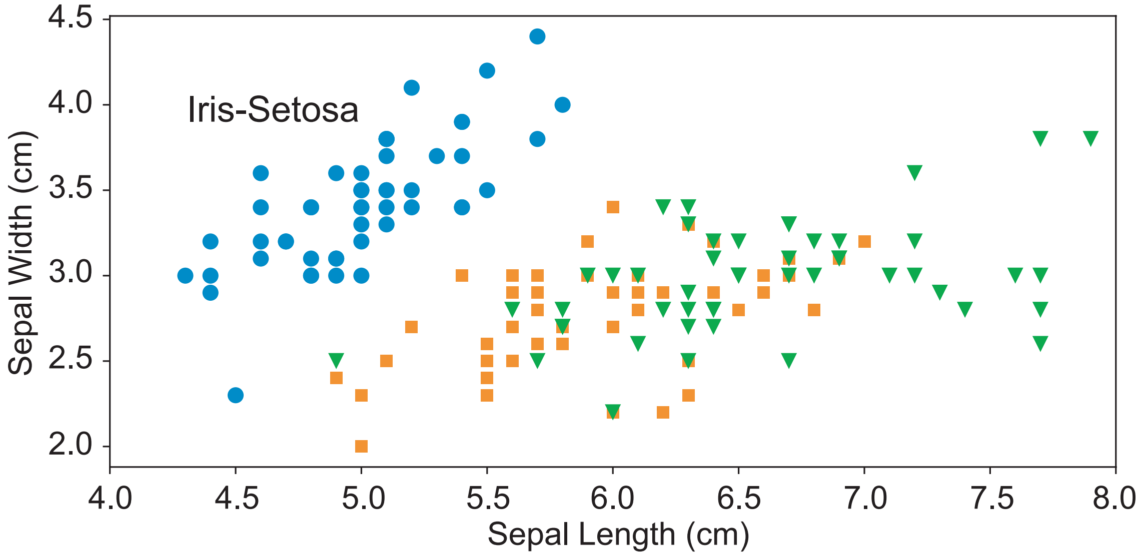

Figure B.2: Iris dataset (sepal measurement).

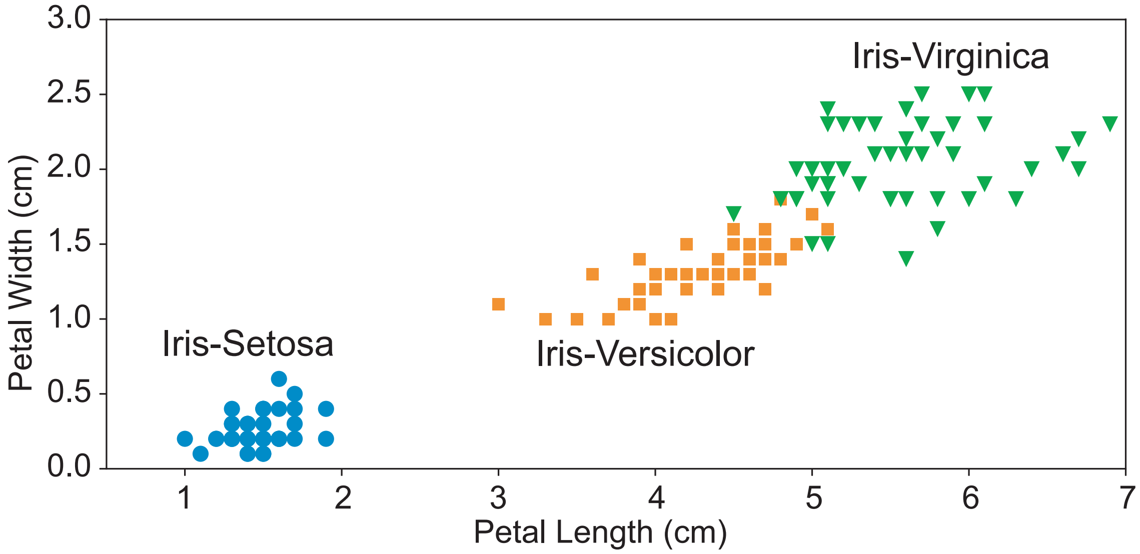

Figure B.3: Iris dataset (petal measurement).

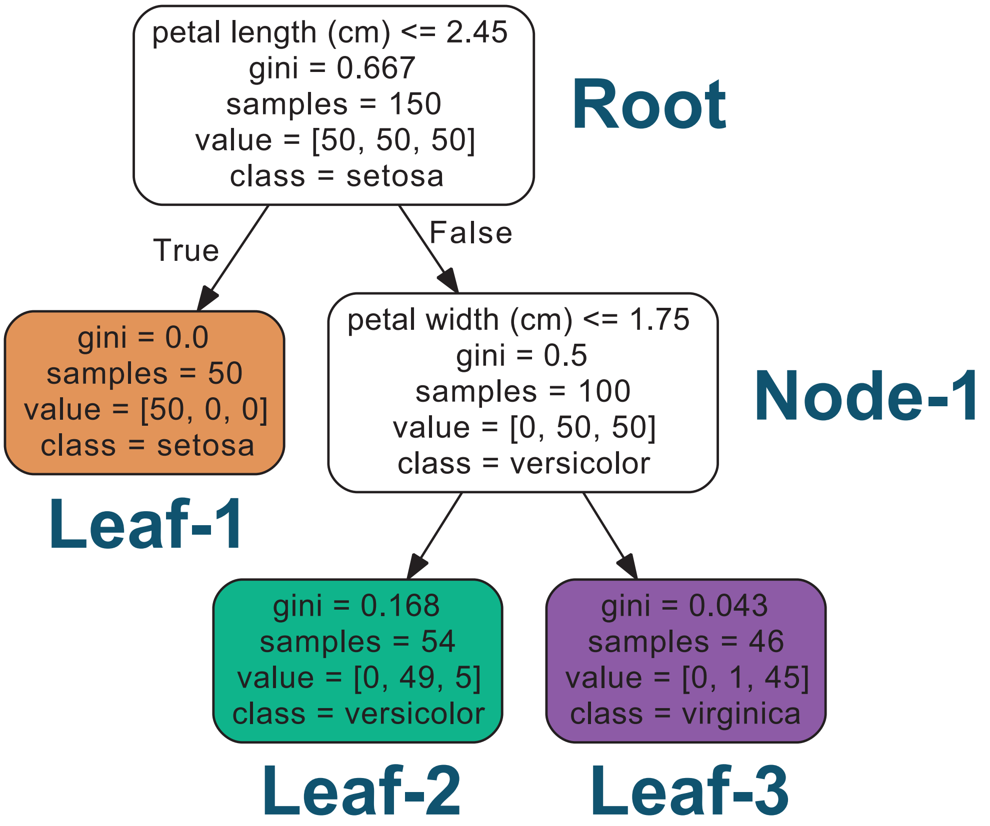

Figure B.4: Decision Tree Classifier for Iris species classification.

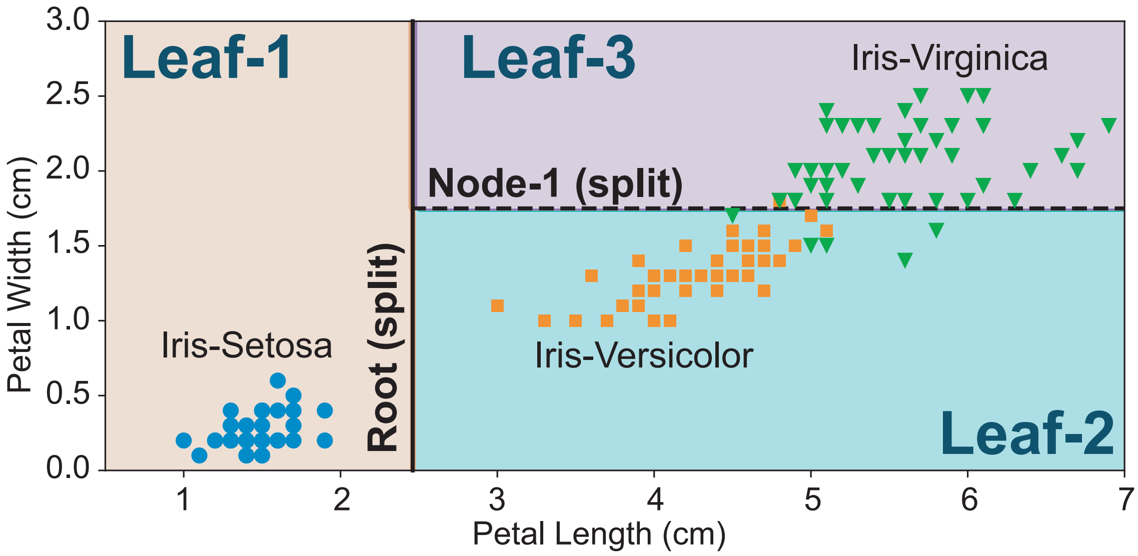

Figure B.5: Decision boundary for the tree classifier.

In essence, the decision tree in Figure B.4 outlines the numerical criteria for the iris species classification while Figure B.5 illustrates the split visually. In Figure B.4, the information included in all the ‘blocks’ are the total number of (remaining) samples, the composition of the samples based on the known label, the dominant class, and the gini index which is an impurity measure and will be explained in later sections. As the cases are being classified while tree ‘grows’ from the root to the leaves, the total number of remaining samples decreases. The composition of the remaining samples are tracked by the ‘value’ parameter. For example, in Leaf-2, there are 0 iris-setosa cases, 49 iris-versicolor cases, and 5 iris-virginica samples.

The Root node and Node-1 set the condition and threshold value for the classification. To be more specific, starting from the root node, any sample with petal length not more than 2.45 cm is identified to be iris-setosa. Node-1 uses the petal width measurement to separate the iris-virginica and iris-versicolor. As illustrated by both Figure B.4 and B.5, there are a few mis-classified instances since the iris-virginica and iris-versicolor class are not linearly separable. The algorithm for locating the most optimal splitting criteria is introduced in the next section.

B.1.2 The CART Algorithm

The Gini index, shown in Equation B.1, measures the ‘impurity’ at each node in Figure B.4. It peaks when the classes are equally distributed and thus the node is ‘impure’. The upper limit of the Gini Index is 0.5 for a binary classification study and is 0.667 for a ternary one (i.e. the Root node in Figure B.4). The lower limit of the Gini Index is 0 when one class dominates a node and thus the node is ‘pure’ (i.e. Leaf-1 in Figure B.4). An alternative measure of impurity to the Gini Index is Entropy[4] [109, 127, 128] which is shown in Equation B.2. In this study, the decision trees obtained through the two criteria are comparable.

Gini index:

$$G_i = 1 - \sum_{k=1}^{n} {p_{i,k}}^2 \tag{B.1}$$

$p_{i,k}$: ratio of class k instances among the trainig instances in the i^{th} node

Entropy:

$$E_i = - \sum_{k=1}^{n} p_{i,k} log(p_{i,k}) \tag{B.2}$$

The Classification and Regression Tree (CART) algorithm produces binary trees. Thus, each node is split into two branches /subsets based on a features and a thresh-

---

[4] Not the same property studied in thermodynamics.

old value as illustrated in Figure B.4. To determine the optimal combination of the feature and the threshold value, the CART algorithm employs the cost function [128] shown in Equation B.3 to produce the purest nodes. This optimisation is conducted locally at each node. The splitting is repeated at each subset in order to 'grow' the tree. This process is terminated when certain criteria are fulfilled. For example, the decision tree shown in Figure B.4 is limited to have a maximum depth of 2. Alternatively, the growth can be terminated when the algorithm cannot find splits to further reduce the impurity of the nodes. To be more specific, Leaf-1 is dominated entirely by the iris-setosa class and hence no further split is possible /necessary.

Tree Classifier (CART) Cost Function [128]:

$$J(k, t_k) = \frac{m_{left}}{m} G_{\text{left}} + \frac{m_{right}}{m} G_{right} \tag{B.3}$$

where

$$\begin{cases} G_{\text{left/right}} \text{ is the impurity of the left/right subset,} \\ m_{\text{left/right}} \text{ is the number of instances in the subset.} \end{cases}$$

To ensure the trained model does not overfit the training dataset and thus can perform well against new data, the *cross-validation* technique is used. Essentially, the training dataset is divided into complementary subsets. The model is trained on different combinations of subsets and validated against the rest. This helps to find the most optimal hyperparameters /tunable parameters (e.g. the maximum depth parameter) to be used on the full training dataset. More detailed discussion on this topic can be found in literature [108, 109, 111].

B.1.3 Strengths and Weaknesses of the Tree Algorithm

The Decision Tree model has various strengths and weaknesses [96, 108, 109, 128]. The following discussion will focus on their implication in the context of the APD & NSV study.

- **Automatic Feature Selection**

  As demonstrated by Section B.1.1 and B.1.2, in order to perform the split which generate the purest nodes, the CART algorithm performs a search for the most optimal combination of features and threshold values. Thus, feature selection is performed to reduce the complexity in the system. This in turn identifies the most useful feature(s) for classification purpose and reveals the hidden structure inside the data. For the NSV study, this process can help to filter out the most important controlling factors for NSV from the complex mis-stagger patterns and is thus extremely useful for the study.

- **Locally optimised**

As mentioned in Section B.1.2, the optimisation of the splitting criteria is optimised locally at each node. Therefore, for datasets with complex hidden structure, there is no guarantee the resulting decision tree model is optimised globally. This issue can be mitigated by training various trees using randomly sampled subsets of the training data and take the majority vote of the trees as the predicted outcome [128]. However, as it will demonstrated later, this is not a major concern for this study since the resulting tree model for the NSV dataset is relatively simple.

- **Interpretability and trustworthiness**

As demonstrated by Figure B.4, the resulting decision tree clearly visualises the hidden structure inside the *iris dataset* and reveals the conditional statements used to classify each case. The easily understood information structure is illuminating and facilitate the understanding of the problem.

The interpretability of the model also contributes to its trustworthiness which is vital from the industry perspective. In general, machine learning models utilise the correlation between features and behaviours for classification. This can result in models that establish irrelevant associations between the two [111, 112]. This is particularly true for the artificial neural networks which are commonly referred to as 'black box' models as they do not explain how the decisions are reached. In fact, as demonstrated by Ribeiro et al. [112], a neural network based classification model incorrectly used the snow in the background (or light background at the bottom) as a dominating feature in the classification of photos of wolves and huskies (a type of sled dog).

Without understanding how and why the model does the classification, it is difficult to establish trust of the model. In the context of canine photo classification, this is nothing of concern. However, in the context of civil aviation where safety concern is fundamental to most of the decision making, the lack of understanding how the model operates would be extremely troubling.

In addition, with no additional effort, the resulting decision tree model provides the probability for both classification and misclassification. In Figure B.4, for an iris measurement not fulfilling either criteria outlined by the Root node and Node-1 (i.e. instance in Leaf-3), it has a 2.2% (i.e. 1/46) probability of being classified as iris-versicolor and a 97.8% (i.e. 45/46) probability of being classified as iris-virginica. This further enhances the trustworthiness in the results as the model output both the predicted outcome and the probability of misclassification. In other words, the strength and weakness of the model in making prediction are clearly shown.

B.2 Logistic Regression Classifier

The logistic regression classifier is a linear model with a non-linear response. To make prediction with the logistic regression classifier, a weighted sum of the features are first calculated as shown in Equation B.4. The corresponding vectorised form is shown in Equation B.5.

$$h_{\boldsymbol{\theta}}(\mathbf{x}) = \theta_0 + \theta_1 x_1 + \theta_2 x_2 + \cdots + \theta_n x_n \tag{B.4}$$

$$h_{\boldsymbol{\theta}}(\mathbf{x}) = \boldsymbol{\theta}^T \cdot \mathbf{x} \tag{B.5}$$

where $h_{\boldsymbol{\theta}}(\mathbf{x})$ is the hypothesis function [109]. θ_i is the weight for the ith features x_i. θ_0 is also known as the bias term. To ensure the machine learning model performs well with features of vastly different ranges, e.g. the features shown in Table 5.2, the features are scaled. In this study, the data is *standardised* [109, 110]. Thus, for each feature, the data are transformed such that the scaled data has a mean value of zero and a unit variance.

The predicted probability of whether the instance belong to a class is then computed through Equation B.6 and B.7. The behaviour of the sigmoid function is illustrated in Figure B.6. The output from the sigmoid function ranges from 0 to 1.

$$\hat{p} = \sigma(\boldsymbol{\theta}^T \mathbf{x}) \tag{B.6}$$

Logistic function:

$$\sigma(t) = \frac{1}{1 + \exp(-t)} \tag{B.7}$$

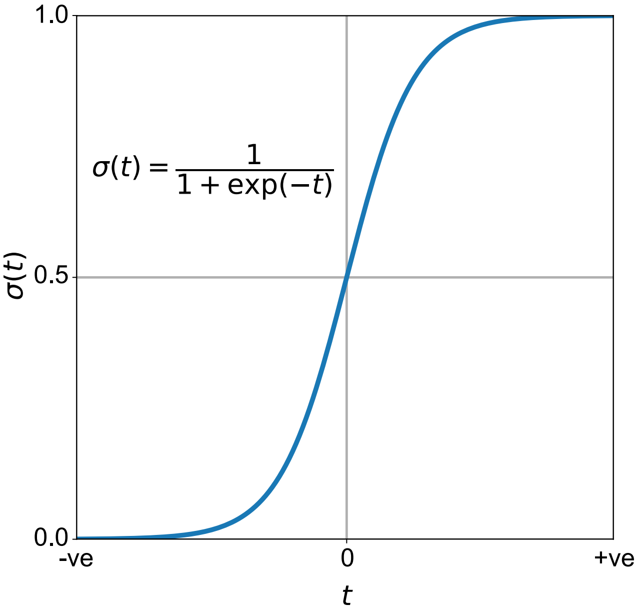

Figure B.6: Sigmoid Function.

The probability $\hat{p}$ determined by the sigmoid function is then used to make prediction based on the criteria shown in Equation B.8. In essence, the model will predict the case of interest belongs to the positive class if the weighted sum $\boldsymbol{\theta}^T \cdot \mathbf{x} \geq 0$, vice versa.

$$\hat{y} = \begin{cases} 0 & \text{if } \hat{p} < 0.5, \\ 1 & \text{if } \hat{p} \geq 0.5. \end{cases} \tag{B.8}$$

To train the model and thus to tune the feature weight parameters, cost functions are used to penalise misclassification errors. The cost function for a single case can be expressed as shown in Equation B.9. For example, a large penalty $-\log(\hat{p})$ is incurred when a case from the positive class (i.e. label $y = 1$) is misclassified to belong to the negative class (i.e. $\hat{p} < 0.5$ and thus the predicted behaviour $\hat{y} = 0$). In fact, the penalty $-\log(\hat{p})$ increases with decreasing $\hat{p}$ value and hence it increases with the difference between the real and the predicted behaviour. In contrast, a correctly predicted outcome only leads to a small penalty.

$$c(\boldsymbol{\theta}) = \begin{cases} -\log(\hat{p}) & \text{if } y = 1, \\ -\log(1-\hat{p}) & \text{if } y = 0. \end{cases} \tag{B.9}$$

The cost function for the entire training dataset (with m cases) can be expressed as shown in Equation B.10. It is also termed the *log loss*. Thus, the classifier can be trained by solving for the set of feature weight values that minimise the cost function $J(\boldsymbol{\theta})$. However, there is no known closed-form solution for this purpose [109]. Fortunately, the optimisation can be achieved iteratively through a *Gradient Descent* approach. In essence, the local gradient of the cost function is determined and the algorithm tunes the parameters in the direction of descending gradient in order to find the minimum value. Further discussion on Gradient Descent can be found in various literature [108, 109].

$$J(\boldsymbol{\theta}) = -\frac{1}{m}\sum_{i=1}^{m}\left[y^{(i)}log\left(\hat{p}^{(i)}\right) + (1-y^{(i)})log\left(1-\hat{p}^{(i)}\right)\right] \tag{B.10}$$

Appendix C

Additional Data for Chapter 5

C.1 Subset of the Dataset used in the Machine Learning Study

The dataset presented in Table C.1 is a subset of the dataset used in Chapter 5. The features, predicted outcomes by the **Decision Tree Classifier**, and labels of 8 instances are presented.

Case ID		HY42	HY44	HY46	HY48	HY50	HY52	HY54	HY56
Features	AmpAbs	0.06885	0.05803	0.09200	0.03699	0.02956	0.02973	0.03985	0.07902
	AmpPlus	0.06885	0.05803	0.09200	0.03699	0.02956	0.02973	0.03966	0.07902
	AmpMinus	-0.06709	-0.05713	-0.09200	-0.03676	-0.02105	-0.02739	-0.03985	-0.07448
	MeanMSTG	0.00653	0.01707	-0.00362	0.00304	0.00111	-0.00248	0.00054	-0.01356
	Variance	0.00249	0.00154	0.00337	0.00053	0.00027	0.00034	0.00054	0.00199
	RDelta	0.11936	0.09839	0.10700	0.06175	0.03629	0.05476	0.06181	0.13229
	RDelta(ABS)	0.12608	0.09839	0.14800	0.07224	0.04723	0.05476	0.06780	0.13229
	DominantND	10	6	6	9	6	11	13	13
	WeakestND	1	1	1	8	13	3	4	9
	APDsignalND	4.559E-17	1.689E-17	6.309E-17	5.975E-03	3.431E-04	5.664E-03	2.101E-02	5.088E-02
Label	NSV behaviour	**0**	**1**	**1**	**1**	**1**	**0**	**0**	**0**
Model Outcome		TN	TP	TP	TP	TP	FP	TN	TN

Table C.1: A subset of the data used in the machine learning study.

Actual NSV behaviour		Nature of the classification outcome	
1	NSV	TP	True Positive
0	Non-NSV	TN	True Negative
		FP	False Positive
		FN	False Negative

C.2 Classifiers' Performance on the Test Dataset

Case	Label	CART	Pred.	LRC-2	Pred.	SVC	Pred.
01	1	1	TP	1	TP	1	TP
02	0	0	TN	0	TN	0	TN
03	0	0	TN	0	TN	0	TN
04	1	1	TP	1	TP	0	FN
05	0	0	TN	0	TN	0	TN
06	0	0	TN	0	TN	0	TN
07	0	0	TN	1	FP	0	TN
08	1	1	TP	1	TP	1	TP
09	0	0	TN	0	TN	0	TN
10	0	0	TN	0	TN	0	TN
11	0	0	TN	0	TN	0	TN
12	1	1	TP	1	TP	1	TP
13	1	1	TP	1	TP	1	TP
14	0	0	TN	0	TN	0	TN
15	1	1	TP	1	TP	1	TP
16	0	0	TN	0	TN	0	TN
17	0	0	TN	0	TN	0	TN
18	0	0	TN	0	TN	0	TN
19	1	1	TP	1	TP	1	TP
20	0	0	TN	0	TN	0	TN
21	0	0	TN	0	TN	0	TN
22	0	0	TN	0	TN	0	TN
23	0	0	TN	0	TN	0	TN
24	0	1	FP	1	FP	0	TN
25	0	0	TN	0	TN	1	FP

Pred.	Error type basd on the predicted behaviour	TP	True Positive
		TN	True Negative
1	NSV	FP	False Positive
0	Non-NSV	FN	False Negative

Table C.2: Predicted behaviour of each test case.

Cases where a disagreement exists among the classifiers are highlighted in red.